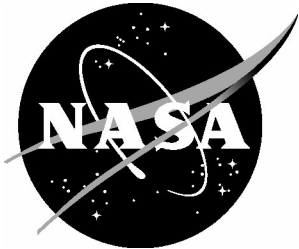


NASA/TP-20220019141



# P-ACTIVE Project Report

*Hyun Jung Kim, Stephen Borg, Scott Bartram, Kiumars Aryana, William Humphreys  
NASA Langley Research Center, Hampton, VA USA*

*Juejun Hu<sup>1,2</sup>, Tian Gu<sup>1,2</sup>, Sensong An<sup>1</sup>, Yifei Zhang<sup>1</sup>, Cosmin-Constantin Popescu<sup>1</sup>*

*<sup>1</sup>Department of Materials & Science Engineering, Massachusetts Institute of Technology,  
Cambridge, MA, USA*

*<sup>2</sup>Materials Research Laboratory, Massachusetts Institute of Technology, Cambridge, MA, USA*

*Calum Williams*

*Departments of Physics, University of Cambridge, Cambridge, UK*

*Matthew Julian*

*Booz Allen Hamilton, Arlington, VA, USA*

*David Bombara*

*John A. Paulson School of Engineering and Applied Sciences  
Harvard University, Cambridge, MA, USA*

# NASA STI Program Report Series

Since its founding, NASA has been dedicated to the advancement of aeronautics and space science. The NASA scientific and technical information (STI) program plays a key part in helping NASA maintain this important role.

The NASA STI program operates under the auspices of the Agency Chief Information Officer. It collects, organizes, provides for archiving, and disseminates NASA's STI. The NASA STI program provides access to the NTRS Registered and its public interface, the NASA Technical Reports Server, thus providing one of the largest collections of aeronautical and space science STI in the world. Results are published in both non-NASA channels and by NASA in the NASA STI Report Series, which includes the following report types:

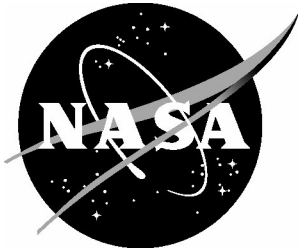
- **TECHNICAL PUBLICATION.** Reports of completed research or a major significant phase of research that present the results of NASA Programs and include extensive data or theoretical analysis. Includes compilations of significant scientific and technical data and information deemed to be of continuing reference value. NASA counterpart of peer-reviewed formal professional papers but has less stringent limitations on manuscript length and extent of graphic presentations.
- **TECHNICAL MEMORANDUM.** Scientific and technical findings that are preliminary or of specialized interest, e.g., quick release reports, working papers, and bibliographies that contain minimal annotation. Does not contain extensive analysis.
- **CONTRACTOR REPORT.** Scientific and technical findings by NASA-sponsored contractors and grantees.
- **CONFERENCE PUBLICATION.** Collected papers from scientific and technical conferences, symposia, seminars, or other meetings sponsored or co-sponsored by NASA.
- **SPECIAL PUBLICATION.** Scientific, technical, or historical information from NASA programs, projects, and missions, often concerned with subjects having substantial public interest.
- **TECHNICAL TRANSLATION.** English-language translations of foreign scientific and technical material pertinent to NASA's mission.

Specialized services also include organizing and publishing research results, distributing specialized research announcements and feeds, providing information desk and personal search support, and enabling data exchange services.

For more information about the NASA STI program, see the following:

- Access the NASA STI program home page at <http://www.sti.nasa.gov>
- Help desk contact information:  
<https://www.sti.nasa.gov/sti-contact-form/> and select the "General" help request type.

NASA/TP-20220019141



# P-ACTIVE Project Report

*Hyun Jung Kim, Stephen Borg, Scott Bartram, Kiumars Aryana, William Humphreys  
NASA Langley Research Center, Hampton, VA USA*

*Juejun Hu<sup>1,2</sup>, Tian Gu<sup>1,2</sup>, Sensong An<sup>1</sup>, Yifei Zhang<sup>1</sup>, Cosmin-Constantin Popescu<sup>1</sup>*

*<sup>1</sup>Department of Materials & Science Engineering, Massachusetts Institute of Technology,  
Cambridge, MA, USA*

*<sup>2</sup>Materials Research Laboratory, Massachusetts Institute of Technology, Cambridge, MA, USA*

*Calum Williams*

*Departments of Physics, University of Cambridge, Cambridge, UK*

*Matthew Julian*

*Booz Allen Hamilton, Arlington, VA, USA*

*David Bombara*

*John A. Paulson School of Engineering and Applied Sciences  
Harvard University, Cambridge, MA, USA*

National Aeronautics and  
Space Administration

Langley Research Center  
Hampton, Virginia 23681-2199

---

February 2023

The use of trademarks or names of manufacturers in this report is for accurate reporting and does not constitute an official endorsement, either expressed or implied, of such products or manufacturers by the National Aeronautics and Space Administration.

Available from:

NASA STI Program / Mail Stop 148  
NASA Langley Research Center  
Hampton, VA 23681-2199  
Fax: 757-864-6500

## Executive Summary

The Phase change material-based actively-tunable filter (P-ACTIVE, Dr. Hyun Jung Kim, the Principal Investigator / PI) project is a NASA Langley Research Center (LaRC)-led research endeavor that began as a NASA CIF (Center Innovation Fund) project in 2019. The goal of P-ACTIVE is to develop all-solid-state tunable optical filters that can serve as low-Size, Weight, and Power (SWaP) replacements to the ubiquitous filter wheel technology current in use, and serve as a starting point for completely new optical component technologies. By using materials commonly used in electronic memory devices, namely chalcogenide phase-change materials (PCMs), in conjunction with nanostructured surfaces with exotic, tailored optical responses (“metasurfaces”), the P-ACTIVE filters are able to tune their optical transmission/reflection behavior in real-time. Because of this new functionality, P-ACTIVE filters are highlighted for NASA science and space programs such as next generation Lidar, landing system (SLS) thermal monitoring, thermal imaging, imaging spectroscopy, and disaster monitoring (e.g., volcanic eruption observations from SmallSats).

This document intends to serve as a compendium of the P-ACTIVE project. We begin by describing the project from background science and assume no prior knowledge of the subject on the part of the reader. We then address experimental and theoretical results of P-ACTIVE device performance, as well as recent results obtained from the MISSE-14 mission related to space qualification of P-ACTIVE devices and constituent materials. We conclude with a prospective view of the P-ACTIVE technology, and discuss the potential for these filters and other similar metasurface devices to serve NASA’s mission.

In addition to the team members at NASA LaRC, the P-ACTIVE project was supported by the following internal and external collaborations:

- NASA Langley Research Center
  - Project Investigator (PI): Dr. Hyun Jung Kim
  - Research and Development (R&D): Dr. Hyun Jung Kim, Mr. Scott Bartram, Mr. Stephen Borg, Dr. Kiumars Aryana
  - Advisors: Mr. William Humphreys (Measurements) and Mr. David MacDonnell (Applications)
- Massachusetts Institute of Technology (MIT)
  - Prof. Juejun Hu, Dr. Tian Gu, Yifei Zhang, Dr. Sensong An, and Cosmin-Constantin Popescu – subject matter expertise, modeling support, device/electrode fabrication/characterization support
- University of Cambridge
  - Dr. Calum Williams – subject matter expertise (bio- /medical-applications, modeling support)
- Booz Allen Hamilton
  - Dr. Matthew Julian – subject matter expertise, modeling support, technology transition
- Harvard University
  - Mr. David Bombara (NIFS 2020~2021)

Following are references published by the various teams:

- **Papers**

1. Cosmin Constantin-Popescu et al. New phase change materials for active photonics, Proc. SPIE 12196, Active Photonic Platforms 2022, 1219606 (3 October 2022); doi:10.1117/12/2631038 (2022).
2. Gu, T. et al. Active metasurfaces: lighting the path to a sparkling success, *Nature photonics*, (2022).
3. Gu, T. et al. Hybrid integrated photonic platform: feature introduction, *Optical Materials Express*, (2022).
4. Kim, H. J. et al. PCM-net: A refractive index database of chalcogenide phase change materials for tunable nanophotonics device modelling, *J. Phys. Photonics* 3, 024008, (2021).
5. Bombara, D. et al. Automated real-time spectral characterization of phase-change tunable optical filters using a linear variable filter and infrared camera, *Optical Engineering*, arXiv:2102.11028, (2021).
6. Shalaginov, M. Y. et al. Reconfigurable all-dielectric metalens with diffraction-limited performance. *Nat. Commun.* 12, 1225 (2021).
7. Shalaginov, M. Y. et al. Design for quality: reconfigurable flat optics based on active metasurfaces, *Nanophotonics* (2020).
8. Williams, C. et al., Tunable mid-wave infrared Fabry-Perot bandpass filters using GeSbTe, *Optics Express* 28(7), 10583 (2020).
9. Julian et al. Reversible optical tuning of GeSbTe phase-change metasurface spectral filters for mid-wave infrared imaging, *Optica*, 7(7), 746-754 (2020).
10. Zhang Y. et al. Broadband transparent optical phase change materials for high-performance nonvolatile photonics. *Nat. Commun.* 10, 4279 (2019).
11. Zhang, Q. et al. Broadband nonvolatile photonic switching based on optical phase change materials: beyond the classical figure-of-merit. *Opt. Lett.* 43, 94–97 (2018).
12. Shalaginov, M. Y. et al. Reconfigurable all-dielectric metalens with diffraction-limited performance. *Nat. Commun.* 12, 1225 (2021).
13. Zhang, Y. et al. Electrically reconfigurable non-volatile metasurface using low-loss optical phase-change material. *Nat. Nanotechnol.* 16, 661–666 (2021).
14. An, S. et al. A Deep Learning Approach for Objective-Driven All-Dielectric Metasurface Design. *ACS Photonics* 6, 3196–3207 (2019).
15. An, S. et al. Multifunctional Design with a Generative Adversarial Network. *Adv. Opt. Mater.* 9, 2001433 (2021).
16. An, S. et al. Deep neural network enabled active metasurface embedded design. *Nanophotonics* (2022). doi:10.1515/NANOPH-2022-0152
17. Ríos, C. et al. Multi-Level Electro-Thermal Switching of Optical Phase-Change Materials Using Graphene. *Adv. Photonics Res.* 2, 2000034 (2020).
18. An, S. et al. Deep learning modeling approach for metasurfaces with high degrees of freedom. *Opt. Express* 28, 31932 (2020).
19. Martin-Monier, L. et al. Endurance of Chalcogenide Optical Phase Change Materials: a Review. *Opt. Mater. Express* 12, 2145–2167 (2022).
20. Zhang, Y. et al. Myths and truths about optical phase change materials: A perspective. *Appl. Phys. Lett.* 118, 210501 (2021).
21. Kim, H. J. et al. Versatile spaceborne photonics with chalcogenide phase-change materials, *Nature Material under-review*, (2022).

- **Invention disclosure and patents**
  1. Hyun Jung Kim, David MacDonnell, Juejun Hu, Tian Gu, Matthew Julian, PCM-based metasurface Optical Phased Array (P-OPA) for eliminating detector saturation and ringing of Lidar, NASA Invention Disclosure, Case No LAR-20255-1, August 2022
  2. Stephen Borg and Hyun Jung Kim, A Multi-Spectral Imaging Pyrometer Utilizing Tunable Optics, NASA Invention Disclosure, Case No LAR-20119-1, December 2021 (Patent application process in February 2022)
  3. Hyun Jung Kim, Calum Williams, Amin Nehrir, and John Smith, Solid-state frequency agile filter for LIDAR: multilayer optical design and exotic phase-change materials-based active tuning, NASA Invention Disclosure, Case No LAR-19870-1, July 2020
  4. Hyun Jung Kim, Matthew Julian, and Calum Williams, Tunable mid-wave infrared (MWIR) filter based on plasmonic nanohole arrays and exotic phase change materials, NASA Invention Disclosure, Case No LAR—19619-1, March 2019 (U.S. Provisional Patent Application # 62/946,285, December 2019)
- **Presentations**
  1. (Oral) Calum Williams, Hyun Jung Kim, Matthew Julian, Nina Hong, Stephen Borg, Scott Bartram, Sensong An, Tian Gu, Juejun Hu, William Humphreys, “Phase-change tunable optical filters for imaging spectroscopy”, SPIE Photonex, December 2022
  2. (Oral) Hyun Jung Kim, Matthew Julian, Kiumars Aryana, Stephen Borg, Scott Bartram, and William Humphreys, “Effects of LEO Space Exposure on GeSbTe Phase-change Metasurface Spectral Filters”, 2023 Photonics West
  3. (Invited talk) Hyun Jung Kim, Scott Bartram, William Humphreys, Cosmin-Constantin Popescu, Tian Gu, Juejun Hu, Matthew Julian, and Steven Vitale, “Phase change reconfigurable optical wavefront synthesis system”, 2023 SPIE Photonics West
  4. (Invited talk) Hyun Jung Kim, P-ACTIVE (PCM-based actively tunable filter) project at NASA, 2023 SPIE Defense + Commercial Sensing
  5. (Invited talk) Tian Gu, “Dynamic light shaping using active optical metasurfaces”, 2023 SPIE Defense + Commercial Sensing
  6. (Invited talk) Juejun Hu, “Active metasurface optics based on chalcogenide phase change materials”, 2023 MRS Spring Meeting
  7. (Oral) Cosmin Constantin Popescu, Brian Mills, Louis Martin Monier, Luigi Ranno, Yifei Zhang, Qingyang Du, Carlos Ríos, Steven Vitale, Christopher Roberts, Paul Miller, Vladimir Liberman, Hyun Jung Kim, Aryana Kiumars, Myungkoo Kang, Kathleen Richardson, Tian Gu, Juejun Hu, “Long live O-PCMs: Understanding Reliability Challenges of Optical-Phase Change Materials”, 2023 MRS Spring Meeting
  8. (Oral) Hyun Jung Kim, Kiumars Aryana, Cosmin-Constantin Popescu, Juejun Hu, “Space-qualified Chalcogenide Materials through ISS MISSE Exposure —from property to application”, MRS Fall Meeting, November 2022
  9. (Invited talk) Hyun Jung Kim, William Humphreys, David Macdonnell, Juejun Hu, and Tian Gu, “Phase change materials-based tunable and reconfigurable optical metamaterials at NASA”, 2022 IEEE Summer Topicals Meeting, July 2022

10. (Poster presentation) Jaden Love, Nuwanjula Samarasinha, Carlos Armenta, Stefan Zollner, and Hyun Jung Kim, “Optical constants of CaF<sub>2</sub> at 300K from 0.03 to 6.5 eV”, APS March Meeting, 2022
11. (Invited panel) Special Session “Opportunities and Challenges for Optical Phase-Change Materials in Foundry-Processed Photonics.” in a CLEO 2022 workshop May 2022
12. (Invited talk) Cosmin Constantin-Popescu, Carlos Ríos, Yifei Zhang, Mikhail Shalaginov, Fan Yang, Hung-I Lin, Sensong An, Christopher Roberts, Paul Miller, Myungkoo Kang, Kathleen Richardson, Hualiang Zhang, Clara Rivero-Baleine, Hyun Jung Kim, Tian Gu, Steven Vitale, Juejun Hu, “New phase change materials for active photonics”, SPIE OPN 2022
13. (Invited talk) Hyun Jung Kim, Phase-change material (PCM) based actively tunable filters for both terrestrial and spaceborne platforms, 2022 Photonic West, January 2022
14. (Invited talk) EPIC online technology meeting on Mid-IR technologies for environmental monitoring, EPIC (European Photonics Industry Consortium), September 2021
15. (Oral) Hyun Jung Kim and William Humphreys, Tunable Mid-Wave Infrared (MWIR) Filters Based on Exotic Phase-Change Materials, A joint CSA / ESA / JAXA / NASA ISS Increment 65 Science Symposium, June 22, 2021
16. (Oral) Hyun Jung Kim, Calum Williams, Stephen Borg, Carey Scott, Thomas Horvath, and Jennifer Inman, Phase-change tunable filters (PCTFs) for hyperspectral thermal imaging, AIAA SciTech, Virtual, January 2021
17. (Oral) Hyun Jung Kim, Calum Williams, Matthew Julian, Nina Hong, and Stephen Borg, Phase-change material based actively tunable MWIR thin-film bandpass filters, SPIE Photonic West, Virtual, March 2021
18. (Oral) Hyun Jung Kim, Stephen Borg, Scott Bartram, David Bombara, and William Humphreys, Active tunable MWIR filters: phase-change tunable filters for MWIR imaging based on GeSbTe-integrated metasurfaces, SPIE Defense and Commercial Sensing, Virtual, April 2021
19. (Oral) Hyun Jung Kim, Matthew Julian, Calum Williams, and Scott Bartram, Active tunable filters based on GeSbTe phase change materials and surface plasmon resonance, SPIE Photonic West, The Moscone Center, San Francisco CA, February 2020
20. (Oral) Hyun Jung Kim, Matthew Julian, Calum Williams, and Scott Bartram, Tunable mid-wave infrared spectral filters based on phase change materials for multispectral imaging, 70th IAC (International Astronautical Congress) conference, The Walter E. Washington Convention Center, Washington D.C., October 2019
21. (Poster) Matthew Julian, Calum Williams, and Hyun Jung Kim, Tunable mid-wave infrared (MWIR) plasmonic filters based on the phase-change material GeSbTe, SPIE Photonics West 2019 – OPTO – Optical Components and Materials XVI, San Francisco, California, February 2019
22. (Oral) Hyun Jung Kim - Technical Exchange Meeting, NASA Research Directorate (RD) Technical Exchange Meeting with Structures and Materials Senior Technologists, “Tunable Metasurface to the Spaceborne Platform”, September 2021
23. (Invited talk) Hyun Jung Kim, The department of Materials Science and Engineering at MIT, December 2019 (Title: Actively Tunable Mid-Wave Infrared Filter for NASA Science and Space applications)

24. (Invited talk) Hyun Jung Kim - Sensors & Instrumentation Webcast hosted by NESC (NASA Engineering and Safety Center), December 2019 (Title: Actively Tunable Filter Components (ATFCs) Using Phase Change Materials (PCM) for Scientific Instrumentation)
25. (Invited talk) Hyun Jung Kim, The electrical & computer engineering colloquium at Old Dominion University, December 2019 (Title: Optical cleanroom fabrication techniques for space flight applications)
26. (Invited talk) Hyun Jung Kim, The physical department colloquium at New Mexico State University, September 2019 (Title: Optical cleanroom fabrication techniques for space flight applications)
27. C.Williams, C.Hooper, G.S.D. Gordon, M.Julian, H.J.Kim, S.E.Bohdiek, Nanostructured optical devices for miniaturised multi-functional imaging, UK Metamaterials Network Conference, May 2022, (<https://metamaterials.network/home/conference/>)
28. C.Williams, M.Julian, H.J.Kim, Phase-change tunable optical filters (PCTFs) for spaceborne imaging spectroscopy, VISIONLAB seminar, Department of Physics, Cambridge, UK, 2020
29. C.Williams, Bespoke multispectral filter arrays for next-generation multispectral imaging, Departmental Seminar Series, Department of Physics, University of Bath, UK, 201
30. C.Williams, Grayscale-to-colour: custom multispectral filter arrays, Seminar Series, Wyant College of Optical Sciences, University of Arizona, US, 2018

- **Book**

1. C. Rios, Y. Zhang, M. Shalaginov, T. Gu, and J. Hu, in Phase Change Materials in Photonic Computation, edited by H. Bhaskaran and W. Pernice (Elsevier, Amsterdam, Netherlands).

- **Recorded video**

1. Hyun Jung Kim, “Actively Tunable Filter Components (ATFCs) Using Phase Change Materials (PCM) for Scientific Instrumentation”, Sensors & Instrumentation Webcast hosted by NESC (NASA Engineering and Safety Center), 2019  
<https://nescacademy.nasa.gov/video/fea786ddcb3d4243b9a54a6472025ee21d>
2. Tian Gu, “Reshaping light with meta-optics”, TED x MIT,  
<https://www.youtube.com/watch?v=EqszFlx9be4>
3. Hyun Jung Kim *et al.*, “Phase-change-material (PCM)-based actively tunable filter s for both terrestrial and spaceborne platforms, SPIE, 2022  
<https://www.spiedigitallibrary.org/conference-proceedings-of-spie/PC12011/PC120110/Phase-change-material-PCM-based-actively-tunable-filters-for-both/10.1117/12.2607826.full>
4. Carlos Rios *et al.*, “Electrically-switchable foundry-processed phase change photonic devices”, SPIE 2021, <https://www.spiedigitallibrary.org/conference-proceedings-of-spie/11796/117961Z/Electrically-switchable-foundry-processed-phase-change-photonic-devices/10.1117/12.2592021.full>
5. Tian Gu *et al.*, “High-performance reconfigurable meta-optics based on optical phase change materials (Rising Researcher), SPIE 2020, <https://www.spiedigitallibrary.org/conference-proceedings-of-spie/11796/117961Z/Electrically-switchable-foundry-processed-phase-change-photonic-devices/10.1117/12.2592021.full>

[proceedings-of-spie/11389/113890O/High-performance-reconfigurable-meta-optics-based-on-optical-phase-change/10.1117/12.2557439.full](https://proceedings-of-spie/11389/113890O/High-performance-reconfigurable-meta-optics-based-on-optical-phase-change/10.1117/12.2557439.full)

6. Mikhail Y. Shalaginov *et al.*, “Reconfigurable all-dielectric metlens for diffraction-limited imaging”, SPIE 2020, <https://www.spiedigitallibrary.org/conference-proceedings-of-spie/11461/114610M/Reconfigurable-all-dielectric-metlens-for-diffraction-limited-imaging/10.1117/12.2565267.full>
7. Yifei Zhang *et al.*, “Designing nonvolatile integrated photonics with low-loss optical phase change materials, SPIE 2019, <https://www.spiedigitallibrary.org/conference-proceedings-of-spie/11081/110811S/Designing-nonvolatile-integrated-photonics-with-low-loss-optical-phase-change/10.1117/12.2528993.full>
8. Yifei Zhang *et al.*, Reconfigurable photonics enabled by optical phase change materials”, SPIE 2018, <https://www.spiedigitallibrary.org/conference-proceedings-of-spie/10686/1068606/Reconfigurable-photonics-enabled-by-optical-phase-change-materials-Conference-Presentation/10.1117/12.2314894.full>

- **Webpages**

1. <https://dbombara.github.io/automated-pcm-characterization>  
: Source code for the MATLAB® application for real-time / reliability testing GUI
2. <http://nekocloud.com/pnet/>  
: PCM-net, online database of the complex refractive indices of a variety of chalcogenide PCMs
3. <https://spaceborne-pcms.github.io>  
: Locations of space material evaluation facilities (academic research laboratories, space agencies, and private companies) including simulated space environments across the world

## Table of Contents

### PART I: P-ACTIVE at NASA

1. Motivation and project goal
2. Description of P-ACTIVE technology

### PART II: P-ACTIVE research & development

1. Filter design and results
    - 1.1 Fabry-Perot multilayer filter
    - 1.2 Plasmonic nanohole array filter
    - 1.3 All-dielectric metasurface filter using deep neural network design methods
  2. Performance analysis results
    - 2.1 Thermal and gas sensing demonstration (using FP filter)
    - 2.2 Thermal imaging demonstration (using PNA filter)
    - 2.3 Real-time / reliability testing
  3. MISSE-14 project (June 2021 – January 2022) for P-ACTIVE space applications
    - 3.1 Motivation
    - 3.2 MISSE-14 campaign procedure
    - 3.3 The emerging space science applications of PCM-based photonics through the MISSE-14
- Appendix A. MATLAB®-Based Graphical User Interface (GUI) development

### BOX 1: PROWESS (Phase-change Reconfigurable Optical WavEfront Synthesis System)

### PART III: NASA Mission / Program-specified scenarios

1. P-ACTIVE for atmospheric gas sensing (NASA SAGE mission case study)
2. P-ACTIVE for space launch vehicle thermal monitoring (NASA SCIFLI project case study)
3. P-ACTIVE for next-generation astronaut health monitoring

### BOX 2: Where will P-ACTIVE shine most?

### PART IV: Forward-looking vision of the P-ACTIVE

1. R&D strategies for PCM-selection, SWaP, and more
2. R&D challenges

Appendix B. Phase Change Material Toolbox

## Conclusions

## References

## Acronyms and Abbreviations

- 1D: One-dimension
- 2D: Two-dimension
- AIST: AgInSbTe (Silver-Indium-Antimony-Telluride)
- AOTF: Acousto-optical tunable filter
- ARMD: Aeronautics research mission directorate
- BP filter: Bandpass filter
- CFD: Computational fluid dynamics
- CHA: Cone half angle
- CIF: Center innovation fund
- CLICK: CubeSat laser infrared crosslink
- CMOS: Complementary metal-oxide semiconductor
- CNN: Convolutional neural network
- CWL: Center wavelength
- DBR: Distributed Bragg reflector
- DIAL: Differential absorption Lidar
- DNN: Deep neural network
- EDL: Entry, descent, and landing
- EDS: Energy-dispersive x-ray spectroscopy
- ENZ: Epsilon-near-zero
- EO: Electro-optic
- EOT: Extraordinary optical transmission
- ERBS: Earth radiation budget
- EXAFS: Extended x-ray fine structure
- FCA: Free carrier absorption
- FCC: Face-centered cubic
- FDTD: Finite-difference time-domain
- FIT: Failures in time
- FLIR: Forward-looking infrared
- FOM: Figure-of-merit
- FP filter: Fabry-Perot filter
- FSM: Fast-steering mirror
- FSO: Free-space optical
- FTIR: Fourier transform infrared
- FWHM: Full width half maximum
- GAN: Generative adversarial network
- GSST: GeSbSeTe (Germanium-Antimony-Seluride-Telluride)
- GST: GeSbTe (Germanium-Antimony-Telluride)
- GUI: Graphical user interface
- HCP: hexagonal close packing
- HDRi: High dynamic range infrared

- HEOMD: Human exploration and operations mission directorate
- HL: High-low index
- HTP: Hypersonic Technology Program
- HYTHIRM: Hypersonic thermodynamic infrared measurements
- IFOV: Instantaneous field of view
- IR: Infrared
- IS: Imaging spectroscopy
- ISS: International space station
- JWST: James Webb Space Telescope
- KK: Kramers-Kronig
- LaRC: Langley Research Center
- LC: Liquid crystal
- LCTF: Liquid crystal tunable filter
- LEO: Low earth orbit
- Lidar: Light detection and ranging
- LSPPR: Localized surface plasmon resonance
- LVF: Linear variable filter
- MEMS: Microelectromechanical systems
- MISSE: Materials International Space Station Experiment
- MIT 1: Massachusetts Institute of Technology
- MIT 2: Metal-insulator transistors
- MQW: Multi-quantum well
- MTF: Metasurface-embedded Fabry-Perot filter
- MWIR: Mid-wave infrared
- NA: Numerical aperture
- NASA: National Aeronautics and Space Administration
- NIFS: NASA Internships and Fellowships
- NIR: Near-infrared
- NTN: Neural tensor network
- OD: Optical density
- P-ACTIVE: Phase change material-based actively tunable filter
- PANI: Polyaniline
- PCM: Phase change material
- PIFS: Plume-induced flow separation
- PNA filter: Plasmonic nanohole array filter
- PNN: Predicting neural network
- PRAM: Phase change random access memory
- PROWESS: Phase-change reconfigurable optical wavefront synthesis system
- R&D: Research & development
- RF: Radio frequency
- RGB: Red-green-blue
- ROI: Region on interest

- RSF: Reset-stuck failure
- SAGE III/ISS: SAGE III/international space station
- SAGE: Stratospheric Aerosol and Gas Experiment
- SAMI: SCIFLI airborne multispectral imager
- SCIFLI: Scientifically Calibrated In-Flight Imagery
- SD: Science directorate
- SDK: Software development kit
- SLS: Space launch system
- SOA: State-of-the-art
- SOS: Silicon-on-SiO<sub>2</sub>
- SPR: Surface plasmon resonance
- SSF: Set-stuck failure
- SST: ScSbTe (Scandium Antimony Telluride)
- STMD: Space technology mission directorate
- SWaP: Size, Weight, and Power
- SWIR: Short-wave infrared
- TBD: To be determined
- TCO: Transparent conducting oxide
- TEM: Transmission electron microscope
- TMM: Transfer matrix method
- TPS: Thermal protection system
- VIS-NIR: Visible- Near infrared
- XRD: X-ray diffraction

## PART I: P-ACTIVE at NASA

### 1. Motivation and Project Goal

In the NASA scientific and research community, imaging spectroscopy (IS) is an invaluable remote measurement technique used to estimate the chemical composition or temperature of an object or scene, such as an aerosol cloud, jet engine, or exhaust plume. As an example, tunable infrared imaging optics are a core technology for health monitoring of hypersonic air-breathing propulsion vehicles—from probing molecular vibrations in chemical species to detecting radiant thermal signatures [Fig. 1-1]. It is critical to know the accurate and sensitive temperature of engine exhaust plume and gas phase ablation material in emission or absorption for pollution monitoring.

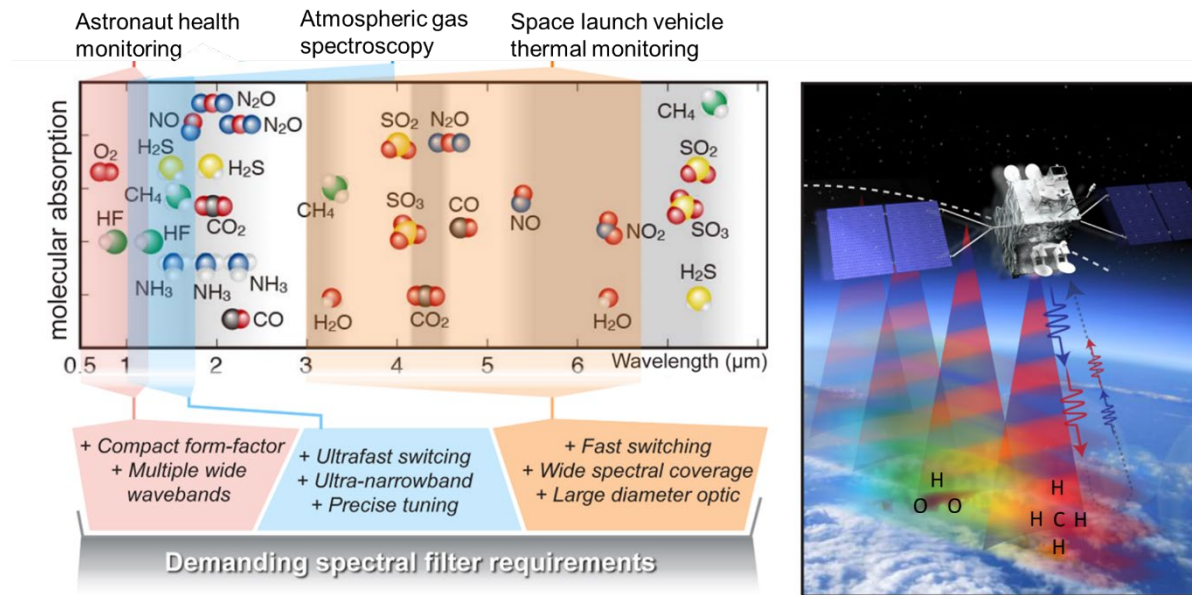


**Fig. 1-1.** Characteristic absorption bands of molecules of interest to aerospace applications as well as application-specific requirements on the tunable spectral filter (left). The satellite-based multispectral imaging for monitoring of atmospheric gas species (right).

Current IS systems are based on motorized filter wheels. These filter wheels hold several (typically 5) single notch optical filters and rotate between each filter to take a new spectral measurement. These mechanical filter wheels are bulky – the exemplar filter wheel weighs ~0.8 kg and comprises a volume of ~725 cm<sup>3</sup> [1]. This volume is problematic and inefficient for satellite platforms, where use of space is crucial, and becomes prohibitive in CubeSat form-factors. The small number of filters held by the filter wheel inherently limits the spectral resolution of the measurement system; the resolution is defined by the number of filters. This reduces the overall amount of data that can be taken by the system and limits the accuracy.

As an example of this, for standoff temperature measurements the spectral measurement resolution is used to compute the emission curve of an object to discern its temperature. Additionally, the switching speed for filter wheel assemblies is on the order of tens of seconds of milliseconds [1], which is much too slow to capture important transient temperature phenomena such as those that occur in exhaust plumes of launch vehicles, or in hypersonic flight. The combination of low spectral resolution and low temporal resolution result in a measurement system that is incredibly volume-inefficient – a large volume is used to generate relatively small amounts of useful data. Additionally, plenoptic imaging architectures have been proposed

for multi-spectral imaging. However, these systems comprise a fixed architecture defined by the spectral wavelength of the individual static filters applied to a lenslet array. Although these are a low-Size, Weight, and Power (SWaP) solution to IS, they offer no real-time tunability and are limited in overall bandwidth, therefore missing out on important spectral and temporal data.

P-ACTIVE (Phase change materials based actively tunable filter) offers significant advantages over the current IS state-of-the-art via the ability to remove the traditional bulky motorized filter wheel used in current IS systems and replace it with a single, low-power-consumption filter, with no moving parts. P-ACTIVE will obtain high quality, real-time spectroscopic image data of high-temperature objects in a relevant environment, with increased accuracy compared to filter wheel systems. P-ACTIVE will accomplish this in a low-SWaP form factor suitable for compact mission platforms.

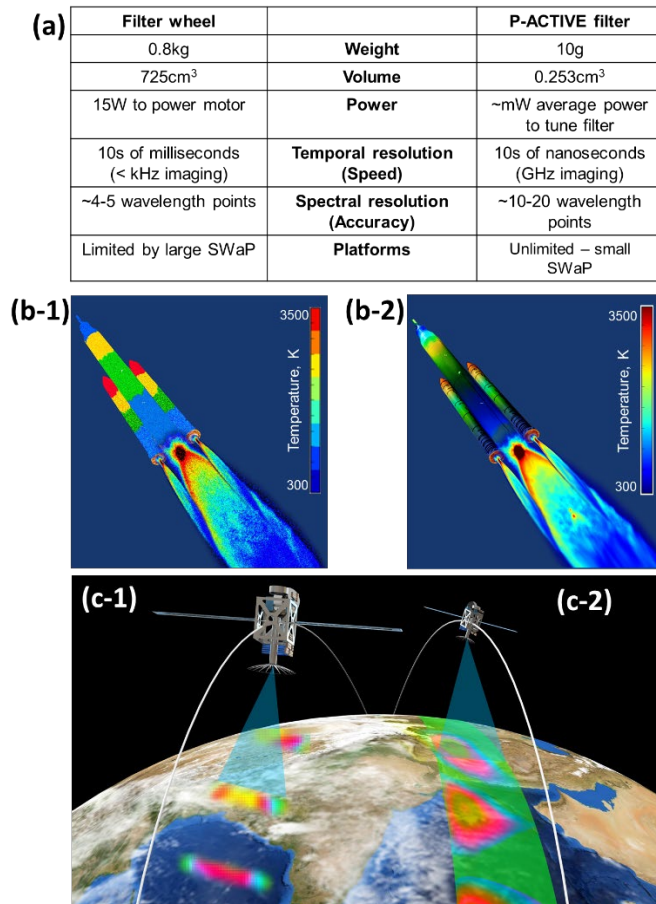


**Fig. 1-2.** (a) Comparison of filter wheel and Phase-change Actively tunable (P-ACTIVE) filter technologies. The system comprising P-ACTIVE filter technology boasts significant advantages over the state of the art in both SWaP and performance. P-ACTIVE's increased spectral and temporal resolution allows for much more accurate data collection for key measurement missions, as shown in the (b-2) images of a rocket launch and (c-2) aerosol cloud compared to images taken from filter wheel, as shown in (b-1) and (b-2).

In comparison to contemporary filter wheels – which comprise a weight of 800 g and a volume of ~725 cm<sup>3</sup> – P-ACTIVE filters are 0.5 mm thick, 2.5 cm in diameter, and weigh ~10 g as shown in Fig 1-2(a). This represents a volume reduction of ~300x and a weight reduction of ~80x. The required power supply will, at most, be comparable to the 12V supplies used by filter wheel systems.

P-ACTIVE also offers significant advantages in terms of data collection. In the case of temperature measurements, a P-ACTIVE system comprised of a single sensor that takes 10 distinct spectral measurements via active tuning would be ~2x as accurate as a 5-slot filter wheel (due to 2x as many spectral measurements). Additionally, P-ACTIVE can be tuned on nanosecond timescales—orders of magnitude faster than the relevant timescales of temperature drift in most measurements—enabling real-time imaging spectroscopy with high data throughput. Such transient effects cannot be captured by current filter wheel technologies, which switch at speeds  $10^3$ – $10^6$  x slower than P-ACTIVE-based IS system. Combining these increases in spectral and temporal resolution results in a 3.2-to-6.2 orders-of-magnitude increase in the total number of data points that can be collected using a P-ACTIVE system. Of course, P-ACTIVE can also be tuned slowly if temporal variations occur on longer timescales.

Because of these unique properties, P-ACTIVE will have far-reaching applicability across a multitude of NASA missions. Its GHz tuning rate enables real-time IS of dynamic targets such as exhaust plumes and volcanic gases in the atmosphere that will facilitate precise mapping of greenhouse gas hotspots and atmospheric

contaminants [Fig 1-2(b) and (c)]. For upcoming Lidar and future CubeSat missions, it is highly desirable to replace bulky filter wheels with solid-state filters to enable volume and weight reductions. Moreover, P-ACTIVE has mission applicability for hypersonic technology as currently being developed through the NASA Hypersonic Technology Program (HTP). I-SSPI would provide unrivalled capability to remotely characterize the performance of entry, descent, and landing systems both in ground test facilities such as the LaRC HYMETS (Hypersonic Materials Environmental Test System) and in-flight campaigns. Further utility includes NASA heliophysics research, whereby P-ACTIVE could provide enhanced spectral imaging of solar phenomena.

In summary, P-ACTIVE can directly impact a variety of NASA missions and programs including the Aeronautics Research Mission Directorate for health monitoring of hypersonic air-breathing propulsion vehicles, the Space Technology and Human Exploration Mission Directorates for thermal imaging of hypersonic atmospheric flight (e.g., the Space Launch System) and astronaut health monitoring, and the Science Directorate for remote atmospheric sensing and monitoring.

## 2. Description of P-ACTIVE technology

Phase change materials (PCMs) are presently being utilized at the core of next-generation solid-state P-ACTIVE technology. The integration of PCMs into nanostructured (i.e., metasurfaces) filter designs enable actively-tunable optical filters capable of quasi-continuous ultrafast tuning of their passbands, with no moving parts. The subwavelength structure of these metasurfaces allows for complete control of their interaction with light, independent of the bulk material properties – the device performance is defined by the structure shown in Fig. 1-3.

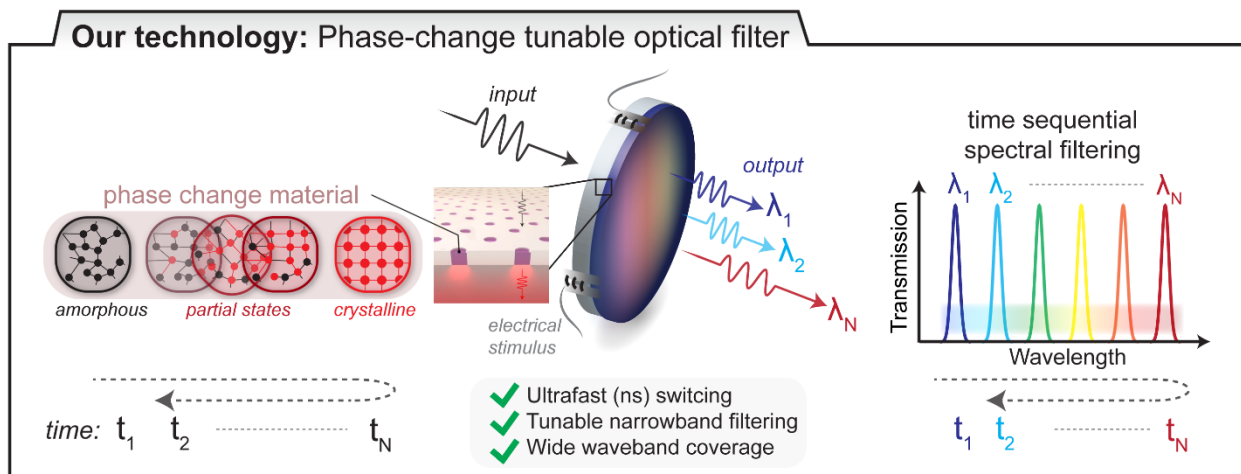


**Fig. 1-3.** Operating principle of the PCM-based metasurface filter (P-ACTIVE): the PCM's structure can be continuously tuned in a non-volatile manner via voltage pulses, thereby spectrally shifting the passband of the metasurface. PCMs are novel materials capable of large, reversible tuning of their refractive index, at GHz rates. The integration of PCMs into nanostructured (i.e., metasurfaces) filter designs enable actively tunable optical filters capable of quasi-continuous ultrafast tuning of their passbands, with no moving parts. The subwavelength structure of these metasurfaces allows for complete control of their interaction with light, independent of the bulk material properties – the device performance is defined by structure.

Recently published work from the LaRC group demonstrated a single, resonance-based metasurface optical filter in the mid-wave infrared (MWIR) spectral regime, based on the PCM material GeSbTe (germanium antimony telluride, GST). By tuning the refractive index of the GST using a laser pulse to locally heat the

material, the device resonance, and thus transmission, was tuned across a broad spectral window [2]. This tuning allowed successfully demonstration of both standoff temperature measurements and CO<sub>2</sub> sensing [Fig. 1-4]. Additional details are discussed in Section II. While reversible tuning between three GST states was demonstrated, GSTs have been shown to be tunable across >10 total states between amorphous and crystalline [3]. This is a property that allows for a single filter to facilitate many unique spectroscopic measurements.

PCMs are non-volatile novel materials capable of large, reversible tuning of their refractive index, at GHz rates. Because of these properties, PCMs based on chalcogenide material alloys are commonly used in computer phase change random access memory (PRAM) applications and have recently become a material platform of interest for a variety of optics and electronics applications [Fig. 1-4(a)]. Since the 1970s [4], gallium and paraffin materials (materials with a solid-liquid phase changes) have been proposed and tested for spacecraft thermal control in LEO or lunar orbit [5] to space applications as well. However, to-date, the application of all-solid-state, and particularly chalcogenide, PCMs for space application has been largely non-existent.

PCMs are solid-state materials that can change between amorphous and crystalline phases as a result of thermal stimulus [6, 7]. The different compositions of germanium (Ge)-antimony(Sb)-telluride(Te) alloys [Fig. 4(b)] present the most widely utilized PCMs [8]. The alloys are listed based on compounds such as binary, ternary, and quaternary of PCMs. Several GST alloys such as Ge<sub>1</sub>Sb<sub>4</sub>Te<sub>7</sub>, Ge<sub>2</sub>Sb<sub>2</sub>Te<sub>5</sub>, and Ge<sub>1</sub>Sb<sub>2</sub>Te<sub>4</sub> were identified [9, 10] all along a pseudo-binary line that connects the GeTe and Sb<sub>2</sub>Te<sub>3</sub> compounds. Phase changes occur on a very short timescale (between tens of milliseconds and a few picoseconds), depending on the material type or composition [6,7]. This is accompanied by a large shift in the material's electronic and optical properties. The amorphous phase boasts higher electrical resistance, a lower refractive index, and less optical absorption, while the crystalline state shows the exact opposite [Fig. 1-4(c)].

In general, moving from GeTe towards Sb<sub>2</sub>Te<sub>3</sub> on the pseudo-binary line, crystallization speed increases, glass-transition temperature ( $T_g$ ) and melting temperature ( $T_m$ ) decrease, and data retention (i.e., the retention of the amorphous state) decreases [11]. In other words, Sb<sub>2</sub>Te<sub>3</sub> offers the fastest crystallization speed, but its amorphous state is unstable. In contrast, GeTe offers a very stable amorphous phase. Films with stoichiometric composition, Te and GeTe, can be crystallized using laser pulses of less than 100 ns duration [12]. Therefore, a compromise between the crystallization speed and the amorphous stability can be made by selecting a ternary composition close to the center of the pseudo-binary line. Standing out in the pool of PCM materials, Ge<sub>2</sub>Sb<sub>2</sub>Te<sub>5</sub> offers a fast crystallization speed (< 100 ns) with moderate  $T_g$  (100–150°C) that ensures long-term data retention (~10 years). The switching behavior and the optical / electronic property contrast, induced by the phase switching, can also be customized by changing the composition of the PCMs. For example, the substitution of Te in GST alloys with selenium (Se) atoms forms a quaternary Ge-Sb-Se-Te PCM that is referred to as GSST [13,14]. The stoichiometry Ge<sub>2</sub>Sb<sub>2</sub>Se<sub>4</sub>Te shows broadband transparency in the near- to mid-IR spectral range while offering a large refractive index change ( $\Delta n \approx 1.5$ ) with minimal loss penalty (i.e.,  $\Delta k \approx 0$ ). Increasing the Se content in GSST monotonically increases the crystallization temperature, which translates into a better stability of the amorphous phase. However, this stability comes at a major drawback of slow crystallization speed as Se replaced the Te in a GST alloy. The total time for crystallization completion of GSST is ~1 ms compared to ~100 ns of Ge<sub>2</sub>Sb<sub>2</sub>Te<sub>5</sub> [14]. It is uniquely interesting that GST alloys remain amorphous for over 10 years at room temperature, but the very same material can be crystallized in only ~100 ns upon heating up to only a few hundred degrees Celsius [°C], a unique trait of chalcogenide PCMs.

Significant physical characteristics of PCMs are detailed below.

1. All the phase changes are nonvolatile, meaning they do not require a constant supply of energy to maintain their phase change; i.e., ‘*set it and forget it*’ if you will. In applications where frequent switching is not needed, this is a significant advantage in terms of energy consumption.
2. The macroscopic properties of PCMs change dramatically between amorphous and crystalline phases. Typical PCMs have a wavelength-dependent refractive index shift much greater than unity (typically ~1–2)[14] accompanied by a small increase in extinction coefficient [Fig. 4(d)], and resistivity shifts of 3 orders of magnitude [15]. It is also possible to exploit a near-continuum of partially crystalline states, with properties that lie more-or-less linearly between those of the amorphous and crystalline states. The magnitude of these changes is because the crystalline phase is characterized by metavalent bonding, whereas the amorphous phase undergoes shifts to covalent bonding. The change in bonding modes causes a sharp divergence in optical, thermal, and electrical properties. Because of the metavalent bonding, crystalline PCMs have higher optical dielectric constants than amorphous PCMs [16]. In the metastable amorphous phase, which exhibits long-range disorder (but also usually with some short-range order), the electrical resistivity of these materials is typically high. In the crystalline phase, which exhibits long-range order, the electrical resistivity is much lower. When PCMs undergo solid-state phase transition, their optical properties are significantly altered as well. Optical property modulation in these classic PCM systems stems from metal-insulator transitions (MIT) accompanying structural transformation [17]. In GST-based PCMs, the large optical contrast emanates from the pronounced change of local atomic arrangement, in which the Ge coordination switches between octahedral (in crystalline) and tetrahedral (in amorphous) bonds. Such an atomic change is reflected in the ~7% volumetric expansion of the GST following the crystalline-to-amorphous conversation [18]. In addition, quantum mechanical calculations, using Fermi’s golden rule, show that such a local structural alteration leads to a large change in the elements of the matrix that govern optical transitions between two initial and final states in GST-based PCMs [19]. Considering the central role of Ge atoms in the coordination change, one can expect that a larger Ge content in GST alloys provides a larger optical contrast [20].
3. PCM’s can switch in picoseconds, nanoseconds or microseconds [2,7,21]. As shown schematically in Fig. 4(c), applying a short- and high-energy pulse heats the c-GST above its  $T_m$  and then suddenly cools it down, yielding a-GST by the melt quenching of the c-GST. A typical cooling rate of  $1^{\circ}\text{C}/\text{ns}$  is sufficient for the melt-quenching of most GST-based PCMs [22,23]. Conversely, applying a long- and moderate-energy pulse to amorphous GST (a-GST) heats the material up to its  $T_g$ , which drives the phase transition to its crystalline state (c-GST). PCMs are categorized as either growth-dominated (e.g., slow nucleation  $\text{Ag}_4\text{In}_3\text{Sb}_{67}\text{Te}_{26}$  (AIST)) or nuclear-dominated (fast nucleation  $\text{Ge}_2\text{Sb}_2\text{Te}_5$ ) materials [15,24]. Growth-dominated PCMs recrystallize at the interface between the crystalline and amorphous matrices, which usually yields large crystalline grains. However, most PCMs are nucleation-dominated featuring stochastic formation of critical nuclei. Nucleation-dominated PCMs such as  $\text{Ge}_2\text{Sb}_2\text{Te}_5$  are characterized by exceptionally high crystal growth rates from the crystal seeds expediting the phase transition [24,25]. Therefore, the formation of nuclei is accompanied by rapid gain growth, leading to a polycrystalline phase of different grain orientations [24]. Switching the phase from a-GST to c-GST generally involves two events: nucleation of small crystallites and the subsequent growth of these crystalline domains [26]. To the first order, the

nucleation process is governed by the thermodynamics of the phase change (i.e., a temperature-controlled process), while the speed of the crystal growth is primarily governed by the kinetics of the phase change (i.e., the atomic motion of elements). The crystallization of GST is thermodynamically allowed once the temperature drops below the melting point, and the probability of crystalline nucleation increases as the temperature further drops, reaching the maximum probability at the glass-transition temperature,  $T_g$ . However, at low temperatures close to  $T_g$ , the crystalline nuclei cannot efficiently grow because the atomic mobility is extremely small. Thus, fast crystallization of a-GST occurs at intermediate temperatures between  $T_g$  and  $T_m$ , which is 150 – 250°C for the cubic structure and 300 – 350 °C for the hexagonal structure. Moreover, crystallization of a melt-quenched GST is significantly faster than that of an as-deposited amorphous film. The crystallization of melt-quenched GST films is strikingly different than the crystallization of as-deposited films. Crystallization of as-deposited films proceeds through a nucleation-dominated process, while in the melt-quenched films crystallizations growth dominated [26]. Apparently, the melt-quenching process leaves some subcritical crystalline domains in the amorphous matrix, so that the nucleation step can be partially bypassed in the subsequent re-crystallization cycles. For instance, using a pre-conditioning laser pulse of 100 ns width, the crystallization time of the GeTe film can be reduced from 1  $\mu$ s to only 30 ns, which reflected the switching of the crystallization mechanism from the nucleation-dominated mode to the growth-dominated mode. The presence of residual crystalline nuclei in melt-quenched films could be explained based on the low interfacial energy between amorphous matrix and crystalline domains, as demonstrated in undercooling experiments performed on GST alloys [27,28].

4. Additionally, PCMs, in particular  $\text{Ge}_2\text{Sb}_2\text{Te}_5$  (GST), are reported to be tolerant to ionizing radiation effects from the appreciable void volume present in the amorphous state [29]. During the radiation-damage cascade, the breakage of atomic bonds due to collisions inside the glass structure results in the formation of large voids within the amorphous network. As the cascade evolves, the density at the surface of these cavities increases and leads to the generation of large, shortest-path ring structures which act possibly as scaffolds for the recovery of the amorphous structure. Consequently, the densification at the boundary of large cavities generated during the initial stages of the ion irradiation, followed by rarefaction, local relaxation, and reordering within the amorphous structure during the natural quench of the radiation-damage cascade, seems to be the driving force for the recovery of the chemical and topological order of amorphous GST as elucidated by ab initio molecular-dynamics simulations [29]. Moreover, in amorphous GST, there are many different local environments with various coordination and degrees of ordering which can coexist inside the glass. This indicates that GST has a highly flexible structure induced by the existence of weak chemical bonds and lone pairs [30]. Thus, the diversity of bonding environments present in the material likely lowers the energy barrier for structural reconfiguration, thereby accelerating the bond reformation and thus facilitating the recovery process of the amorphous network after irradiation [29].

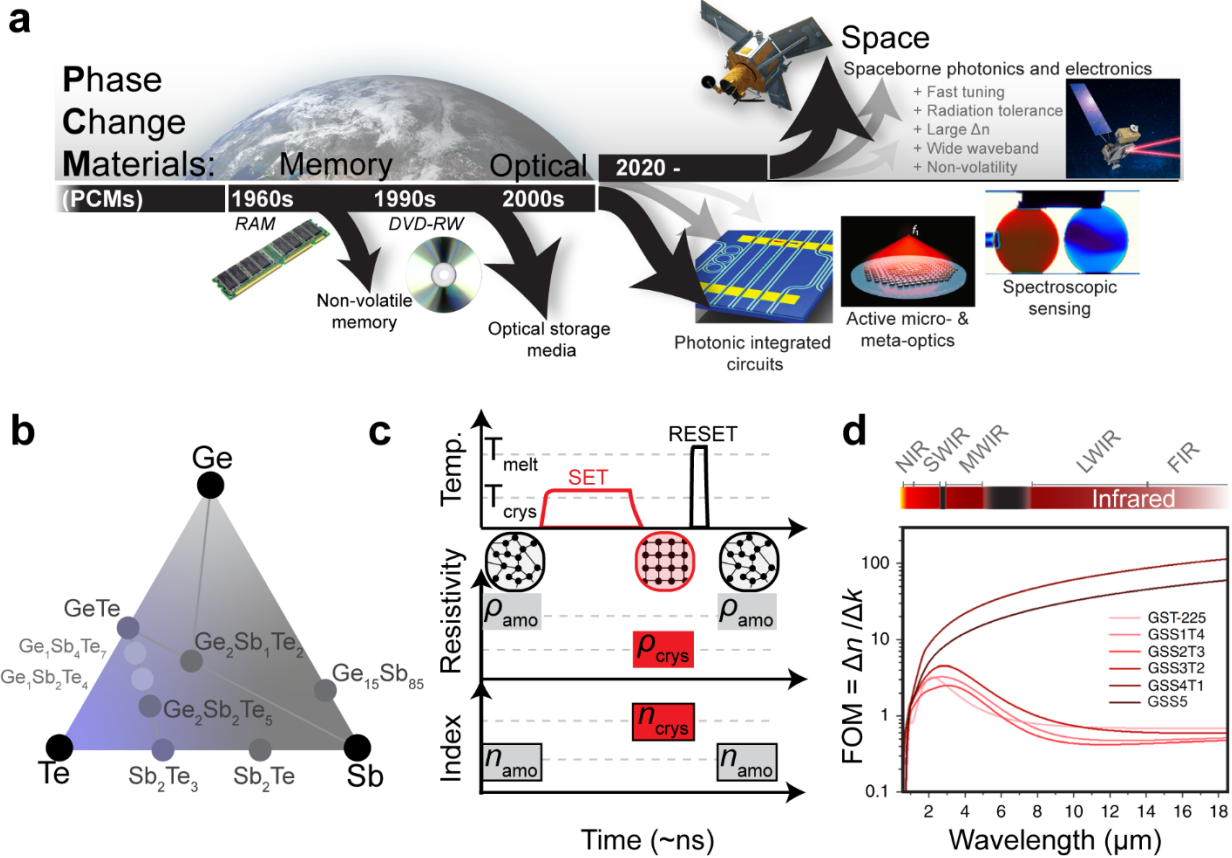


**Fig. 1-4. Prototypical phase-change materials and their characteristics, application-driven interest of PCMs since 1960.** (a) Interest of PCMs from terrestrial to spaceborne applications. (b) Ge-Sb-Te ternary phase diagram - popular GeSbTe (GST)-based PCMs include Ge<sub>2</sub>Sb<sub>2</sub>Te<sub>5</sub>, Ge<sub>1</sub>Sb<sub>2</sub>Te<sub>7</sub>, and Ge<sub>1</sub>Sb<sub>2</sub>Te<sub>4</sub>. (c) Switching the crystalline phase into the amorphous phase involves heating above  $T_{\text{melt}}$  (melting point) and then rapidly quenching the PCM. Switching the amorphous phase into a crystalline phase involves heating above  $T_{\text{crys}}$  (crystallization temperature) for sufficient time to crystallize the PCM. PCM devices are programmable via the “SET” state (akin to writing a logic “1”) and “RESET” state (writing a logic “0”). (d) FOM (figure-of-merit) of PCMs, real part ( $n$ ) / imaginary part ( $k$ ) of measured refractive index change induced by the phase transition. The generic FOM quantitatively correlates with the performance of many different classes of photonic devices.

## PART II: P-ACTIVE research & development

Throughout the course of the P-ACTIVE CIF project, a number of numerical and experimental results were demonstrated, all appearing in peer-reviewed publications [1–3]. Three main device designs were demonstrated: a Fabry-Perot (FP) multilayer filter layer [31], a plasmonic nanohole array (PNA) filter [32], and an all-dielectric nanostructure filter designed using a deep neural network [33]. All these filters showed good optical performance, and all are amenable to active tuning methods using optical or electrical pulses (the experiments described subsequently were conducted using optical pulses due to convenience in the lab setup). All the filters were contained a PCM material. The following subsection are summaries of previously-published peer-reviewed manuscripts [1–3].

### 1. Filter design and results

#### 1.1 Fabry-Perot (FP) multilayer filter

GeSbTe (GST) was utilized as a phase-change cavity embedded between Ge:Si distributed Bragg reflectors (DBRs) to enable spectrally tunable (bi-stable) all solid-state FP-bandpass (BP) filters operating across the MWIR waveband. The optical path length of the GST cavity, hence resultant passband center wavelength (CWL), is spectrally red-shifted under phase transformation due to GST-induced refractive index modulation. Therefore, through external stimuli, a filter's CWL can be spectrally switched to two different states (passbands) and is a reversible process. The fabricated 1-inch diameter filters have narrowband full-width, half-maximums (FWHMs) of 50–65 nm (with Q-factor 70–90) and high transmission efficiencies of 60–75%. Multispectral thermal (IR) imaging capability was demonstrated by integrating the filters with a commercial thermal camera and imaging two separate wavelengths. Moreover, by designing the GST-BP filter's CWL to correspond to a molecular vibration mode of CO<sub>2</sub> (4.25 μm), sensing (imaging) of both atmospheric (native) CO<sub>2</sub> and externally added CO<sub>2</sub> gas was demonstrated with imaging of a dynamic plume for the latter. The GST-based thin-film filters have wide applicability for IR imaging and sensing applications which require compact, cost-effective tunable spectral filters. These gas sensing results are summarized in Section 4 (performance analysis results).

Filter Design: The simplest thin-film optical bandpass filters are composed of a single-spacer (resonant cavity) between two multi-layer dielectric mirrors. The dielectric mirrors (DBRs) consist of a series of alternating high-and-low index materials (i.e., N bi-layers) with ¼-wave optical thickness, that provides a spectral ‘rejection region’. An embedded spacer opens up a transmission passband, with optical thickness governing the filter’s center wavelength (CWL) of operation. A material’s optical thickness is dependent on its refractive index, hence by utilizing the phase-change material GST – which exhibits a significant index modulation across the waveband of interest (MWIR) – as the spacer material, it is possible to control the passband CWL through the phase transformation of GST.

As the LaRC bandpass filters are designed for operation across the MWIR, Ge (H – *high index*) and Si (L – *low index*) are chosen as the DBR materials, with CaF<sub>2</sub> as the substrate. GST is then utilized as a tunable spacer material, with capability to operate in either its amorphous (a-GST) or crystalline (c-GST) state (induced through external stimuli). The tunable resonant cavity design concept is shown schematically in Fig. 2-1(a). The simulated transmission response of this design, for the two GST states, is shown in Fig. 2-1(b) as a function of N bi-layers. From this, N = 6 bi-layers were chosen for the proof-of-concept filters – a compromise between the filters’ optical properties and total deposition time – with simulated response of this arrangement shown in Fig. 2-1(c). A resultant passband spectral shift of 300 nm is expected

between the two GST states along with a minimal decrease in transmission and a small increase in FWHM.

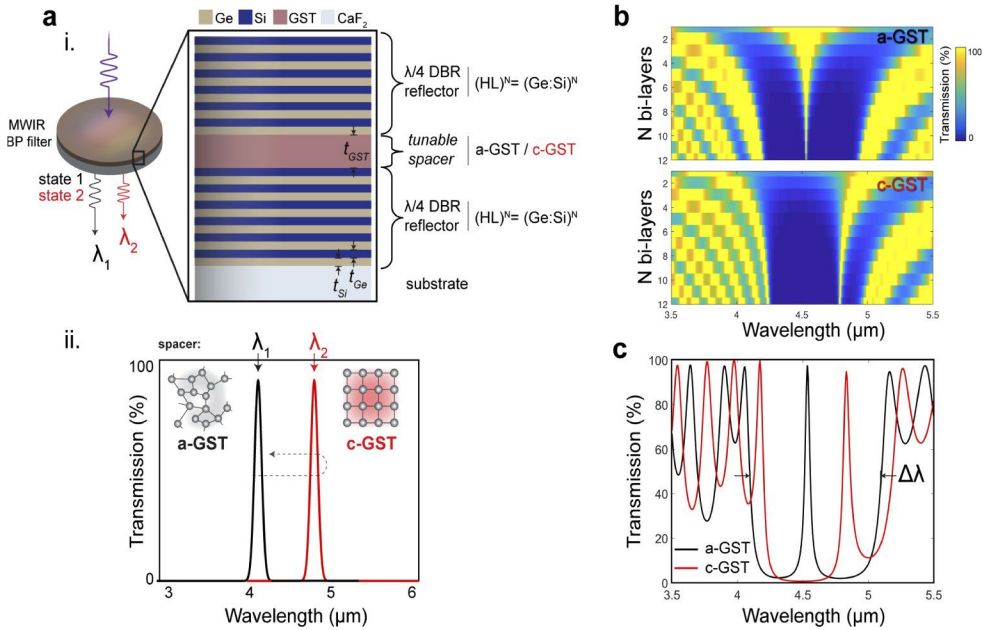


**Fig. 2-1. Device concept and simulations.** (a) Tunable MWIR Fabry-Perot bandpass filter layer design, with thicknesses of filter materials (e.g., t GST) indicated in (i), whereby the center wavelength ( $\lambda_1$  or  $\lambda_2$ ) of the narrowband transmission response will spectrally shift (ii) (a reversible process) depending on the spacer's optical thickness, hence GST crystallinity (refractive index). (b) Simulation of the effect of N-bilayers on the transmission response of the filter for a-GST and c-GST spacer layers with quarter-wave DBR stacks. (c) Simulation of the 6-layer designed FP filter. DBR = distributed Bragg reflector, BP = bandpass, HL = high- low index bi-layer,  $\Delta\lambda$  = blocking wavelength range (rejection region).

**Materials and Methods:** Double-side polished 25.4 mm (1-inch optics) CaF<sub>2</sub> wafers (Esco Optics, Inc.) were sonicated in acetone, iso-propanol, and deionized water sequentially twice, followed by an ultra-high purity compressed nitrogen (N<sub>2</sub>) blow dry before deposition. All thin-films were deposited via 50W RF magnetron sputtering at a base pressure of  $2.6 \times 10^{-6}$  Torr and a deposition pressure of 7 mTorr (10 sccm Ar flow, research-grade, 99.9999% purity). Three separate sputtering targets were used for the high-index, low-index and cavity (spacer) layers: Ge (99.999% purity), Si (99.999% purity) and Ge<sub>2</sub>Sb<sub>2</sub>Te<sub>5</sub> target (14.3 wt% Ge, 23.8 wt% Sb, 61.9 wt% Te, Mitsubishi Materials, Inc.). The chemical composition of as-deposited GST thin-films was determined by DCP-AES (Direct Current Plasma-Atomic Emission Spectroscopy, Luvak, Inc.). The composition was measured as 22% Ge, 23.5% Sb, and 54.5% Te, which is close to a nominal composition of bulk Ge<sub>22.2</sub>Sb<sub>22.2</sub>Te<sub>55.6</sub>. Fourier Transform Infrared (FTIR) spectroscopy (ThermoFisher) was used to measure the transmission intensity data of the bandpass filters. X-ray diffraction (XRD) was used to determine the crystallinity, and ellipsometry used to measure complex refractive indices of the respective layers. RC2 ellipsometry (Model: DI, J.A. Woollam) was used to measure up to 1.6 μm and IR-VASE (Infrared Variable-angle spectroscopic ellipsometry, J.A. Woollam) used to measure up to 7 μm. Results of both the XRD and ellipsometry measurements of as-deposited a-GST and c-GST (HCP) are shown in Fig. 2-2. A significant index modulation across the IR can be observed, with  $\Delta n$  2.4 at  $\lambda = 4.5$  μm. The refractive index measurements for RF sputtered thin-film Ge and Si (high-low bi-layer respectively) are shown in Figs 2-2(e) and 2-2(f) respectively. The measured refractive index values are summarized in Table 2-1 and compare closely with similar studies in the literature. These values are subsequently used to determine the  $\frac{1}{4}$ -wave thicknesses for the fabricated FP-bandpass filters.

**Table 2 - 1. Summary of experimentally derived MWIR optical constants (at  $4.5\mu\text{m}$  and  $4.52\mu\text{m}$ ) of the RF sputtered thin-films: Si, Ge, and  $\text{Ge}_2\text{Sb}_2\text{Te}_5$  (GST-225) in amorphous and crystalline states.**

Material	$\lambda = 4.5\mu\text{m}$		$\lambda = 4.2\mu\text{m}$	
	$n$	$k$	$n$	$k$
Ge	4.100	$\sim 0$	4.103	$\sim 0$
GST-225 ( <i>amorphous</i> )	2.948	0	2.952	$\sim 0$
GST-225 ( <i>crystalline</i> )	5.336	0.089	5.354	0.086
Si	3.42	$\sim 0$	3.424	$\sim 0$

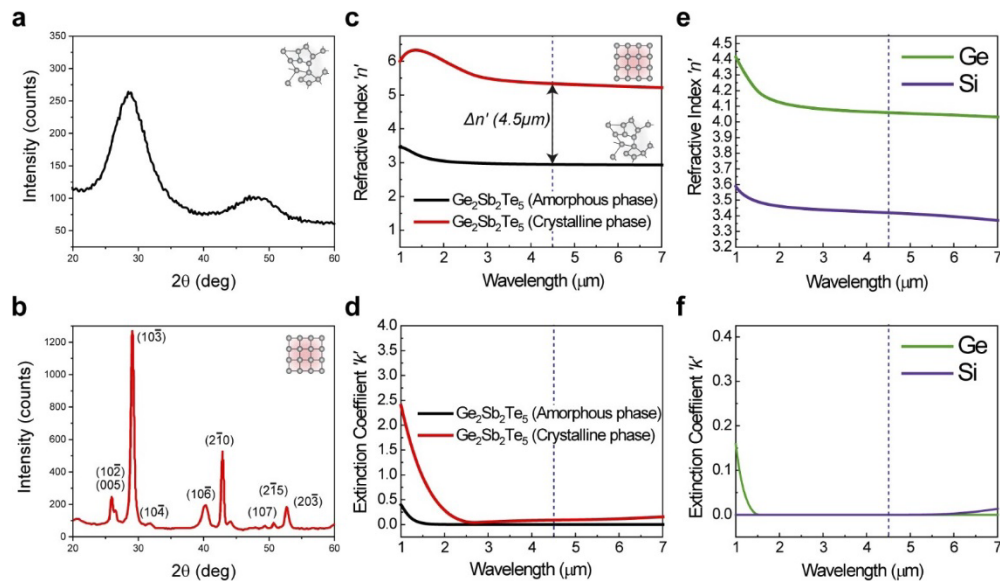


**Fig. 2-2. Thin-film materials characterization.** XRD data for sputtered amorphous  $\text{Ge}_2\text{Sb}_2\text{Te}_5$  (a) and (b) crystalline (HCP)  $\text{Ge}_2\text{Sb}_2\text{Te}_5$  states. (c) Real and imaginary (d) part of the refractive index for thin-film a-GST and c-GST across  $\lambda = 1-7\mu\text{m}$ , obtained through ellipsometry, with index modulation ( $\Delta n'$ ) of 2.4 at  $4.5\mu\text{m}$  indicated. (e) Real and imaginary (f) part of the refractive index for sputtered Ge and Si across  $\lambda = 1-7\mu\text{m}$ , obtained through ellipsometry. The design CWL of  $4.5\mu\text{m}$  is overlaid for visual reference.

**Numerical Simulation and Parameter Optimization:** Recursive propagation matrices (transfer matrix method, implemented in MATLAB®) are employed to determine the optical output of the thin-film multilayer dielectric stacks. The transmission and reflection coefficients at each interface of the thin-film stack are calculated as a function of wavelength, and overall transmission response determined recursively. Each layer is assigned its material-specific refractive index, with values obtained experimentally through ellipsometry measurements. For the two DBRs on either side of the GST spacer,  $N = 6$  bi-layers with thicknesses =  $\lambda_0/4n$ , where  $n$  is the experimentally determined refractive index of each high-low layer and  $\lambda_0$  the design CWL. As such, the stack arrangement is  $(\text{HL})^N(\text{spacer})(\text{HL})^N = (\text{Ge:Si})^6(\text{GST})(\text{Ge:Si})^6$ , where GST can be in either its amorphous or crystalline state. At  $4.5\mu\text{m}$ , an index modulation of ( $\Delta n$ ) = 2.4 exists between the two GST states (Table 2-1) which provides the change in optical path length for the spacer and thus the spectral shift in passband CWL. The comparably low number of bi-layers (with respect to commercial BP-filters) was chosen as a balance between desirable filter performance (narrow FWHM, high transmission etc.) and total deposition /processing time for a proof-of-concept set of devices.

**Experimental Results:** Two bandpass filters (25.4 mm diameter) with  $N = 1$  and  $N = 6$  alternating (HL) $N$  bi-layers, and layer thicknesses designed for  $\lambda_0 = 4.5 \mu\text{m}$ , were fabricated and optically characterized [Fig. 2-3(a)]. With the arrangement (Ge:Si) $N$ (GST)(Ge:Si) $N$ , the physical layer thicknesses were,  $t_{\text{Si}} = 329 \text{ nm}$ ,  $t_{\text{Ge}} = 280 \text{ nm}$  and  $t_{\text{GST}} = 375 \text{ nm}$  spacer (single cavity). The filters were annealed at 400°C inside a vacuum chamber to induce GST crystallization, then re-measured. Figure 2-3(b) shows the transmission results of the  $N = 1$  GST-BP filter for the two GST states. The a-GST state has CWL  $4.5 \mu\text{m}$  with 85% transmission efficiency, and c-GST state CWL  $4.9 \mu\text{m}$  with 70% transmission efficiency. The longer wavelength state (with the c-GST spacer) has a slightly reduced transmission peak attributed to the increased infrared absorption [extinction coefficient, Fig. 2-2(d)] of the c-GST compared to a-GST. Fig. 2-3(c) compares the transmission spectra of the two ( $N = 1$  and  $N = 6$ ) BP filters with the initial a-GST spacer. As expected, the FWHM (50 nm) narrows at the CWL, but the transmission decreases, which in this case we speculate is attributed to cumulative optical scattering from grain boundary defects of the multiple layers. The blocking wavelength range ( $\Delta\lambda$ ) is  $4.1\text{--}5 \mu\text{m}$ , and higher order ‘ripples’ can be observed outside this region. Figure 2-3(d) compares the  $N = 6$  filter in its two operating states. The initial a-GST state has CWL  $4.5 \mu\text{m}$  (as designed) with 75% transmission efficiency, and c-GST state CWL  $4.75 \mu\text{m}$  with 60% transmission efficiency and slight increase in FWHM to 65 nm (corresponding to a Q-factor 70–90). This proof-of-concept filter design can be further improved through incorporation of multiple-cavity GST-cavities and optimization of additional layers that will suppress out-of-band ripples.

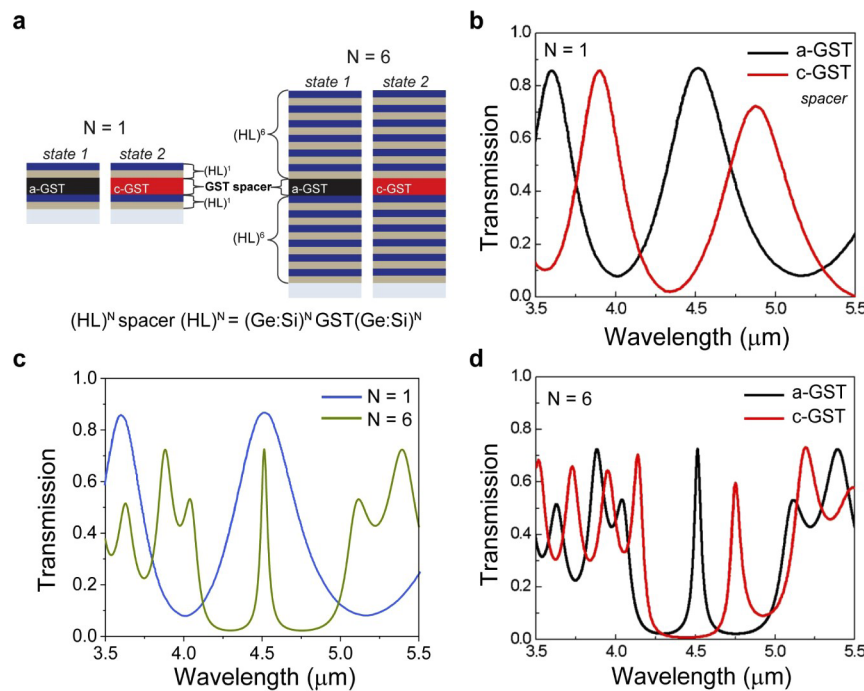


**Fig. 2-3. Tunable GST-FP MWIR bandpass filter characterization.** (a) Schematic of the two BP filters, with  $N = 1$  and  $N = 6$  bilayers, which can operate in two states: a-GST or c-GST spacer. (b) Transmission spectra of the two GST spacer states for a  $N = 1$  bi-layer stack -  $(\text{Ge:Si})^N(\text{GST})(\text{Ge:Si})^N$ . (c) Transmission spectra of the two filter types (with  $N = 1$  and  $N = 6$ ) in their a-GST states. (d) Transmission spectra of the  $N = 6$  filter in its two states: a-GST and c-GST.

## 2.2 Plasmonic Nanohole Array (PNA) filter

Presented for the first time are phase-change tunable MWIR metasurface spectral filters based on GST-embedded plasmonic nanohole arrays (PNAs) with high transmission efficiency, narrowband performance, a continuous tuning range, and fully reversible operation. Reconfigurability is achieved through accessing a continuum of partial-GST crystallinities using single nanosecond laser-pulse-induced phase

transformation. These partial crystallinities—previously unexploited/under-utilized experimentally—exhibit repeatable, stable behavior across several phase change cycles. Testing shows excellent optical performance characteristics, namely high transmittance (70%) on resonance, narrow bandwidth (74 nm) within the 3–5  $\mu\text{m}$  (MWIR) waveband, and near perfect reflection off-resonance.

The devices can both operate in transmission mode and offer narrowband performance due to the large field enhancement arising from the high-index GST being deposited inside the nanoholes, as opposed to a continuous, un-patterned film below the entire array. This high field enhancement appears to negate an increased extinction coefficient associated with c-GST, and the device geometry—with PCM filling the full volume of the nanoholes—provides the necessary design novelty to enable best-in-class optical performance. Real-world applicability has been shown through multispectral thermal imaging demonstrations by integrating the metasurfaces with an MWIR camera. The device design framework can be tailored to operate across any optical waveband through phase-change alloy selection. The results presented represent a significant step toward robust, tunable spectral filters, with applications in compact, fast-switching, and all-solid-state tunable filter systems for imaging in a wide variety of fields, from astronomy to remote Earth sensing.

The GST-based PNA MWIR metasurface filter concept is shown in Fig. 2-4. The extraordinary optical transmission (EOT) response, thus local field enhancement, of PNAs strongly depends on the surrounding index. Typically, this is exploited by modulating the index above or below the entire array. However, the resonance appears to be sensitive to the index inside the individual holes—a fact that has been unexplored experimentally. Here, the GST-PNA metasurface response is therefore dependent on the crystallization state of GST, which is subsequently tuned (continuously) through differing partial crystallizations, using a ns laser pulse (Fig. 2-4). This operating principle is summarized in Fig. 2-4(c), where an increasingly large pump energy incident upon the active area continuously adjusts the GST crystallinity, changing its index, and hence spectrally shifting the surface plasmon resonance (SPR) mode and changing the resulting transmission (EOT) response of the device. A “reset pulse” (high energy) is then used to revert the device back to a-GST, thus allowing for repeatable operation. Using the experimentally measured complex refractive index of GST [Figs. 2-5(d) and 2-5(e)], electromagnetic simulations (Lumerical FDTD) of the GST-PNA device, shown schematically in Fig. 2-6(a), were performed in order to optimize geometric parameters for narrowband optical performance across 3–5  $\mu\text{m}$ . Ag is chosen due to its superior optical properties across the MWIR in comparison to other noble metals (e.g., Al, Au). A hexagonal array was chosen in order to

decrease polarization sensitivity and increase overall space utilization. Additionally, hexagonal arrays have been shown to exhibit higher  $Q$  resonances compared to square arrays.

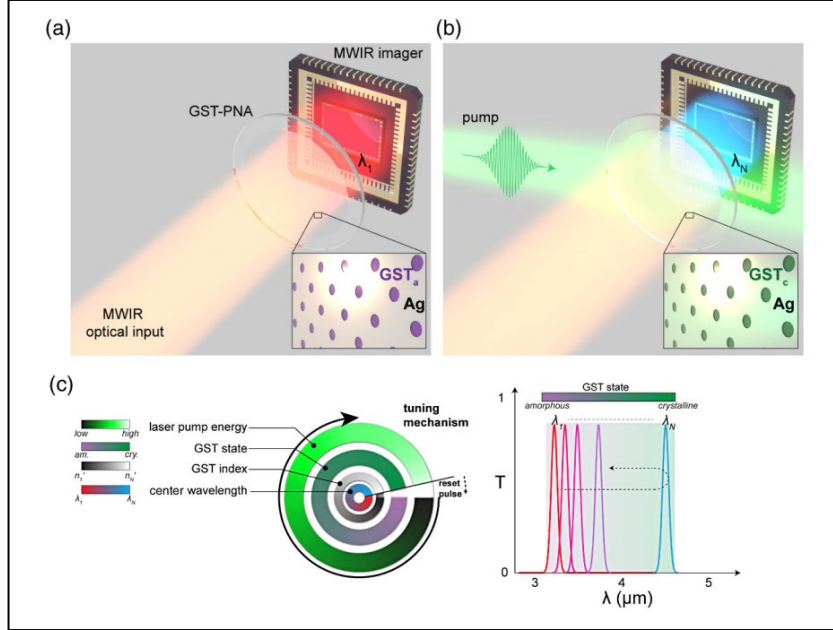


**Fig. 2-4.** Device concept. Tunable GST-plasmonic nanohole array meta- surface for the MWIR waveband. The MWIR optical input is imaged through GST-PNA filer in its initial, amorphous state (a), with initial center wavelength,  $\lambda_1$ . Through a laser pulse incident on the GST-PNA active area, the GST crystallinity is modified (phase change), and the resultant transmission response (center wavelength, with initial center wavelength,  $\lambda_N$ ) is spectrally shifted (b). This behavior is summarized in (c), whereby the pump energy controls GST-state, which in turn changes its refractive index, hence spectrally shifts the center wavelength from the resonant PNA. A “reset pulse” returns the GST to its initial state, thus device to initial transmission center wavelength.

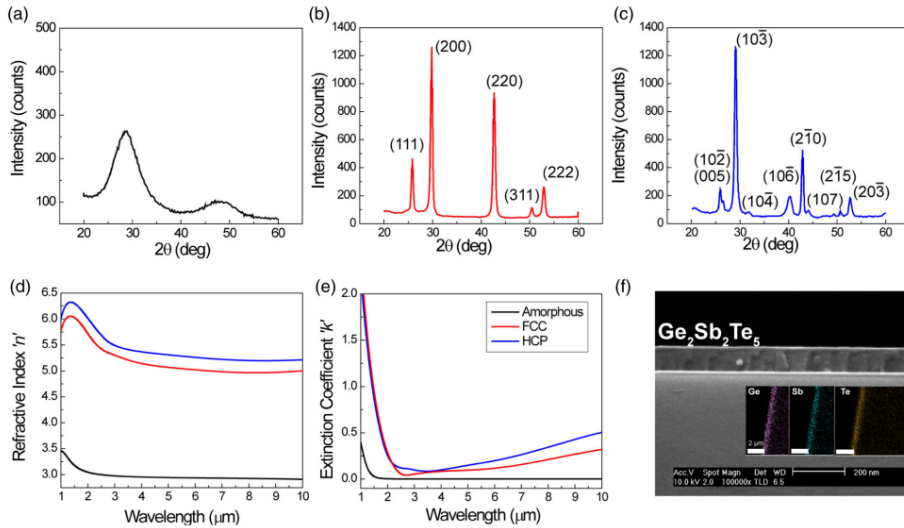


**Fig. 2-5.** Thin-film GST characterization. XRD (a)–(c) and ellipsometry (d), (e) data for a-GST (black curves), FCC c-GST (red curves), and HCP c-GST (blue curves). The average  $\Delta n$  is 2.0 between a-GST and c-GST, with HCP c-GST exhibiting slightly higher refractive index and extinction coefficient compared to FCC c-GST. (f) SEM cross-section image of the GST film deposited on  $\text{CaF}_2$ . The inset shows a top-

view energy-dispersive x-ray spectroscopy (EDS) mapping of the film edge, showing the clear presence of Ge, Sb, and Te species.

The hole diameter of the hexagonal array was optimized via sweeping the ratio of hole diameter ( $d$ ) to period ( $\Lambda$ ) at a given period; a ratio of  $0.4 \times \Lambda$  was found to be optimal with  $\Lambda = 1800$  nm and 60 nm thickness. The effect of array periodicity and embedded refractive index GST/Ag PNAs (with  $d = 720$  nm) is presented in Figs. 2-6(b) and 2-6(c). As expected, a near linear dependence on both quantities is observed, and the simulated FWHM is consistently 80 nm throughout the simulated range (with a slight increase at longer resonance wave-lengths), with low reflection shown off-resonance corresponding to a high out-of-band blocking region of optical density (OD)  $\sim 3\text{--}4$ , competitive against established tunable filter technologies. The simulations performed show a tuning range of 2.9–4.1  $\mu\text{m}$ ; however, by further increasing/decreasing the period of the nanohole array, this range can be extended to include the NIR/long-wave infrared (LWIR). At resonance, the large field enhancement provided by the SPR [Fig. 2-6(d)] partially mitigates the non-zero c-GST extinction coefficient, leading to a larger-than-expected transmission efficiency. The SPR origin of the enhancement phenomenon—consistent with EOT—was confirmed by also analyzing the fields in out-of-plane hole cross sections [Figs. 2-6(e) and 2-6(f)] and performing simulations with non-plasmonic metal films. In Figs. 2-6(e) and 2-6(f), both a-GST (i) and c-GST (ii) states, at resonance, are investigated with experimentally derived refractive index data for both a-GST and c-GST states. The SPR mode couples to the Ag–GST interface inside the hole, leading to an increased transmission response.

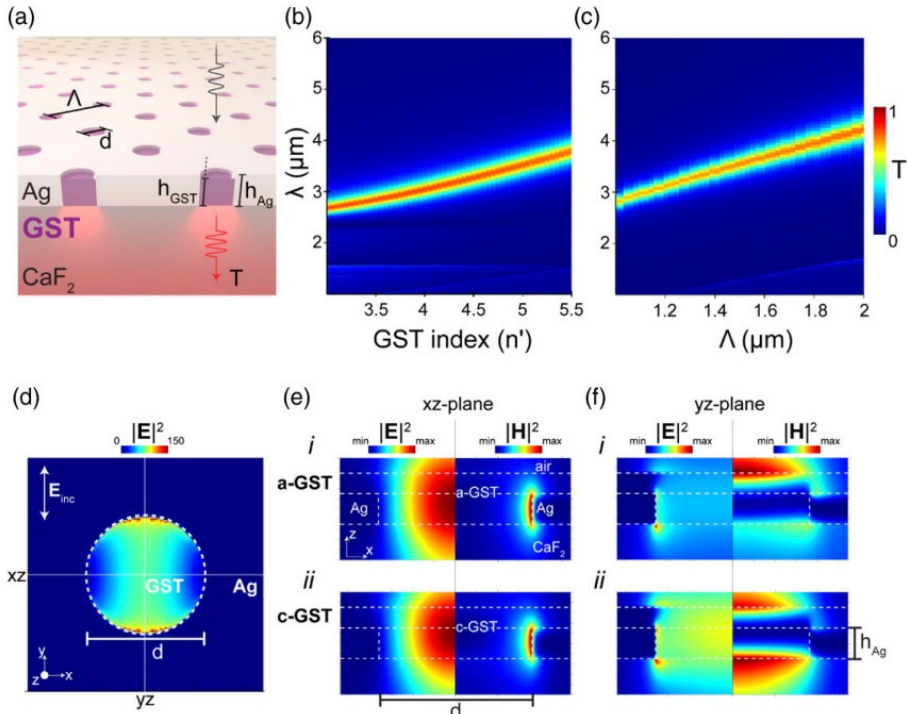


**Fig. 2-6.** FDTD simulations of the optical response of the GST-PNA concept (a). Simulated transmission response of the GST-PNA device as a function of GST refractive index (b), and as a function of hole period (c), for  $h_{\text{Ag}} = 60$  nm metal film thickness and  $d = 0.4\Lambda$ . E-field plot (d) showing SPR-generated field enhancement on-resonance at the boundary between Ag/GST inside the PNA cavity. (e), (f) E- and H-field enhancement plots, on-resonance in respective states, of the GST-PNA at xz and yz cross-section slices of a single hole in an array, in amorphous (i) and crystalline (ii) GST states, where  $\Lambda$  period,  $d$  hole diameter 720 nm, and the experimentally derived GST complex refractive index data in Figs. 5(e) and (f) utilized Fig. 6. FDTD simulations of the optical response of the GST-PNA concept (a). Simulated transmission inside the hole array. Source injection from  $\text{CaF}_2$  side.

**Metasurface Fabrication:** The metasurface spectral filter devices were designed for an a-GST resonance at 3.0  $\mu\text{m}$ , which corresponds to a period of 1800 nm (hole diameter 720 nm). A SEM micrograph of one of the GST-PNA devices is shown in Fig. 2-7(a). 60 nm of Ag was deposited via magnetron sputtering onto  $\text{CaF}_2$ , patterned via direct-write photolithography and dry etched to generate the nanohole array; the total patterned device area was 15 mm x 15 mm. 70 nm of GST was then deposited to ensure the nanoholes were completely filled with GST (100% hole volume). This resulted in a <10 nm layer of GST above the Ag surface boundary. FDTD simulations confirm that any ultrathin layer of additional GST has a negligible effect on the device behavior. Last, an encapsulation (capping) layer of  $\text{SiO}_2$  (total thickness <5 nm) was deposited in order to prevent oxidation of the Ag–GST, as well as any partial volatilization that may arise as a result of switching. This layer is fully transparent across the visible-MWIR wavebands. The GST thin film morphology and optical properties were characterized in the same way described in the previous section.

Transmission-mode Fourier transform IR spectroscopy (FTIR) was used to optically characterize the GST-PNA metasurfaces. A laser pulse induces crystallization of the as-fabricated a-GST devices; it is then re-characterized in its crystalline state (c-GST). The resulting transmission response due to the respective GST state is shown in Fig. 2-7(b). FTIR data are shown for both the HCP and FCC phases of c-GST. Samples were subsequently heated by applying a single 160 mJ  $\text{cm}^2$  100 ns laser pulse to return to the amorphous phase to be re-characterized. A total of 10 complete phase-change switching cycles was performed, while recording resonance peak position [Fig. 2-7(c)] to demonstrate the stability of the filtering response. The devices show high stability across all cycles in both the amorphous and crystalline phases, and the shape of the spectral response in each phase is unchanged [Fig. 2-7(d)], which is a result of the addition of the capping layer. A typical feature of PCMs is thermal hysteresis: the difference between the melting and crystallization temperatures, due to the differing heating and cooling paths. The magnitude of the hysteresis is proportional to the energy loss in the system, which is dependent on PCM stoichiometry, film thickness, laser energy density, and phase-change switching speed.

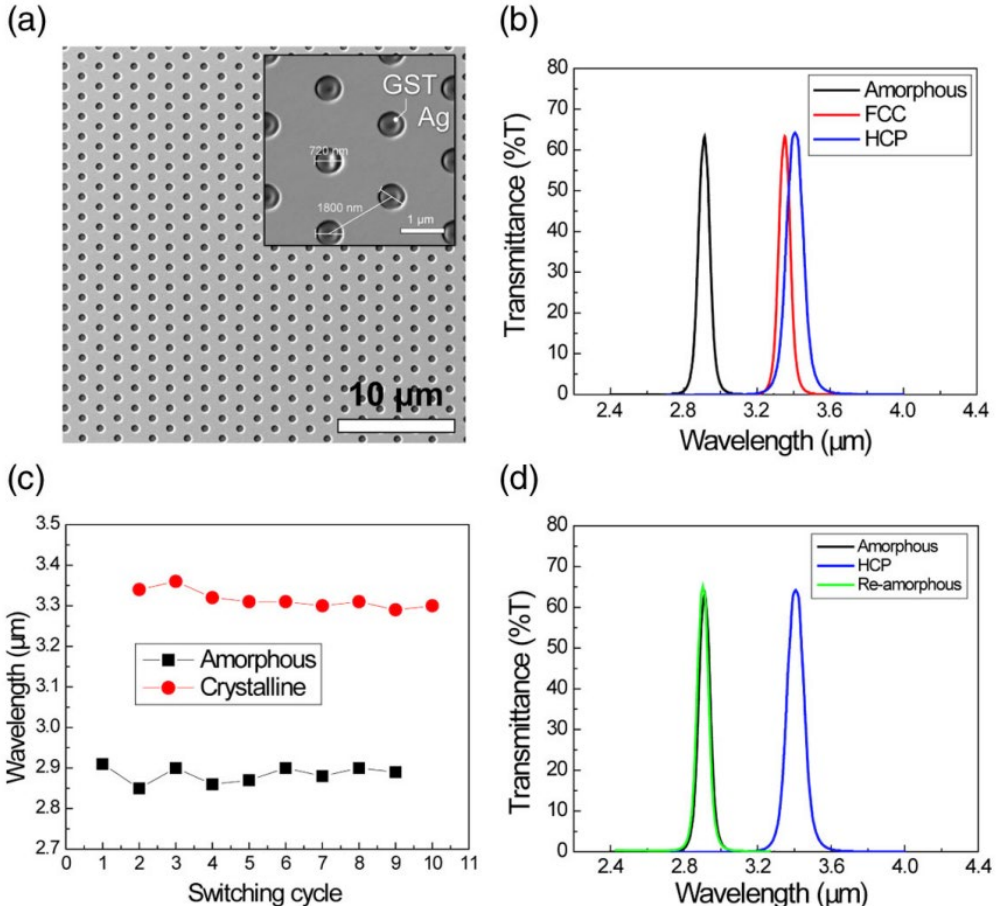


**Fig. 2-7.** GST-PNA device tuning. (a) SEM micrographs of the fabricated tunable GST-PNA metasurface device showing the full hexagonal array geometry and individual hole morphology (inset). The GST embedded within the Ag PNA can be seen. (b) FTIR (transmission) characterization of the fabricated PNA device showing 70% transmission at the resonance and perfect reflection outside the resonance bandwidth. Stability in the spectral response was maintained across many switching cycles; shown through center wavelength reproducibility (c) and spectral shape consistency (d).

**Experimental Results:** The reversal property in our device is shown to be stable across a number of switching cycles, as shown in Figs. 2-7(c) and 2-7(d), with no observable hysteresis, suggesting that irreversible changes in GST-PCM are not significant in our film or device design in contrast to VO<sub>2</sub>-based PCM. The devices show a transmission efficiency of ~70% in both crystalline phases, which is among the highest transmission for such a structure reported in the literature, irrespective of spectral band. FWHMs of 74 nm in the amorphous phase and 100 nm in the crystalline phase are in good agreement with simulation results. Moreover, the peak center wavelengths lie at ~2.9 μm in the amorphous state and 3.35 μm in the crystalline state, which are also in good agreement to the simulated values of 3.0 μm and 3.5 μm, respectively. This small deviation is likely the result of either batch- to-batch variation in the refractive index of the deposited GST, microfabrication tolerances, and/or as a result of the addition of the capping layer.

Due to the confined growth circumstances of deposition in nanoholes, the GST inside of the holes likely has a smaller grain size compared to GST deposited on planar substrates. A reduced grain size leads to a larger band gap, and thus less absorption, in the GST inside of the holes. This may explain the low

absorption measured in the crystalline phase of the experimentally demonstrated device. This phenomenon suggests that the GST extinction coefficient can be independently optimized based on the GST film growth conditions. Additionally, c-GST grain size is largely influenced by the fluence, wavelength, and pulse duration of the switching-laser, with nanosecond pulses in the ultraviolet regime producing the smallest grain sizes. Therefore, we expect that the lack of c-GST absorption results from a reduced grain size as a result of the confined film growth and the nanosecond optical switching pulse.

**Reversible, All-Optical Continuous Tuning:** For many imaging/spectroscopy applications, active (or rapid) optical tuning is highly desirable, i.e., the passband center wavelength can be reversibly spectrally shifted. This is traditionally achieved through optical, electrical, or thermal stimuli, but an all-solid-state solution has been challenging. Here, an all-optical approach has been implemented due to the challenges associated with fabricating micro-heater elements across 1-inch diameter optical elements, and subsequently demonstrating continuous spectral tuning of a  $\sim 8.4$  mm<sup>2</sup> device with a ns laser pulse. The setup is shown schematically in Fig. 2-8(a). A 532 nm laser (100 ns) is used to rapidly switch the GST crystallinity, and thus output optical response. The pulse energy, with 7 mm beam diameter, was increased linearly from 2–250 mJ, in order to study the effect of incident pulse energy on the GST crystallinity. A laser spot size of 8.4 mm was chosen due to the 6.5 mm measurement area probed by the FTIR system. By varying the fluence from 10 – 60 mJ cm<sup>2</sup>, intermediate (partial crystallinity) phases of GST were generated, with full crystallization being achieved at 60 mJ cm<sup>2</sup> fluence. Here, three unique partial crystallinity (p-GST) states were formed, with refractive index values ranging from  $\sim 3.0$ – 3.75, and  $\Delta n \sim 0.25$  between each state. By implementing finer control of the pulse energy (e.g., with a polarizer and half-wave plate) a virtual continuum of p-GST states can be generated (i.e.,  $\Delta n$  between adjacent states can be minimized, and the number of states increases). In order to return to the amorphous phase, it was found that a fluence of 160 mJ cm<sup>2</sup> was required (i.e., reset pulse). Ellipsometry data and FTIR characterization of the optically tuned GST films (a-GST, c-GST, and two p-GST states) are shown in Figs. 2-8(b) and 2-8(d). The transmission response in each state is approximately constant despite the small increase in extinction coefficient with increasing GST crystallinity, which only slightly increases the FWHM of the fully crystalline state. This is due to the increased field enhancement observed in PNA devices filled with a high-index dielectric medium. As the laser energy density increases, a GST refractive index change is induced through partial phase change, and thus peak resonance spectrally red shifts [Fig. 2-8(e)]. This behavior is in strong agreement with simulations. Moreover, the a-GST devices—before switching and after laser-induced return (i.e., reset pulse to the amorphous state)—show nearly identical spectral responses, demonstrating stability in the optical tuning mechanism. To the best of our knowledge, this is the first-time tunable operation across the MWIR with high transmission efficiency (70%) and narrowband filtering (70 nm FWHM, Q-factor 45) has

been achieved.

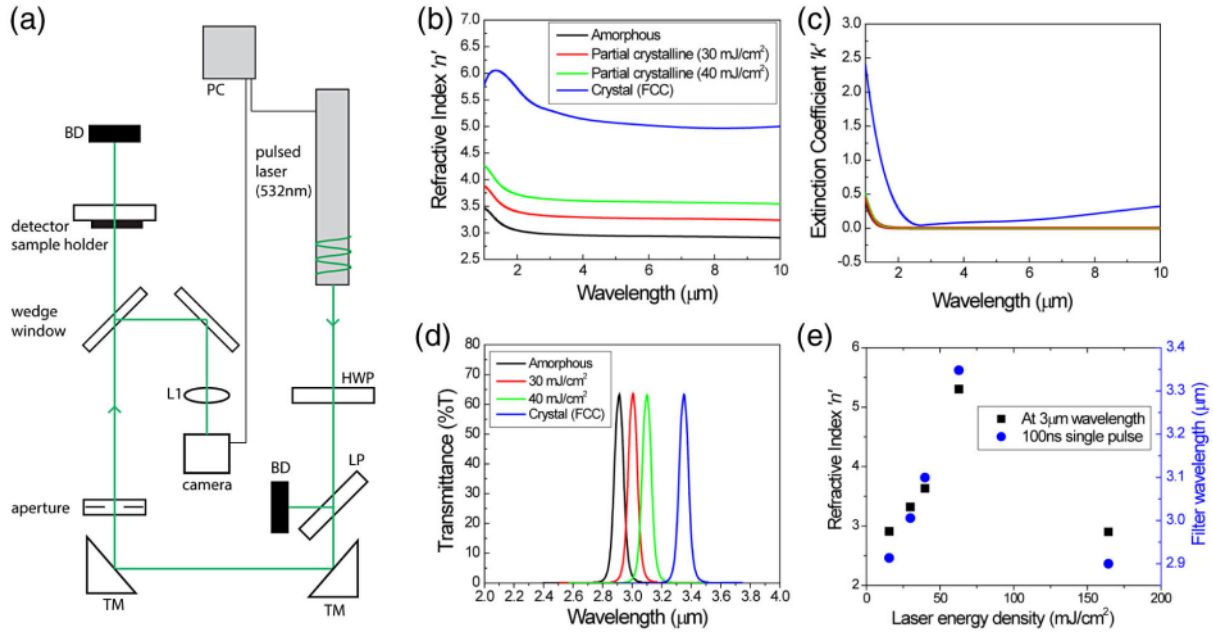


**Fig. 2-8.** Optically tuned GST-PNA metasurface devices. (a) Setup used for the laser switching demonstration. Complex refractive index measurements (b), (c) of the a-GST, p-GST, and c-GST films (tuned using the all-optical approach), along with the corresponding spectral response of the full GST-PNA metasurface device for each case as experimentally measured via FTIR (d). It can be seen in (e) that with increasing pulse energy, the crystallinity increases until c-GST is achieved. Further increasing the pulse energy allows for the return to a-GST. Upon returning to the amorphous state, the device exhibits nearly identical spectral response to the as-deposited amorphous phase device.

Due to the conformal deposition of the GST films, there is essentially zero heat dissipation in the Ag film as a result of the shallow absorption depth of GST at 532 nm. As a result, the Ag film is not subjected to high temperatures ( $T_m$ : 916.8 °C). This, along with the nanosecond timescale of the overall heating/cooling process, prevents the Ag from melting and diffusing into the GST. This lack of Ag diffusion is evidenced by the consistent switching behavior of the device, as Ag atom diffusion into the GST-filled holes would result in absorption and therefore lower transmission, which is not observed in the experimental data. However, for an increasingly large number of phase-change cycles, Ag diffusion mitigation techniques are required because the GST needs to achieve a 635 °C melting temperature for phase transition with the mJ-level power laser. To prevent possible diffusion of the Ag into GST after many switching cycles, an atomically thin buffer layer (such as Al<sub>2</sub>O<sub>3</sub>) can be integrated (through atomic layer deposition or otherwise). This will enable long device lifetimes and stable operation across many switching cycles.

### 2.3 All-dielectric metasurface filter using deep neural network design methods

In recent years, deep learning approaches and deep neural networks (DNNs) have been investigated as a solution to handle complex photonic design problems including design of multilayer structures and freeform meta-atoms. In these examples, DNNs were constructed to directly predict the transmission or reflection spectra of passive photonic structures. Here, we expand the repertoire of deep-learning-based photonic design by showing that DNNs can also be implemented to both predict and inverse design broadband complex S-parameters of active metasurface elements. The DNNs can then be used in conjunction with

transfer matrix method (TMM) based analytical optimization to facilitate computationally efficient design of metasurface-embedded tunable photonic devices.

As one example illustrating the hybrid design approach, an actively tunable bandpass filter was designed integrating a PCM metasurface with two DBRs operating in the MWIR waveband. Such a filter is currently being explored for space-borne multispectral imaging and sensing applications given their substantial size, weight, and power (SWaP) advantages. The PCM metasurface is constructed with a periodic array of GeSbSeTe (GSST) meta-atoms sitting on a doped Si-on-SiO<sub>2</sub> (SOS) substrate and the DBRs are composed of quarter-wavelength-thick a-Si and SiO<sub>2</sub> layers. By applying voltage pulses to the doped silicon heater underneath the meta-atoms to electrothermally trigger structural transition of GSST, the optical phase delay between the two DBRs and hence the transmission band can be actively tuned. Compared to a simple FP structure with a flat PCM cavity layer, this design not only enables versatile dispersion engineering but also offers a realistic architecture for electrical reversible switching of PCMs. By singulating a PCM film into discrete meta-atoms surrounded by a thermally conductive capping layer (MgF<sub>2</sub> in this case), we can significantly expedite heat extraction during the PCM amorphization process to achieve uniform switching throughout the entire PCM volume.

**Design Method:** The metasurface-embedded FP filters (hereinafter referred to as the “MFP filters”) were constructed with two DBRs and one metasurface layer sandwiched in between (Fig. 9(a)). Each meta-atom element [Fig. 2-9(c)] consists of a freeform GSST structure sitting on a square-shaped SiO<sub>2</sub> substrate. Between the substrate and the GSST material, one thin layer of doped silicon was also added which acts as an electrically controlled resistive heater. By carefully engineering the amplitude and duration of the voltage pulses applied to the heater, the GSST material can be dynamically switched between amorphous, partially crystalline, or fully crystalline states. Both the top and the bottom DBR consists of pairs of a-Si-SiO<sub>2</sub> (high-low index) films, and the pair numbers are analytically optimized using TMM. The meta-atoms are encapsulated in MgF<sub>2</sub>, whose thickness can be tuned to adjust the cavity length. Without loss of generality, the spectra of interest were set to be from 60 to 100 THz (3 μm to 5 μm in wavelength), with a center wavelength of 4 μm. The incident light is a linearly polarized plane wave illuminated from the substrate side. Considering the electronically large structure size (usually several wavelengths in the propagating direction) and the resonant nature of this MFP filters, full-wave simulation of the entire MFP filter structure is usually time-consuming. Therefore, exhausting the full design space—including tunable refractive indices of the GSST material, thickness of the DBR layers, spacing between DBRs, lattice size, as well as the geometry of freeform meta-atoms—by parametric sweep alone to find the globally optimal design is computationally unfeasible. Instead, we resorted to the TMM approach. As shown in Fig. 2-9, the transfer matrices of the top DBR [Fig. 2-9(b)], center meta-atom [Fig. 2-9(c)], and bottom DBR [Fig. 2-9(d)] can be separately calculated and multiplied together subsequently to obtain the total transfer matrix. The transmission characteristics the entire MFP filter can be derived by converting its total transfer matrix into S-matrix. Due to the near-field effects and coupling between the freeform meta-atom and its surroundings, the S-matrix of the meta-atom cannot be numerically analyzed, which limits the modeling efficiency of this TMM approach. To tackle this challenge, a forward prediction DNN was trained [Fig. 2-9(e)] that generates accurate S-parameters of GSST meta-atoms given its dimensions and crystallization state. Since the DNNs calculate the output on a one-time-calculation basis, optical performance of the MFP filters can be predicted with minimal time cost which further accelerates their optimization and inverse design.

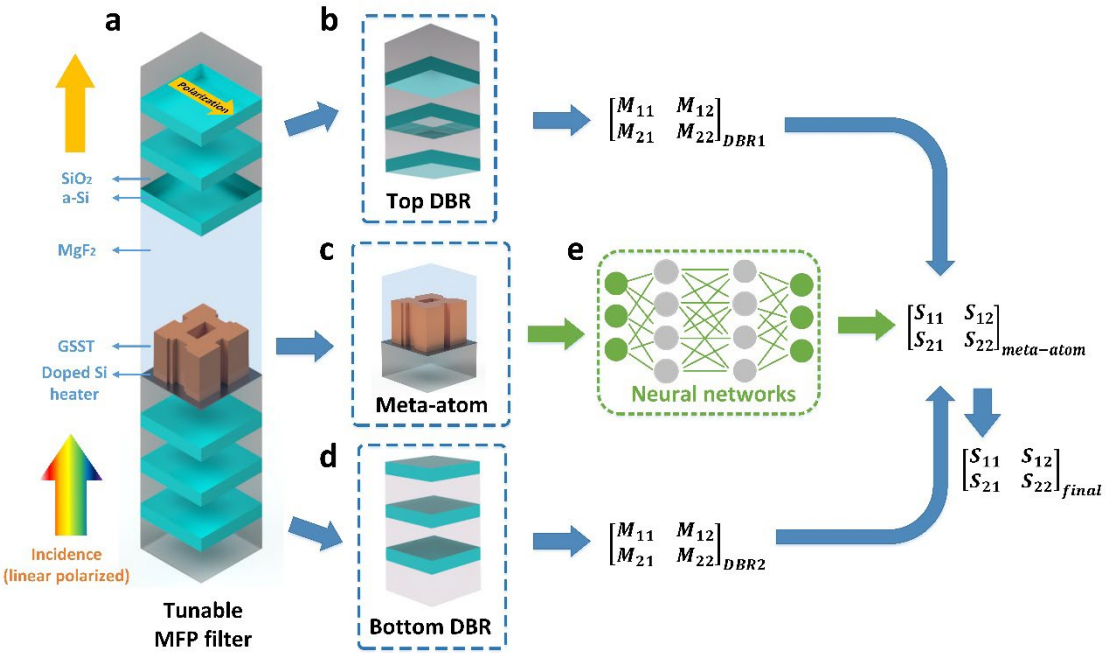


**Fig. 2-9. MFP filter analysis.** (a) A schematic diagram of the tunable filter structure. (b) The top DBR. (c) the GSST meta-atom in the center of the cavity. (d) The bottom DBR. (e) The forward prediction DNN to evaluate the S-matrix of the meta-atom. The S-matrices were then translated into transfer matrices and multiplied with the transfer matrices of the DBRs to calculate the final S-matrix of the whole structure.

**Forward Prediction DNN:** A forward prediction DNN was constructed and trained to achieve fast and accurate evaluation of meta-atoms shown in Fig. 2-9(c). The forward prediction DNN was constructed based on a convolutional neural network (CNN) architecture [Fig. 2-10]. The meta-atom designs can be described with two sets of parameters: the 2-D cross-section of the meta-atom and other properties, including the crystallization fraction of GSST (between “0” representing amorphous and “1” corresponding to fully crystalline), thicknesses of the  $\text{SiO}_2$  layer between doped Si heater and the bottom DBR, the GSST meta-atom and the  $\text{MgF}_2$  capping layer, as well as the lattice size (period) of the meta-atoms. The 2-D cross-sections were processed through a 2-D image processing network (bordered in green in Fig. 2-10), which is composed of three consecutive convolutional layers. The rest of the meta-atom’s properties were processed with a 1-D property processing network (bordered in blue in Fig. 2-10), which includes a Neural Tensor Network (NTN). The NTN relates the input parameters multiplicatively instead of only implicitly, which effectively accelerates the training process when the relationship between input and output is highly non-linear. The output of the NTN was then spatially tiled and concatenated with the output of the 2-D image processing network. The combined output was then further processed with more convolutional layers, during which more high dimensional hidden features of the original meta-atom were revealed and extracted. Finally, two dense layers translated the extracted features into the wideband S-parameters of the meta-atom. Since the meta-atom can be treated as a two-port network, the final output is composed of wideband  $S_{11}$ ,  $S_{12}$ ,  $S_{21}$ , and  $S_{22}$  responses. Two prediction networks with the same architecture (as shown in Fig. 2-10) were trained to predict the real and imaginary parts of the complex S-parameters of the meta-atoms, respectively.

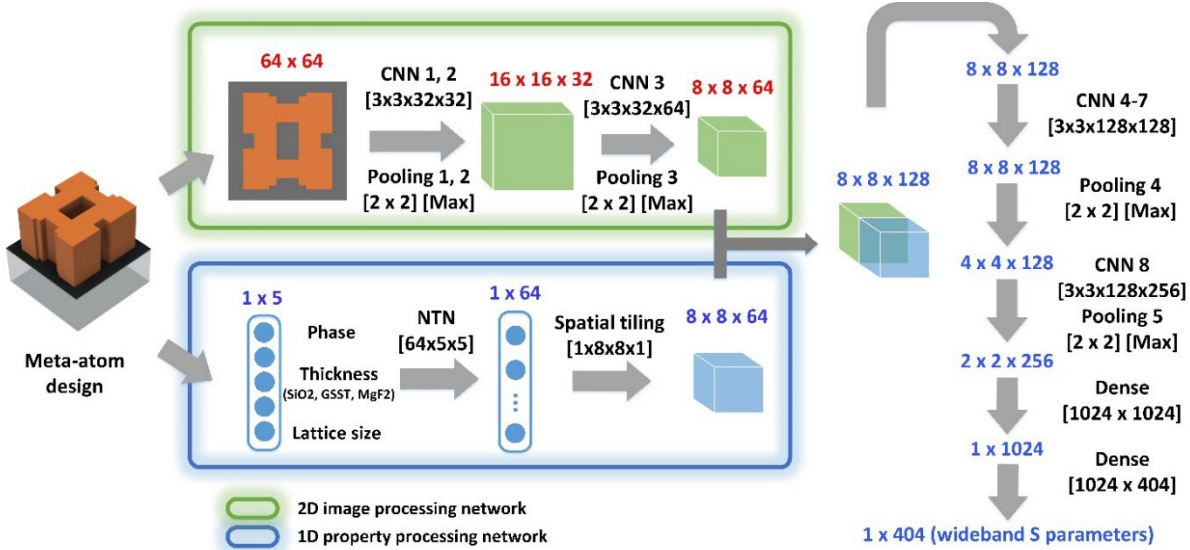


**Fig. 2-10. Network architecture.** The meta-atom design parameters were evaluated using a 2-D image processing network (circled in green) and a 1-D property processing network (circled in blue). After processing with several convolutional layers and dense layers, the S-matrix (real and imaginary part) of the meta-atom over the spectrum of 60 -100 THz were generated as the final output. 101 frequency points, with a spacing of 0.04 THz, were used to represent the full spectra for each S-parameter.

To train the network, over  $10^5$  groups of meta-atoms with quasi-freeform 2D cross-sections were randomly generated using the “needle drop” approach. The other parameters including the state of the PCM and the dimensions of the meta-atoms were created randomly within the following range (with lengths all in  $\mu\text{m}$ ): material state  $\in [0, 1]$ , SiO<sub>2</sub> substrate thickness  $\in [0.6, 0.8]$ , GSST thickness  $\in [0.5, 2]$ , MgF<sub>2</sub> thickness  $\in [1, 3]$ , lattice size  $\in [0.5, 1.5]$ , since these ranges provides ample samples of the meta-atoms’ S-parameters. The S-matrices of these randomly generated designs were evaluated using the full-wave simulation tool CST Studio Suite. The 2-D cross sections of the meta-atoms, along with the 1-D properties were assigned as the input of the network, while their corresponding wideband S-matrices were designated as the outputs. Among the 100,000 groups of training data, 70% were used during the training process, the remaining 30% were used to evaluate the fully-trained network. The parameters of the hidden layers shown in Fig. 2 were optimized during the training to minimize the difference between predicted results and the ground truth. Upon completion of the training, the average mean square error (MSE) was  $7.3 \times 10^{-4}$  for the real part and  $7.8 \times 10^{-4}$  for the imaginary part of the complex S-parameters. To showcase the DNN’s accuracy, we randomly selected a meta-atom design from the test dataset and employed the prediction network to evaluate its performance in different crystallization states [Fig. 2-11]. The real part (in blue) and imaginary parts (in red) of their complex S-matrices, including the S<sub>11</sub>, S<sub>12</sub>, S<sub>21</sub>, and S<sub>22</sub> are shown on the right in each subplot. The dotted symbols are the prediction results generated by the network, while the solid curves are the ground truth derived with the full-wave simulation tool. Among the 101 sample points that were used

across 60–100 THz, only 26 were plotted in each subplot in Fig. 2-11 for the sake of clarity. As indicated by the small training error, the prediction results agreed well with the ground truth in all cases.

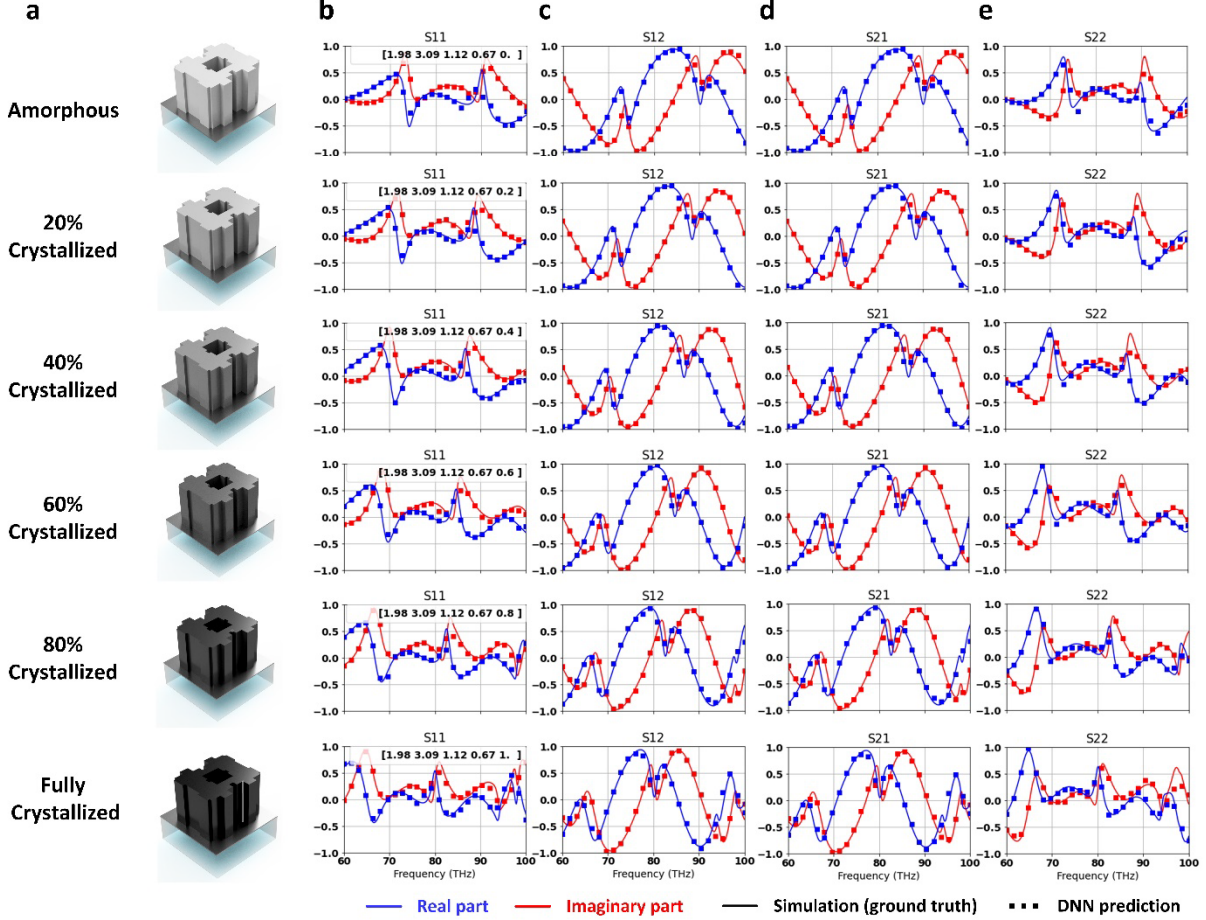


**Fig. 2-11. S-matrix prediction using forward DNN.** (a) Meta-atoms in different crystallization states. 3-D model of each meta-atom is shown on the right. (b) S11 plots. (c) S12 plots. (d) S21 plots. (e) S22 plots. Dotted symbols represent the DNN prediction results, while solid curves are simulation results (ground truth). Parameters including lattice size, the thicknesses of MgF<sub>2</sub>, GSST meta-atom, and SiO<sub>2</sub> substrate, as well as the crystallization states are shown on the top-right corner of the S11 subplots (parameters listed in the same order as here; all lengths in  $\mu\text{m}$ ).

Using the TMM approach in Fig. 2-9, with the help of this fully-trained network, the spectral responses of a MFP filter structure can be rapidly calculated (in milliseconds). This forward DNN has two major advantages: (1) due to its high computational efficiency, this forward DNN can be adopted to evaluate the performance of the designs in closed-loop optimization algorithms, which otherwise would have been the most time-consuming process (usually takes minutes) during the optimization, and (2) since we are building this forward prediction DNN in a way that it can handle meta-atoms with different design parameters, the network can be employed to quickly assemble sub-datasets with less degrees of freedom for more specific design problems. For example, since most metasurface and meta-devices are composed of elements with the same lattice size and thickness, we can use the prediction network to choose the right parameter combinations (including the lattice size, thickness, and material indices) that leads to the largest modulation depth of phase and amplitude. Besides, given the fabrication complexity associated with freeform meta-

atoms which entail small critical dimensions, we can utilize the forward DNN to predict the spectral responses of a class of meta-atoms with simple shapes such as rectangles and ‘‘H’’. These patterns can be easily described using a limited number of parameters, which largely reduces the difficulty of inverse design. In the following section, we demonstrate how to construct and train a MFP filter inverse design network with a sub-dataset generated by the forward prediction DNN which is composed of only ‘‘H’’-shaped meta-atoms.

Inverse Design DNN: With meta-atoms constructed with PCMs such as GSST, if we found a specific design with high transmission and large phase delay tuning range when it’s in different crystallization states, then it is possible to realize tuning of FP resonances inside the MFP filter structure at will. Specifically, for bandpass filters with a given tuning range, we can calculate the target electrical length of the spacing between two DBRs at two ends of the tuning range [Fig. 2-12(a)] and then realize a similar optical response of the shorter electrical length using one GSST meta-atom design in the amorphous state, and likewise use the same design in the fully crystalline state to attain the longer electrical length [Fig. 2-12(b)]. The continuous tuning of the FP resonances between these two states can be achieved by manipulating the crystallization state of the GSST material through adjusting voltage pulse parameter. Inspired by this idea, we constructed an inverse design DNN for the design of actively tunable filters with given tuning range targets and filter functions (edge, bandpass, etc.). As a proof of concept, we focused on the bandpass filters across the MWIR band. As shown in Fig. 2-12(c), the target wideband S-matrices (in both the amorphous and the fully crystalline states) were assigned as the inputs of the inverse DNN while the shape and dimensions of the corresponding meta-atoms were defined as the output. Since the meta-atoms with the shape of letter ‘‘H’’ provides sufficient transmission and phase delay responses while maintaining a low fabrication difficulty comparing to the freeform shapes, we used the ‘‘H-shaped’’ meta-atoms to assemble the training dataset for the inverse DNN. Specifically, we drew ‘‘H-shaped’’ patterns with random dimensions on a  $64 \times 64$  canvas, then sketched the 2-D ‘‘H-shaped’’ patterns with four parameters ( $L_x, L_y, L_{x_1}, L_{y_1}$ , as shown in Fig. 2-12(d)) and combined these four parameters with the other dimensions ( $t_{MgF_2}, t_{GSST}, t_{SiO_2}, lattice$ ) that were randomly created within the preset data range mentioned above. The S-matrices of these randomly generated meta-atoms were evaluated with the fully trained prediction DNN. The final training dataset contains over  $5 \times 10^4$  groups of ‘‘H-shaped’’ meta-atom designs, along with their wideband S-matrices within the 60–100 THz range in both amorphous and crystalline states.

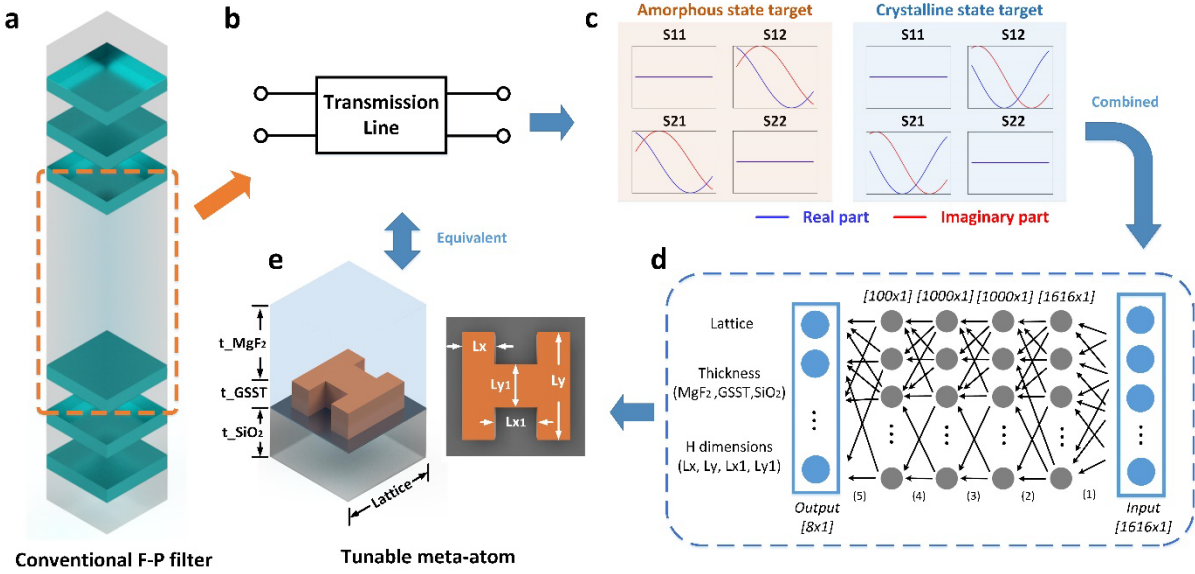


**Fig. 2-12. Inverse design DNN.** (a) A conventional -P filter. (b) The spacing between two DBRs was treated as a two-port transmission line. (c) S-matrices of the transmission lines were designated as input of the inverse DNN. (d) The meta-atom inverse DNN constructed based on fully connected neural networks.  $\epsilon$  Output of the inverse DNN, which is a combination of design parameters including all meta-atom dimensions.

After the inverse DNN in Fig. 2-12d was fully trained, this network was employed to design two tunable bandpass filters with different tuning ranges. The top and bottom DBRs each consist of 3 pairs of a-Si ( $n = 3.4$ ) and SiO<sub>2</sub> ( $n = 1.39$ ) films. Taking  $\lambda = 4 \mu\text{m}$  as the center wavelength of the bandpass, the thicknesses of the quarter-wavelength a-Si and SiO<sub>2</sub> layers were set to 294 nm and 719 nm, respectively. As shown in Fig. 2-13(a), the first design target has a tuning range from 3.75  $\mu\text{m}$  to 3.95  $\mu\text{m}$ , which requires the distance between DBRs [Fig. 2-13(b)] changing from 2.6  $\mu\text{m}$  to 2.8  $\mu\text{m}$ . S-matrices of this meta-atom between the 60-100 THz frequency range, including S-parameters in both amorphous state (in red) and fully crystalline state (in blue) were fed to the inverse DNN as inputs. The generated design [Fig. 2-13(d)] has optical responses very similar to the preset targets [Fig. 2-13e]. The optical response of the final MFP filter design [Fig. 2-13(f)] is therefore close to the design objective [Fig. 2-13(a)]. For the second design (showing at the bottom of each subplot), the center wavelength tuning range was set to be  $\in [4.3 \mu\text{m}, 4.6 \mu\text{m}]$ . Similarly, the optical performance of the design generated by the inverse DNN are similar to the design target. It is noted that due to the non-zero S<sub>11</sub> and S<sub>22</sub> values of the meta-atom designs, this multilayer filter design was not perfectly matched at the interfaces between the meta-atom and the DBRs, which leads to a certain amount of reflected energy at resonances. This mismatch, along with the unneglectable loss of the GSST material and the doped silicon heaters, has limited peak transmission (<50% and decreased as the material switched to fully crystalline) of the designs [Fig. 2-13(f)].

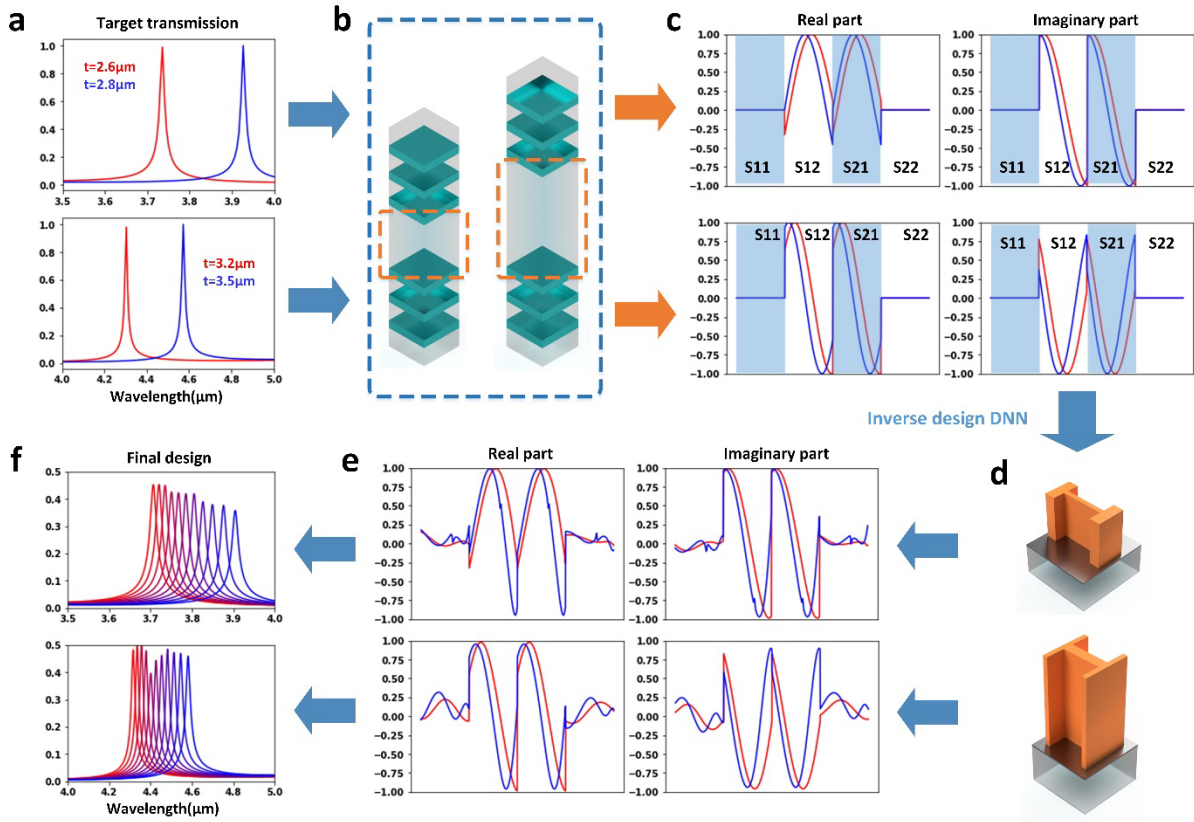


**Fig. 2-13. Design examples with the inverse DNN.** (a) Target transmission spectra. The positions of the two peaks (red represents target response in the amorphous state, blue represents target response in the crystalline state), along with the tuning range were defined. (b) The distance between DBRs (in both states) was calculated based on the target spectrum. (c) Corresponding S-matrices (amplitude vs. frequency, 60-100THz) were calculated and fed into the inverse DNN. (d) Design parameters generated by the inverse DNN. S-matrices (amplitude vs. frequency, 60-100THz) of the generated designs showing in (d). (f) Transmission spectra of the final design. Red and blue curves represent the transmission of the filter design in the amorphous and the fully crystalline state. The other 9 curves represent the responses of the design in intermediate states between amorphous and fully crystalline.

In summary, a design approach has been developed for complex photonic structures involving embedded phase-change material metasurfaces inside a multilayer cavity and have applied this methodology to the generation of tunable mid-wave infrared bandpass filters. The design approach decouples the metasurface design (accomplished via DNN) and the multilayer optimization (analytically solved by the TMM method guided with intuitive insights from the coupled mode theory), enabling computationally efficient and yet accurate inverse design of such structures. We believe that the hybrid design scheme can be generalized to other photonic structures incorporating metasurfaces where the S-matrix description is applicable, for instance waveguide devices, photonic crystals, and stacked multilayer metasurfaces.

### 3. Performance analysis results

As mentioned in Section 3, the FP and PNA devices were used in demonstration of gas sensing and thermal imaging, respectively. The results of those demonstrations are summarized in this section.

### 3.1 Thermal and gas sensing demonstration using FP tunable filters

Short term applications for these filters include both ground-based and remote-sensing based differential absorption Lidar (DIAL). Such systems are critical for measuring the molecular composition of the atmosphere in order to better understand climate behavior and atmospheric contaminants. DIAL systems output two /several NIR- or IR-laser wavelengths corresponding to the ‘on/off’ resonance of the molecular absorption signature of specific greenhouse gases such as CO<sub>2</sub> in the MWIR as well as other chemical species such as water vapor in the NIR. This process requires ultra-fast switching of the laser wavelength to rapidly determine gaseous absorption contrast in the atmosphere and typically utilizes several optical sub-systems (including FP-etalons and acoustic-optical-modulators) for spectral filtering. GST-FP filters can be designed to operate at specific points across IR wavebands, due to both the GSTs broadband index modulation at these wavelengths and through layer thickness design. In addition, GSTs can be switched on nanosecond timescales. As a result, cost-effective tunable GST-FP filters may be ideal candidates for integration into DIAL sub-systems. Both thermal imaging and CO<sub>2</sub> gas sensing demonstrations with GST-FP bandpass filters supports the applications as shown in Fig. 2-14 and Fig. 2-15.

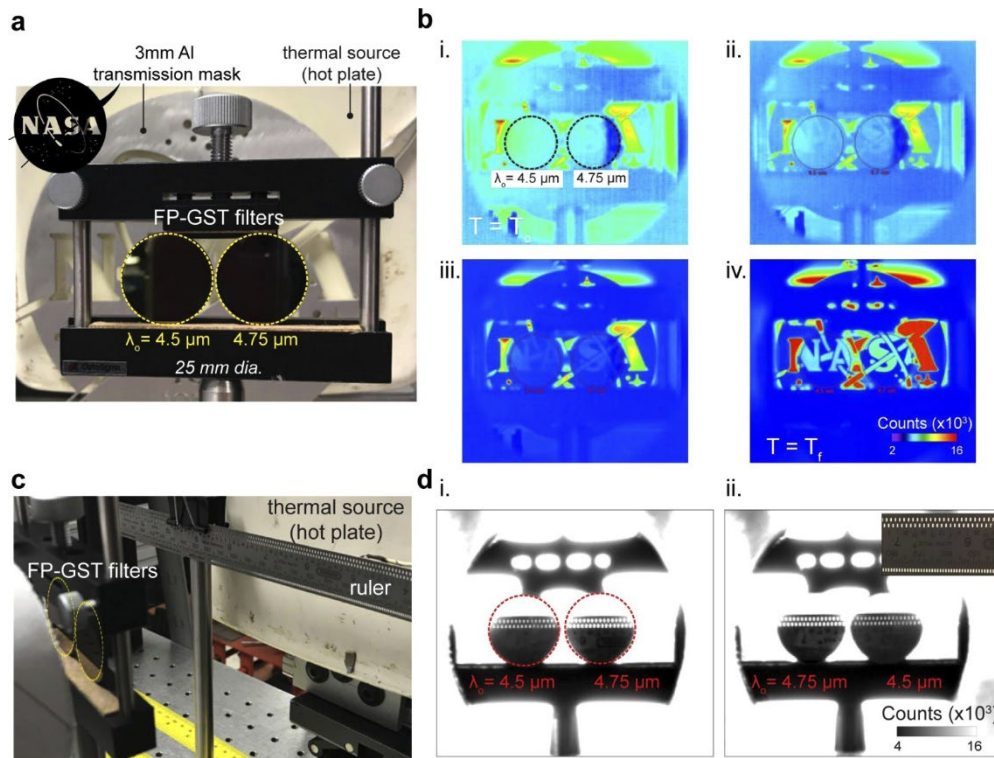


**Fig. 2-14. Thermal imaging with GST-FP bandpass filters.** (a) White light (RGB) image of the thermal imaging setup showing the hotplate, NASA Insignia logo (transmission mask) and the two mounted filters (left) a-GST spacer, and (right) c-GST spacer, with CWL(a-GST) 4.5  $\mu\text{m}$  and CWL(c-GST) 4.75  $\mu\text{m}$ . (b) Shows the thermal (IR) image of the same scene but using a MWIR digital camera. The hotplate temperature (blackbody source) is increased from 320K (i) to 486K (iv). (c,d) Comparison of the 4.5  $\mu\text{m}$  and 4.7  $\mu\text{m}$  filter at 515 K. (a) test setup, (b) the smaller objects (i.e. higher spatial frequencies) image from 4.5  $\mu\text{m}$  than the 4.7  $\mu\text{m}$ , and (c) the filter positions have been swapped to check repeatability.

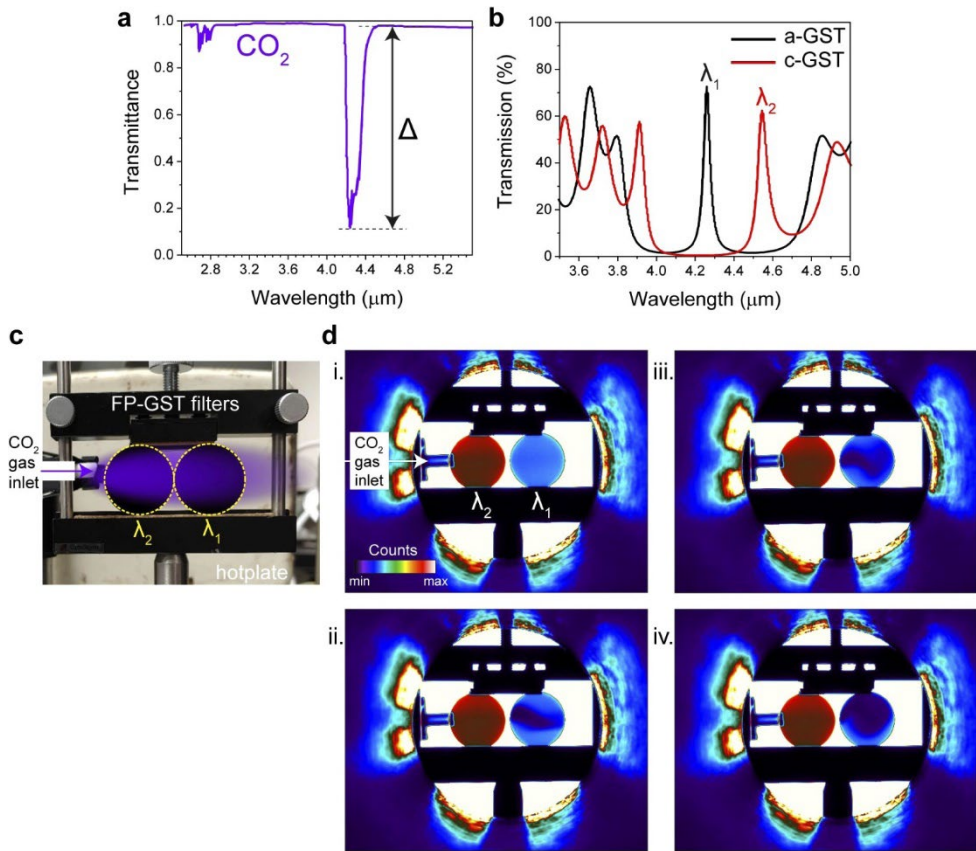


**Fig. 2-15.** CO<sub>2</sub> gas sensing with GST-FP tunable bandpass filters. (a) IR transmittance spectra of CO<sub>2</sub> (gas phase)– with intensity modulation ( $\Delta$ ) between 4.25  $\mu\text{m}$  and 4.55  $\mu\text{m}$  indicated. (d) Transmission spectra of the two CO<sub>2</sub> gas filter states: a-GST and c-GST, which were used for imaging. (c) Image (RGB) of the gas sensing setup with two filters at the two respective CWLs ( $\lambda_1$  and  $\lambda_2$  indicated). (d) IR-imaging of the two GST-FP bandpass filters in front of the hotplate (set at T = 486 K) with a supply of CO<sub>2</sub> gas fed via inlet nozzle, between the hotplate and the filters. The CO<sub>2</sub> gas supply, initially turned off (i), is varied and MWIR camera is used to capture the resultant response. The gas plume can be observed (ii-iv) as the supply is varied.

### 3.2 Thermal imaging demonstration using PNA tunable filter

The thermal radiation from an object is described through its blackbody emission curve, i.e., the cooler an object the longer the peak wavelength of its emission curve. A contact hotplate, for example, with only a relatively small temperature change from 320 K (47°C) to 480 K (213°C) exhibits significantly different spectral emissive power responses [Fig. 2-16(a)]. To demonstrate real-world imaging applicability, tunable GST-PNA metasurface filters were used in combination with a contact hotplate (thermal source) and commercial FLIR MWIR camera (imager). A setup schematic is shown in Fig. 2-16(b). Fixing the source temperature at 480 K, the metasurface filters provide tunable filtering operation across the region of 2.91-3.41  $\mu\text{m}$  [Fig. 2-16(c)] based on the switching between five different GST-crystalline states (from a-GST to p-GST to c-GST). Because the blackbody emissive power from a 480 K source increases at the longer wavelengths in the targeted spectral region, the tunable filter is expected to provide an increasing transmitted intensity; this is clearly observed in Fig. 2-16(c).

To further demonstrate thermal imaging applicability, to verify transmission homogeneity across the filters

through spatial variation of the thermal source, a metal (Al) transmission mask (3-mm thick) with the NASA Insignia logo was fixed in front of the thermal source [Fig. 2-16(d)]. By gradually increasing its temperature (from  $T_0$  320-480 K) and optically tuning two separate fabricated GST-PNA filters to exhibit passband center wavelengths of 2.91  $\mu\text{m}$  and 3.41  $\mu\text{m}$ , selective MWIR imaging of the logo was shown at two separate passbands simultaneously [Fig. 2-16(e)].

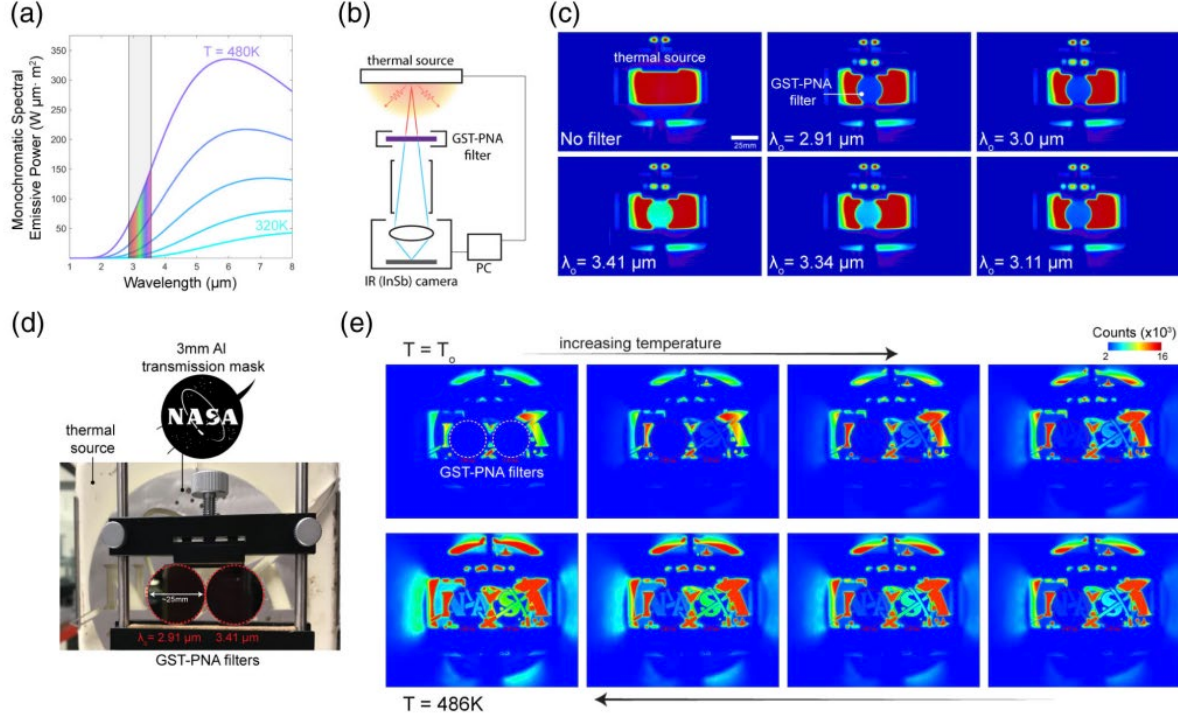


**Fig. 2-16. MWIR imaging using tunable GST-PNA metasurface filters.** (a) Blackbody thermal emission curves for varying temperature sources with over-laid spectral coverage of the tunable GST-PNA metasurface filters fabricated here. (b) Thermal imaging setup schematic for the results shown in (c), (e). (c) MWIR imaging results at a fixed 486 K hotplate temperature, as a function of varying GST-PNA filter states with varying passband center wavelength,  $\lambda_0$ . (d) RGB image of the setup imaged in (e), which shows the IR image of the same scene, as the temperature of the hotplate is increased from 320 K to 486 K. The left and right filters are centered at 2.91  $\mu\text{m}$  and 3.41  $\mu\text{m}$ , respectively. Variable transmission response through the filters, and subsequent identification of the logo (spatially variant thermal profile), can be observed.

### 3.3 Real-time / reliability testing

This section details the progress in the automated real-time spectral characterization of P-ACTIVE. The progress is divided into four phases that are graphically shown in Fig. 2-17(a) and 2-17(b):

- Phase I: Manual spectral characterization of the P-ACTIVE using a linear variable filter (LVF) and infrared (IR) camera. This strategy enables the measurement of the tunable filter's center wavelength (CWL). This method is simpler to construct for the research community and enables in situ measurement across the entire filter area (1D spatirospectral measurement).
- Phase II: Development of a MATLAB®-based graphical user interface (GUI) for automated real-time characterization. The GUI is designed to record the tunable filter's CWL, transmittance (%T), and full-width half-maximum (FWHM). However, the actual capabilities of the GUI depend on the available instruments and hardware.

- C. Phase III: Utilization of the MATLAB®-based GUI for automated real-time measurement of the tunable filter's CWL.
- D. Phase IV: Combination of the MATLAB®-based GUI with a Fourier Transform Infrared (FTIR) spectrometer to automatically measure and record CWL, transmittance, and FWHM in real time. Although this phase has not yet been completed, the proposed experimental setup and procedure are explained.

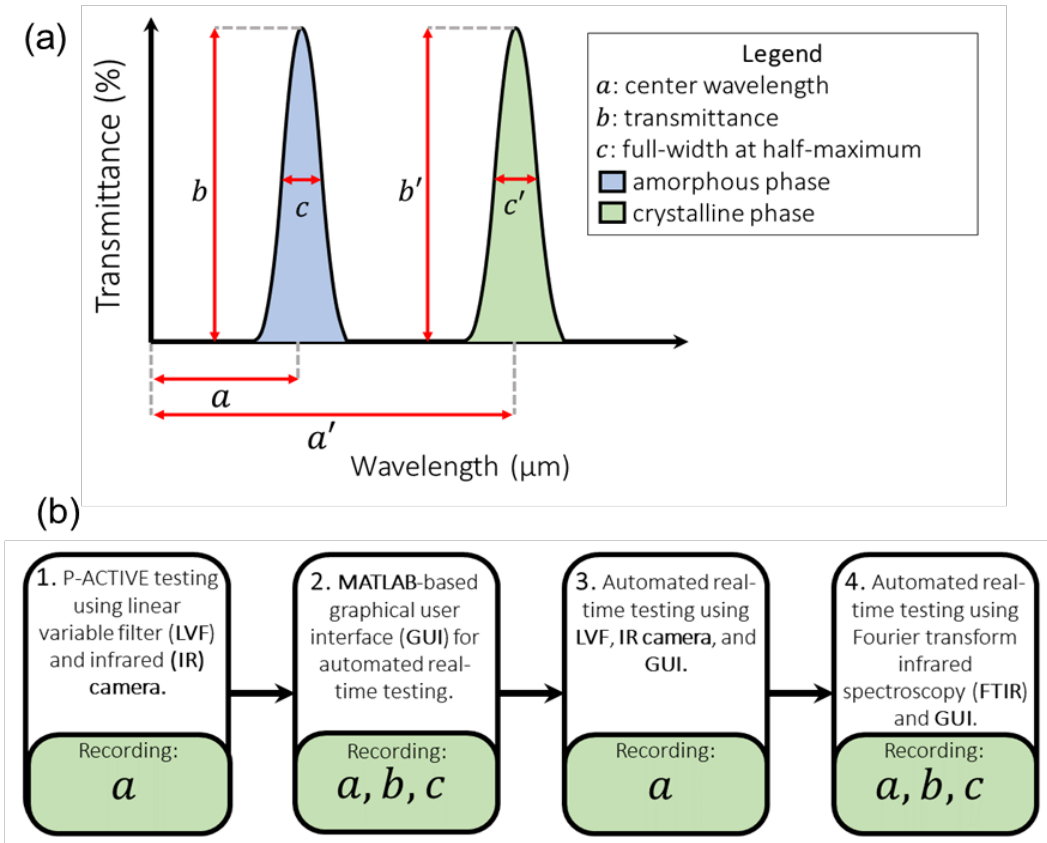


**Fig. 2-17.** (a) An illustration of the various metrics to be recorded from the P-ACTIVE. (b) An illustration of the four phases that lead to the automated real-time spectral characterization of the P-ACTIVE. Center wavelength (CWL), transmittance (%T), and FWHM are symbolized using  $a$ ,  $b$ , and  $c$ , respectively.

Phase I - Spectral Characterization using Linear Variable Filter (LVF) and Infrared (IR) Camera: The approach is to utilize a compact and inexpensive (relative to an FTIR spectrometer) LVF—a small

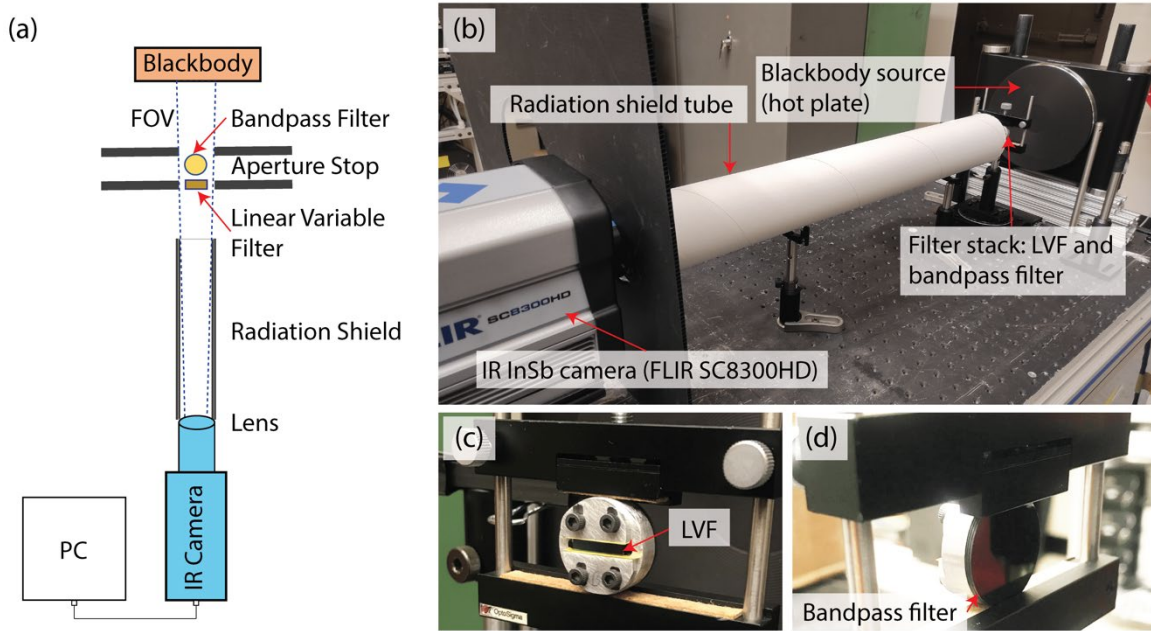


**Fig. 2-18. Experimental setup.** (a) A schematic of the experimental setup. The infrared (IR) camera images the linear variable filter (LVF) with a fixed-wavelength bandpass filter behind it. They are both illuminated by the contact hot plate (blackbody). (b) A photograph of the experimental setup. The hot plate acts as a blackbody thermal radiation source. (c) The LVF is mounted in the IR camera's field of view. (d) The bandpass filter is between the blackbody source and LVF.

rectangular optical filter that has its CWL varying linearly along the length of the filter [34]. Therefore, in combination with the P-ACTIVE, simply by imaging (recording) the intensity response through an LVF, it is possible to characterize the spectral performance. The accuracy of this method is high enough such that the phases of the PCM (amorphous and crystalline) are unambiguously distinguishable and the error margin of the CWL measurement is  $0.085 \mu\text{m}$ . Our work realized a P-ACTIVE (PNA filter) with a CWL of approximately  $2.9 \mu\text{m}$  and  $3.3 \mu\text{m}$  in its amorphous and crystalline states, respectively [32]. With this LVF-based system, the CWL shift of  $0.4 \mu\text{m}$  is detectable. Further, this approach has the advantageous feature that it is simpler to modify in order to evaluate (test) other switching mechanisms or imaging approaches, such as trialing different electrode designs, different laser technologies, off-axis illumination, etc.

To characterize a filter with tunable CWL, a system that validates the spectral performance of static bandpass filters is first needed. The experimental setup consists of (1) an IR camera (Indium antimonide detector, FLIR SC8000 Series), (2) a radiation shield tube, (3) a contact hot plate (blackbody radiation source), and (4) the filter stack [Fig. 2-18]. The IR camera is capable of imaging the MWIR waveband ( $2.5\text{--}5.0 \mu\text{m}$ ) with a resolution of  $1344 \times 784$  pixels. The camera utilized a lens with a focal length of  $50 \text{ mm}$ . The distance between the lens and filter (target) was  $122 \text{ cm}$ . The IR images are recorded using FLIR ResearchIR software. The blackbody radiation source was an iron plate with emissivity  $\varepsilon \approx 1$  and a

diameter of 17.8 cm. A tube between the camera and filter stack shielded against unwanted background radiation.

A top-down schematic of the experimental setup is shown in Fig. 2-18(a), whereas the photograph of the entire setup is shown in Fig. 2-18(b). The LVF (Vortex Optical Coatings, Ltd.) and bandpass filter are shown in Fig. 18(c) and 18(d), respectively. The bandwidth of the LVF at 50% peak transmittance is specified by the manufacturer to be 2% of the peak wavelength with peak transmittance typically greater than 60% across the CWL band [35]. The LVF also has out-of-band blocking within its spectral range of optical density greater than 2.5 [35]. The LVF has nominal dimensions of 15 mm × 3.5 mm × 0.1 mm. The CWL of the passband ranges from 2.5 μm to 5.0 μm, depending on the longitudinal distance along the filter. The LVF is placed between the camera lens and as close to the bandpass filter as possible, minimizing any deviation due to converging/diverging beams. Similarly, the bandpass filter is placed between the LVF and the blackbody radiation source. The bandpass filters are manufactured by Andover Corporation and had CWL of 3.10 μm, 3.37 μm, 3.50 μm, 3.60 μm, 4.26 μm, 4.50 μm, and 4.70 μm. These filters each have a transmission of 75% and an out-of-band blocking of optical density 3.0. The tolerance of the CWL of each filter is 40 nm. Each filter is 1.0mm ± 0.2mm thick. The bandwidths of the filters are between 120 nm ± 30nm and 140nm ± 30nm.

Background on Linear Variable Filters: An LVF can be considered an FP-interferometer that consists of a tapered resonator between one flat and one tilted dielectric (or metallic) mirror [36]–[39]. This type filter is also sometimes known as a Fizeau interferometer [36] and for spectroscopic analysis an LVF can be considered a Fizeau interferometer illuminated with a broadband light source [6, 7]. The thickness and particular material of the tapered layer enables LVFs with different wavelength ranges to be realized [6, 10]. In the all-dielectric LVF case, for mirror reflectivities <90%, the wavelength range (bandwidth) can be simplified to a conventional FP-model, which varies with the materials' refractive indices according to the following reduced equation [38]:

$$\Delta\lambda = \frac{4\lambda_{min}}{\pi} \arcsin\left(\frac{n_2 - n_1}{n_2 + n_1}\right), \quad (1)$$

where  $\lambda_{min}$  is the reference wavelength.  $n_1$  and  $n_2$  are the refractive indices of the dielectric materials. In this study, the dielectric materials in the LVF enabled a wavelength bandwidth of  $\Delta\lambda = 2.5$  μm and a reference wavelength of  $\lambda_{min} = 2.5$  μm.

If the incoming light to the LVF first passes through collimating optics, the following relationship results [10]:

$$f = \frac{L}{2(NA)}, \quad (2)$$

where  $L$  is the length of the LVF,  $f$  is the focal length of the collimating lens, and  $NA$  is the numerical entrance aperture. According to the Smith-Helmholtz invariant theorem [41],  $d \times NA = D \times \theta$ , where  $\theta$  is the maximum incidence angle of the LVF, and  $d$  is the aperture diameter. According to the above equation, decreasing the aperture diameter or focal length would decrease the prediction error but reduce the amount of light entering the optical system.

The collimation of light can strongly affect the transmission and CWL of the LVF. A greater cone half angle (CHA) would decrease the transmittance of the LVF while blue-shifting the CWL [8]. Because LVFs may be approximated to spatially-varying FP filters, this behavior can be explained using the theoretical model of FP interferometers [37]. For more details on the theory behind LVFs, the reader is referred to work by Ayerden *et al.* [37].

One purpose of this system is to track the changes in phase of the PCM during a reliability test. During a phase-change, the PCM filter may undergo a change from a 2.9- $\mu\text{m}$  CWL to a 3.3- $\mu\text{m}$  CWL for a change in CWL of 0.4- $\mu\text{m}$ . In that case, the uncertainty of 0.085  $\mu\text{m}$ , although greater than other methods, is acceptable because it enables the clear detection of phase changes in the tunable optical filter.

**Experimental Results:** Using the MWIR camera, the LVF was imaged with seven different bandpass filters behind it. Figure 2-19 shows the experimental results. The superimposed view of the IR intensity image and RGB image is shown in (a) for illustration purposes. As shown in Fig. 2-19, the CWL of the LVF varies along the length of the filter beginning at 2.5  $\mu\text{m}$  and gradually increasing to 5.0  $\mu\text{m}$  at the opposite end. However, due to variations in the manufacturing of our particular LVF, experimental data confirmed that it reached its 5  $\mu\text{m}$  peak in just 10mm of filter length. The “scan line pixel number” in Fig. 2-19 refers to the numbering of the camera’s pixels along the horizontal axis of the LVF. The CWL here is defined to be the wavelength at which the transmittance is maximum. “Detector counts” from the IR camera are used as a proxy for transmittance; the location of peak detector counts is the location of the peak filter transmission. To find this location on the LVF, a single horizontal line of pixels is sampled in the center of the filter and parallel to the long axis. In Fig. 2-19(b), the locations of peak transmission can be identified as regions of higher relative intensity, where the brightness of the pseudo-color image corresponds to the number of counts recorded during a given detector integration time. For each bandpass filter, the particular integration time was determined experimentally to obtain the high-contrast image and depended on the temperature of the blackbody radiation source.

In this experiment, it was demonstrated that the CWL can be detected and its location along the LVF accurately measured. The plot of normalized detector counts versus scan line pixel number is shown in Fig. 2-19(c) for each bandpass filter. The experimental results confirm that the LVF accurately indicates the CWL of the filter that is placed behind. The correlation between CWL and the scan line pixel number is shown in Fig. 2-19(d). The pixel number of the scan line is a proxy for the linear distance along the filter. For the experimental setup and detector/optics combination, the minimum horizontal spatial resolution for each pixel is approximately 0.341 mm. The instantaneous field of view (IFOV) of the imaging system represents the spot size on the LVF for an individual pixel and also corresponds to an estimated spectral measurement uncertainty. Using a 50-mm lens in combination with a 1344  $\times$  784, 14- $\mu\text{m}$ -pixel-pitch sensor, the 15-mm LVF was sampled with approximately 104 pixels along the filter’s horizontal (longitudinal) axis. As stated previously, the LVF did not use the full 15-mm length to cover the 2.5–5.0- $\mu\text{m}$  wavelength span. The 2.5- $\mu\text{m}$  CWL shift on the LVF was measured as 10 mm rather than 15 mm. This slightly reduced the spectral resolution of the system. With the 10-mm (effective) LVF, it can be seen that there is a 0.25- $\mu\text{m}/\text{mm}$  shift spatially along the filter rather than an expected 0.17- $\mu\text{m}/\text{mm}$  shift.

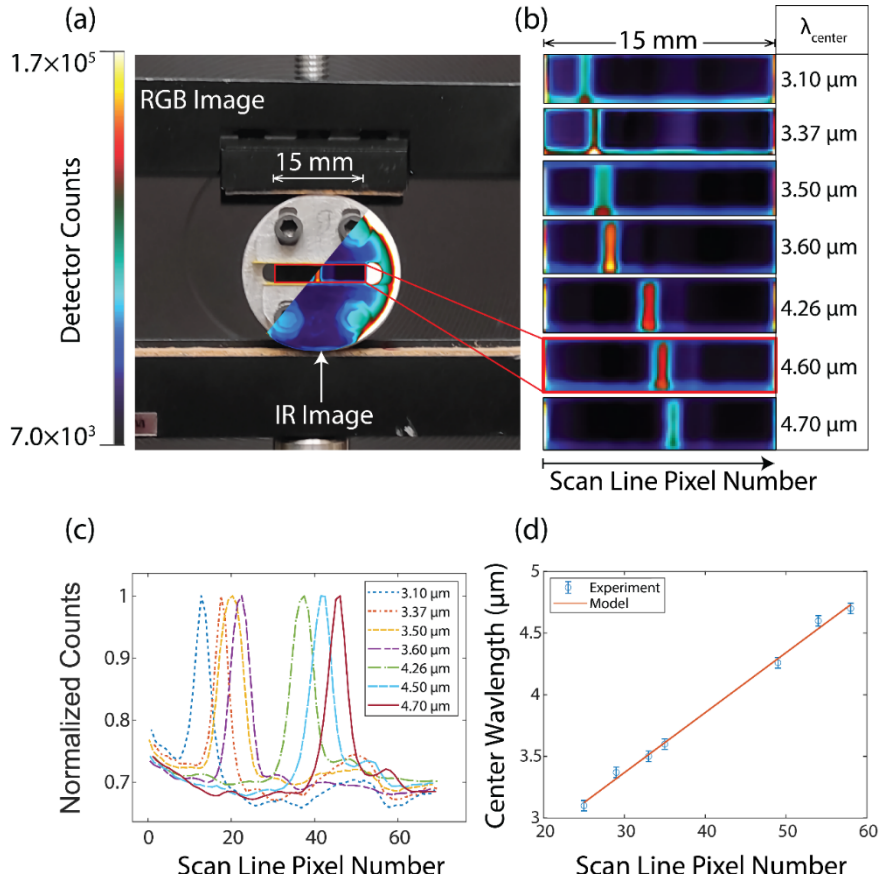


**Fig. 2-19.** The results of the bandpass filter characterization using the LVF. (a) An IR image of the LVF overlaid on top of a red-green-blue (RGB) image of the filter stack that includes the LVF and bandpass filter. (b) The IR images of the LVF when bandpass filters of different CWL are placed behind it. (c) The normalized detector counts versus the scan line pixel number for each bandpass filter, with CWL shown in the legend. (d) The CWL versus scan line pixel number of the bandpass filter. The correlation is linear such that the scan line pixel number can be used to predict the CWL of the optical filter.

Error Analysis: When combined with the IFOV of the imaging system (0.341 mm), the spectral measurement uncertainty of the experiment can be computed as 0.085  $\mu\text{m}$ . A 0.341-mm spot size on the filter corresponds to a 0.085- $\mu\text{m}$  change in wavelength across a pixel. In Fig. 2-19(d), the CWL of the bandpass filter is the independent variable whereas the scan line pixel number is the dependent variable. If the CWL was unknown and the scan line pixel number was used to predict the CWL, the prediction error may be  $\pm 0.085 \mu\text{m}$ . The spectral measurement uncertainty is inversely proportional to the length of the LVF. However, the uncertainty is proportional to the change in wavelength of the LVF. It is computed as follows:

$$U = \frac{\lambda_{max} - \lambda_{min}}{L} (IFOV), \quad (3)$$

where  $U$  is the measurement uncertainty and  $L$  is the effective length of the LVF. The minimum and maximum wavelengths of the LVF are  $\lambda_{min}$  and  $\lambda_{max}$ , respectively. In this study, although the LVF was

15 mm long, the effective length was  $L = 10$  mm because  $\lambda_{max} = 5.0 \mu\text{m}$  occurred at 10 mm, not 15 mm. The IFOV is a function of the target distance and camera resolution. It is computed as follows:

$$IFOV = \frac{FOV_H}{R_H}, \quad (4)$$

where  $FOV_H$  is the horizontal field of view and  $R_H$  is the horizontal resolution of the system.  $FOV_H$  is derived as follows:

$$FOV_H = \frac{2D_T}{\tan(\beta/2)}, \quad (5)$$

where  $\beta$  is the angle of the horizontal FOV and  $D_T$  is the target distance. The complete system parameters are provided in Table 2-2. The measurement uncertainty may be minimized in future implementations through a change in imaging optics. For example, a camera lens with a longer focal length, an image sensor with greater spatial resolution, and a longer ( $>15$ -mm) LVF would each decrease the uncertainty.

**Table 2-2. Parameters of the system for experimental characterization.**

Parameter	Symbol	Value	Unit
<b>Lens and Target</b>			
Focal Length	$f$	50	mm
Target Distance	$D_T$	1219.2	mm
Horas. FOV angle	$\beta$	21.3	°
Vert. FOV Angle	$\theta$	12.5	°
Diag. FOV Angle	$\phi$	24.6	°
<b>Sensor Geometry</b>			
Horas. Resolution	$R_H$	1344	Px
Vert. Resolution	$R_V$	784	Px
Horas. Pixel Pitch	$P_H$	0.0140	mm
Vert. Pixel Pitch	$P_V$	0.0140	mm
<b>Linear Variable Filter</b>			
Length	$L$	10.0	mm
Width	$W$	3.5	mm
Minimum Wavelength	$\lambda_{min}$	2.50	mm
Maximum Wavelength	$\lambda_{max}$	5.00	mm

Determination of Center Wavelength: The location of the scan line,  $y_{scan}$ , is shown in Fig. 2-20. To find the location of the CWL, first, a region of interest (ROI) is drawn over the filter image.  $y_{scan}$  was chosen to be in the center of the LVF. It was initially assumed that the horizontal position of the peak transmittance may depend on the chosen location of  $y_{scan}$ , due to fabrication tolerances. However, Fig. 2-21 shows otherwise, which shows the variation of the detector counts in the 2D pixel grid. Figure 21 shows that the location of peak transmission along  $x$  does not change depending on the chosen scan line location,  $y_{scan}$ . Another method to determine the location of peak transmittance would be to scan every pixel in the 2D

ROI for every CWL measurement. Compared to scanning a single line, this method is less computationally efficient, making it less suited for the real-time characterization application. The number of detector counts is evaluated within two bounds, where  $x_{lb}$  and  $x_{ub}$  are the lower and upper bounds, respectively. In Fig. 2-20(a),  $x$  and  $y$  refer to the numbering of the image's horizontal and vertical pixels, respectively. The detector counts must be evaluated within bounds because the detector counts increase dramatically outside the range of pixel numbers that do not cover the LVF. This increase can be seen in Fig. 2-20(b), where beyond  $x_{lb}$  and  $x_{ub}$  the colors that correspond to the detector counts appear brighter. Figure 2-20(b) shows results for the 3.60  $\mu\text{m}$  filter with labeled spectral properties. The locations of the CWL, FWHM, and peak transmittance are shown. The CWL is a function of the scan line pixel number; the two variables vary according to the equation,

$$\lambda_C = a(x - x_{lb}) + \lambda_{min}, \quad (6)$$

where  $\lambda_C$  is the CWL,  $a$  is the proportionality constant,  $\lambda_{min}$  is the passband CWL when  $x = x_{lb}$ , and  $x$  is the numbering of the pixels horizontally. Least-squares regression identified  $a = 0.04787 \mu\text{m}$  and  $\lambda_{min} = 2.50 \mu\text{m}$ .

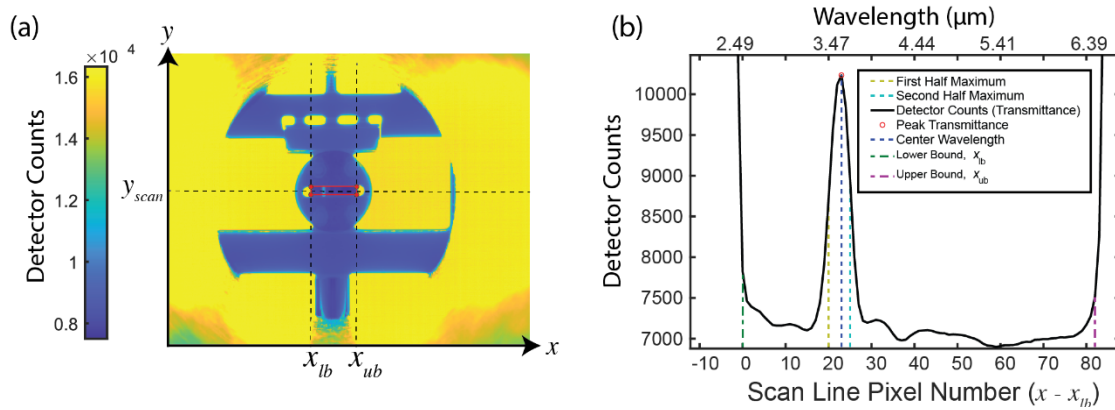


**Fig. 2-20.** The method for determining the CWL of the filter from raw pixel data. (a) The IR image used to obtain CWL. The scan line is located at  $y = y_{scan}$ . The upper and lower bounds of the horizontal pixel number are  $x_{lb}$  and  $x_{ub}$ , respectively. (b) The spectral results of the 3.60  $\mu\text{m}$  bandpass filter. Spectral properties shown include the locations of the CWL, peak transmittance, intensity half-maximums, and bounds of the filter.

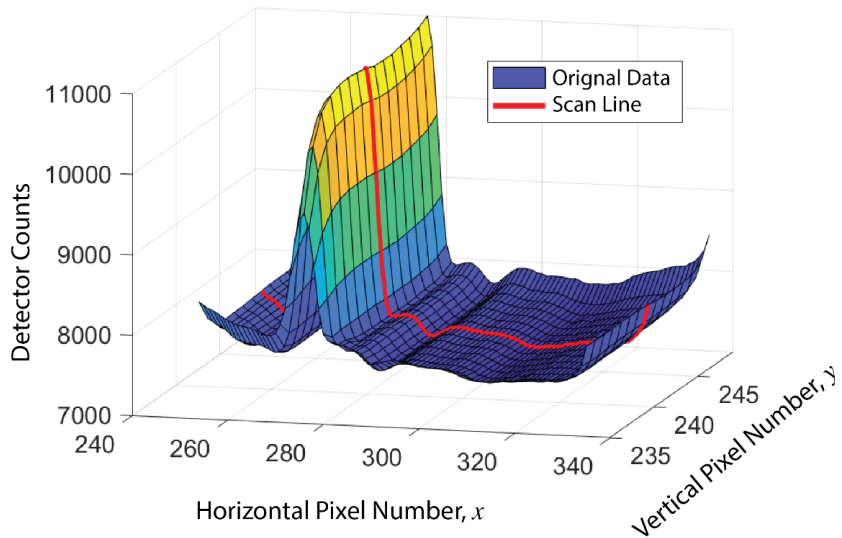


**Fig. 2-21.** A three-dimensional plot showing the variation of the detector counts with the horizontal and vertical pixel numbers that correspond to the area of the IR image that the LVF occupies. As long as the scan line passes through the entire length of the LVF, the location of peak transmittance does not depend on the exact location of the scan line.

Phase II - MATLAB®-Based Graphical User Interface (GUI) development: A MATLAB®-based GUI was custom-developed to control the hardware systems and analyze incoming data. The GUI is designed with the user's inputs on the left quadrants of the window and the system's outputs on the right quadrants. A screenshot of the GUI is shown in Fig. 2-22. The various aspects of the GUI are organized with tabs. The names of the tabs include “Instruments”, “Measurement Mode”, “Stop Condition”, “Pulse Settings”, and “Testing”. There are additional groups of tabs for monitoring the performance characterization of the PCM by displaying raw data and plotting spectral properties (*Note: More detailed on the each tap is located end of this section as ‘Appendix A’*). The source code for the MATLAB® application is available at <https://dbombara.github.io/automated-pcm-characterization>.

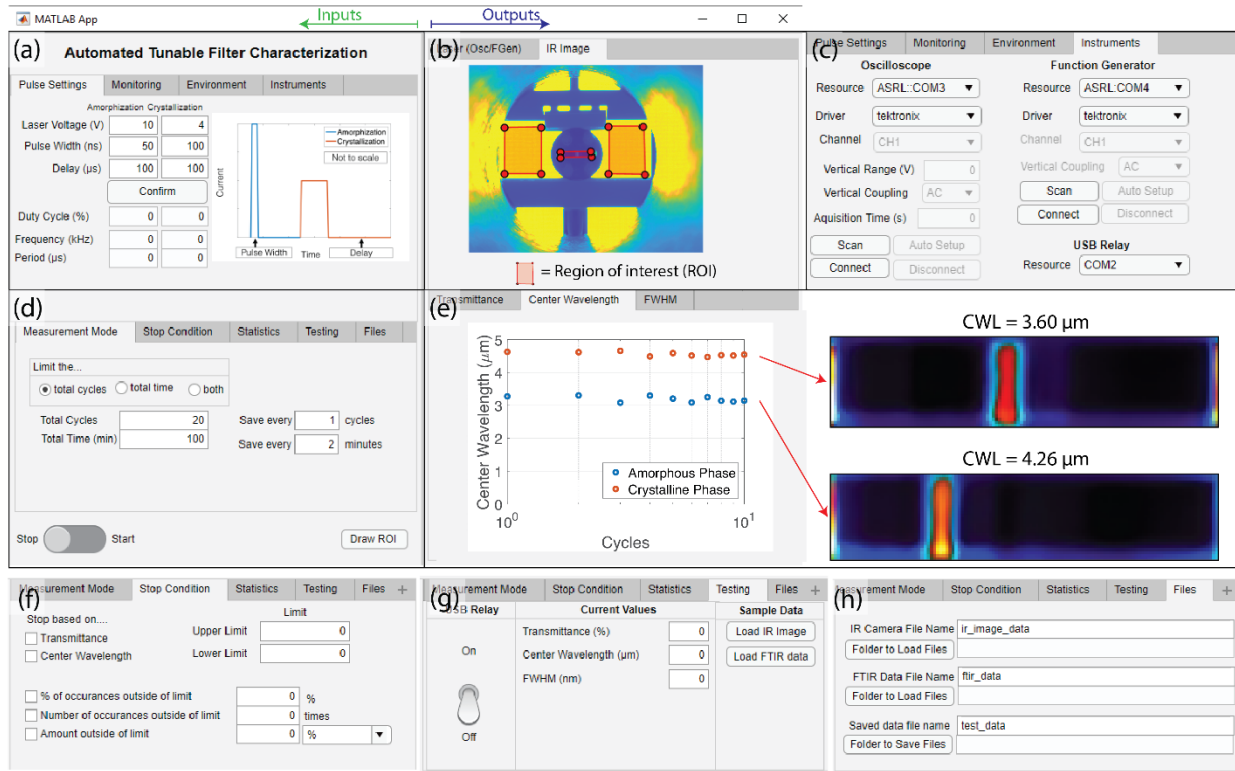


**Fig. 2-22.** Real-time filter characterization: A screenshot of the custom MATLAB® GUI. The source code and packaged application are available at <https://dbombara.github.io/automated-pcm-characterization>. The window contains four quadrants (a)-(e), which each contain tabs. The left half of the GUI is generally for inputs by the user, whereas the right half displays the output from the instruments and computed spectral properties. (a) The top-left quadrant of the GUI contains tabs for hardware-based settings and conditions. (b) The top-right quadrant of the GUI displays “raw” data from the IR camera and laser. (c) The Instruments tab, which is a part of the top-left quadrant, enables the user to connect to the different instruments. (d) The bottom-left quadrant is for software-based settings. (e) The bottom-right quadrant displays the spectral properties of the P-ACTIVE. With the current LVF-based approach, only the CWL may be plotted. In future work, other properties, such as transmittance and full width at half maximum (FWHM) will be calculated. The (f) Stop Condition tab, (g) Testing tab, and (h) Files tab allow the user to have more control over the experiment.

Phase III - Automated Real-Time Performance Characterization using LVF and IR Camera: The evaluation of the P-ACTIVE is automated in two aspects: phase switching and performance characterization. Figure 2-23 details the main loop that runs in order to switch and characterize the filter.

Once the user begins the experiment, the filter automatically switches between the amorphous and crystalline states while its CWL is automatically calculated and saved for each cycle. The sequence of functions that automates the system is shown in Fig. 2-23. The GUI allows the user to conveniently control and monitor the experiment's progress. At the start of the experiment, MATLAB® establishes connections to each instrument. The initial IR image is then loaded, with the ROIs displayed on the screen. At this point, the user may redraw the ROIs, based on the exact position of the LVF in the view of the camera. The selected ROIs are displayed on the screen and remain in view while the experiment runs. Before firing a laser pulse, first, the desired state is evaluated. Typically, the desired state alternates on each cycle between amorphous and crystalline. The desired state of the PCM determines the intensity and duration of the fired laser pulse. A closed relay switch instructs the IR camera to save its image. The laser waveform is then plotted for that cycle. Then, the file of the IR image is imported and displayed in the GUI. An image mask is applied that allows the CWL to be calculated and plotted within two bounds on the horizontal axis. All data from that cycle are then saved to a file. The experiment runs until the cycle limit is reached, which can be preset by the user or determined by the GUI based on the data from each cycle. More details on these processes are described subsequently.

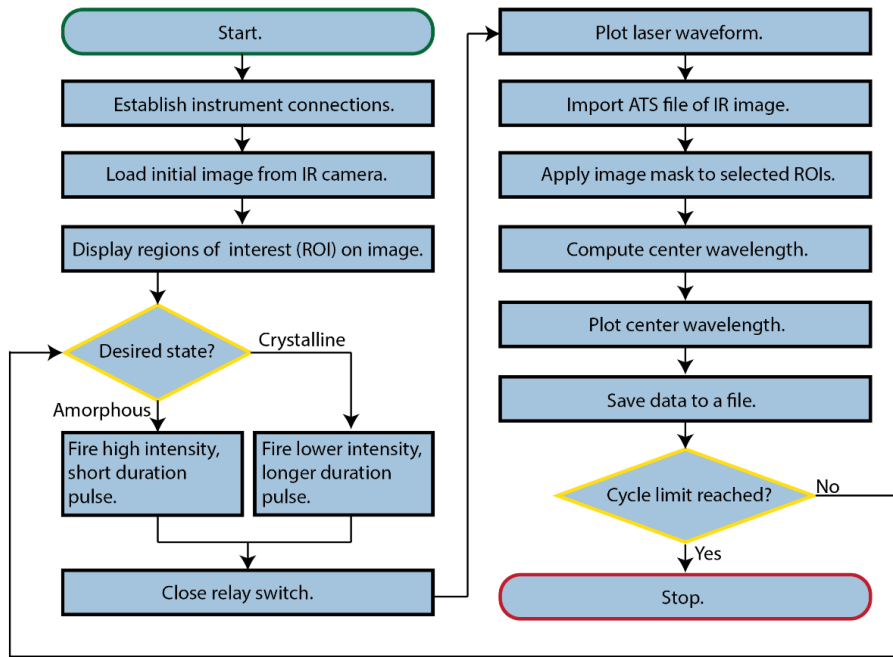


**Fig. 2-23.** Operation flowchart: The general commands and processes executed by the MATLAB® graphical user interface (GUI). The program runs in a loop until the cycle limit is reached but can be terminated by the user at any time.

The switching of the PCM between amorphous and crystalline states is triggered by the heat of an incoming laser pulse. A Quantel Evergreen HP pulsed laser is chosen in this study to deliver up to 340 mJ of energy at 532-nm CWL. The pulses are delivered at a rate of up to 20 Hz. The wavelength and energy level were chosen based on our previous work on PNA filter [32]. The pulsed laser output is controlled with a function generator and is viewed with an oscilloscope; this conveniently enables the user to monitor the waveform.

The laser consists of two components: the power supply and the “head”, which emits the pulsed laser beam. In this study, the oscilloscope (Tektronix MDO4024C) and function generator (Tektronix MDO4AFG) functionalities are combined into a single instrument (MDO stands for mixed-domain oscilloscope). The particular oscilloscope and function generator were chosen due to their high-level programming commands that are available in MATLAB®.

The laser, function generator, and oscilloscope are controlled within the MATLAB® user interface. From MATLAB®’s Instrument Control Toolbox™, Quick Control Oscilloscope commands are employed to issue high-level commands to the instruments. This aspect of the GUI builds upon the Oscilloscope App from MathWorks® and incorporates similar functionality [42]. Serial commands can also be issued directly to the laser to adjust the settings of the instruments, such as the power level [43].

To automate the image acquisition process, a USB-controllable relay (8-Channel 5-Amp ProXR Lite, Relay Pros) triggers the camera to record the IR images. In this study, the switch is “dry”; the closure of the relay switch draws no electrical current. The FLIR ResearchIR software saves the image in a proprietary file format known as ATS. Then, the FLIR File Reader Software Development Kit (SDK) is used to import the ATS file into MATLAB®. Functions from the SDK then extract the image’s metadata and raw pixel information so that the image can be displayed in the GUI. Using the imported image, the CWL of the tunable filter is calculated using Eq. (6).

Phase IV - Automated Real-Time Performance and Reliability Testing FTIR Spectroscopy: The reliability of the PCM-based filters will be evaluated using the MATLAB® GUI in future experiments. Despite its advantages, the LVF-based characterization strategy cannot measure the transmittance or FWHM. Therefore, an FTIR spectrometer must be used in order to capture these variables. The FTIR instrumentation will be combined with the MATLAB®-based GUI to enable automated and real-time spectral characterization.

Figure 2-24 shows the schematic of the reliability test that will utilize the MATLAB® GUI. The setup is similar to that in Fig. 2-18(a), but with added components to facilitate the laser-based tuning of the PCM-based filter. Because the laser will heat the PCM-based filter during the phase change, the IR camera must wait for that heat to dissipate before taking an image. This is because the IR camera cannot differentiate between surface heating of the filter and blackbody radiation. During the reliability experiment, the laser firing and the IR image acquisition will be separated for a duration that allows the heat of the PCM to

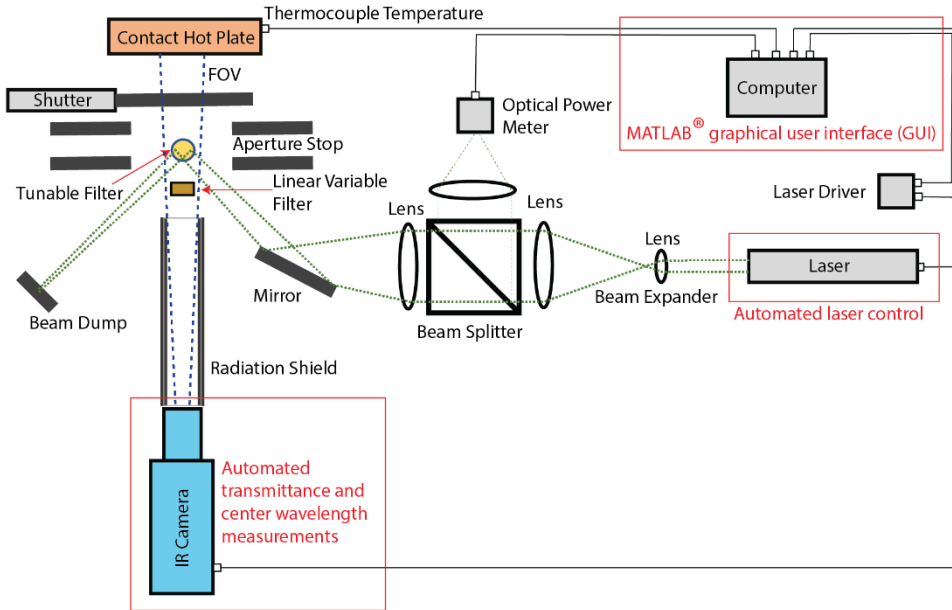


**Fig. 2-24.** The reliability test setup: The reliability test will rely on the MATLAB® GUI for automated laser control and automated measurement of the filter's CWL. The CWL will indicate the current state of the filter.

sufficiently dissipate. However, the experiment will still be automated, since the filter may be potentially be switched for  $10^3$ – $10^6$  cycles until it fails; the moment of failure can be identified with our approach. Previous PCM reliability studies have demonstrated long operational longevity, with one example demonstrating  $1.4 \times 10^8$  switching cycles before failure [44]. To be used in NASA's Space and Science missions, the filter must be reliable, with any drop-off in performance as a function of the tuning cycle known in advance. NASA mission / program-specified scenarios using P-ACTIVE will be addressed in Part IV.

In summary, P-ACITVE is emerging as an alternative technology platform for ultrafast spectral filtering across a wide range of operating wavelengths. However, the ability to accurately and easily characterize their performance remains challenging. This part detailed the four phases leading to the automated real-time characterization and reliability testing of a P-ACTIVE.

In Phase I, a system for tunable filter characterization was designed and implemented as an alternative to FTIR spectroscopy. The LVF was shown to accurately indicate the CWL of the bandpass filter behind it.

In Phase II, a MATLAB® GUI was designed to automatically control the subsystem instrumentation, display the filters' spectral properties, and record the output data. In Phase III, the overall system enabled 1D spatirospectral (bright field) characterization and allows for easier integration of other tuning mechanisms in comparison to FTIR systems. In Phase IV, plans were detailed for a future reliability experimental system that utilizes the FTIR spectrometer for extreme accuracy.

The system in this work enabled the automated detection and tuning of the PCM-based filter's state via the IR images of an LVF. The CWL of the P-ACTIVE is greatest in its fully crystalline state and least in its fully amorphous state; partial crystallinity of the filter results in a CWL between those extremes. Previous work has shown that the CWL of the tunable filter is strongly dictated by the device's design [1, 3]. Because of this strong dependence of the CWL on the design, recent work has established a database of chalcogenide phase change materials to model tunable nanophotonic devices [45].

Future work will build upon the MATLAB® application and experimental results to advance the state of the art in PCM-based optical filters. Reliability studies in the future will reveal the filter's long-term performance. This work has wider applications in systems that utilize spatially-varying optical filters, such as circular variable filters. The software that was developed in this work can also be modified to incorporate more-sophisticated image processing algorithms, such as an algorithm to automatically detect the location of the LVF and determine the ROI. For devices and materials with more complicated spatially-varying spectral profiles, machine learning techniques may be used for more robust spectral characterization. The MATLAB® application is available at <https://dbombara.github.io/automated-pcm-characterization>.

#### 4. MISSE-14 project (June 2021 – January 2022) for P-ACTIVE space applications

##### 4.1 Motivation

The space sector has witnessed tremendous growth within the past decade from not only government agencies but also entrants from the private sector. This is attributed to: (1) the increased availability and cost reduction of launch platforms, (2) expanded utilization of Low Earth Orbit (LEO) for crewed and uncrewed missions, and (3) the development of plans for lunar missions and ones further into the solar system. As a result, sector growth is expected to accelerate in the coming decades [46]. A host of complementary technological innovations and capabilities are underpinning this growth from reusable rockets to miniaturized satellites. These are enabling applications including planetary exploration missions, remote sensing studies and high speed satellite broadband. Spaceborne sensing, imaging and communications capabilities are provided through electronic and photonics subsystems. Terrestrially, photonic components are rapidly displacing electronic counterparts to enable next-generation power efficient, high speed and highly versatile technologies, from reconfigurable photonic integrated circuits to tunable optical filters [47]. The technological demands of next-generation space systems are yet more demanding, and require operation in harsh environments while constrained by lean SWaP-C (Size, Weight, Power, and Cost) budgets. To realize subsystems that meet such performance demands requires novel photonic material platforms and innovative multifunctional design schemes.

PCMs have been proposed for spaceborne solid-state memory modules because of their nonvolatile, reconfigurable, fast-switching and space radiation tolerant capabilities[48]. In recent years, developments in PCM-based reconfigurable and tunable photonic technology have given rise to the notion of PCMs as a

material platform enabling versatile, compact spaceborne photonics[32], [49]. Such multifunctional photonic devices are expected to find LEO applications such as optical modulators in integrated photonic modules aboard miniaturized satellites (SmallSats), reconfigurable optical devices in remote sensing missions, multifunctional lab-on-a-chip astronaut health monitoring systems, and rapid environmental sensors on the NASA Orion crew transport vehicle[49].

The concept of applying different, non-chalcogenide PCMs to space applications is not entirely unheard of. Since the 1970's [4], gallium and paraffin materials (materials with a solid-liquid phase changes) have been proposed and tested for spacecraft thermal control in LEO or lunar orbit [5]. However, to-date, the application of all-solid-state, and particularly chalcogenide, PCMs for space applications has been largely non-existent.

#### 4.2. MISSE-14 campaign procedure

Key advances have also been made in material survivability qualification. Although PCMs have previously been noted for their resilience to various forms of radiation [48], they have not been tested in a realistic space environment until very recently. In March 2021, twenty-four samples of various PCM thin films, along with metasurface optical components comprised of these PCMs [22], were delivered to the International Space Station (ISS) as part of the Materials International Space Station Experiment (MISSE-14) test campaign. During the MISSE experiment, samples were flown outside of the ISS in open exposure to the space environment. During the experiment, high-resolution cameras scanned and captured photographs of the samples about once a month to detect changes as a function of time. Along with the image data, temperature, UV radiation, total atomic oxygen fluence, and total ionizing radiation doses were measured on-orbit. The samples were returned to NASA Langley Research Center in March 2022 for post-flight characterization. This study will provide valuable information on the limitations and suitability of PCMs in harsh environments, as there has been no other study of this kind performed previously.

Figure 2-25 shows the detailed mission operation cycle. On February 20<sup>th</sup>, 2021, a Northrup Grumman (NG) Cygnus spacecraft delivered twenty-four PCM specimens including four PCM-based MWIR filters for 6-months of exposure to the space environment. After system check-out, on April 8<sup>th</sup>, JAXA astronaut Soichi Noguchi installed the MISSE-14 Science Carriers (MSC) on the MISSE Transfer Tray (MTT) and placed it on the Japanese Experiment Module (JEM) ORU Transfer Interface (JOTI) inside the JEM airlock. The follow-up depressurization of the JEM airlock was completed on April 16<sup>th</sup>. MISSE-14 installation on the MISSE-Flight Facility (MISSE-FF) was completed on April 25<sup>th</sup> and the MSCs were opened to start the PCMs expose in space on June 21<sup>st</sup>. High-resolution cameras (owned by Aegis Aerospace Inc.) scanned and captured photographs of the samples about once a month to detect changes as a function of time from July 21<sup>st</sup> to December 6<sup>th</sup>. Along with the science data, temperature, UV radiation, and total ionizing radiation doses were measured on-orbit. MISSE-14 completed the final closing of the MSCs on December 26<sup>th</sup> with a total open exposure time of 133 days 5 hours, 6 minutes on Wake and 148 days 21 hours 11 minutes on Zenith directions, respectively.

MISSE-14 MSCs were removed from the MISSE-FF from December 26-28 with the support of the Canada Space Agency (CSA) ISS Robotic Systems Team. The MISSE-14 MSCs entered the Japanese Module Airlock (JEM) on December 29<sup>th</sup> that was repressurized on December 31<sup>st</sup>. Finally, the MSCs were packed by ISS Crew members Kayla Barron and Mark Vande Hei. MISSE-14 returned on SpaceX CRS-24 (also

known as SpX-24) on January 25<sup>th</sup>, 2022 [51]. The PCMs arrived at Aegis Aerospace two weeks after splashdown for de-integration. Finally, all samples were returned to NASA LaRC in March, 2022 for post flight characterization similarly to the preflight characterization conducted before launch.

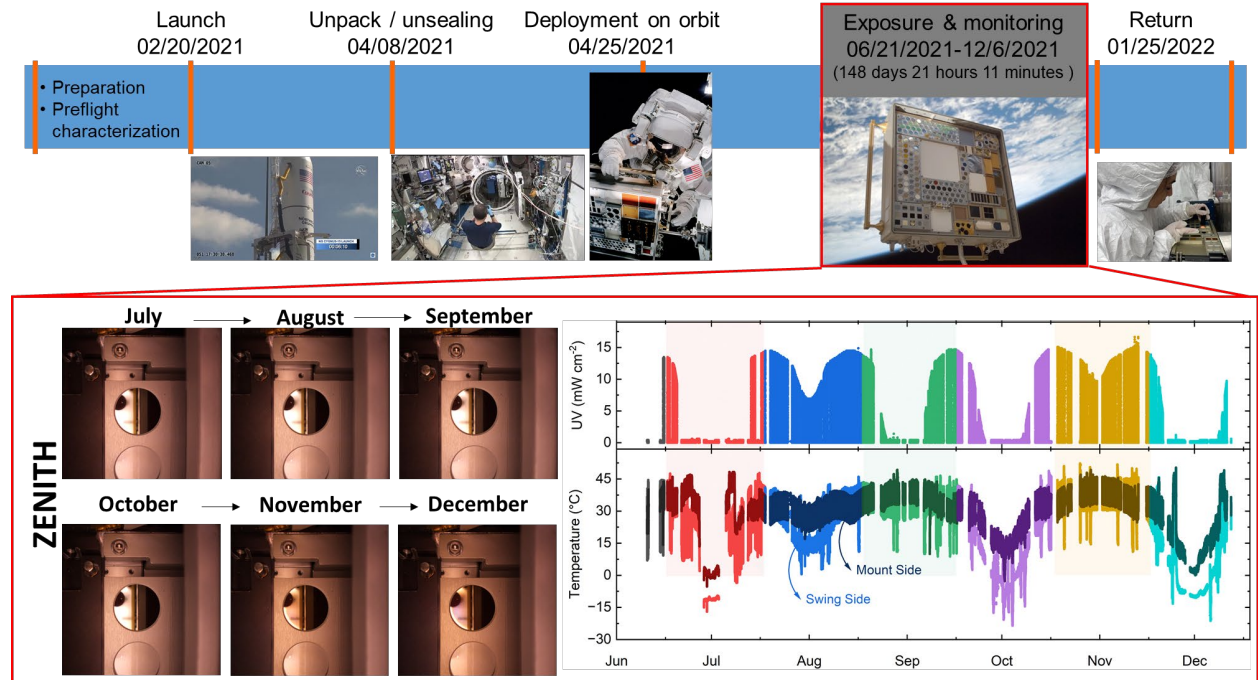


**Fig. 2-25** MISSE-14 mission operation cycle with on-orbit PCM images and science data in Zenith. A total of twenty-eight samples consisting of PCMs and PCM-based tunable filters were returned to NASA for post flight characterization.

A total of twenty-eight samples consisting of two sets of ten PCMs and four PCM-based tunable filters, fourteen on Zenith and fourteen on Wake carrier orientations were tested. Both CaF<sub>2</sub> and sapphire substrates were selected as the range of transparency (125 nm – 10 μm) made them a prime substrate for the design of metasurface optical devices such as optical filters. Moreover, the low mismatch in coefficient of thermal expansion (CTE) between the PCM and the substrate would mitigate cracking or peeling in the film on CaF<sub>2</sub> substrates from the sixteen thermal cycles a day as the ISS orbits Earth. PCM structure changes from amorphous to crystalline yield a significant refractive index variation that affects the filter's performance. To evaluate the correlation between material properties and the performance and lifetime of tunable filters, the PCM's and resultant filters must be exposed to a relevant LEO space environment simultaneously.

The ten PCM films were prepared to evaluate protective layer effects, PCMs crystallinity effects, and substrate effects from three different PCMs: Ge<sub>2</sub>Sb<sub>2</sub>Te<sub>5</sub>, Ge<sub>2</sub>Sb<sub>1-x</sub>Se<sub>x</sub>Te<sub>5</sub>, and Sb<sub>2</sub>Se<sub>3</sub> [24, 25]. The microstructure, thickness, density, and surface roughness of SiO<sub>2</sub> capping films, PCM films, and calcium fluoride (CaF<sub>2</sub>) and sapphire substrates were measured by using instruments such as atomic force microscopy (AFM), x-ray reflectance (XRR), and x-ray diffraction (XRD). The crystallinity and composition ratio of PCMs were evaluated and the transmission spectra and ellipsometric angles of PCMs coated on substrate covered with a SiO<sub>2</sub> capping layer were determined over a broad spectral (190 nm - 40 μm) and temperature range (80 to 750 degrees Kelvin) at an incidence angle of 70 degrees in an ultra-high

vacuum cryostat. The combined data set determines the optical constants (complex dielectric function, refractive index, extinction coefficient) as a function of wavelength and temperature. The optical-clarity, transmittance, and haziness of both CaF<sub>2</sub> and sapphire substrates were characterized.

For PCMs in space applications, it is suspected that extreme temperatures cycling, -120°C to 120°C, with sixteen cycles per day for the ISS, imparts the most impact since this can lead to degradation of data retention periods related to the thermal stability of the amorphous state[53], [54]. Further, atomic oxygen (AO) can induce PCM degradation and erosion by producing surface recession and mass loss which have the most severe impact on optic characteristics such as transmittance[55], [56]. To address this problem, an AO-resistant SiO<sub>2</sub> coating was applied[55]–[57]. The vacuum environment of LEO, with typical pressures less than 10<sup>-6</sup> Torr, is similar to the base pressure of solid-state PCMs film deposition and would not lead to outgassing following mass change of materials or system contamination.

The second sample set consists of the same configuration of PCMs. However, this sample set has geometry features manufactured into it as required for the tunable filter. This will allow us to understand, should failure occur, whether the fault lies in the PCM sample or the geometrical layout of the tunable filter configuration. Four different wavelength filters were prepared based on different crystal structures for the PCM. These included an amorphous-phase of the GST for a 3.46 μm or a 4.25 μm center wavelength filter and a crystalline-phase of the GST for a 4.55 μm or a 4.7 μm wavelength filter on CaF<sub>2</sub> substrate with SiO<sub>2</sub> capping layer.

The performance of the four PCM-based filters (i.e., center wavelength, bandwidth, transmittance) and filter tunability (i.e., tuning range, tuning speed, and switching cycles) were evaluated with the resultant values baselined in a laboratory at NASA prior to departure to the ISS. It was expected that the several changes would be observed in the tunable filter components due to exposure to the space environment. First, the filter transmittance can be changed from a potential alteration of the PCM micro-structure, thickness, and optical transmittance as the crystallinity changes from the extreme thermal cycles at the ISS. Second, the optical constants (i.e., refractive index, extinction coefficient) of PCMs and/or geometry changes of the filter would alter the filter wavelength and bandwidth characteristics. This will be quantified using Fourier-Transform Infrared (FTIR) spectroscopy. Finally, changes of the composition ratio of GST and the geometry of filter can affect the filter tunability. The filter switching cycle test (>1000 cycles) will be conducted with subsequent recording of the wavelength change of the filter depending on the laser energy density to impart phase changes in the GST. Other transition behaviors of the filter such as the tuning speed and power requirements will be quantified during the tunability cycles test as characterized before the ISS exposure. Exposure testing of both PCMs and PCM-based tunable filter samples will allow the exploration of possible failure modes associated with the PCM material itself or with the geometric layout of the tunable filter. (Results of these characterizations are currently pending and will be published separately.) Such qualification of PCMs is integral to their adoption in space-based applications.

**4.3 The emerging space science applications of PCM-based photonics through the MISSE-14 campaign**  
Broadly speaking, PCM-devices enable low-SWaP and high performance for a number of capabilities with relevance to space missions (listed alongside the capabilities in parenthesis), such as: (1) photonic integrated circuits (high speed communications and sensing), (2) Lidar and imaging spectroscopy (spatial light

modulators, beam steerers, tunable filters), (3) deep-space imaging (autofocus/real-time phase-corrective lenses, planar adaptive optics), and (4) satellite temperature management/thermal homeostasis (tunable/dynamic thermal emission control) [47]. Performance parameters, including switching speed and contrast, endurance (cycling lifetime), and power consumption can vary depending on the specific use cases [17, 19]. Moreover, the target wavelengths of the components are dependent on mission requirements. These include visible wavelengths for astronaut health monitoring, visible to infrared wavelengths for atmospheric gas monitoring, and infrared wavelengths for space launch vehicle thermal monitoring. Our perspective on the emerging applications is summarized in Figure 2-26 whereby notable advancements in terrestrial applications can be exploited for the space sector.

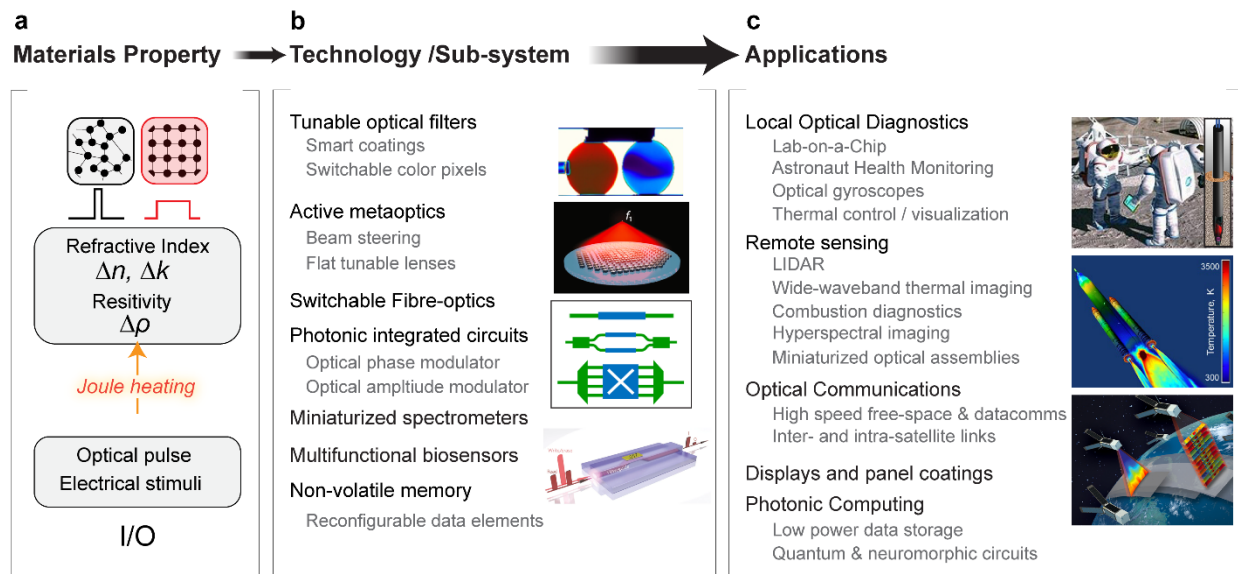


**Fig. 2-26. PCM-based photonics for spaceborne applications based on technologies and subsystems.** The refractive index and resistivity of PCMs can be rapidly changed through optical or electrical stimuli (a). This behavior can be exploited to enable a host of active and reconfigurable optical and electronic technologies / devices (b), which in turn can be integrated into a diverse range of application areas (c) across the space sector.

The first viable technology for space applications is P-ACTIVE. Again, the PCM-based tunable optical filter (P-ACTIVE) is an ‘all encompassing’ acronym—technically it includes any filter design, which incorporates a PCM as the tunable constituent to effectively tune the transmission passband. Such filters have recently been shown for a variety of device architectures [2, 3, 31], operating across the near to mid-wave infrared wavebands. Thermography and imaging spectroscopy (IS) are critical measurement techniques for a variety of NASA missions including gas spectrometer and vehicle ascent and vehicle Entry, Descent, and Landing (EDL) projects [Fig. 2-27 (a), (b), (c)]. Additionally, the PCM-based tunable filter can support human exploration and operational missions in space through astronaut health monitoring, including natural biological signatures and fluorescently-labeled biomarkers for in-situ monitoring of a variety of tracked quantities (e.g., cell counts) [59]. Detailed NASA Mission and / or program-specified scenarios will be detailed in Part III including gas spectrometers (Lidar), thermal monitoring (Space launch system), and astronaut health monitoring.

Beyond filters, another technology of PCM-based photonics consists of reconfigurable optical wavefront lenses for exoplanet imaging as shown in Fig. 2-27 (d) and (e). Exoplanet imaging in space requires real-time wavefront corrections to mitigate the effects of thermal gradients, optical imperfections, and diffraction issues [25]. Current methods of performing these corrections involve deformable mirrors, requiring many actuators to provide the necessary authority to the mirror. Recent demonstrations suggest that PCM optics could be used to simplify the correction system and introduce a transmissive correction element versus a reflective one [33, 34]. The PCM-based optical wavefront lens would be beneficial for the application since the wavefront correction system has to exhibit the control authority to compensate for very small aberrations at high speed [62]. The fast-tuning capability of PCM-based optics is by far the most important feature since exoplanet imaging requires control of high frequency spatial and temporal aberrations.

Free-space optical (FSO) communication is another application for PCM-based photonics where high fidelity laser beam steering is critical. Recent demonstrations in reconfigurable PCM-based optics [36–38] suggest that such devices could be utilized at both the transmission and receiving ends of a FSO system to remove the effects of vibration and thermal gradients as replacements for deformable mirrors. This would permit higher bandwidth optical communications through space. Additionally, PCMs beam steerers with broad angular ranges can be used to maintain optical links across satellite constellations without the need to maneuver satellites into a direct line-of-sight configuration, reducing fuel usage and coordination complexity across the constellation. Moreover, the small volume of the PCM-based photonics is important for operation in CubeSat platforms in space.

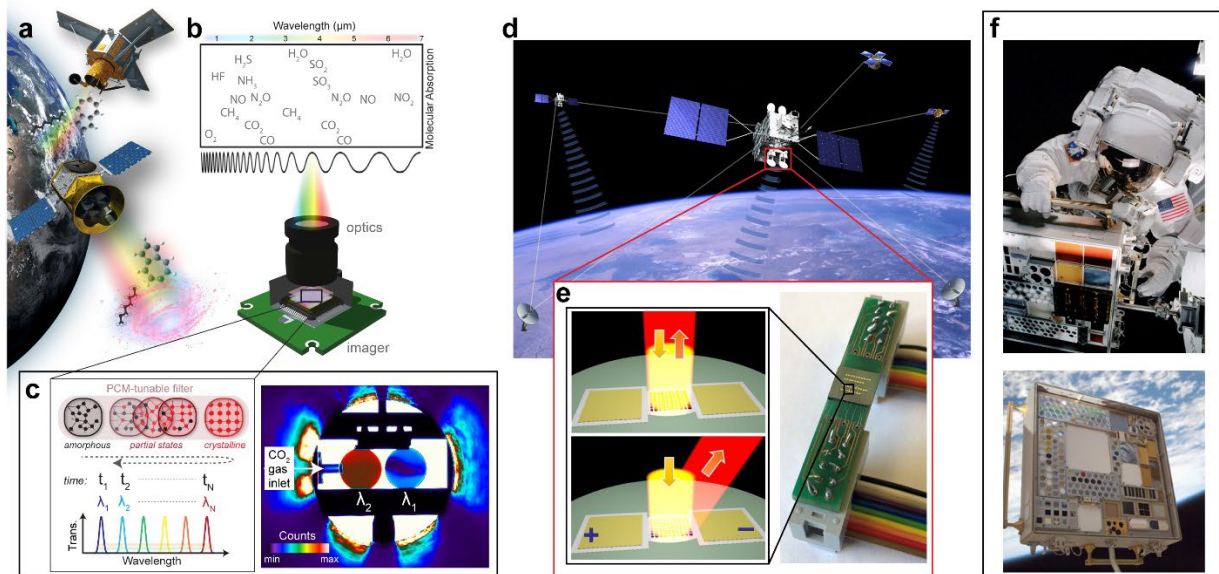


**Fig. 2-27. Application areas for PCM-integrated active devices.** (a) Tunable bandpass filter for Spaceborne LIDAR; (b) the SAGE passive Lidar system measures the composition of the atmosphere with specific aerosols and molecules of interest. (c) SAGE can use a PCM tunable filter to switch between different chemical absorption channels. Through an optical or electrical stimuli on the filter active area, PCM crystallinity is modified, and the resultant transmission response ( $\lambda_N$ ) is spectrally shifted as demonstrated by CO<sub>2</sub> gas sensing with GST-Fabry Perot tunable bandpass filters[31].

(d) Reconfigurable planar optics for free-space optical communications: PCM-based beam steerers and highly pixelated “meta-correctors” can achieve a broad range of phase coverage, translating to large angular scanning and phase-correction ranges. (e) schematic rendering showing the reconfigurable metasurface beam deflector in its amorphous (top) and crystalline (bottom) states of PCM in a packaged metasurface array device[3]. (f) MISSE exposure testing of both PCMs along with metasurface optical components comprised of these PCMs will significantly expedite PCM integration into spaceborne platforms and open emerging applications. (Credit: NASA)

Webpage (<https://spaceborne-pcms.github.io>) is generated as Supporting Information for the NASA-TP readers. Scan the QR code for “The Maps”, the locations of space material evaluation facilities (academic research laboratories, space agencies, and private companies) including simulated space environments across the world.



## Appendix A. MATLAB®-Based Graphical User Interface (GUI) development

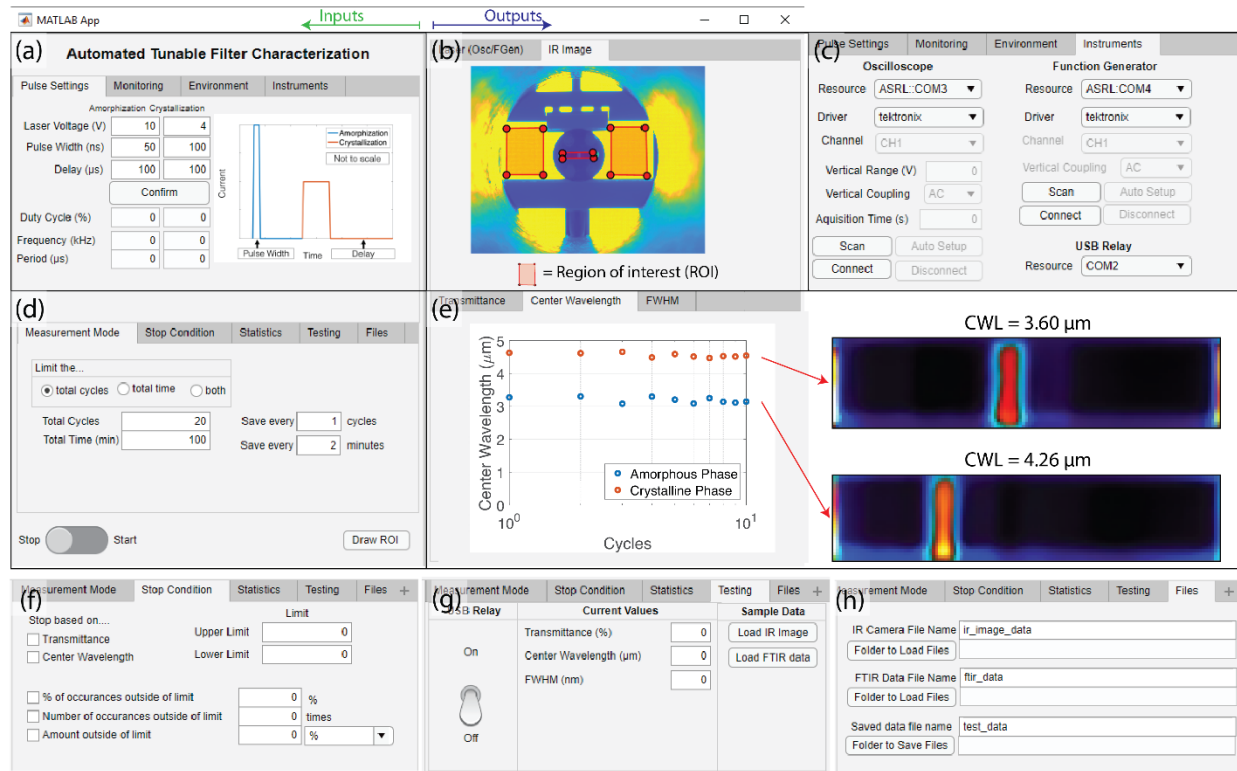


**Fig. A-1.** Real-time filter characterization: A screenshot of the custom MATLAB® GUI. The source code and packaged application are available at <https://dbombara.github.io/automated-pcm-characterization>. The window contains four quadrants (a)-(e), which each contain tabs. The left half of the GUI is generally for inputs by the user, whereas the right half displays the output from the instruments and computed spectral properties. (a) The top-left quadrant of the GUI contains tabs for hardware-based settings and conditions. (b) The top-right quadrant of the GUI displays “raw” data from the IR camera and laser. (c) The Instruments tab, which is a part of the top-left quadrant, enables the user to connect to the different instruments. (d) The bottom-left quadrant is for software-based settings. (e) The bottom-right quadrant displays the spectral properties of the P-ACTIVE. With the current LVF-based approach, only the CWL may be plotted. In future work, other properties, such as transmittance and full width at half maximum (FWHM) will be calculated. The (f) Stop Condition tab, (g) Testing tab, and (h) Files tab allow the user to have more control over the experiment.

### • Instruments Tab

It is crucial to ensure all instruments are properly connected before beginning the experiment. For that reason, the Instruments tab, shown in Fig. A-2, includes information to connect and operate the oscilloscope and function generator. Options such as the resource (the instrument identifier), driver, channel, voltage

range, and acquisition time are selected by the user. The Instrument tab also contains buttons for connecting to the relay and laser power supply via serial connections.

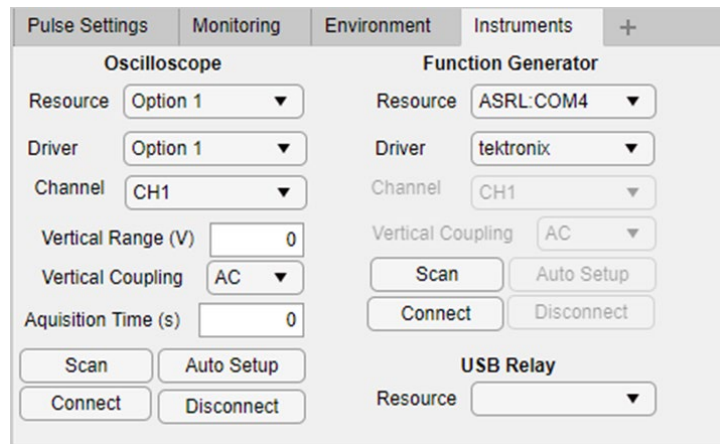


**Fig. A-2** The Instruments tab.

- **Measurement Mode and Stop Condition Tabs**

The Measurement Mode tab (Fig. A-3) and Stop Condition tab (Fig. A-4) both allow the user to select options for terminating the experiment when a particular condition, or combination of conditions, is met. These tabs are especially useful for hours-long reliability tests. In the Stop Condition tab, the user can choose to stop the experiment when either the transmittance, CWL, or both properties fall outside a predetermined limit. Similarly, the experiment may stop after a particular number of occurrences outside that limit, or when the number of occurrences reaches a set percentage of tuning cycles completed thus far. In contrast, the conditions in the Measurement Mode tab—total cycles and total time—are calculated in the GUI itself without relying on the connected hardware.

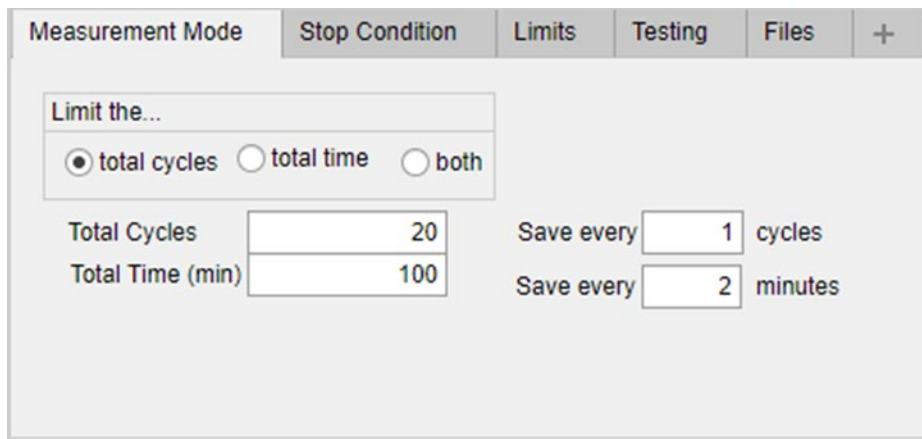


**Fig. A-3.** The Measurement Mode tab.

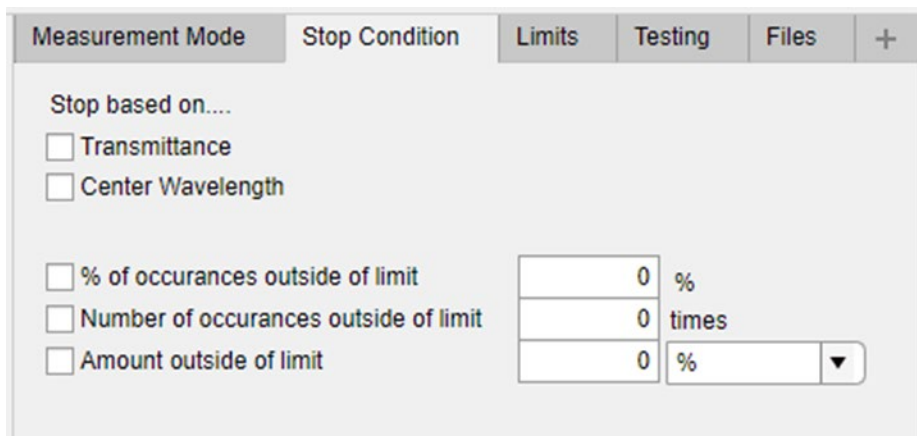


**Fig. A-4.** The Stop Condition tab.

- **Pulse Settings Tab**

The required energy and pulse duration may change depending on the particular PCM that is under test. In the Pulse Settings tab (Fig. A-5), the user can set the desired laser voltages (V), pulse widths (ns), and delays ( $\mu$ s) between pulses. The GUI then calculates the duty cycles (%), frequencies (MHz), and periods ( $\mu$ s) of the pulses for amorphization and crystallization. The specific values of the laser voltage, pulse width, and delay are determined experimentally and vary depending on the particular materials utilized in the tunable filter.

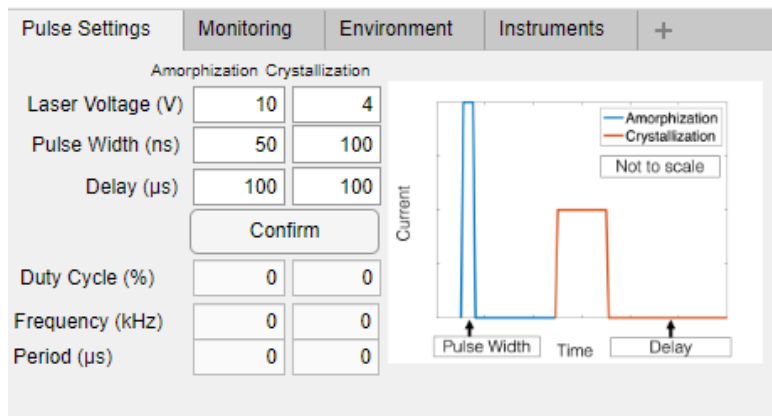


**Fig. A-5.** The Pulse Settings tab.

- **Environment Tab**

The Environment tab (Fig. A-6) was developed with the goal to monitor not only the spectral properties of the filter, but also the environmental properties during the experiment: temperature, humidity, and pressure. This is because the tunable filter's environment may undergo significant changes during the filter's operation. For example, the tunable filter may potentially be used on aircraft that undergo extreme changes in temperature and pressure during flight. For example, NASA Langley's SCIFLI (Scientifically Calibrated In-Flight Imagery) team is developing the SAMI (SCIFLI Airborne Multispectral Imager) system. This system contains a rotating filter wheel and operates on an airplane. After significant technological development, the tunable filter could potentially replace the rotating filter wheel in the SAMI system.

During flight, the system's temperature and pressure will change greatly. For that reason, the SAMI system is required to withstand temperatures from -40 °C to 50 °C, as well as pressures at altitudes between sea level and 50,000 ft. Before it can replace the filter wheel, the tunable filter must be tested at those extreme conditions as well. This tab may be useful in future work.

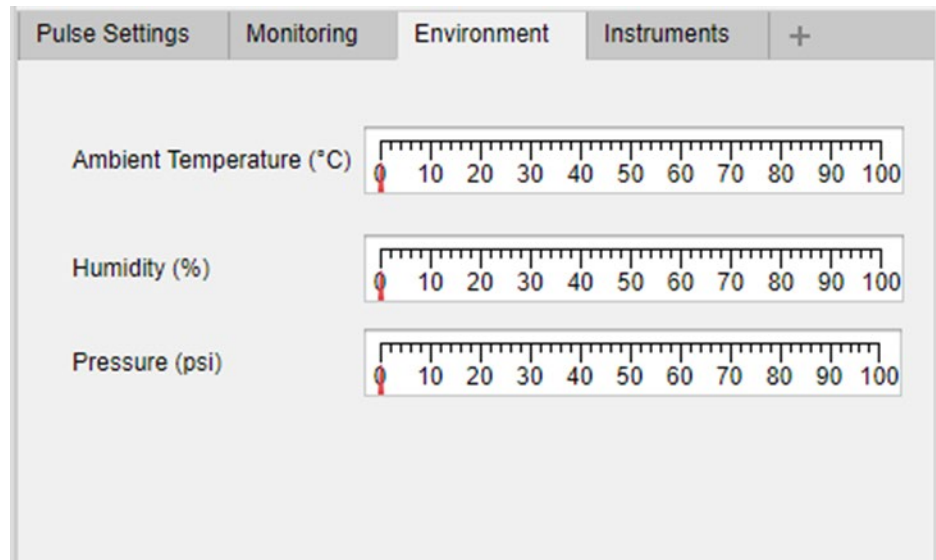


**Fig. A-6.** The Environment tab.

- **Files Tab**

The Files tab (Fig. A-7) allows the user to specify file and folder names from which data will be imported and to which it will be saved. There are two types of files that must be imported into MATLAB®: the IR image of the ATS file type and the FTIR data in the form of a CSV file. The experimental data are

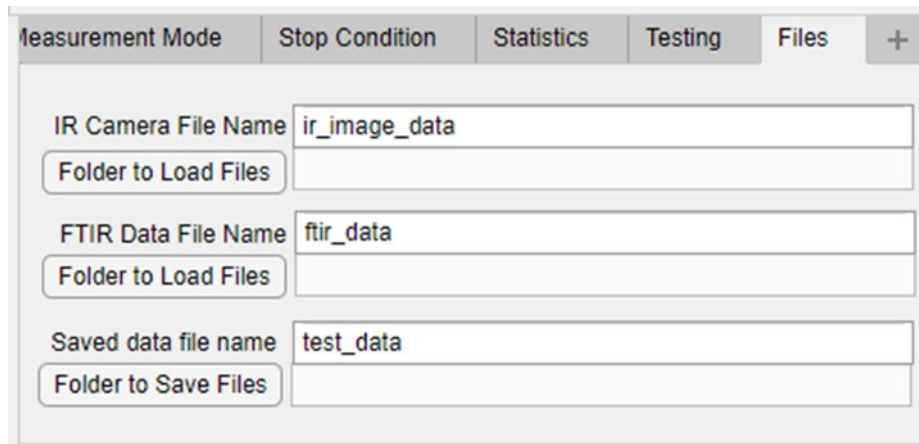


**Fig. A-7.** The Files tab.

automatically saved as a MATLAB® file type (readable in MATLAB® only). During data post-processing, the file can be converted into a CSV or TXT file.

- **Tabs for Monitoring Raw Data**

The top-right quadrant (Fig. A-8) of the GUI window is for displaying “raw” data: in general, data that come directly from instruments, not values that are computed as a result of the instruments’ data. In this quadrant, there are two tabs: the “Laser (Osc/FGen)” tab and the IR Image tab (Fig. A-9). As the names imply, the former plots the input to and output from the laser, as determined by the function generator and oscilloscope. The input signal to the laser differs from the output signal; the laser requires two pulses of 5-



**Fig. A-8.** The tab for showing the laser data (from the function generator and oscilloscope).

V amplitude and 10- $\mu$ s duration, with 170  $\mu$ s between pulses. However, the output pulse from the laser head is only nanoseconds-long. The IR Image tab displays the IR image and ROI that are selected before the experiment. As the CWL of the PCM-based filter is tuned, the IR image will change based on the indicator on the LVF.

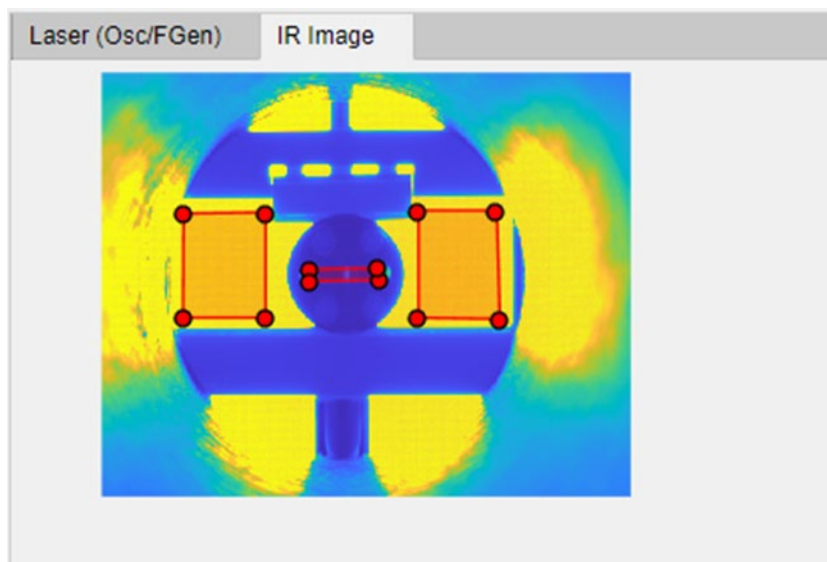


**Fig. A-9.** The IR Image tab.

- **Tabs for Testing and Performance Characterization**

The Testing tab (Fig. A-1(g)) contains buttons for the user to test the functionality of the GUI before running the experiment. The relays can be turned on and off with the click of a button. Sample files can also be imported, after which the IR image can be plotted, and the spectral properties can be calculated. The bottom-right quadrant (Fig. 2-28(e)) of the GUI window contains plots of values computed from the IR image above. The cycle number is plotted on each abscissa whereas the CWL, FWHM, and transmittance intensity are each plotted in separate tabs on the ordinate axes.

The MATLAB® GUI has much utility in the current experimental system, but in future work, the GUI will be applied to (1) an experiment to investigate the PCM-based filter's reliability and (2) a compact, and custom-designed circuit to optically switch the PCM-based filter and characterize its phase changes in the NIR waveband.

### Box 1. PROWESS: Phase-change Reconfigurable Optical WavEfront Synthesis System

Since 2020, the P-ACTIVE team has expanded the PCM-based reconfigurable optic project to PROWESS, a reconfigurable planar optic for wavefront correction and beam steering for spaceborne Lidar and free-space optical (FSO) communications.

The use of MEMS-based micromirror arrays and fast-steering mirrors (FSMs) is common in various imaging Lidar and FSO communications systems in order to capture high-spatial-resolution data within a given field of regard, correct for wavefront aberrations caused by scatter/turbulence, or maintain optical links without having to maneuver satellite constellations to maintain direct line-of-sight. Recent work in the development of FSO communications has concentrated on adapting this technology for use in SmallSat and CubeSat platforms since FSO communication systems can potentially increase signal to noise ratios significantly within the communication channel[65]. However, the actuator response times and pointing requirements for these applications can be strict. PCM-based tunable metasurfaces such as beam steerers and tunable metalenses have recently been demonstrated as proof-of-concept devices, and have significant potential to address both of these applications[60], [66].

Due to their large refractive index contrast, PCM-based beam steers and highly pixelated “meta-correctors” can achieve a broad range of phase coverage, translating to large angular scanning and phase-correction ranges. Although these devices have only recently been demonstrated in the lab, targeted research into high-resolution control of intermediate PCM phases and highly pixelated metasurfaces could soon play a transformative role in space-based adaptive optics such as the aforementioned applications.

Therefore, PROWESS technology offers many benefits for both terrestrial and space-based applications given its lack of moving parts and its ability to provide addressable wavefront control. The current state of the art in wavefront control relies heavily on mechanical actuators and assemblies, with single- and multi-element deformable mirrors used almost exclusively in current imaging systems[67]–[70]. A diagram of a typical deformable mirror system is shown in Figure 1 (a). A control loop is implemented where a portion of the reflected wavefront is passed via a beam splitter to a wavefront sensor (for example a Shack-Hartmann sensor) and used to control the mechanical actuators on the mirror. Due to the lag in detecting the wavefront coupled with the mechanical actuation time, the correction bandwidth of the deformable mirror is limited to a few 100’s of Hertz typically, although much higher actuation speeds using MEMS technology have been reported.

Wavefront correction and multi-focal imaging can also be performed using plenoptic imaging systems (see Figure 1 (b))[71]–[73]. These have no moving parts but rely on a fixed geometric pattern of lenslet arrays and transfer lenses that must be tailored for specific applications. Images can be acquired at high speed; however, extraction of focused images can be computationally expensive. Plenoptic systems have also been utilized in hyperspectral imaging applications, eliminating the need for traditional rotating filter wheels[74], [75].

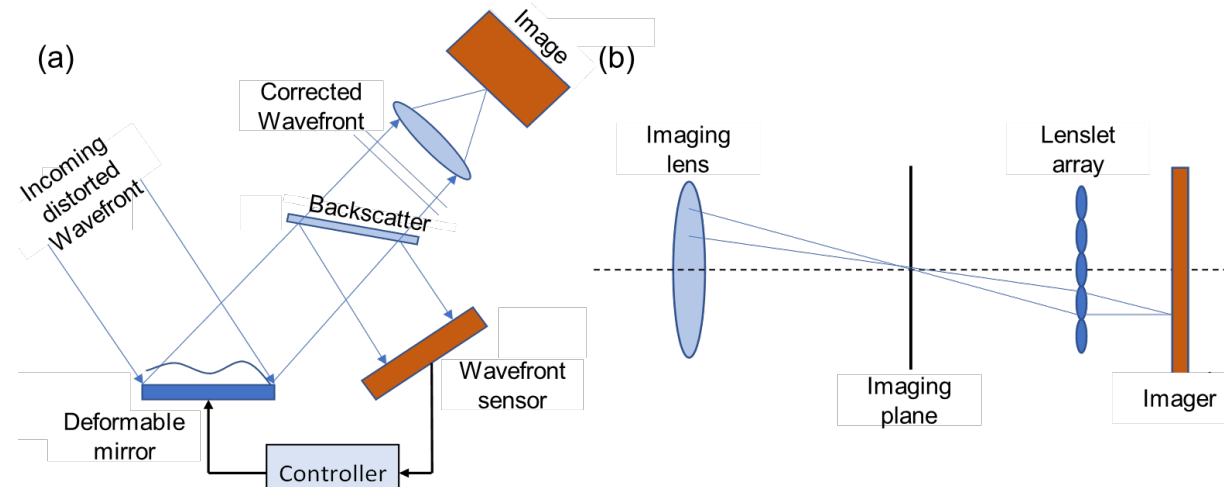


**Fig. B-1-1.** (a) Typical Deformable Mirror Wavefront Corrector and (b) Plenoptic Imaging Concept

The PROWESS concept overcomes the limitations of the mirror and plenoptic systems illustrated in Figures 1 (a) and (b) via implementation of an addressable array of PCM-based elements that provides on-demand refocusing and wavefront correction. This opens the possibility to utilize PROWESS in several applications, three of which are outlined below.

- Multi-focal Imaging for Aerospace Applications: Aerospace ground facility testing (i.e., wind tunnel testing) is increasing reliant on the use of advanced imaging systems [Fig. 2(a)] to acquire flow visualization and quantitative density, temperature, pressure and velocity measurements to characterize vehicle concepts[76]. These techniques include Schlieren and shadowgraphy for measuring density gradients, particle image velocimetry for measuring global velocity fields, and laser induced fluorescence for boundary layer and shock interaction measurements, among others. A common element of these measurement techniques is the use of one or more camera systems to capture the phenomena of interest. Typically, the cameras and associated optics need to be repositioned using mechanical actuators and scanners to allow coverage of the regions of interest (ROI) in the flow. The PROWESS concept introduces an intriguing possibility of replacing these mechanical scanning systems with PCM-based refocusing elements both as part of the imaging system, and also possibly for laser optics used for illumination of the flow fields. Multiple PROWESS elements could be stacked to provide a fully programmable multi-focal system to allow ROI interrogation.
- Exoplanet Imaging: Exoplanet imaging in space requires real-time wavefront corrections to mitigate the effects of thermal gradients, optical imperfections, and diffraction issues[77]. An active exoplanet imaging mission at present is the James Webb Space Telescope (JWST). The NIRCam on the telescope [Fig. 2(b)], has several coronagraphs for imaging in the IR[78]. Using PCM-based optics, a space-based correction system can be simplified to introduce a transmissive correction element versus a reflective one. The concept for exoplanet imaging would be to use a coronagraph to block out the light from the central star and then use a PROWESS-enabled system to correct the incoming wavefront. This would permit characterization of the light from an exoplanet and perhaps even allow direct imaging of the planet. A PROWESS-based optical wavefront corrector could provide the necessary control authority to compensate for very small aberrations at reasonably high speed. The fast-tuning capability of PCM-based optics is by far the most important feature since exoplanet imaging requires control of high frequency spatial and temporal aberrations.
- Optical Communication: Another application for PCM optics is in free-space optical communication where high fidelity laser beam pointing is critical[79]. Reconfigurable PCM-based optics could be utilized at both the transmission and receiving ends of the optical communication system to remove the effects of vibration and thermal gradients as replacements for deformable or steering mirrors. This would permit higher bandwidth optical communications through space. Moreover, the small volume of the PCM-based optic is important for operation in proposed CubeSat platforms in space, such as the upcoming NASA CubeSat Laser Infrared CrosslinK (CLICK) mission [Fig. 2(c)]. CLICK uses a fine steering mirror control system for pointing; however, PROWESS technology could also be utilized for this.

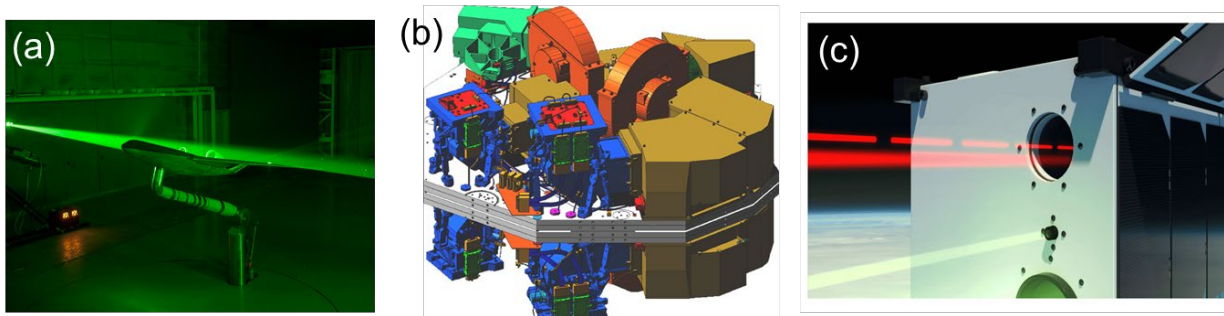


**Fig. B-1-2.** (a) Example of light sheet / imaging system utilized in ground testing, (b) James Webb Space Telescope NIRCam engineering diagram, and (c) CLICK concept for Smallsat optical communication.

### **PART III: NASA mission / program scenarios based on science rationale**

Throughout Parts I and II, P-ACTIVE has shown promise as a multifunctional wide-band replacement for bulky filter wheels in spaceborne remote sensing sub-systems. This is achieved through the integration of PCMs into a filter design to tune the transmission passband in real time. The integration of PCMs with on-chip micro-heaters (*More information available in Part IV, ‘R&D strategies’*) will lead to orders-of-magnitude reduction in total SWaP.

The filters can be tuned within nano- / micro-seconds, enabling real time imaging spectroscopy with high data throughput. Moreover, multi-spectral filters that cover MWIR wavebands have wide-ranging imaging and sensing applications, from probing molecular vibrations in chemical species to detecting radiant thermal signatures. Unique features of P-ACTIVE envisage that spaceborne systems to small satellite form factors incorporating P-ACTIVE will continue to be in demand in the foreseeable future with broad applications. The applications include atmospheric gas sensing, space launch vehicle thermal imaging, and astronaut health monitoring. In this part, three NASA mission / program scenarios with science benefits from P-ACTIVE are introduced.

*(Note: P-ACTIVE and filter wheels are not in competition but are complementary technologies. P-ACTIVE yields research-level (low TRL) components for future versions of systems to support science information missions.)*

#### **1. P-ACTIVE for atmospheric gas sensing: NASA SAGE mission case study**

The visible to mid-wave infrared (MWIR) waveband is the spectral fingerprint for many chemical species. Lidar missions can utilize P-ACTIVE technology for chemical remote sensing, where the broadband tuning capability provides unprecedented views of earth’s atmospheric constituents and surface altimetry. Moreover, the accurate records of chemical species such as aerosols, ozone, and carbon dioxide are a vital piece of the puzzle regarding climate change.

History of mission: As an example, consider the Stratospheric Aerosol and Gas Experiment (SAGE), a current NASA mission with strict performance requirements [80]. SAGE is a passive Lidar system that measures the composition of the atmosphere, with specific aerosols and molecules of interest. The SAGE missions are a series of remote sensing instruments deployed in Low-Earth Orbit (LEO) with the intent of observing key atmospheric constituents, in particular aerosol, ozone, and water vapor.

SAGE I, operational between 1979 and 1981, successfully used the technique of solar occultation (i.e., using the Sun as a light source through long atmospheric path lengths to measure weakly absorbing/scattering species) to make some of the first vertically resolved measurements of stratospheric aerosol and ozone. SAGE II, an Earth radiation budget (ERBS) satellite (1984-2005) and SAGE III, a third generation, satellite-borne instrument in NASA’s Earth observing system (EOS) (2001-2005) were launched and measured the atmospheric composition. Since 2017, SAGE III/ISS has demonstrated an ability to provide high quality measurements of stratospheric ozone [81], aerosols [82], and water vapor [2, 4]. These atmospheric species are of particular importance. Stratospheric ozone, for example, was a targeted observable in the 2017 Decadal Survey [84], and NASA is mandated to monitor the health of the ozone layer under the Clean Air Act as amended [85]. Aerosol is a designated observable under the Decadal

Survey because it is a key input to climate models, has an important role in atmospheric chemistry [86], and is a large source of uncertainty to Earth’s energy balance [87]. Water vapor is another key component of Earth’s energy budget [87], a key driver of stratospheric chemistry [88], and a tracer for stratospheric circulation and stratosphere–troposphere exchange [10].

Justification of P-ACTIVE for SAGE: The following justifications for the use of P-ACTIVE technology in future SAGE missions are presented:

- Despite the importance of these atmospheric constituents, there is uncertainty about the future of availability of measurements and data continuity. While the SAGE III mission is in extended operation, it is important to consider what instruments can be deployed in the future to ensure proper continuity of these critical data records.
- SAGE-IV is the next generation SAGE instrument prototype in NASA’s instrument incubator program (launch date TBD). The SAGE-IV concept is a solar occultation imager CubeSat capable of measuring ozone, aerosols, and other trace gas species at the same quality as previous SAGE instruments (including SAGE III/ISS). The SAGE IV instrument adapts successful ideas from its predecessors but with a modified approach to fit inside a 6U CubeSat bus as is seen in Figure 3-1 (a). The methodology has been transformed from a legacy solar-scanning technique with a grating spectrometer to imaging of the entire solar disk directly. Direct imaging is now possible through increased accuracy in CubeSat pointing and higher data rates from LEO. SAGE IV is capable of providing continuity for critical data products, particularly ozone and aerosol in the stratosphere, as described in the 2017 Decadal Survey for Earth Science and Applications from Space [13], albeit at a significantly reduced size and cost. Table 3-1 contains the species-dependent precision and vertical resolution requirements for the mission.
- The SAGE-IV platform design fulfills the Decadal Survey requirement to reduce earth observing mission costs. It is currently designed to work in the visible / NIR / MWIR to continue building on the valuable SAGE datasets. The design is flexible and can be customized to other types of measurements using different detectors for different wavelengths (i.e., SAGE-IR, expand SAGE-IV into IR for additional atmospheric species and targeted needs).
- There is potential interest in using the SAGE IV chassis for future missions, optimizing its IR measurement capability for Mars (CO<sub>2</sub>, N<sub>2</sub>, H<sub>2</sub>O, NO) and / or Venus (CO<sub>2</sub>, N<sub>2</sub>, H<sub>2</sub>O, CO) atmospheric monitoring (Table 3-2).

**Table 3-1. Science requirements**

Species	Altitude Range	Best Precision	Vertical Resolution
Ozone	0km *- 70km	1%	1km
Aerosol Extinction	0km *- 40km	5%	1km
Water Vapor	0km *- 60km	10%	2km
Nitrogen Dioxide	10km *- 50km	5%	1km

\* Stated altitude or cloud-top, whichever is higher

**Table 3-2. Mars and Venus atmosphere composition**

**Mars Atmosphere Composition**

Surface pressure: 6.36 mb at mean radius (variable from 4.0 to 8.7 mb depending on season)  
6.9 mb to 9 mb (Viking 1 Lander site)

Surface density: ~0.020 kg/m<sup>3</sup>

Scale height: 11.1 km

Total mass of atm: ~2.5 x 10<sup>16</sup> kg

Average temperature: ~210 K (-63 C)

**Atmosphere composition (by volume):**

Major:	Carbon Dioxide (CO <sub>2</sub> ) - 95.32%	Nitrogen (N <sub>2</sub> ) - 2.7%	Argon (Ar) - 1.6%
	Oxygen (O <sub>2</sub> ) - 0.13%	Carbon Monoxide (CO) - 0.08%	
Minor (ppm):	Water (H <sub>2</sub> O) - 210	Nitrogen Oxide (NO) - 100	Neon (Ne) - 2.5
		Hydrogen-Deuterium-Oxygen (HDO) - 0.85	Krypton (Kr) - 0.3
	Xenon (Xe) - 0.08		

**Venus Atmosphere Composition**

Surface pressure: 92 bars

Surface density: ~65. kg/m<sup>3</sup>

Scale height: 15.9 km

Total mass of atm: ~4.8 x 10<sup>20</sup> kg

Average temperature: 737 K (464 C)

**Atmosphere composition (surface, by volume):**

Major:	96.5% Carbon Dioxide (CO <sub>2</sub> )	3.5% Nitrogen (N <sub>2</sub> )
Minor (ppm):	Sulfur Dioxide (SO <sub>2</sub> ) - 150	Argon (Ar) - 70 Water (H <sub>2</sub> O) - 20
	Carbon Monoxide (CO) - 17	Helium (He) - 12 Neon (Ne) - 7

P-ACTIVE technology for future mission: To make these measurements, SAGE-III/ISS uses and SAGE-IV proposes filter wheels to switch between different chemical absorption channels such as H<sub>2</sub>O, N<sub>2</sub>O, CO<sub>2</sub> and CH<sub>4</sub> [80]. This requires tuning to ~8 discrete wavelengths from 386 nm to 1020 nm (for SAGE-IV) but expands with SAGE-IV into the IR for additional atmospheric species (1.4 - 4.1 μm) with a transmission passband of ~10 nm and high transmission. P-ACTIVE will enable Lidar and active remote sensing of atmospheric compositions with significant SWaP reduction in 6U CubeSat architectures by empowering a dynamically tunable, all-solid-state solution without moving parts. Table 3-3 addresses the P-ACTIVE design parameters targeting for the SAGE mission.

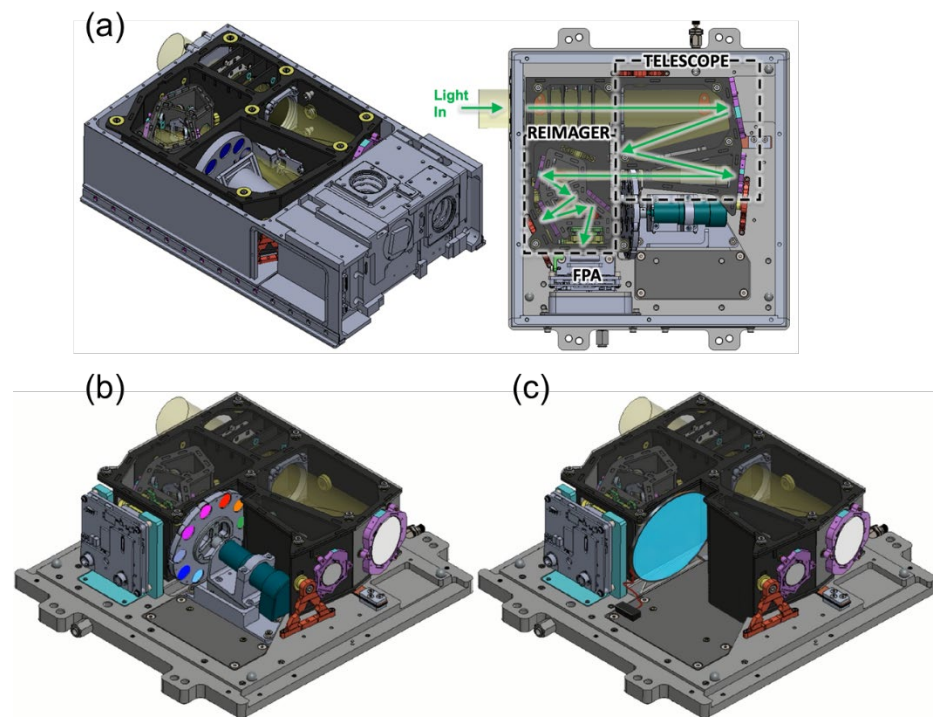


**Fig. 3-1.** Illustration of the SAGE-IV instrument concept in a 6U CubeSat on the left and optical train on the right (b) Planned filter wheels and (c) proposed P-ACTIVE with extra space for optics and / or electronics in the SAGE-IV in a CubeSat.

**Table 3-3. P-Active design parameters targeting SAGE missions**

Design Parameter	Target	Explanation
Wavelength	<ul style="list-style-type: none"> <li>Application-dependent</li> <li>WL: 1.4~4.2<math>\mu</math>m</li> <li>FWHM: 10 ± 3.0nm</li> <li>Transmission: &gt;70%</li> <li>Out-of-band / OD &gt; 2</li> </ul>	<ul style="list-style-type: none"> <li>For SAGE-IR example:</li> <li>Including H<sub>2</sub>O (1.375<math>\mu</math>m, 1.845<math>\mu</math>m, 2.6<math>\mu</math>m), N<sub>2</sub>O (3.885<math>\mu</math>m), CH<sub>4</sub> (1.666<math>\mu</math>m and 2.3<math>\mu</math>m), CO<sub>2</sub> (2<math>\mu</math>m and 4.1<math>\mu</math>m)</li> <li>Specific WLs: Greenhouse gases and H<sub>2</sub>O vapor profiles for deeper understanding of clouds responding to warming climate.</li> <li>Broad WLs: Water vapor atmosphere monitoring (not change much) but volcano ash and industry gases (change and unexpected)</li> </ul>
# of channels	<ul style="list-style-type: none"> <li>0.948<math>\mu</math>m – 1.452<math>\mu</math>m (#1 channel)</li> <li>1.44<math>\mu</math>m – 2.99<math>\mu</math>m (#2 channel)</li> <li>2.97<math>\mu</math>m – 7.83<math>\mu</math>m (#3 channel)</li> </ul>	<ul style="list-style-type: none"> <li>Channel #1: Sb<sub>2</sub>Se<sub>3</sub>, #2: GeSbSeTe, and #3: Ge<sub>2</sub>Sb<sub>2</sub>Tes</li> <li>Filters designed and optimized using custom deep neural network tool</li> <li>Analog-type continuous tuning is possible across all channels via joule heating from electrodes</li> </ul>
Tuning mechanism	Electrode heater for tuning	Si heater
Detector	Single detector	TBD (i.e., CIRAS, CubeSat Infrared Atmospheric Sounder program' IR detector)
Platform	6U CubeSat	
P-ACTIVE diameter	1.3cm clear aperture	The beam size is 1.3cm (i.e., bigger than the beam size of the SAGE-IV)
P-ACTIVE reliability (based on instrument duration)	$2.0124 \times 10^7$ switches per year	SAGE example: SAGE-IV switches 4.5 times per second. If we had 20 filters it would be 10 times per second. The science events are a maximum length of 6 minutes (depends on beta angle). Normal LEO orbits are approximately 90 minutes long, so when the events are the longest it would be 6 minutes measuring followed by 78 minutes off followed by another measurement. Therefore, $3.154e7$ [seconds/year] * 10 [switches/second] * (6/90) [% of time filter is actively switching] = $2.0124 \times 10^7$ [switches/year]
Power budget	~ few hundred mW (average power)	<ul style="list-style-type: none"> <li>15W to power motor for filter wheel</li> <li>Even P-ACTIVE stacking does not increase power budget (i.e., beam block on/ off switch add)</li> </ul>
Weigh budget	10g	800g of filter wheel
Target Measurement Performance Parameters	Same as SAGE-IV	<ul style="list-style-type: none"> <li>Measurement vertical resolution:&lt; 1km</li> <li>Stratospheric gases resolution: &lt; 1%</li> <li>Exoatmospheric Measurement Precision: &lt; 0.05%</li> <li>Provide accurate ozone concentration profiles from upper troposphere (12-15km) up to the lower mesosphere (~60km) with a relatively high geographical sampling</li> </ul>

For PCM-based filters to apply to the SAGE scenario, arguably one of the most strict science requirements to which they can be applied – and certainly more strict than IR multispectral imaging – they must meet or exceed these specifications. Careful design of the PCM metasurface filter – for example, via deep neural networks – along with the proper choice of PCM material can likely satisfy the requirements for tuning range and transmission passband width. The switching requirement seems likely to be trivial for PCM

devices, as they are currently used in PRAM electronics. However, switching stability and failure analysis for photonic PCMs need to be fully characterized and improved, and is a key research element required to transition PCMs from the lab and into scientific instruments. R&D strategies and challenges are addressed in Part IV.

**Differential absorption LIDAR (DIAL):** DIAL is another potential application for P-ACTIVE for atmospheric gas sensing. DIAL is a strategically important measurement technique within NASA, mapping range-resolved concentrations of trace/greenhouse gases such as H<sub>2</sub>O (~890 nm wavelength) and CH<sub>4</sub> (1.6  $\mu$ m wavelength) in the atmosphere that are important to many processes that underpin weather and climate systems [46]. Spaceborne DIAL would provide direct and unbiased profiles of gases throughout the atmosphere with high vertical resolution and global coverage beyond the existing airborne systems [Fig. 3-2]. The benefit of developing a PCM-based tunable filter is that only one filter and one detector are required regardless of the number of wavelengths needed to transmit for sampling the gases at various spectral locations. This is in direct contrast to the established approach of using a combination of bulky optical components (beamsplitters, filters, etalons etc.) which as a system has a large footprint, high power consumption and has demanding alignment tolerances. A single element tunable filter (PCM-based) allows a SmallSat-based spaceborne DIAL to decrease the SWaP-C risk, and reduce systematic bias that could result from non-linear time dependent degradation of the different detectors. For the DIAL application, Sb<sub>2</sub>S<sub>3</sub>, Sb<sub>2</sub>Se<sub>3</sub>, or Sb<sub>2</sub>Te<sub>3</sub> can be selected as material candidates due to their low-loss. These phase change materials can switch from a low-index ( $n = 3$ ), amorphous state to a high-index ( $n = 4.5$ ), crystalline state with low loss ( $k < 0.005$ ) over a wavelength range of 600 nm – 2  $\mu$ m or more, matching the targeted spectral ranges for DIAL of 800 nm – 1.6  $\mu$ m [48]. PCM and FP multiple-cavity bandpass filter designs have been proposed as frequency agile filters for DIAL applications [89]. However, the strict performance requirements of > 100 pm/ $\mu$ s temporal tuning rate and 300pm free spectral range are big challenges with P-ACTIVE.

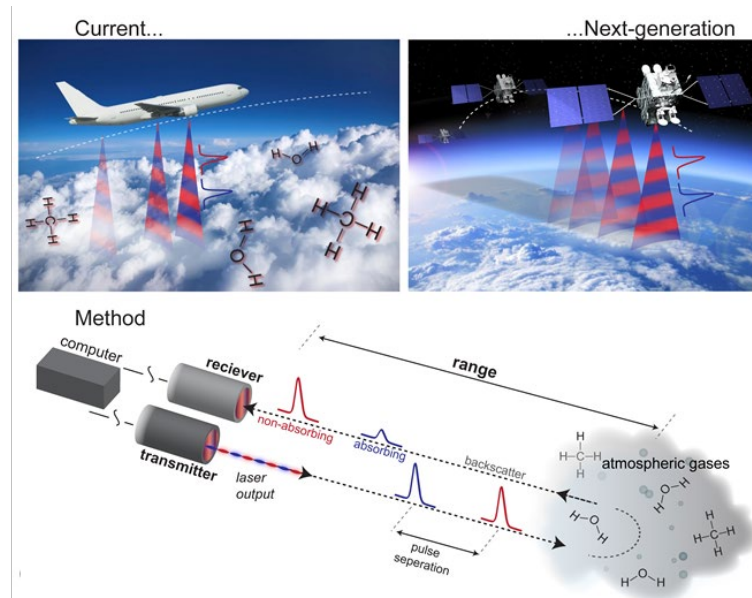


**Fig. 3-2.** Spaceborne DIAL concept for the water vapor profile (top) and Differential Absorption LIDAR (DIAL) operating schematic (bottom)

## 2. P-ACTIVE for space launch vehicle thermal monitoring: NASA SCIFLI project case study

### 2.1 History of Project

The SCIFLI (Scientifically Calibrated In-Flight Imagery) project at NASA Langley Research Center (LaRC) was derived from the previous HYTHIRM (Hypersonic Thermodynamic Infrared Measurements) project. HYTHIRM arose from the Columbia accident to thermally map the shuttle orbiter heatshield during reentry, building on an invaluable collection of in-flight data that helped correlate and extend the utility of wind-tunnel tests and computational aerothermal analysis in the hypersonic regime.

Today, the SCIFLI team pursues the development and deployment of state-of-the-art (SOA) remote thermal, visual, and spectral imaging capabilities from ground-based, sea-based, and airborne-based platforms over a visible / infrared waveband spectrum [Fig. 3-3]. The team helps researchers gain insight into some of the most challenging regimes in fluid dynamics. With each successful mission the SCIFLI team builds on an invaluable collection of in-flight data that will help correlate and extend the utility of wind tunnel tests and computational aerothermal analyses in the hypersonic regime. The team's future projects will utilize cutting edge technology such as SAMI (SCIFLI Airborne Multispectral Imager) to collect calibrated temperature images of the space launch system (SLS) base heat region and plume-induced flow separation (PIFS) during ascent. These data will validate the thermal protection system of the launch vehicle and spacecraft and evaluate their performance. The motivation is to validate thermal protection system (TPS) margins and potentially reduced TPS mass for future flights to increase payload. The two major sources of TPS heating are: (a) the base heat shield (BHS) convective / radiative heating and (b) after body convective heating due to PIFS.

The Saturn-V first stage utilized kerosene fuel and liquid oxygen for combustion and showed a visible plume. However, the first integrated mission of the SLS with NASA's Orion spacecraft will burn liquid hydrogen and liquid oxygen, resulting in an invisible flame to the human eye. Therefore, remote infrared measurements of the base heat shield on the core of the SLS booster rocket becomes important. Computational Fluid Dynamics (CFD) model predictions and high-fidelity subscale shock tube ground tests have been conducted and indicate that simulation of the complex flow field to produce accurate surface heating remains a challenge. In addition, full-scale static firings have been uncertain in how representative these predictions and ground measurements will be to actual flight conditions. Consequently, the SLS TPS incorporates larger than necessary design margins required to protect critical avionics and ultimately ensure crew safety. SCIFLI aims to obtain in-flight temperature measurements remotely to mitigate risk and optimize the TPS design. In order to acquire these measurements, the SAMI instrument was developed. SAMI is an imaging payload that measures different wavebands of lights (visible – MWIR) using a filter wheel assembly in order to obtain scientific imagery for launches and re-entry missions. Currently, SAMI is an airborne asset flown on a WB-57 aircraft flying at high altitude to provide reduced atmospheric attenuation and emissions compared to imaging at lower altitudes [90].

The SAMI filter wheels hold several (typically ~5) single-notch optical filters and rotate between each filter to take a spectral measurement. However, the wheel offers only discrete transmission windows and has limitations to the frequency of the measurements at each wavelength and to the aperture to the camera. By rotating between filters, a multispectral image can be formed, and key data (such as object temperature) can be indirectly measured. For the SAMI system, the filter passbands are 200-300 nm wide, operate (discontinuously) across the mid-infrared, and have total transmittances of 85-90%. The SAMI mechanical

filter wheels are bulky – the exemplar filter wheel weighs ~800 g and comprises a volume of ~725 cm<sup>3</sup>. This volume is problematic and inefficient for airborne, gimbal-based, and satellite platforms, where use of space is crucial, and becomes prohibitive in a CubeSat form-factor. The small number of filters held by the filter wheel inherently limits the spectral resolution of the measurement system; the resolution is defined by the number of filters. This reduces the overall amount of data that can be taken by the system and limits the accuracy. As an example of this, for standoff temperature measurements the spectral measurement resolution is used to compute the emission curve of an object to discern its temperature – fewer spectral measurements directly translate to a greater uncertainty in the object temperature, especially when emissivity is unknown. Additionally, the switching speed for filter wheel assemblies is on the order of 10s of milliseconds [1], which is much too slow to capture important transient temperature phenomena such as those that occur in exhaust plumes of launch vehicles, or in hypersonic flight. The combination of low spectral resolution and low temporal resolution result in a measurement system that is incredibly volume-inefficient – a large volume is used to generate relatively small amount of useful data.

P-ACTIVE can obtain high quality, real-time spectroscopic image data of high-temperature objects (e.g., the space launch system) in a relevant environment, with increased accuracy compared to filter wheel systems. P-ACTIVE will accomplish this in a low-SWaP form factor suitable for compact mission platforms. P-ACTIVE is intended to be readily integrated with a variety of thermal imaging or thermal imaging spectroscopy missions with improved spectral resolution, speed, and blackbody temperature measurement accuracy. Such systems are used in spaceflight diagnostics and (potential) planetary surface mapping, both of which are critical to the Space Technology Mission Directorate (STMD) by creating a disruptive advancement in measurement technologies – generating more reliable spectroscopic data while simultaneously freeing up asset payloads.

## Scientifically Calibrated In-Flight Imagery



### SAMI: The SCIFLI Airborne Multispectral Imager

Apollo Saturn V	Artemis-1 Program
<p><b>Apollo Saturn V</b></p> <p>Plume induced flow separation (PIFS)</p> <p>Kerosene + LOX</p> <ul style="list-style-type: none"> <li>• Plume in VIS spectrum</li> <li>• No temperature data</li> </ul>	<p><b>Artemis-1 Program</b></p> <p>Imaging payload installed gimbal on NASA WB-57</p> <p>SLS Core Stage Base Heat Region</p> <p>Hydrogen + LOX = H<sub>2</sub>O</p> <ul style="list-style-type: none"> <li>• Plume in MWIR spectrum</li> <li>• Temperature retrieval possible</li> </ul> <p>Base Heat Shield</p> <p>Thermal Protection System</p>

**Fig. 3-3.** The SCIFLI team at NASA Langley Research Center requires an ultrafast tunable filter for remote IR (thermal) measurements of the base heat shield of the booster rocket core stage, for use during an observation of the Space Launch System. The accurate temperature images use to validate Thermal Protection System (TPS) and potentially reduce required TPS mass for future flight. The state-of-the-art thermal imaging system employs a high-speed filter wheel to make spectral measurements. However, such

filter wheels offer only discrete transmission windows and has number of filter limitations that can be accommodated. Finally, the project needs Actively Tunable Filter- such as probing more than a single wavelength and operating across wide wavelength bands from MHz ~ GHz tuning speed to increase temperature measurement accuracy.

## 2.2. Advancing SAMI through P-ACTIVE technologies

There are several advancements that P-ACTIVE can impart to the SAMI architecture. These are addressed in this section.

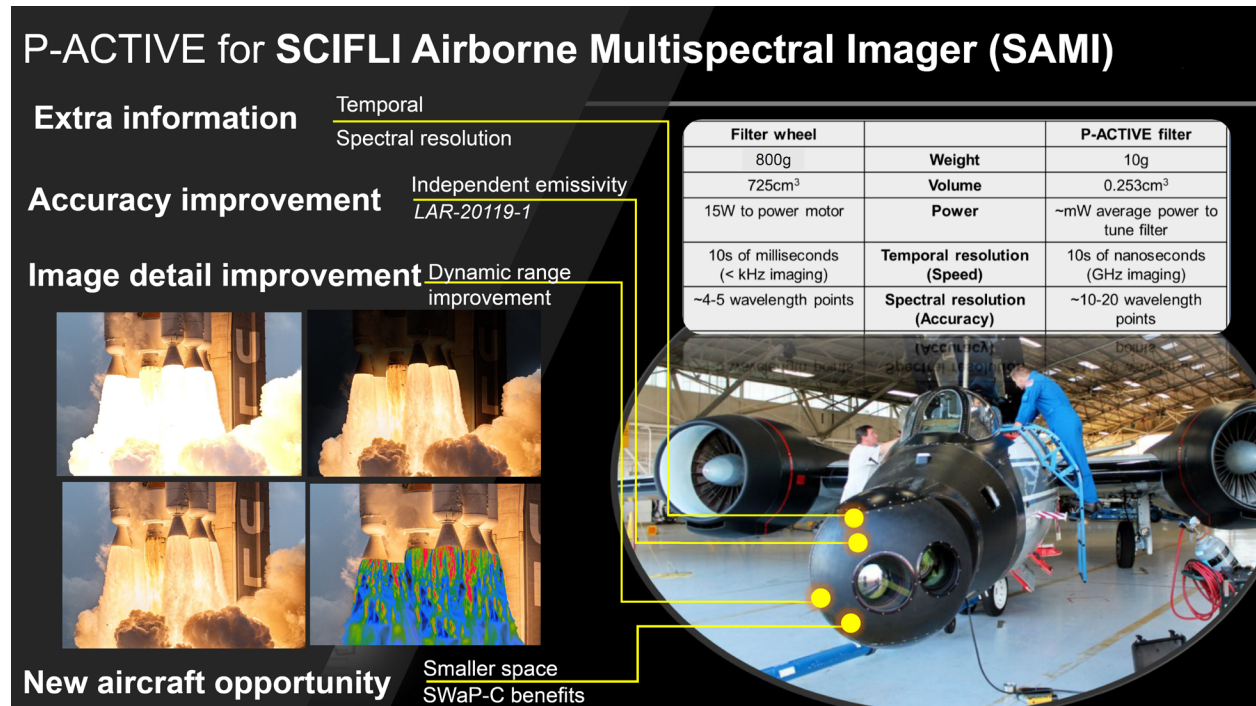


**Fig. 3-4.** Advancing SAMI image quality and payload options from P-ACTIVE technology. The P-ACTIVE system is intended to be readily integrated in a variety of thermal imaging or thermal imaging spectroscopy missions to improve upon existing spectroscopic measurement accuracy. P-ACTIVE can generate more reliable spectroscopic data while simultaneously freeing up asset payloads.

Temporal / Spectral resolution enhancements: P-ACTIVE offers significant advantages in terms of data collection. In the case of temperature measurements, a tunable filter system comprised of a single sensor that takes 10 distinct spectral measurements via active tuning would be ~2x as accurate as a 5-slot filter wheel (due to 2x as many spectral measurements). Additionally, P-ACTIVE can be tuned on nanosecond timescales—orders of magnitude faster than the relevant timescales of temperature drift in most measurements—enabling real-time imaging spectroscopy with high data throughput. Such transient effects cannot be captured by current filter wheel technologies, which switch at speeds  $10^3$ – $10^6$ x slower than a tunable filter system. Combining these increases in spectral and temporal resolution results in an order-of-magnitude increase in the total number of data points that can be collected using a P-ACTIVE system. Of course, the filter can also be tuned slowly if temporal variations occur on longer timescales.

Blackbody accuracy and imaging detail enhancements: By using P-ACTIVE technology, high quality thermal images (accuracy and details) of the SLS can be achieved by eliminating the emissivity uncertainty problem (from the center wavelength tuning filter) and expanding the dynamic range (from full-width-half-maximum / FWHM tuning filter) of the images [91].

By incorporating a PCM-based filter with variable CWL and Q into a conventional quantum-based infrared imaging system, the system can be operated as a tunable, multi-wavelength pyrometer with imaging capabilities. Through careful tuning of the filter's CWL and Q factor, accurate temperature measurements can be obtained beyond the ability of currently available conventional IR imaging cameras and multiwavelength ratio pyrometers. For an accurate temperature measurement using a two-wavelength, ratio technique, the assumption is that the emissivity ( $\epsilon$ ) at the sampled wavelengths  $[\lambda_1, \lambda_2]$  remains constant  $[\epsilon_{\lambda_1} = \epsilon_{\lambda_2}]$ . If that is the case, the ratioed emittance values  $[\epsilon_{\lambda_2}/\epsilon_{\lambda_1}] = 1$ , and will have no effect on the measured radiance. Emissivity is a function of temperature and wavelength, and the ability to dynamically vary  $\lambda_1, \lambda_2$  gives the system greater flexibility over conventional pyrometric systems in the case where  $[\epsilon_{\lambda_1} \neq \epsilon_{\lambda_2}]$ , allowing alternate wavelengths to be selected which satisfy the constant emissivity requirement. Additionally, a PCM optic isn't limited to transitioning between only two wavelengths corresponding to its fully crystalline/fully amorphous states. The CWL can be tuned to any number (n) of intermediate wavelengths,  $\lambda_1, \lambda_2, \lambda_3, \dots, \lambda_n$  that exist between the fully crystalline/fully amorphous states, with the number of possible states limited only by the resolution of the phase-change power supplied by the switching electronics. This degree of instant tunability isn't possible with current pyrometric systems that rely on conventional, fixed CWL/Q factor optical components to make their measurements.

The P-ACTIVE-based imaging pyrometer will be able to limit the radiation flux by changing the PCM filter Q factor. Varying the filter Q factor behaves like a solid-state adjustable aperture, effectively increasing/decreasing the radiant energy on the sensor and preventing pixel over/under saturation. In Fig. 3-5 can be seen an illustration of a typical algorithm that would be used in an imaging pyrometer to adjust the PCM filter CWL, Q factor for optimal pixel signal levels, create an image pair  $[i_{\lambda_2}/i_{\lambda_1}]$  and calculate global temperature. Using the tunability of the PCM filter's Q factor, one can create a composite radiometric image with an extended dynamic range from a series of images that were optimized using different Q factors. It is required to first create a series of image pairs, each taken at different Q factors ( $Q_{min}, Q_{max}$ ) and optimized for regions of the scene with high/low radiance respectively. Fig. 3-5 illustrates how varying the Q factor can increase/decrease the transmitted energy to the detector, thereby enhancing an image for high/low radiosity targets. Combining these optimized images together yields a composite image with an extended dynamic temperature range. This high dynamic range IR (HDRi) image would not be possible by using an image pair taken with a fixed Q factor. An HDRi image algorithm is shown in Fig. 3-5.

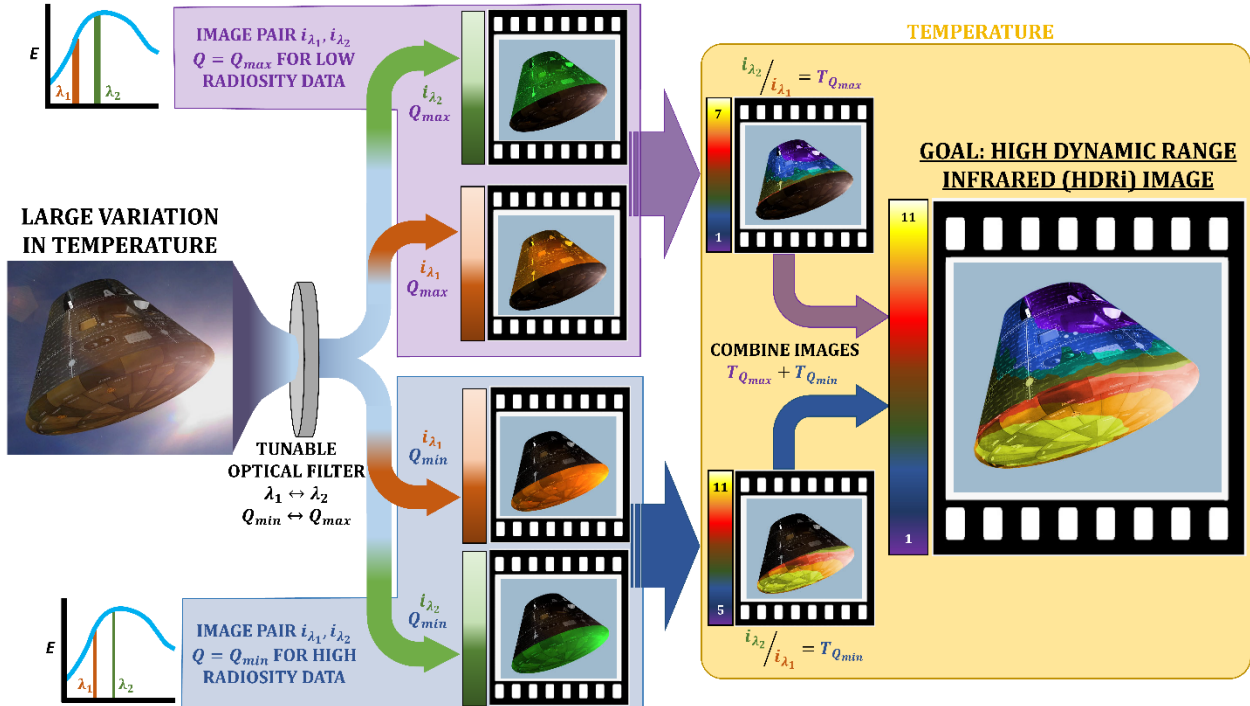


**Fig. 3-5.** Image acquisition algorithm for a High Dynamic Range Infrared (HDRi) image. In this example the final HDRi image is composed of two image pairs, where the filter Qs is optimized to create for partially overlapping temperature ranges. The image pairs are then combined into a single, expanded temperature range HDRi temperature image,

**SWaP benefits:** Because state-of-the-art imaging spectroscopy systems such as SAMI and P-ACTIVE both require a single camera, the required optics and motors dominate the overall system SWaP. In comparison to contemporary filter wheels – which comprise a weight of 0.8 kg and a volume of  $\sim 725 \text{ cm}^3$  – P-ACTIVE filters are 0.5 mm thick, 2.5 cm in diameter, and weigh  $\sim 10 \text{ g}$ . This represents a volume reduction of  $\sim 300\times$  and a weight reduction of  $\sim 80\times$ . The required power supply will, at most, be comparable to the 12V supplies used by filter wheel systems. P-ACTIVE is a single, low-power consumption filter, with no moving parts. The space reduction allows room for other optics, electronics, and even another set of P-ACTIVE components as an emergency platform any case there is a need to switch to an alternate platform during the observation (i.e., malfunction of the original filter). Moreover, the small footprint of P-ACTIVE can reduce the entire SAMI payload size and open other small aircraft including drones to fit the system after critical design and safety reviews.

**Unexpected / extra information achieve from the wavelength flexibility:** These filter wheels hold several A ~5) single-notch optical filters and rotate between each filter to take a spectral measurement. The notch filters wavelength is fixed as selected for targeted science information (i.e.,  $2.9\mu\text{m}$  for  $\text{H}_2\text{O}$ ,  $4.5\mu\text{m}$  for  $\text{CO}_2$  plume gas). With P-ACTIVE it is possible to continuously tune the filter wavelength. This broad / continuous spectral coverage allows unexpected and extra data (i.e.,  $3.5\mu\text{m}$  for  $\text{HCl}$ ,  $4.3 \mu\text{m}$  for  $\text{CO}_2$ ,  $4.8\mu\text{m}$  for  $\text{CO}$ ) that will be useful in providing meaningful science information.

### 3. P-ACTIVE for next-generation astronaut health monitoring

Microgravity environments generate numerous physiological issues [13, 14]. For example, microgravity-adverse effects (illustrated in Fig. 3-6) include body fluid redistribution, muscle atrophy, and bone demineralization [93]. Vital sign monitoring (blood pressure, blood oxygenation etc.) provides limited insight into the astronauts' health status. Typically, biological samples obtained from astronauts are regularly transported to Earth for analysis. Doing so is impractical, costly and can be inaccurate due to the lengthy time between obtaining the sample and analysis on Earth [92]. These problems are further exasperated with long-duration manned missions. Accurate, real-time assessment and monitoring of specific physiological properties and biomarkers is critical for diagnosis, prognosis or therapy for next-generation astronaut health monitoring [93].

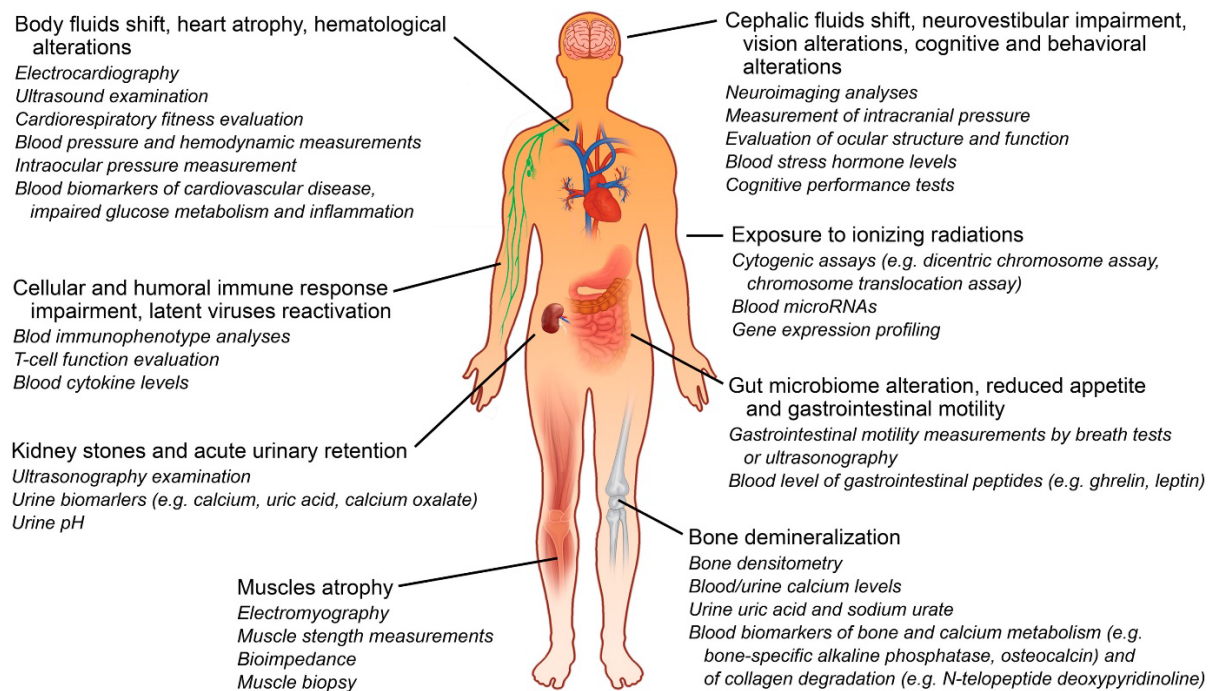


**Fig. 3-6.** Main physiological effects of long-term exposure to microgravity and diagnostic techniques and/or biomarkers suitable for their monitoring. Adapted from [93].

**Nanophotonic biosensing technologies:** Advanced biosensors for monitoring astronaut health during long duration space missions is a rapidly developing area [94]. Biosensors are broadly classified into different categories, depending on the detection mechanism (i.e. optical, electrical, etc.) and whether they're label-based or label-free [93]. Optical approaches have shown tremendous potential in recent years due to offering a highly sensitive, compact and low-cost diagnostic sensing platform. Optical biosensors provide detection of a wide range of analytes. Within biomedicine, this includes toxins, antibodies, viruses and tumor biomarkers; however, there is widely applicability across food quality control, gas sensing and environmental monitoring.

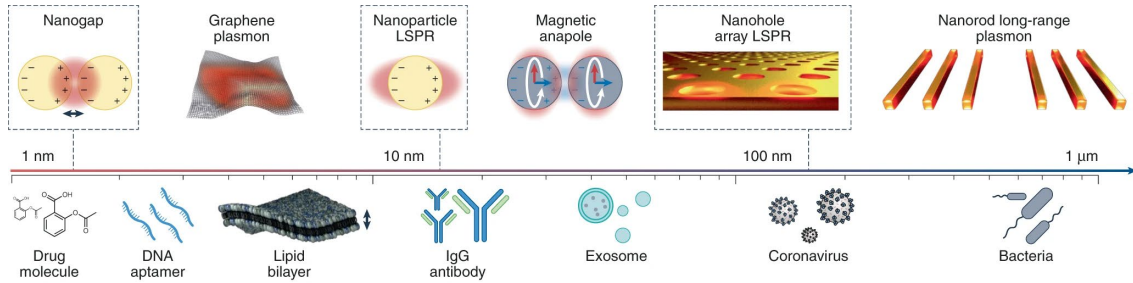


**Fig. 3-7.** Size comparison between common biological analytes and the decay length of the evanescent field in various nanophotonic structures. Adapted from [94].

Nanophotonic biosensors exploit nanoscale light-matter interactions to detect changes in the optical properties of light (wavelength, absorption etc.) due to the interaction between the receptor (antibody, enzymes, proteins, etc.) and the target analyte [16, 17] [Fig. 3-7]. The nanostructures typically utilize evanescent field sensing, localizing fields near the surface of the structure to create small ‘hot spots’ which are highly sensitive to their surroundings / index (i.e., analyte molecules). They are label-free (i.e., a fluorescent or enzymatic tags are not required), adaptable to different target analytes, and their high level of sensitivity means no further amplification step is required. Simultaneous detection of different sensing channels can be enabled through multiplexing different sensing channels (functionalizing different regions) on the same chip using 2D microarrays.

Typically, nanophotonic biosensing is underpinned by *nanoplasmonic* or *silicon photonic* technologies, both shown in Fig. 3-8. The former [Fig. 3-8(a),(b)] utilizes surface plasmon resonances (SPRs) in dielectric-metal (usually gold) structures. Selective binding and capture of target analytes change the surrounding refractive index of the highly sensitive plasmon resonance, thereby shifting the optical properties (wavelength) that are monitored in real-time. Initial designs exploit propagating SPRs on thin-film gold surfaces, but localized SPRs (LSPRs) through 2D nanohole / nanostructure arrays were shown to provide greater levels of field confinement, hence larger signals. Short-lived or ‘weak’ light-matter processes such as fluorescence or Raman scattering can also be enhanced with LSPR-based sensors. For example, the enhancement factor enabled in surface-enhanced Raman spectroscopy can be  $\sim 10^{10}$ .

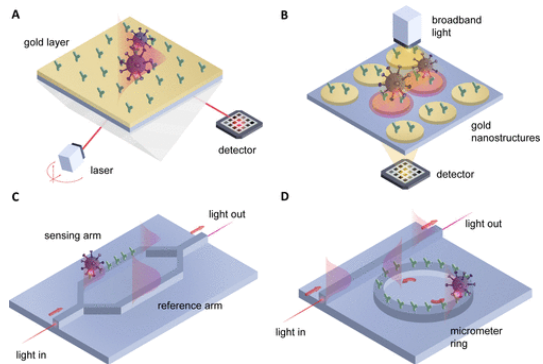


**Fig. 3-8.** Schematic illustrations of the main label-free nanophotonic biosensor technologies: (a) Surface Plasmon Resonance (SPR) biosensor in Kretschmann configuration; (b) Localized Surface Plasmon Resonance (LSPR) biosensor based on gold nanodisks; (c) Mach–Zehnder interferometric (MZI) biosensor; and (d) ring resonator biosensor. Adapted from [16].

used for antigen detection in clinical samples, screening of drug–target protein interactions, detection of cancer proteins, and kinetic analysis of biointeractions [96]. Waveguide-based biosensors (silicon photonic or otherwise) have been used for the study of cellular responses, detection of serum tumor biomarkers, and toxic screening [96].

**P-ACTIVE applicability in biosensing and future outlook:** There is significant effort to create miniaturized, highly sensitive, fast readout and low-cost, label-free optical biosensors for next-generation point of care diagnostics [94]. Moreover, next-generation biosensors require extreme sensitivity (e.g., down to single-to-few molecule concentrations), multiplexed-detection (offering simultaneous detection of different biomarkers / analytes) and reconfigurable functionality (dynamically controlling the light-matter interaction or output optical response) [15, 17]. As such, *active* biosensors based on emerging materials platforms such as 2D materials and PCMs are potentially an exciting route towards enabling the aforementioned desirable characteristics [94]. Further, metasurface based biosensors are also now being developed which utilize light-matter interactions such bound-states-in-the-continuum resonances using high-index nanostructure arrays [94].

PCMs can be integrated in biosensors such that the optical detection mechanism can be enhanced or tuned depending on requirements [15, 19]. For example, tunable biosensors could be developed such that the sensitivity of the device can be tuned electrically or optically through the index modulation of the PCM. A tunable differential response would enable selective detection of higher- and lower-molecular-weight biomolecules [98]. Another example includes tunable refractometric biosensors, commonly applied to glucose or hemoglobin detection and dynamic monitoring. The wavelength shift and detection sensitivity can be tuned through the index modulation of PCMs integrated into nanophotonic structures [99] similar to devices developed through P-ACTIVE. The use of PCMs in integrated photonics for fast phase or intensity modulators is compatible with silicon photonics-based biosensors and would provide a similar tunable differential response along with dynamic sensing regions for multiplexed sensing. Moreover, the integration

of PCM-based active elements in tunable phase-modulators in integrated photonic platforms can further facilitate fast tuning miniaturized spectroscopy for precise detection of biomarkers based on their absorption spectrum.

**Diagnostic spectral imaging technologies:** Early diagnosis and treatment of pathologies in manned space missions is vital—biosensors will play a critical role [93]. Nonetheless, depending on the severity of the pathology, it may be important to visualize specific regions of the body (tissue) for further analysis and do so regularly. For example, if a biomarker associated with a gastrointestinal disease is detected with a biosensor, localization would be needed. Optical imaging provides a non-ionizing, non-invasive and low cost means of characterizing human tissue.

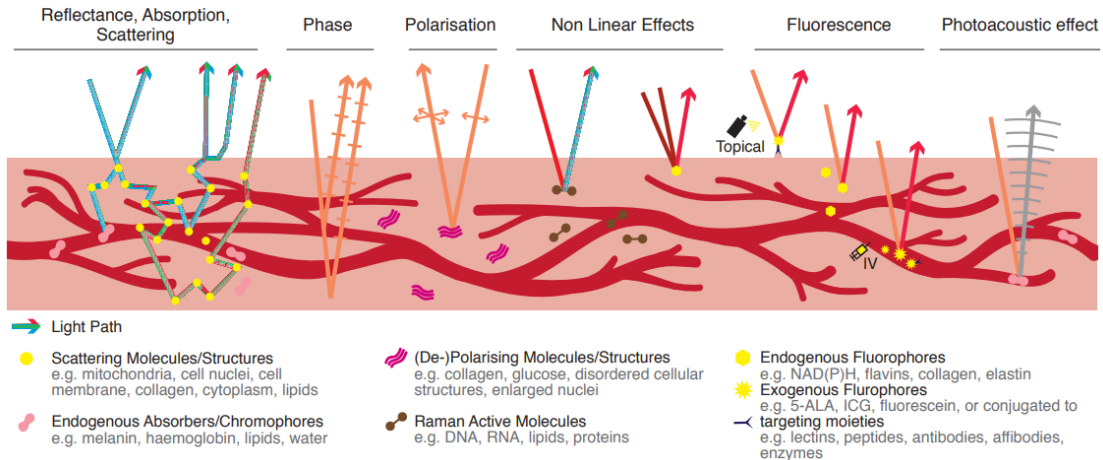


**Fig. 3-9.** Light–tissue interactions. Visible and near-infrared light experiences a wide range of complex interactions with tissue constituents. Optical imaging biomarkers exploit these interactions in clinical applications. Adapted from [100].

Light undergoes a range of complex interactions with tissue [Fig. 3-9]. Vascular, metabolic and microstructural changes in early disease can be revealed by detecting light-tissue interactions such as fluorescence, scattering and de-polarization [21, 22]. However, conventional minimally invasive surgical techniques such as endoscopy, are only designed to detect reflected white light (i.e., broadband red, green and blue), therefore losing the diagnostically relevant information associated with specific light-tissue interactions. This results in poor detection sensitivity and specificity of diseased tissue [21, 22]. Tissue delineation is improved using advanced spectroscopic techniques across the visible to infrared wavebands, such as Raman spectroscopy, multi-and hyperspectral imaging, and fluorescence. Fig. 3-10 illustrates several spectral detection mechanisms [101] and highlights similarities with P-ACTIVE. Spectroscopic imaging exploits endogenous or exogenous contrast mechanisms across the visible-infrared to improve guidance, viability monitoring and disease-detection [101]. Advances in biomedical imaging often align with the advances made in other spectral imaging technologies, such as increasing acquisition speed, miniaturization, higher optical throughput, combining imaging techniques etc.

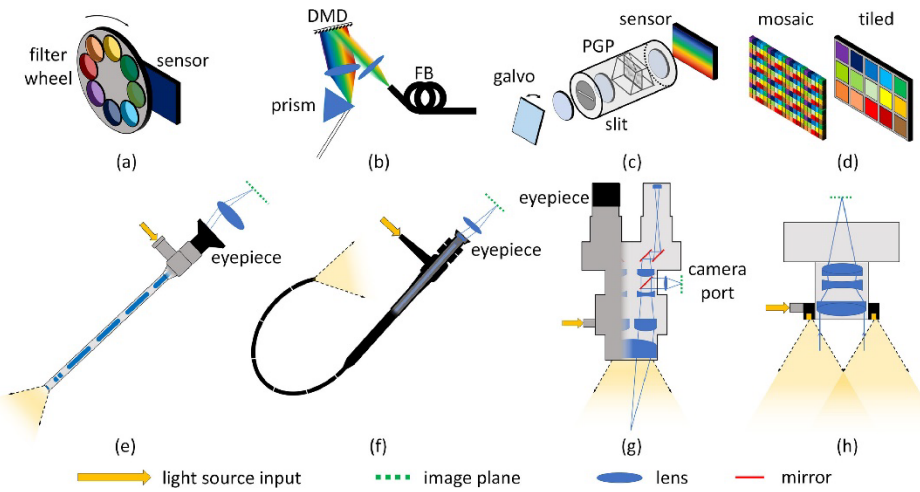


**Fig. 3-10.** Representative selection of spectral detection mechanisms: (a) Spectral scanning using a filter wheel (b) Spectral scanning using tunable light source (c) Spatial scanning with a hyperspectral line sensor. (d) Snapshot sensors with mosaic and tiled filter arrangements. Commonly used clinical imaging devices, excluding chip-on-tip instruments, are shown, with cross-sections illustrating imaging mechanisms: (e) laparoscope, (f) fibrescope, (g) operating microscope with co-axial illumination; (h) externally mounted imager for open surgery. Adapted from [101].

#### 4. P-ACTIVE applicability in biomedical imaging and outlook

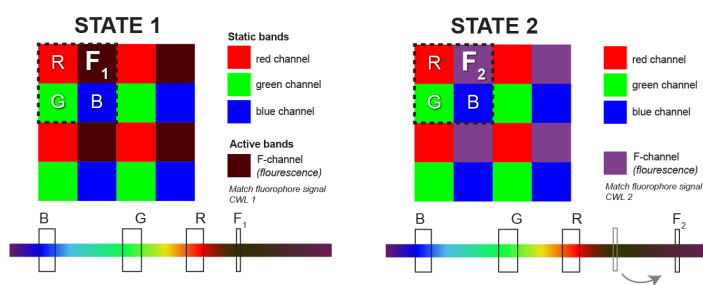


**Fig. 3-11.** Tunable NIR fluorescence channel using pixelated PCM bandpass or edge filter in a multispectral filter array.

Conventionally, multiple imaging systems are needed to visualize different chromophores and/or different optical filter systems (tunable or spatially separated) are required to differentiate between spectrally separated signals. P-ACTIVE can enable tunable optical filters designed to match the absorption / emission spectra of chromophores / fluorophores, thereby providing a means to improve the sensitivity and reduce the weight and size of conventional biomedical optical imaging systems.

Aside from the clear overlap between the goals in the P-ACTIVE project (i.e., replacing filter wheels), two specific fluorescence guided imaging examples are shown in Fig. 3-11 and Fig 3-12:

- *Example 1* [Fig. 3-11]: Ideally in fluorescence-guided imaging, the operator can visualize both white light (red, green, blue) imagery to replicate human vision and detect the NIR fluorescence

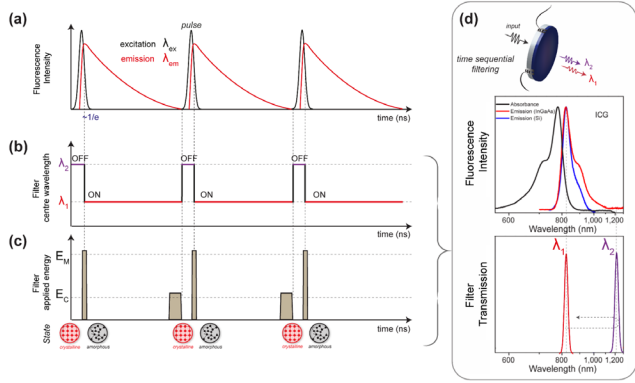


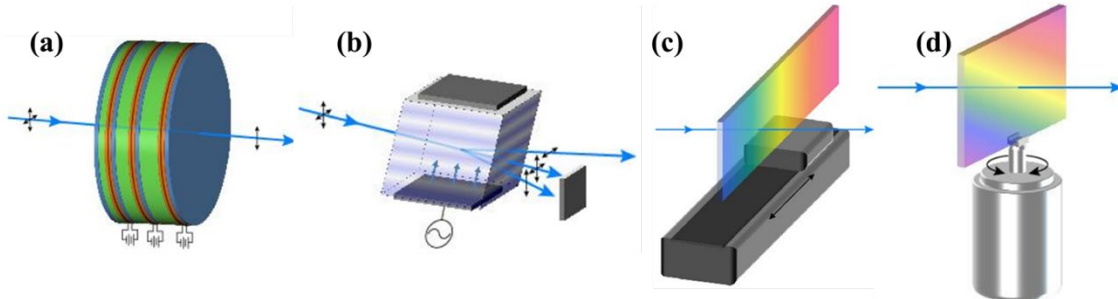
**Fig. 3-12.** Time-gated fluorescence-lifetime imaging optical filter (a) Excitation and emission intensity. (b) The ideal scenario of a tunable optical filter which overlaps with the fluorescence signal. (c) Envisaged operation of the P-ACTIVE filter (d).

- *Example 2* [Fig. 3-12]: Fluorescence-lifetime imaging provides molecular contrast based on the differences in the exponential decay rate of the photon emission of a fluorophore. A time-gated P-ACTIVE optical filter with ultrafast tuning speed (ps-ns) could selectively ‘lock’ onto the signal from a fluorophore and act to boost its signal thereby improving signal-to-noise and enabling the possibility of detecting multiple fluorophores with different output profiles.

from an added dye. This is usually implemented using two separate imaging systems with separate image sensors, optical filters, and co-aligned optical systems. Further, each fluorophore has a unique absorption and emission spectral profile thereby meaning different optical filter sets are required. The envisaged implementation here is a custom multispectral filter array atop a VIS-NIR sensor which has a fast-tuning fluorescence-channel which can be tuned to the unique emission profiles of the target fluorophore. This greatly reduces the total system complexity, offers unique capability of detecting different fluorophores and increases sensitivity.

## Box 2. Where will P-ACTIVE shine most?

Although there have not been any P-ACTIVE systems developed, there are a couple of other niche wavelength filtering technologies: the acousto-optic tunable filter (AOTF) and liquid crystal tunable filter (LCTF) [49], [102]. Both are capable of rapid wavelength selection with microsecond to millisecond tuning speeds while preserving imaging integrity[1]–[4] even with different operating principles [Fig. B-2-1].



(e) Tunable filter	Advantages	Disadvantages
LCTF	<ul style="list-style-type: none"> <li>Wide wavelength tuning range</li> </ul>	<ul style="list-style-type: none"> <li>Volatile (continuous power needs to keep the wavelength)</li> <li>Poor transmission</li> <li>Poor edge steepness</li> <li>Poor out of band blocking</li> <li>Low laser damage threshold</li> <li>Polarization dependent</li> </ul>
AOTF	<ul style="list-style-type: none"> <li>Wide wavelength tuning range</li> <li>High tuning speed</li> <li>Ability to control multiple output simultaneously</li> </ul>	<ul style="list-style-type: none"> <li>Poor compatibility for imaging</li> <li>Complex RF-powered system (costly)</li> <li>Poor edge steepness</li> <li>Poor out of band blocking (typically <math>&lt;10^2</math>)</li> <li>Lack of adjustable bandwidth</li> <li>Polarization dependent</li> </ul>
LVTF	<ul style="list-style-type: none"> <li>High transmission</li> <li>High laser damage threshold</li> <li>Polarization insensitive</li> </ul>	<ul style="list-style-type: none"> <li>Poor edge steepness</li> <li>Slow tuning speed</li> </ul>
P-ACTIVE	<ul style="list-style-type: none"> <li>Non-volatile</li> <li>High tuning speed (<math>\text{ns} \sim \mu\text{s}</math>)</li> <li>Polarization insensitive</li> <li>Wide wavelength tuning range</li> <li>High transmission</li> <li>High out of band blocking</li> <li>Adapt existing fabrication technique (Microelectromechanical systems/ MEMS)</li> <li>Small size and weight</li> </ul>	<ul style="list-style-type: none"> <li>Limited visible wavelength tuning range (material limit)</li> <li><b>Low TRL (Technology readiness levels) and need time to be apply for real-world applications</b></li> </ul>

**Fig. B-2-1**[105]. Diagram of tunable filters capable of transmitting an image-carrying light beam. (a) liquid-crystal tunable filter (LCTF); linear polarizers are blue, fixed birefringent plates are green, and liquid-crystal plates are red. (b) acousto-optic tunable filter (AOTF); an RF voltage applied to an acoustic transducer on the bottom of the crystal generates a volume diffraction grating. (c) linear-variable tunable filter (LVTF); tuning is achieved by translating the filter along its length with a stage. (d) angle-tuned-thin-film; tuning results from a rotation of the filter. (e) competing tunable filter technology and their advantages / disadvantages.

- The LCTF is a birefringent filter which uses the retardation in phase between the ordinary and extraordinary light rays passing through a liquid crystal to create constructive and destructive interference, to pass a single wavelength of light as shown in Fig. B-2-1 (a).  
LCTF technology is useful in niche devices, but it has some limitations: the bandwidth is fixed, the input must be linearly polarized, and for un-polarized light the total throughput efficiency is  $<25\%$ . In addition, the out-of-band extinction is much lower than a monochromator or bandpass filter, and the transmission edge slope is poor. For some illumination applications the low damage threshold can be another limitation.
- An AOTF is a diffraction-based, optical-band-pass filter that can be rapidly tuned to pass various wavelengths of light by varying the frequency of an acoustic wave propagating through an anisotropic crystal medium as shown in Fig. B-2-1 (b) [106].

The main advantage of the AOTF is that it has fast switching time and can control multiple outputs simultaneously. However, it has numerous drawbacks. First, it is a complex RF-powered system that is relatively costly. In addition, this cost increases non-linearly with aperture size. The AOTF has poor-out-of-band performance, and the output angle shifts with wavelength.

- Linear (as well as circular) variable tunable filters (LVTF) are based on the concept of nonuniform thin-film layer thickness variation as a function of position along a linear direction (for linear-variable filters) or around the azimuthal direction of round filter (for circular-variable filters) as shown in Fig. B-2-1 (c). As a results, the spectral properties of the filter, which scale with the layer thickness, vary spatially as well. By varying the location of an optical beam on the filter – either by moving the beam across the filter or moving the filter across the path of the beam, the spectral properties can be changed. LVTFs share some of the advantages of other tunable thin-film filters, such as high transmission, high laser damage threshold and excellent imaging properties. In addition, because light is always incident at or near 0° angle of incidence (AOI), they can be polarization insensitive. The bandwidth can be adjusted arbitrarily for any center wavelength. Significant disadvantages include poorer spectral performance (edge steepness) due to the variation of the spectral properties across a non-zero width optical beam and slow tuning speed due to the need to translate the filters mechanically. Angle-tuned-thin-film filters are a type of motorized wavelength tuning filter which requires moving parts by adjusting the angle of incidence with essentially no change in spectral performance [Fig. B-2-1 (d)]. Inertia limits the speed with which a filter can be rotated by a given amount in each time. Moreover, current devices are limited to visible range tuning[105].

**Table B-2-1.** Advantages and disadvantages of the different approaches described here. The most significantly limiting or advantageous features are highlighted in red and green.

Property	Liquid-crystal	Acousto-optic	Linear-variable	Angle-tuned thin-film
High passband transmission	+	O	+	+
"Top-hat" passband shape	-	-	O	+
Steep spectral edges	+	+	+	+
High out-of-band blocking	+	+	+	+
Constant bandwidth over full wavelength range	-	-	+	O
Adjustable bandwidth	+	+	+	-
Wide tuning range	+	+	+	+
Arbitrary wavelength access	+	+	+	+
Fast tuning speed (random access)	-	+	+	+
Two-dimensional imaging capability	+	-	O	+
Excellent imaging Modulation Transfer Function (MTF)	O	O	+	+
Large aperture	+	+	O	+
Polarization insensitive	+	+	+	+
Wide angular field of view	+	-	-	+
High Laser Damage Threshold (LDT)	+	+	+	+
High environmental durability/reliability	+	+	+	+
Minimal physical thickness	-	-	+	O
Low power consumption	O	+	O	O

There exist several other thin-film and non-thin-film approaches to tunable optical filters capable of selecting a band of wavelengths from a two-dimensional imaging beam, including bulk Sagnac, Mach-Zehnder, and Michelson type interferometers. Interferometers tend to involve large, complex, and expensive instrumentation not suitable

for imaging or remote sensing, and are primarily suited for light source tuning applications involving the modulation of a device's reflective or absorptive properties.[107].

Why is P-ACTIVE unique? One of the benefits of a P-ACTIVE device is the non-volatility, and no continuous input power required to maintain the filter characteristics compared with LCTFs [Fig. B-2-1 (e)]. Their small **Size, Weight, and Power (SWaP)** metrics promise reconfigurable optical systems that are ultracompact, lightweight, energy-efficient, and rugged. Their optically thin, pixelated device architecture further enables fast tuning mechanisms not compatible with conventional bulk optics such as filter wheels. Moreover, such size down-scaling does not come with the usual penalties of compromised optical quality or lack of fine control, thereby setting P-ACTIVE apart from other competing tunable filter technologies relying on liquid materials and mechanically moveable materials. **Space applications** represents an emerging arena where small SWaP and non-volatile characteristics are highly prized. A spectroscopic imaging system will shine the most using P-ACTIVE, especially in space applications.

Tunable filters have widespread potential uses, in areas including (fluorescence) microscopy, spectral imaging, high-throughput spectroscopy. Key applications for tunable filter "systems" are divided into tunable light sources (i.e., sensor or detector modulation, fluorescence microscopy) and spectral imaging system (i.e., environmental monitoring, remote sensing). In fluorescence microscopy and other fluorescence measurements, optical filters are critical to control the spectral of the excitation and emission light. Filters make it possible for the sample to 'see' only light within the absorption bands of the fluorescence with which it is labeled, and the detectors to 'see' only light within the emission bands. Achieving maximum measurements speed, highest sensitivity in low-signal experiments, and the best possible signal-to-noise ratio for the clearest contrast and discrimination all require optimal choices of optical filter spectra, especially when trying to distinguish multiple components labeled with distinct yet overlapping fluorophores. Even the tunable light source approaches require detectors (i.e., a spectrometer for signals or a camera for imaging). Spectral imaging is categorized as scanning-based imaging and wide-field imaging [Fig. B-2-2].

Scanning-based imaging is usually implemented by scanning a collimated or focused laser beam (in the form of a spot or a line) across the specimen [Fig. B-2-2 (a) and (b)]. Compared with wide-field imaging approaches, scanning approaches can provide improved spectral resolution by collecting a highly resolved spectrum at each point or line of pixels on the sample, but at the cost of decreased imaging speed. High spectral resolution enables accurate demultiplexing and quantification of imaging probes. A variety of detectors such as photomultiplier tubes (TMP), and avalanche photodiodes (APD) can be used for the case. Here, wide-field imaging is defined as a method that illuminates a region and detects the emitted light from an array of points (pixels) within the area using a camera (a 2D detector array). Compared with scanning-based imaging methods, it can image a large area with one acquisition [Fig. B-2-2 (c) and (d)]. CCDs and scientific CMOS (sCMOS) sensor arrays are the most widely used detector arrays for wide-field imaging.

The DIAL equivalent to something like in Fig. B-2-2 (a) and the 'laser on/off' is technically on the illumination end while the SCIFLI system would be equivalent to (c). Essentially, if we only need spectral information (i.e., no spatial data), then a small filter element will suffice (i.e., DIAL), but if we need lots of spatial information, then we need a larger aperture or need to scan objects (i.e., SCIFLI).

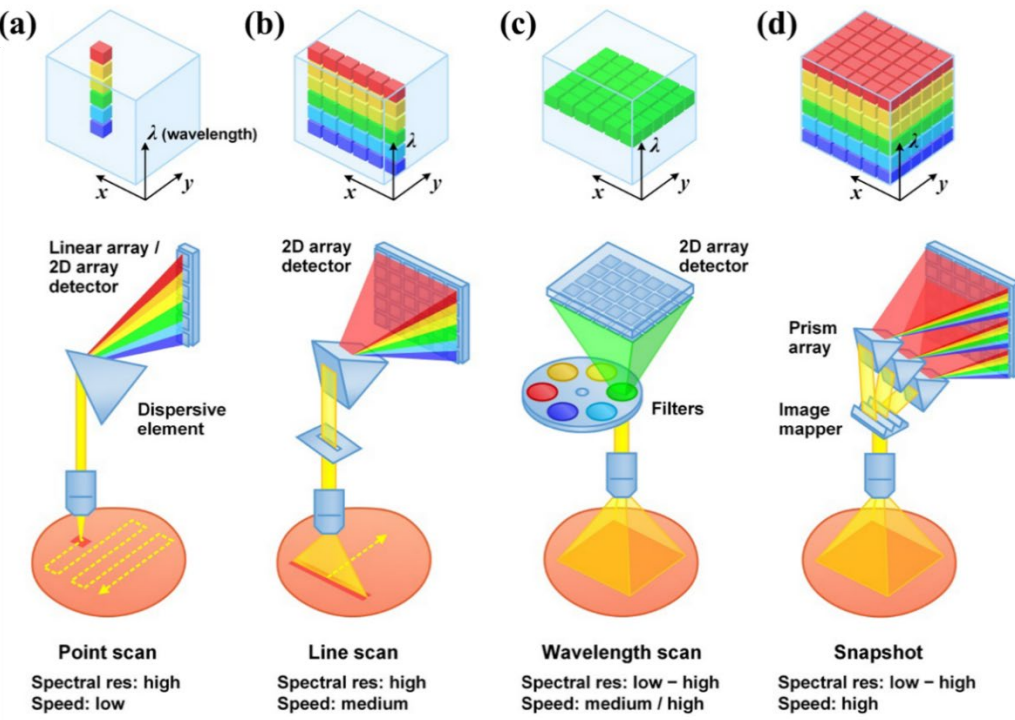


**Fig. B-2-2[108]** Typical spectral imaging approaches (a) point scan, (b) line scan (i.e., ‘pushbroom’), (c) wavelength scan, and (d) snapshot.

The scanning-based approach can achieve a high spectral resolution by using LCTF and AOTF but both are less commonly used for imaging purposes due to the off-axis arrangement, polarization sensitivity, low optical throughput, and large SWaP costs associated with RF driving (for AOTF specifically[109], [110]).

Thus, where will P-ACTIVE shine the most on NASA programs when it is ready to be applied to a real-world system or instrument? To address the question, a Pugh matrix analysis / method-based trade study (ranking the technologies between among performance matrices in terms of most applicable applications) is conducted among a set of selected NASA applications (Table B-2-2).

Based on the decision making, the most accepted technology is the mid-wave infrared (MWIR) multispectral imaging spectroscopy system such as Space Launch System (i.e., SLS) thermal monitoring based on the current / best technology readiness (i.e., material and filter design limitations on visible wavelength for  $386 \sim 1020$  nm wavelengths tuning for SAGE IV [5] and 10 pm +/- 5 pm FWHM bandwidths for DIAL, respectively). A more accurate trade study is ongoing based on an analytic hierarchy process and Kepner-Tregoe with more data and time including technology maturity perspectives. From the technology maturity perspective, liquid crystal (LC) and MEMS based filters are among the most established candidates. Both technologies make use of proven industry-standard technologies to introduce active tuning capabilities and can also take advantage of an established industrial ecosystem to facilitate high-volume device manufacturing and packaging. However, P-ACTIVE has outstanding advantages compare to SOA technologies, and main technologies for the filter have been demonstrated up to TRL 2-3. Continuing an approximately 3-year effort will advance the technology to TRL 4-5 with industry partnership on filter integration atop the sensor, accurately aligned within the housing, etc. P-ACTIVE based systems will obtain high quality, real-time spectroscopic image data of objects (i.e., space launch system thermal monitoring) in a relevant environment, with increased accuracy compared to other filters including wheel systems, LCTF, and AOTF. Moreover, to select the most acceptable technology compared to current ready-to-use COTS filters, the P-ACTIVE TRL level needs to be matured to update the tradeoff decision criteria to include accurate power budgets, aperture sizes, laser damage thresholds, and environmental durability and reliability for trade studies in the near future [Table B-2-2].

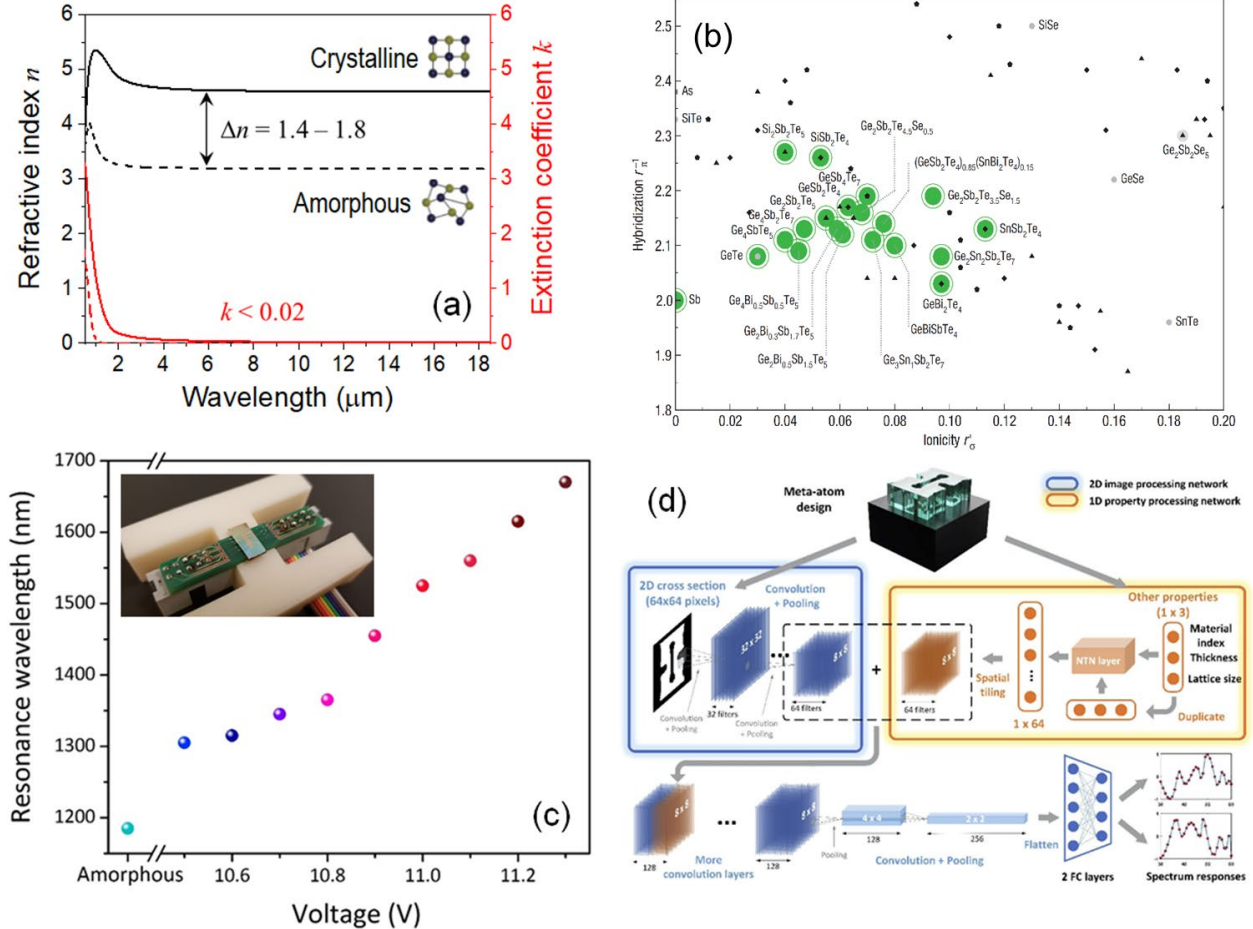
**Table B-2-2** Pugh matrix method-based trade study of the P-ACTIVE among three NASA projects (SAGE IV and SCIFLI, the wavelength scan imaging and DIAL, the point scan image).

Decision criteria	SAGE IV 	DIAL 	SCIFLI 
Non-volatile	S (Same)	S	S
Tuning speed (GHz)	S	+ +	+
Tuning range (800nm ~ 10μm)	- 	S	S
Multiple wavelength tuning	+ +	S	+
10 <sup>7</sup> tuning cycles	S	S	S
Max. 1nm FWHM	S	- 	S
Space qualification (MISSSE)	+ +	+ +	S
Sum of (+)	2	2	2
Sum of (-)	1	1	0
Sum of (Same)	4	4	5
Most acceptable mission			(highlighted)
<b>Further criteria to consider aperture size, laser damage threshold, environmental durability / reliability, etc.</b>			

Because of its unique properties, P-ACTIVE can support commercial crew programs such as Blue Origin, Boeing, and Space-X for vehicle health monitoring. Continuously tunable metaoptics have wide imaging and sensing applications for hypersonic air-breathing propulsion vehicles—from probing molecular vibrations in chemical species to detecting radiant thermal signatures. Radiometric components are the basis of hypersonic flight health monitoring. Further, important measurements can be obtained on large-area heat shields for boundary layer transition studies and on engine plumes for pollution monitoring.

## PART IV: Forward-looking vision of P-ACTIVE

### 1. R&D strategies for PCM selection, SWaP, and more



PCM Selections: The large refractive index difference between the amorphous and crystalline phases of chalcogenide PCMs exemplified by GST-225 is one of the most striking properties of these materials [114]. In most other materials, for instance Si, re-arrangement of the same set of atoms does not produce a pronounced change of electronic polarizability. Thus, the refractive index of Si (in spectral regions away from the band gap where absorption loss is low) only has a weak dependence on the material's crystalline state, yielding a small index change  $\Delta n$  of the order of 0.1 upon amorphous-crystalline transition. Therefore, the enormous index contrast characteristic of PCMs implies a fundamental modification of PCM's electronic structure accompanying the phase transformation.

To explain this phenomenon, it was postulated that the interatomic bonding type switches from the classical covalent bonding in the amorphous phase, to 'resonant bonding' in the crystalline state [7, 8]. In the amorphous state, the valence electrons are tightly localized between the atomic pairs forming the covalent bond. In contrast, in the crystalline state, the 'resonant bonding' is conducive to electron delocalization, giving rise to significantly enhanced electron polarizability and hence a much higher refractive index. First-principle calculations [9–11] and extended X-ray fine structure (EXAFS) measurements [12–14] further corroborated the presence of bonding configuration change during the phase transformation process. The term 'resonant bonding', however, causes unnecessary confusion with interatomic bonding in benzene or graphene formed by delocalized  $\pi$  electrons [123]. A different term, metavalent bonding, is coined to specifically describe the bonds found in crystalline PCMs [16, 17]. The bonding nature is also regarded as unique fingerprints for identification of PCMs [2, 17]. Fig. 4-1(b) [111] gives an example of a map which can be used to identify potential PCM compositions with large optical contrasts based on chemical nature of the constituent elements. Specifically, these PCMs in general exhibit small ionicity and a limited degree of hybridization, where the ionicity and hybridization parameters are defined following Lencer *et al.* [111]. The screening criterion favors compounds comprising heavy non-metallic elements including Te, Sb, Ge, Bi, Sn, etc. Since heavy-element compounds tend to have small band gap energies, this criterion inevitably introduces a trade-off between refractive index contrast and optical opacity when looking for PCMs operating at near-IR or visible wavelength ranges.

Concerning optical loss engineering in PCMs, there are two diverging objectives depending on the specific application needs:

- Applications including optical data storage, reflective free-space optical devices, and on/off optical switches benefit from maximizing the absorption *contrast* between the two phases. In optical analog computing and photonic memory devices, optical absorption is used to encode numerical values, and therefore a large absorption *contrast* is likewise favorable [126], [127]. These applications thus require PCMs with low loss in the amorphous state, and high absorption in the crystalline state.
- In contrast, for other use cases such as programmable photonic circuits and active transmissive optics like P-ACTIVE, low losses in *both* phases are desirable to realize phase-only modulation [20, 21].

Optical absorption in PCMs exemplified by GST-225 is dominated by band-to-band transition in the short wavelength domain for both phases, and free carrier absorption at the long wavelength end for the crystalline phase. The band gap of PCMs is most conveniently tuned by modifying the stoichiometry or

elemental substitution. One example of band gap change in the  $(\text{GeTe})_x(\text{Sb}_2\text{Te}_3)_y$  pseudobinary system with different stoichiometries has been reported [130]. The increase of the crystalline phase band gap with higher GeTe fraction is ascribed to augmented Peierls-like distortion, which opens up the band gap and at the same time leads to carrier localization. The carrier localization effect also tends to weaken the metavalent bonding character in the crystalline PCM phase, which implies a trade-off between increasing band gap and attaining large refractive index contrast. The trade-off similarly exists for elemental substitution. Substitution with lighter elements, for example Te by S or Se [23–31], enlarges the material band gap. However, the lighter elements increase ionicity of bonds when combined with other non-metallic PCM constituents, and thus according to Fig. 4-1 diminishes the metavalent bonding contribution and refractive index contrast.

Examining free carrier absorption (FCA), the main loss contributor in the mid- and long-wave infrared, it is found that crystalline Ge-Sb-Te PCMs are degenerate p-type semiconductors with high concentrations of holes which are responsible for the FCA. The high concentration of holes, often on the order of  $10^{20} \text{ cm}^{-3}$ , stems from large amounts of excess vacancies present in PCM structures [32–34]. Here the term ‘excess vacancies’ is used to distinguish these self-doping defects from their stoichiometric counterparts, since the stoichiometric vacancies are inherent to the crystalline structure of cubic (rock salt) Ge-Sb-Te compounds, where Te atoms occupy one set of the face-centered cubic sublattices while Ge, Sb, and stoichiometric vacancies occupying the other [35–37]. First-principle calculations reveal that the formation energy of these non-stoichiometric defects, in particular Ge vacancies, is small [33, 38]. As a result, the concentration of excess vacancies can reach the order of  $10^{20} \text{ cm}^{-3}$  when PCM crystals are formed from a melt-quench process, leading to degenerate p-type conduction. The high free carrier concentration of crystalline PCMs in the Ge-Sb-Te family produces Drude-like FCA with an absorption coefficient scaling quadratically with wavelength. The ensuing large absorption contrast at long wavelength regimes empowers applications in the mid- and far-infrared such as adaptive thermal camouflage and infrared beam shaping [39–41].

The free carrier absorption can be tuned by either modulating the free carrier concentration through PCM composition tuning and/or engineering the free carrier mobility. As an example of how the free carrier concentration varies with PCM composition, the  $\text{Ge}_3\text{Sb}_2\text{Te}_6$  yields the lowest free carrier density in the  $(\text{GeTe})_x(\text{Sb}_2\text{Te}_3)_y$  pseudobinary system, which translates to minimal FCA in the infrared [130]. In general PCM compositions with large band gaps also tend to manifest small free carrier density.

Engineering the carrier mobility represents another technique to regulate FCA in crystalline PCMs. Crystalline chalcogenide PCMs typically exhibit hole mobility in the range of  $0.1 - 10 \text{ cm}^2/\text{V}\cdot\text{s}$  [23, 42]. Within this low mobility regime, FCA approximately scales linearly with carrier mobility. A practical method to tailor the carrier mobility in PCMs and thereby FCA is to leverage disorder-induced carrier localization. For instance, substitution of Te with Se in  $\text{Ge}_2\text{Sb}_2\text{Se}_x\text{Te}_{5-x}$  alloys has been found to lower the hole mobility by more than two orders of magnitude, and carrier localization due to mixed sequences of Se/Te atomic planes has been suggested as a possible mechanism for the mobility depression [131]. Carrier mobility in crystalline PCMs can also be modulated simply by heat treatment without compositional change. For instance, cubic GST-225 formed at lower annealing temperatures holds large amounts of randomly distributed vacancies. This structural disorder triggers Anderson localization of holes which suppresses their mobility. With further heat treatment, vacancy ordering takes place and carrier mobility rises because of delocalization. The mobility dependence on heat treatment temperature of GST-225 has

been validated with direct field effect measurement [150], showing an order of magnitude mobility change within a 40 °C annealing temperature window.

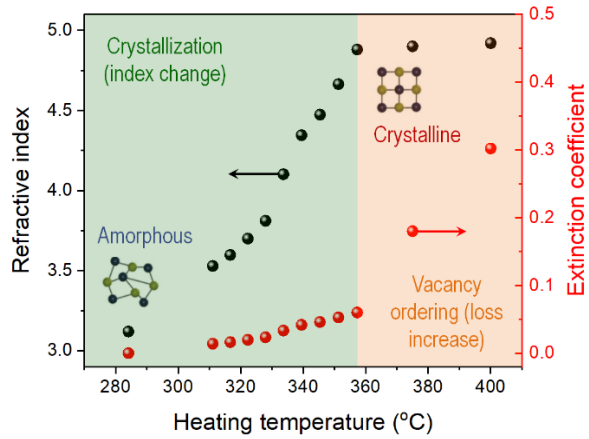


**Fig. 4-2.** Optical constants of  $\text{Ge}_2\text{Sb}_2\text{Se}_4\text{Te}_1$  as functions of transient heat treatment condition

The ability to tune carrier mobility and hence optical absorption in PCMs via heat treatment offers a facile route for controlling both their index of refraction  $n$  and absorption  $k$ . This capability is illustrated in Fig. 4-2 [151], which presents the measured evolution of  $n$  and  $k$  for thin film  $\text{Ge}_2\text{Sb}_2\text{Se}_4\text{Te}_1$  at 2  $\mu\text{m}$  wavelength after transient heat processing using an on-chip resistive heater [152]. The optical property evolution can be divided into two separate regimes. At temperatures below 350 °C, the refractive index steadily grows with rising annealing temperature with only a minor increase in optical absorption. This is attributed to progressive crystallization of the material, and the data points within the intermediate temperature range correspond to mixtures of amorphous and crystalline phases. Beyond 350 °C, the refractive index increase is minimal, signaling that the crystallization transformation is mostly complete. Meanwhile, the absorption becomes much more pronounced presumably due to vacancy ordering in the PCM. The result indicates a powerful method to *independently* tune the refractive index and absorption of PCMs, a coveted capability for many active photonics applications (*Note: more information appears in the ‘2.2 Visible and SWIR range PCMs’ section under the R&D challenges below*).

Finally, PCM-net is introduced (<http://nekocloud.com/pnet/>): an online database of the complex refractive indices of a variety of chalcogenide PCMs. PCM-net is for both in terms of accurate representation of experimentally derived material properties in different phase states, and standardization of results and indexed repository for data sharing across the research community. For the database, refractive indices ( $n$ ) and extinction coefficients ( $k$ ) between amorphous and crystalline states are (a) directly extracted from experimentally derived data (graph plots, supplementary datasets, etc.) in numerous academic research articles, (b) collected from experiments directly, (c) submitted by research contributors (crowdsourcing), and computationally generated (simulated). Table 4-1 shows the summarized pros and cons of each data collection method [114].

**Table 4-1. Pros and cons of data collection methods for material characteristics**

Approach	Pros	Cons	Potential solutions
<i>From experiments</i>	Original source of data Control on generation of data types	Might need processing and error corrections Highly dependent on experimental apparatus and methods	Development of data quality checking methods needed
<i>Data extraction from papers</i>	Availability of quality data Software tools available for extracting data from chart plots	Time-consuming manual work and data cleaning still needed for the tools	Potential for paper repositories to provide chart plot datasets (metadata) bundled with the paper document file
<i>Crowdsourcing</i>	Potential for obtaining a large number of contributed datasets	Data submission system needs implementation Validation or quality assurance of submitted data are required	Development of data quality checking methods needed Making data submission template in spreadsheet format can serve as a starting step for the development of the data submission system
<i>Simulation</i>	Capable of generating diverse datasets with control on the data types	Simulated data might show different characteristics than the real-world data depending on the simulation configurations	

The refractive index database of PCMs from PCM-net is beneficial for P-ACTIVE modelling, in which both knowledge of waveband-appropriate PCM to use and its subsequent accurate index values are required. PCM-net collates and provides dataset plots of this information and Figure 4-3(a) shows the waveband-appropriate PCMs based on a minimal extinction coefficient consideration and the large figure of merit. A large figure of merit ( $\Delta n/\Delta k$ ) and low extinction coefficient ( $\Delta k \approx 0$ ) between amorphous and crystalline phases are critical for identifying the most appropriate PCM for the waveband, and application, of interest. One or multiple PCMs can be selected for P-ACTIVE modelling depending on the targeted wavelength (or waveband). PCM-net is leveraged in the design and simulation of several tunable devices utilized in multiple NASA program scenarios, which all have varying, but stringent, performance requirements. At present, these missions, which are utilizing PCM-net, are: DIAL (Differential Absorption Lidar) science missions, the SAGE (Stratospheric Aerosol and Gas Experiment) mission, and SCIFLI (Scientifically Calibrated In-Flight Imagery) program; highlighted in Figure 4-4(b) and discussed in Part 3.

As each device (i.e., SAMI for MWIR thermal imaging and SAGE for VIS-NIR atmospheric monitoring) requires optimization of specific performance metrics dependent on their respective application, any inaccuracies will lead to erroneous outcomes. We anticipate that the coordinated research efforts enabled by PCM-net will promote repositories with a goal to select the most appropriate PCM for targeted real-world applications using P-ACTIVE and more. The examples include reflective displays (similar to electronic papers) [45–49], self-holding optical switches used for signal routing (e.g. in data centers [158] or wavelength division multiplexing networks [159]), reconfigurable optics such as zoom or autofocus lenses [52–54], programmable photonic circuits [55–60], optical limiters [169], smart glazing [170], and certain adaptive optical systems.

In summary, over twenty PCM datasets have been made available in the database and the plan is to grow this database with community collaboration over forthcoming years. The final goal is to build a PCM-based filter library. Designing reconfigurable optics based on active PCM-based metasurfaces is presented with a unique challenge, as optical quality of the devices must be optimized at multiple optical states. The traditional parameter sweeping approach is highly inadequate. To optimize the actively tunable filter design, active and advanced design processes are needed. The toolbox is the active platform as agile framework for tailored tunable optical devices design for diverse applications including space and science at NASA, biomedical area, optics, and other industry (*Note: More detailed about the toolbox is located end of this section in ‘Appendix B’*).

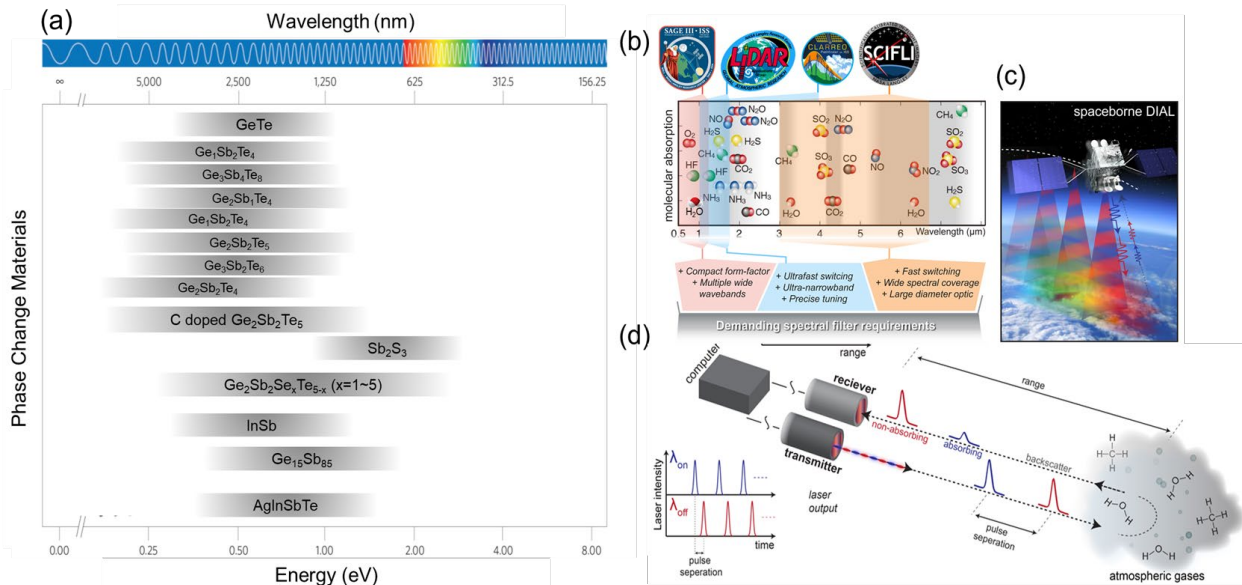


**Fig. 4-3.** (a) Plot of suitable wavebands for different PCMs based on extinction coefficient consideration and figure of merit. (b) Phase-change tunable optical filters for NASA applications based on targeted (operational) wavelength (the molecular absorption image has been adapted from Hamamatsu, <https://www.hamamatsu.com/us/en/support/inquiry/index.html>, and edited by authors). (c) SmallSat-based Differential Absorption LIDAR (DIAL) concept and (d) operating schematic based on the P-ACTIVE.

Machine learning-based filter design: Design of P-ACTIVE furnishing many optical states (from precisely controlling the fraction of crystallization and thereby tuning the refractive index quasi-continuously)

becomes extremely inefficient with the conventional parameter sweep design method. The challenge is further exacerbated since optical cross-coupling between the subwavelength pitch meta-atoms (i.e., nano-sizes hole array for PNA filter) becomes a sensitive function of the varying structural states. Deep neural network (DNN) approaches have been successfully developed for the design of passive or static (also known as freeform) metasurfaces with large geometric degrees of freedom [4, 63, 64]. For the P-ACTIVE project, one can explore emergent deep learning approach to enable strongly-coupled active filter design.

To achieve the objective, two types of deep neural networks are developed: (1) a ‘forward’ predicting neural network (PNN) and (2) an ‘inverse’ design network based on a generative adversarial network (GAN) architecture. Both of these NNs can account for practical fabrication constraints, allowing one to probe not only the fundamental limits of performance, but also what can realistically be fabricated. The PNN takes a PCM-based active meta-atom design and its neighboring meta-atom configuration as the input and predicts the complete electromagnetic responses across different structural states of the PCM while accounting for mutual coupling between meta-atoms. The PNN provides a computationally facile means to evaluate metasurface designs without resorting to brute-force full-wave simulations and is therefore indispensable for efficient training of the inverse design network. The inverse design network, on the contrary, starts from a set of user-defined electromagnetic responses as the target, and generates designs (including both meta-atom structure and local neighbor arrangements) which reproduce the target responses at different PCM structural states. Given its capability to rapidly predict arbitrary metasurfaces’ responses across different PCM states, the proposed PNN is especially powerful when used in conjunction with a deep-learning based inverse design network. The inverse design network is based on a GAN architecture composed of a generator and a discriminator, as shown in Fig. 4-4.

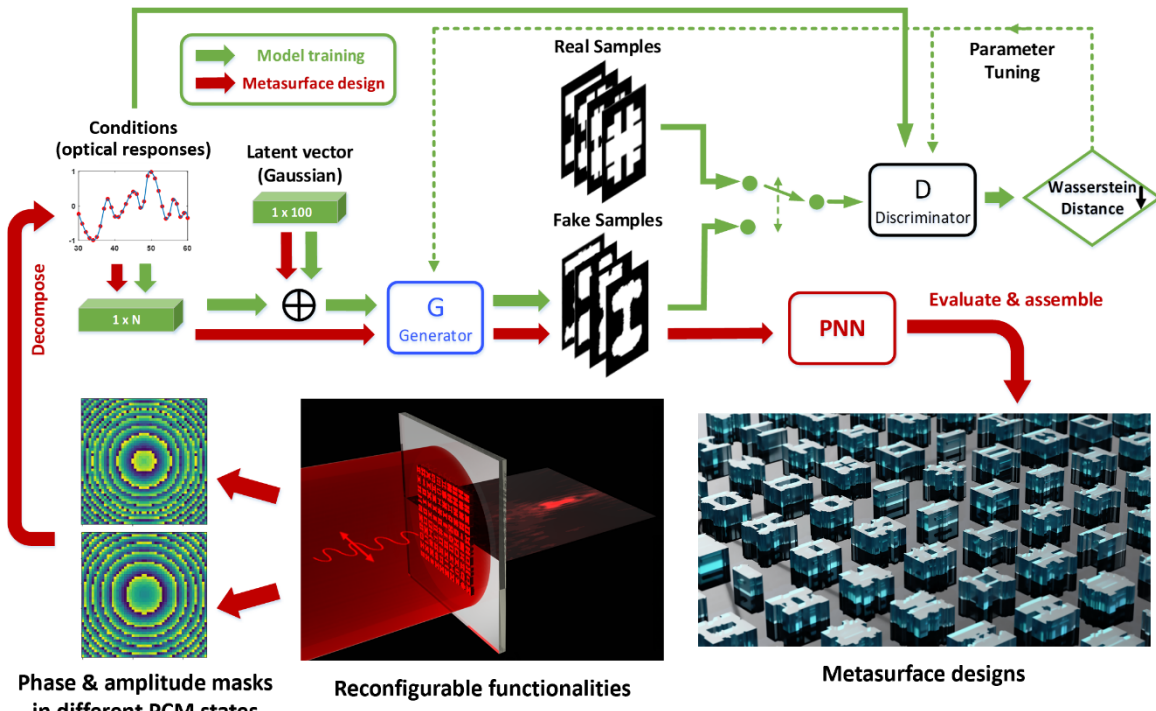


**Fig. 4-4.** Architecture of the P-ACTIVE (and general PCM-based active metasurface) design framework

During training of the GAN, the parameter optimizations for the generator and the discriminator are processed in turns, aiming for opposite objectives. The generator  $G$  is trained to produce samples that cannot be distinguished by the discriminator, while the discriminator is trained to detect generated samples as fake. After the network is fully trained, the generator takes the design targets (e.g., reconfigurable phase masks) as the input and generates a set of meta-atoms configurations. To ensure that the generated meta-atoms meet the design targets, the PNN is integrated with the GAN network to provide a quick assessment of the performance. As shown in Fig. 4-4, it will function as a critic in this integrated network to eliminate the unqualified designs produced by the GAN. During this design process, both the inverse design network (GAN) and the forward predicting network (PNN) are functioning on a one-time calculation basis, which significantly speeds up the whole design process. The ‘adversarial’ characteristic of the network empowers the proposed network with the capability to *‘learn and compose’*, which is the key for achieving non-intuitive metasurface design with complex functionalities.

As a proof-of-concept, Fig. 4-5 also presents preliminary designs of a PCM meta-atom targeting 0 to  $2\pi$  optical phase modulation. The design offers continuous phase tuning across the  $2\pi$  range when the PCM is progressively switched from the amorphous state to the crystalline state, while maintaining high optical transmittance  $> 70\%$ .

Moreover, as addressed in Part II (P-ACTIVE R&D), a design (accomplished via DNN) has been developed for complex photonic structures involving embedded phase-change material metasurfaces inside a multilayer cavity and metasurface as a hybrid filter. The DNN has applied this methodology to the generation of tunable mid-wave infrared bandpass filters, enabling computationally efficient and yet accurate inverse design of such structures.

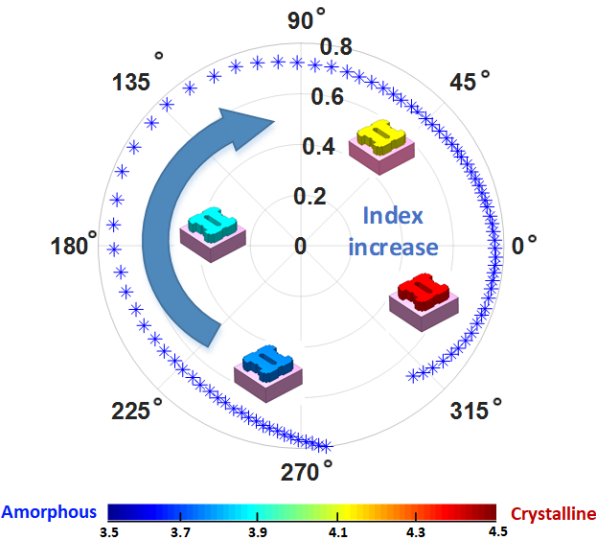


**Fig. 4-5.** Free-form PCM meta-atoms via the deep learning scheme for full  $2\pi$  ( $360^\circ$ ) phase tuning

Electrode heater for active tuning of P-ACTIVE: Researcher collaborators at MIT have demonstrated fully-electrical tuning of similar PCM- based metasurfaces for optical applications such as switchable mirrors and reflection filters [44]. They have also recently developed a novel transparent heater/electrode design based on doped Si, wherein the electrodes and heaters are one in the same and offer broadband transparency

in the infrared, making them an ideal platform for infrared filter applications [113]. To create a larger electrical pixelated switch (bigger than the beam of 1.3 cm for SAGE-IV and camera detector of 2.5 cm for SCIFLI projects with optical uniformity) with a low power budget, Si diode integration to prevent sneak-path current and scalable electrical packaging is considered as well.

## 2. R&D challenges

Despite the explosive progress and strategies developed since 2018, several technological gaps still loom for real-world applications. Three critical areas are examined in this section where more R&D efforts are mandated before the application prospects portrayed in Part III ('NASA Mission / Program scenarios based on science rationale') can be fulfilled .

Understanding the performance of materials under extreme conditions sets bounds to where and how they can be used and informs the range of system engineering that may be needed to enable their use in applications. Similarly, space missions necessarily come with extremely challenging and wholly inflexible performance metrics to ensure mission success. Understanding the capabilities of devices comprised of such materials with respect to inflexible mission metrics is equally important. There are key technical challenges that must be addressed before PCMs can make an impact on photonic applications in space. These are addressed individually below.

Importance of Reliability: The reliability (cycle lifetime or endurance) of P-ACTIVE (and PCM-based reconfigurable optics in general) remains to be validated or improve [172]. In electronic memory, PCM endurance and failure mechanisms have been extensively characterized and have indicated an endurance value of over  $2 \times 10^{12}$  cycles. However, these studies have been solely focused on electronic PCMs (and related properties). There is still significant effort required to fully validate optical PCM longevity (e.g. GeSbTe and GeSbSeTe) [173]. Reproducible PCM optical device properties are important throughout the mission period and its importance to practical applications cannot be over-emphasized.

As is evident from Tables 4-2 and 4-3, the endurance of many reconfigurable metasurface technologies is still lagging application demands. Even for those labeled with 'very large' endurance, their reliability under realistic deployment conditions has often not been verified.

*(Note: Exceptions exist where PCMs only need to be switched once or a small number of times throughout their life cycle (e.g. in post-fabrication trimming [174] or transient devices for photonic testing purposes[175]) while being able to switch PCMs reversibly and reproducibly over many cycles is an essential attribute for most of their applications[173].)*

Taking the Stratospheric Aerosol and Gas Experiment (SAGE) as an example, the science observation events are a maximum length of 6 minutes, and the filter will be switched 5 times per second during the event. Normal low earth orbits are approximately 90 minutes long, and one science observation event will take place per orbit. Approximately  $10^7$  cycles are performed per year on orbit (under space harsh environment) based on the estimation [49]. Addressing the reliability challenge warrants scrupulous characterization of degradation kinetics in application-relevant environments through material investigations to elucidate the pertinent failure mechanisms and judicious device designs guided by the

fundamental insights to improve robustness. The MISSE-14 study informed the essential path for P-ACTIVE (and PCM-based reconfigurable optics in general again) to make a lasting impact on space applications. Understanding of failure modes specific to photonic devices and implementation of the presently-used design rules to boost device lifetime will be imperative to facilitating adoption of PCMs in practical applications.

The issue of PCM cycle lifetime or endurance has been extensively investigated in electronic phase change memory devices. There are two failure modes: Set-stuck failure (SSF) and Reset-stuck failure (RSF, also called open failure) [70, 71]. The former refers to phase change memory cells being stuck in the SET (high electrical conductance) state, and RSF is the opposite case where the cell becomes effectively open-circuit. The specific failure mechanisms that have been identified include [178] (1) phase segregation induced by electromigration and incongruent melting which is mainly responsible for SSF [73–75], (2) void formation at the PCM-electrical contact interface due to electromigration and cyclic stress which accounts for RSF [75–77], (3) interdiffusion between PCM and adjacent materials [78, 79], and (4) surface oxidation when the PCM is not suitably encapsulated [186].

The failure mechanisms witnessed in electronic memories are nonetheless not necessarily relevant to photonic applications given the different switching mechanisms employed. In photonics, it is customary that a PCM volume considerably larger than that in today's deeply scaled electronic memory cells must be switched. An important implication of the large PCM volume is that the material cannot be properly switched by directly passing an electric current through PCM as it is done in memory cells due to the filamentation effect [43, 81]. A thin wire of PCM that initially crystallizes becomes an electrical current conduit with significantly higher conductivity than the surrounding amorphous matrix, preventing uniform crystallization of the entire PCM volume. Since the size of a filament is orders of magnitude smaller than the wavelength, the modulation of optical properties is negligible. For this reason, PCMs are usually optically switched via laser pulses [188] or electrothermally switched using micro-heaters in photonics applications. The absence of an electric field in both optical and electrothermal switching schemes means that electromigration – perhaps the most prominent cause of failure in electronic memories – is not relevant to PCM-based photonic devices. This leaves incongruent melting, cyclic stress, interdiffusion and surface oxidation as possible failure mechanisms in photonic devices. Additionally, we note that interdiffusion and surface oxidation can be effectively prevented by selecting appropriate encapsulation materials for PCMs.

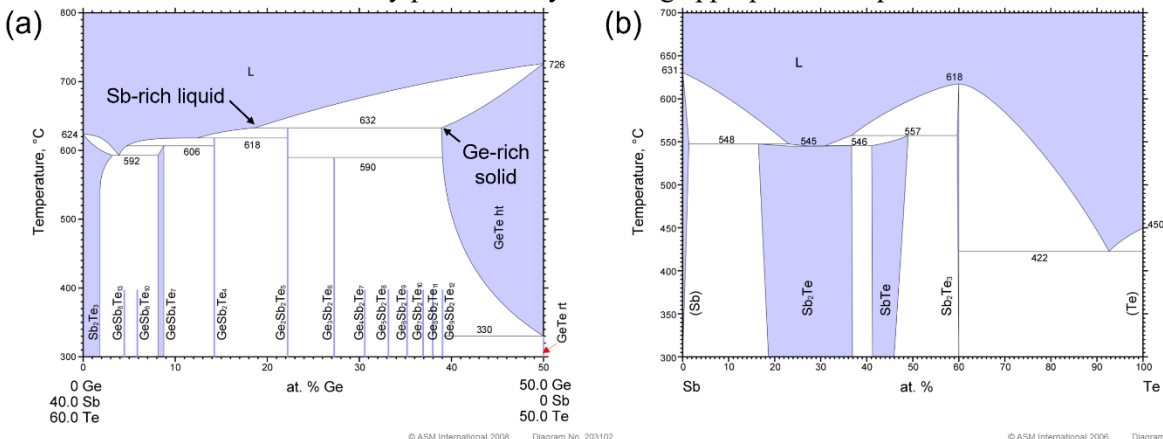


**Fig. 4-6.** (a) Pseudobinary GeTe-Sb<sub>2</sub>Te<sub>3</sub> phase diagram; (b) Sb-Te binary phase diagram. Images courtesy of ASM International.

The origin of incongruent melting is revealed by examining the phase diagram of the GeTe-Sb<sub>2</sub>Te<sub>3</sub> pseudobinary system [Fig. 4-6(a)]. During heating and cooling cycles, Ge<sub>2</sub>Sb<sub>2</sub>Te<sub>5</sub> passes through a two-phase region between 632 °C (solidus temperature) and 648 °C (liquidus temperature). Within this region, Ge<sub>2</sub>Sb<sub>2</sub>Te<sub>5</sub> can spontaneously separate into two phases, a Sb-rich liquid phase and a Ge-rich solid phase. When a temperature gradient is present, the phase separation can lead to directional solidification and elemental segregation[189]. A possible way to mitigate incongruent melting is to ensure that the entire PCM volume is heated to above the liquidus temperature during re-amorphization with adequate dwelling time such that any Ge-rich solid phase formed can be dissolved into the liquid phase in every cycle. Indeed, it has been found that melting can ‘heal’ elemental segregation in phase change memory cells [183]. Minimizing temperature non-uniformity in the re-amorphization process is also critical against incongruent melting, as it prevents directional solidification and also ensures that the entire PCM can be uniformly heated to avoid both regions below liquidus temperature and hot spots that can damage the PCM. This can be accomplished by shaping the beam profile in laser switching, and geometric optimization of micro-heaters in electrothermal switching [152]. Another solution is to use alternative PCM compositions that remain single-phase during thermal cycling. For example, the Sb-Te phase diagram [Fig. 4-6(b)] suggests two compositions fulfilling the single-phase criterion: Sb<sub>2</sub>Te<sub>3</sub> and Sb<sub>7</sub>Te<sub>3</sub> [190].

Cyclic stress originates from both thermal stress and the large volume change of PCMs during phase transition (6.5% between amorphous and crystalline phases of GST-225). Cyclic stress has been associated with void formation in PCMs even in the absence of an electric field [191]. The voids, driven by electromigration [192], eventually coalesce at the PCM-electrode interface, resulting in an open circuit aka RSF [182]. The impact of cyclic stress on longevity of PCM-based photonic devices, however, has not been systematically studied. Unlike in electronic memories, it is anticipated that the voids likely only have a minor effect on optical properties of PCMs given their small size (~ 10 nm). Moreover, since PCM is not part of the current path, it may be possible to heal the voids in a cyclic laser or electrothermal switching process [181], which would not be interrupted by open-circuit failure as in memory cells. On the other hand, cyclic stress could degrade structural integrity of photonic devices, especially considering that the PCM volume being switched is much larger for most photonic applications. The stress effect can be mitigated through selection of PCM compositions with a small volume change between phases [76, 87]. On the contrary, PCM compositions with large volume change during crystallization, for instance GeTe which shows ~ 10% contraction upon crystallization [193], are known to generate severe mechanical damage during cyclic switching.

From the analysis above, it appears that there is no fundamental limit to realizing PCM-based photonic devices with cycle lifetime comparable or even exceeding state-of-the-art in phase change memories. Indeed, cycle lifetime exceeding  $1.5 \times 10^8$  has been reported in electrothermally switched devices made of Sb<sub>7</sub>Te<sub>3</sub> [88, 89] – notably a PCM stoichiometry meeting the single-phase condition we set forth above. From a practical perspective, the much larger PCM switching volume in photonic devices could introduce elevated temperature non-uniformity, which should be mitigated through beam profile shaping in laser switching, and heater design optimization in electrothermal switching [152].

Table 4-2. Summary of active metasurface technologies<sup>a</sup>

Type	Material or mechanism	Refractive index tuning range	Optical absorption	Endurance (cycling lifetime)	Failure mechanism limiting cycling lifetime	3-dB bandwidth or 10-90 rise/fall time <sup>b</sup>	Speed limiting factor	Volatility	Foundry manufacturing compatibility	Potential challenges	Relevant industry ecosystem
Mechanical	Displacement	-	None <sup>c</sup>	Very large	Mechanical failure	~ 1 Hz	Speed of mechanical motion	-	Compatible	Integration challenge	-
	Elastic deformation	-	None <sup>c</sup>	15,000[196]	Material fatigue or interface delamination	~ 1 Hz	Speed of mechanical motion	-	-	Reproducibility and stability	-
	MEMS actuation	-	None <sup>c</sup>	> 10 <sup>9</sup> [197]	Material fatigue; stiction; delamination; wear	1 MHz[197]	Resonant frequencies of mechanical eigenmodes	Design-dependent	Compatible	High voltage	MEMS
Free carrier density modulation (electrical injection)	Semiconductors (junction biasing)	0.08[198] <sup>d</sup>	Free carrier absorption (FCA)	Very large[199] <sup>e</sup>	-	0.18 MHz[200]	-	Volatile	Compatible with III-V foundry processes	-	Semiconductor
	TCOs (field gating) <sup>f</sup>	1.39[202] <sup>g</sup>	FCA	Very large	-	10 MHz[203]	Carrier transit time; RC delay	Volatile	Backend processing available in selected foundries	Optical loss; small index change or optical modal overlap with the active region	Display
	2-D materials (field gating)	~ 1[204]	Material absorption	Very large	-	> 1 GHz[205]	-	Volatile (capacitive)	Backend integration currently under development[206]	-	-
Thermo-optic	Semiconductors (thermal free-carrier refraction)	1.5[207] <sup>g</sup>	FCA	Likely large[208] <sup>h</sup>	-	5 kHz[209]	Thermal time constant	Volatile	Compatible if only CMOS materials are used	Optical loss; relatively slow response	Integrated photonics
	Semiconductors or dielectric materials	0.15[210] <sup>i</sup>	Minor FCA due to carrier thermalization	-	-	-	-	-	Relatively slow response; large energy consumption	-	-
Electro-optic	EO polymers	0.11[211] <sup>j</sup>	None <sup>c</sup>	Very large	-	50 MHz[211], [212]	RC delay	Volatile (capacitive)	-	High voltage	-
	EO crystals	0.001[213]	None <sup>c</sup>	Very large	-	95 MHz[214]	RC delay	Volatile (capacitive)	Backend processing available in selected foundries[215], [216]	Small modulation amplitude	Integrated photonics
	Liquid crystals	0.15[217] <sup>k</sup>	None <sup>c</sup>	> 10 <sup>10</sup> <sup>l</sup>	-	350 Hz[218]	Relaxation time of liquid crystal molecules	Volatile (capacitive)	Backend processing and packaging available	Relatively slow response	Display
Phase transition	Semiconductor multi-quantum-well (quantum confined Stark effect)	~ 0.01[219]	Electroabsorption dictated by the Kramers-Kronig relations	Very large	-	< 10 ns[220]	RC delay	Volatile (capacitive)	Compatible with III-V foundry processes	Full 2π phase coverage	III-V optoelectronics
	VO <sub>2</sub>	Up to ~ 0.5 in visible and near-IR[221], [222]	FCA in the metallic state	> 24,000[223] <sup>m</sup>	Defect migration[225]	450 fs / 2 ps[226] †	Kinetics of Mott transition or structural phase transition <sup>n</sup>	Volatile <sup>o</sup>	Backend processing available in selected foundries	Optical loss	-
	Chalcogenide PCMs	3.3 (Ge <sub>2</sub> Sb <sub>2</sub> Te <sub>5</sub> )[114] <sup>p</sup> 1.8 (Ge <sub>2</sub> Sb <sub>2</sub> Se <sub>4</sub> Te)[131] <sup>p</sup>	None[131] <sup>c</sup>	> 5 × 10 <sup>5</sup> [230] <sup>q</sup>	Elemental segregation; cyclic strain	200 ns / 300 ns[194] †	Crystallization speed[151]	Non-volatile <sup>r</sup>	Backend processing available in selected foundries[233], [234]	High voltage	Memory
Electrochemical	Electrochromic polymers	0.7[235] <sup>s</sup>	Electronic absorption at the oxidized state	> 10 <sup>7</sup> [236]	Photochemical degradation[237]	> 25 Hz[236] <sup>t</sup>	Ion transport kinetics in the polymer and electrolyte[239]	Non-volatile	-	Relatively slow response; optical loss	Smart windows
	Ionic conducting oxides (protonation)	0.45 (SmNiO <sub>3</sub> )[240] <sup>p</sup> ~ 0.4 (GdO <sub>x</sub> )[241] <sup>u</sup>	FCA in the metallic state	Several hundred[241] <sup>v</sup>	Dielectric breakdown[241]; defect migration	13 ms[241]	Ion transport kinetics; film thickness	Non-volatile	-	Endurance; relatively slow response	-
	Ionic conducting oxides (lithium intercalation)	~ 0.2 (WO <sub>3</sub> )[243] <sup>u</sup> 0.65 (TiO <sub>2</sub> )[244] <sup>w</sup>	FCA in the metallic state	400[244]	Ion trapping[245]	3 s[246]	Ion transport kinetics; film thickness	Non-volatile	-	Endurance; slow response	Smart windows
Chemical	Metal electrodeposition	-	Absorption of electrodeposited metal	> 200[247] <sup>x</sup>	Metal oxidation	~ 1 Hz[247]	Electrodeposition reaction rate	Non-volatile	-	Integration challenge	-
	Metals (hydrogenation)	~ 4 (Mg)[249] <sup>p</sup>	FCA	3,000[250]	Strain due to volume change; oxidation and hydroxylation	~ 0.1 Hz[251]	Hydrogen diffusion in metal; film thickness[252]	Non-volatile	-	Integration challenge	-
	Cover material addition/removal	~ 0.5[253], [254]	None <sup>c</sup>	> 10[255]	Residue and contamination[256]	Seconds to minutes	Speed of dissolution or removal process	Non-volatile	-	Integration challenge	-
Magnetic	Magnetooptical oxides	~ 0.01[257]	None <sup>c</sup>	Very large	-	5 GHz[258] <sup>y</sup>	Kinetics of magnetic domain wall motion	Both	-	Integration challenge	-
All-optical	Kerr nonlinearity	Light intensity dependent	Nonlinear absorption	Very large	-	40 fs[260]	Ultrafast electronic nonlinearity	Volatile	Compatible if CMOS materials are used	Integration challenge	-
	Free carrier injection	0.14[261]	FCA	Very large	-	~ 100 fs / 20 ps[262] †	Carrier lifetime	Volatile	Compatible if CMOS materials are used	Integration challenge	-

<sup>a</sup> Here we focus on active metasurfaces operating in the optical frequency range, specifically from ultraviolet to long-wave infrared. Only experimental demonstrations are included in the table.<sup>b</sup> In the case of active metasurfaces with asymmetric rise/fall responses (marked with †), both rise and fall time values are reported.<sup>c</sup> Here ‘none’ implies that the optical loss can be negligible throughout the entire active tuning cycle. However, this condition does not necessarily hold for all materials or devices belonging to the category.<sup>d</sup> Refractive index change of Si at 1550 nm wavelength with 10<sup>20</sup>/cm<sup>3</sup> hole concentration<sup>e</sup> Wear-out failure rates of semiconductor modulator devices have been found to be negligible (below 1 Failures in Time, FIT).<sup>f</sup> In addition to TCO, the same field gating configuration can also be applied to modulate carrier concentrations in semiconductor materials to realize optical tuning within their optical transparency window, for example in[201].<sup>g</sup> The refractive index change was amplified by operating near the epsilon-near-zero (ENZ) point.<sup>h</sup> Thermo-optic devices exhibit minimal degradation after 5,000 hours of accelerated aging tests.<sup>i</sup> Index change in a Si metasurface when temperature increases from 300 K to 800 K at 1.1 μm wavelength.<sup>j</sup> Index change quoted at 1500 nm wavelength for an applied electric field varying from -100 to 100 V/μm<sup>k</sup> Refractive index change of E7 liquid crystal (from Merck, formulation commonly used in active metasurfaces) in the near-infrared when transitioning from the nematic to the isotropic phase.<sup>l</sup> While the lifetime of liquid crystal metasurfaces has not been extensively investigated, commercial liquid crystal displays usually specify a lifetime of up to 60,000 hours, which at 60 Hz refresh rate corresponds to > 10<sup>10</sup> switching cycles.<sup>m</sup> Over 6.8 × 10<sup>8</sup> switching cycles have been demonstrated in VO<sub>2</sub>-based RF switches[224].<sup>n</sup> Mott-Hubbard type phase transition induced by optical pumping of carriers exhibits ultrafast transition kinetics down to 26 fs[227]. In contrast, structural phase transition in VO<sub>2</sub> is slower and occurs at a sub-nanosecond time scale or longer[228].<sup>o</sup> VO<sub>2</sub> devices can operate in a nonvolatile mode within a finite temperature range defined by its phase-transition hysteresis[229].<sup>p</sup> Refractive index change at 1550 nm wavelength.<sup>q</sup> Endurance values of over 1.5 × 10<sup>8</sup> and > 2 × 10<sup>12</sup> have been demonstrated in RF switches[194] and electronic phase change memories[231] based on chalcogenide materials, respectively.<sup>r</sup> Volatility of switching phase change materials can be tuned by adjusting pulse parameters[232].<sup>s</sup> Refractive index change at 633 nm wavelength.<sup>t</sup> Switching time down to 100 μs has been observed in polyaniline (PANI)[238].<sup>u</sup> Refractive index change at 400-800 nm wavelengths.<sup>v</sup> In memristive electronic device made of the rare earth nickelate NdNiO<sub>3</sub>, stable performance over 1.6 × 10<sup>6</sup> cycles have been demonstrated[242].<sup>w</sup> Refractive index change at 649 nm wavelength associated with transition from TiO<sub>2</sub> to Li<sub>0.5</sub>TiO<sub>2</sub>.<sup>x</sup> 5,500 reversible electrodeposition cycles of metals have been realized in large-area smart windows[248].<sup>y</sup> Here the magnetic state is controlled by ultrafast optical excitation. Current driven magnetic switching with a 3-dB bandwidth of 6 GHz has been achieved in integrated magneto-optical waveguide modulators at cryogenic temperatures[259].

**Table 4-3. Potential applications of reconfigurable metasurfaces: green-yellow-gray colors indicate decreasing relevance of the metric to the target use case: very important-somewhat important-minimally relevant**

Application	Tuning scheme	Optical tuning parameter (phase/amplitude) <sup>26</sup>	Optical contrast (relevant metrics)	Optical loss suppression	Endurance (cycling lifetime requirement)	Speed (bandwidth requirement)	Power consumption
Tunable filters for multispectral sensing[263]–[265]	Continuous	Amplitude	Extinction ratio		$10^7$ <sup>27</sup>	1 kHz <sup>28</sup>	
Beam steering for LiDAR[266], [267]	Continuous	Both	Full $2\pi$ phase tuning range <sup>29</sup>		$10^9$ <sup>30</sup>	10 Hz	
Light field display[271]–[273]	Continuous	Both	Field-of-view and image contrast		$10^{10}$ <sup>31</sup>	30 Hz <sup>32</sup>	
Computational imaging[274]	Discrete	Phase	Full $2\pi$ phase tuning range		$10^{10}$ <sup>31</sup>	100 Hz <sup>33</sup>	
Analog optical computing (pre-trained weight setting)	Continuous	Both	Full $2\pi$ phase tuning range		$10^3$	1 Hz	Nonvolatile or capacitive
Analog optical computing (adaptive network training)	Continuous	Both	Full $2\pi$ phase tuning range		$10^8$	1 kHz	
Dynamic projection display[275]–[277]	Continuous	Amplitude	Image contrast		$10^{10}$ <sup>31</sup>	30 Hz <sup>32</sup>	
Electronic paper (reflective display)[278]–[280]	Discrete or continuous	Amplitude	Color saturation and image contrast		$10^7$ <sup>34</sup>	1 Hz	Nonvolatile or capacitive
Zoom lens[161]	Discrete or continuous	Phase	Full $2\pi$ phase tuning range		$10^5$ <sup>35</sup>	1 Hz	
Digital signal modulation for free-space communications[211], [281], [282]	Discrete	Either	Modulation contrast		$10^{18}$ <sup>36</sup>	10 GHz	
Adaptive optics[283]	Continuous	Phase	Full $2\pi$ phase tuning range		$10^9$ <sup>37</sup>	100 Hz[284]	
Nonreciprocal optics based on spatiotemporal modulation[285]–[287]	Discrete	Either	Isolation ratio		$10^{18}$ <sup>36</sup>	10 GHz	
Optical limiter[288], [289]	Discrete	Amplitude	Extinction ratio		$10^3$	> 1 GHz	Nonvolatile
Adaptive thermal camouflage[148], [290]	Continuous	Amplitude	Dynamic range		$10^8$ <sup>38</sup>	10 Hz <sup>39</sup>	

<sup>26</sup> Note that amplitude modulation can be implemented with phase modulation via interference effects although the reverse is not true: phase modulation cannot be realized by amplitude modulation alone.

<sup>27</sup> Taking the Stratospheric Aerosol and Gas Experiment as an example, the science observation events are a maximum length of 6 minutes, and the filter will be switched 5 times per second during the event. Normal low earth orbits are approximately 90 minutes long, and one science observation event will take place per orbit. Approximately  $10^7$  cycles are performed per year on orbit based on the estimation.

<sup>28</sup> Specification of high-speed motorized filter wheels (~ 1 ms per filter).

<sup>29</sup> It is possible to realize beam steering (or generally other optical functions as well) with phase coverage well below  $2\pi$  albeit at the expense of optical performance[268]–[270].

<sup>30</sup> Assume 20-year lifetime with 5 hour daily use at 10 Hz frame rate.

<sup>31</sup> Assume 100,000-hour lifetime (comparable to that of state-of-the-art display modules) at 30 Hz frame rate.

<sup>32</sup> National Television Standards Committee (NTSC) video frame rate.

<sup>33</sup> The speed must be higher than the frame rate of single images.

<sup>34</sup> Comparable to the lifetime of E-ink displays.

<sup>35</sup> Typical mechanical lenses are capable of ~ 100,000 cycles.

<sup>36</sup> Assume 5-year lifetime at 10 GHz modulation.

<sup>37</sup> Assume 30,000 hour lifetime at 100 Hz.

<sup>38</sup> Assume 3,000 hour lifetime at 10 Hz.

<sup>39</sup> The speed needs to be at least better than that of low frame rate infrared cameras which is generally specified at 9 Hz.

Visible and SWIR range PCMs: Another materials science challenge is identifying a PCM that can operate efficiently across the visible and near infrared (NIR) wavelengths—which are important for several spectroscopic applications, particularly aerosol remote sensing (i.e., SAGE III-type instrument with center wavelengths of 386nm (Aerosols / Blue-end response), 448nm (Nitrogen dioxide), 452nm (Nitrogen dioxide), 525nm (Aerosols), 600nm (Ozone), and 1020nm (Aerosols / Red-end response)) [80].

For MWIR wavelength, the focus is on using  $\text{Ge}_2\text{Sb}_2\text{Te}_5$  as the PCM given its well-established reversible switching properties, fast ( $< 50\text{ns}$ ) switching speed, and large refractive index contrast at the targeted wavelength (i.e.,  $\Delta n = 3.3$  at 1550nm). Considering the central role of Ge atoms in the coordination change, one can expect that a larger Ge content in GST alloys provides a larger optical contrast. The optical losses in GST, however, precludes its application in shorter wavelength range ( $< 1\mu\text{m}$ ), for instance,  $\text{Ge}_8\text{Sb}_2\text{Te}_{11}$ , with  $\Delta n + \Delta ik \approx -1.48 + i1.35$  and  $\text{Ge}_2\text{Sb}_2\text{Te}_5$  with  $\Delta n + \Delta ik \approx -1.2 + i1.05$  at 405 nm wavelength [20]. Herein,  $\Delta n$  and  $\Delta k$  denotes the real and imaginary parts of refractive index change induced by the phase transition, respectively. Besides GST, a wide variety of PCMs have also been developed to push operation near and into the visible spectrum such as GSST [131],  $\text{Sb}_2\text{Se}_3$  [291], and  $\text{Sb}_2\text{S}_3$  [133]. For instance, GSST reports exceptionally large FOMs, over two orders of magnitude larger than that of classical GST alloys, throughout almost the entire infrared spectrum [14]. Moreover, using  $\text{Sb}_2\text{S}_3$  has a wide bandgap that potentially allows one to scale the operation wavelength down to  $\sim 600\text{nm}$  into the visible regime. This flexibility and material agnosies enable the use of an agile design process wherein designs for many different wavelength regimes can be iterated simultaneously, potentially allowing for this effort to result in multiple devices applicable to different spectral regions of interest. Moreover, the Si-heater platform developed for the active tuning of the P-ACTIVE is completely material-agnostic and will also function as a common vehicle for testing and qualification of different PCMs.

The best effort is to develop a new class of PCMs where the phase transition only triggers refractive index (real-part) modulation with a minimal loss penalty related through the Kramers–Kronig (KK) relations [14]. Decoupling of the two effects is customarily characterized using the material figure-of-merit (FOM), expressed as  $\text{FOM} = \Delta n / \Delta k$ , and FOM quantitatively correlates with the performance of many different classes of photonic devices [292], [293]. Breaking such coupling allows independent control of the phase and amplitude of light waves, a game changer for optical engineers that would open numerous applications [47].

Fundamental understanding of phase change behavior: How can one increase the effective switchable thickness reliably for millions of cycles? The question is simple but the answer is complicated. In PCMs, switching phase between ordered and disordered states requires a solid-liquid phase transformation. The focus of this discussion is primarily on amorphization of PCMs as it is a more complicated process, yet, significantly understudied. It is noted that the temperature dependence of the unique bonding mechanism utilized in crystalline PCMs is not fully understood either [16], [294].

Another question that continues to fascinate material scientists is why the macroscopic properties of the phase can change so dramatically [15], given the relatively subtle changes in atomic positions.

Again, these simple questions play a consequential role in the repeatability and the effectiveness of switching process of P-ACTIVE. In order to design P-ACTIVE elements that meet arbitrary performance specifications and address virtually any mission-driven filter requirement, fundamental understandings of phase change behavior are crucial.

The P-ACTIVE team is working on the effect of enthalpy of melting on solidification of PCMs as part of controlling phase change kinetics. Moreover, microstructures evaluation of P-ACTIVE (uncycled, cycled, and failed) using transmission electron microscope (TEM) is on-going to understand the origins of failure and design the versions of devices with improved thermal engineering (i.e., cross talk, quench rate from heat passivation, and finally low power consumption).

Switching speed and design trade-offs: This section is also related to the previous section of ‘2.3 Fundamental understanding of phase change behavior’ namely the importance of the fundamental understanding of the PCM behavior, especially fast switching speed for targeted application (i.e., SAMI with GHz filter wavelength tuning speed for the in-situ thermal monitoring).

In terms of speed, the bidirectional switching process of PCMs is asymmetric. Speed of the crystallization process is limited by crystallization rate of the PCM and critically depends on the PCM chemistry. Since amorphization must be adequately rapid to kinetically bypass crystallization, amorphization is *necessarily* faster than crystallization in the same device, and thus engineering the switching speed of PCM devices is often synonymous with controlling crystallization kinetics of the PCM. Speed of the amorphization process is only bound by thermal time constant of the PCM component, which is primarily dictated by geometric dimensions of the PCM component and is largely independent of the PCM composition.

To engineer the switching speed of PCMs, it is instructive to revisit the key structural signature that accounts for the rapid nucleation kinetics in GST-225: the presence of crystalline precursors (ABAB rings in the case of GST-225) in the amorphous phase. These precursors not only catalyze the formation of crystalline nuclei, but also hint structural similarity between the amorphous and crystalline phases which lowers the interface energy and barrier to nucleation. In GST-225, the ABAB rings undergo spontaneous formation and dissolution swiftly within a picosecond timescale [295], [296]. This statistical fluctuation underpins the stochastic nature of crystallization in GST-225 and necessity of an incubation period during crystallization cycles to warrant nuclei formation [297]. Stabilization of the precursor structures can thus expedite crystallization kinetics. This concept culminated in the discovery of  $\text{Sc}_{0.2}\text{Sb}_2\text{Te}_3$  (SST), where Sc doping stabilizes the four-fold ring structure and crystalline seeds (atomic clusters consisting of the four-fold rings) against thermal fluctuation [295]. Sub-nanosecond crystallization was realized in SST capitalizing on the abundance of nucleation sites. The same principle can be implemented in the contrary direction to slow down the crystallization kinetics and increase the reversible switching volume of PCMs, a useful trait especially for free-space photonic applications. A case-in-point is AIST, a growth-dominant PCM. Recrystallized AIST has an A7 structure with a broad distribution of atomic ring size [298]. Unlike GST-225 where the four-fold ABAB rings act as crystalline precursors, nucleation in AIST necessarily involves ring reconstruction and bond interchange, which results in sluggish nucleation kinetics. The incubation delay in AIST is on the order of tens of microseconds versus nanoseconds in GST-225 [299].

Finally, it is noted that the growth-dominant crystallization behavior in selected PCMs provides a potential solution to break the speed-thickness trade-off [151]. The concept exploits the very high crystal growth velocity in growth-dominant PCMs exemplified by AIST. Growth rates as high as several m/s have been measured in AIST [300]. As an example, the main PCM element can be connected to a crystalline zone located outside the active switching zone. The zone allows the PCM element to sidestep the nucleation period to achieve fast crystallization. During re-amorphization, the connection between the crystalline zone and the PCM element can be more rapidly quenched to sever the crystal growth path, thereby preventing crystallization in the PCM element due to the slower cooling rate it experiences.

Scalable manufacturing and packaging: The scalable manufacturing and packaging is the last challenge as it is not the biggest concern for the FP multilayer filter but foremost barrier of tunable metasurfaces with sub-microns feature sizes. Their passive counterparts used to encounter the same challenge: in the early phase of development, metasurfaces were almost exclusively prototyped in university cleanrooms using electron beam lithography with painstakingly low throughput. Recent advances have nonetheless circumvented this bottleneck, as fabrication of passive metasurfaces on full glass wafers have been validated via deep ultraviolet lithography in silicon foundries [200, 201] and other high-throughput fabrication methods such as nanoimprint lithography [303] have been implemented as well. Manufacturing of reconfigurable metasurfaces not only stipulates similar requirements on large-area, fine-line lithographic patterning, but is also appreciably more complicated than their passive counterpart. Therefore, commercially viable manufacturing practices of reconfigurable metasurfaces will need to maximally leverage standard semiconductor processing and packaging to manage the escalating fabrication and assembly complexity. The foundry manufacturing process may be complemented with backend integration to introduce new materials and functions, in which case the integration process shall capitalize on a mature industrial ecosystem (as summarized in Table 4-1) to access existing infrastructures, knowledge base, and supply chain to expedite the technology's learning curve.

Scaling the electrically controlled P-ACTIVE marks another technical milestone. This is motivated by the demand for 1.3 cm (diameter) clear aperture which is bigger than the beam size for SAGE-IV. MIT team has recently developed a novel transparent heater/electrode design based on doped Si, wherein the electrodes and heaters are one in the same and offer broadband transparency in the infrared, making them an ideal platform for P-ACTIVE [234]. This practical solution for scaling the electrically tuning of P-ACTIVE could mitigate major challenges of heat passivation, electrical wiring and heat uniformity.

## Appendix B. Phase Change Material Toolbox

A PCM toolbox is introduced as an agile optimization process to synthesize customized and / or tailored tunable optic device with sufficient computational resources of the material, structure, and application database (library) to form a complete application-driven tunable optic device. The toolbox is the active platform as agile framework for tailored tunable optical devices design for diverse applications including space and science at NASA, biomedical area, optics, and other industry. The project will utilize an agile project management framework. Using the agile framework from the effective working design, we will quickly get to a usable prototype and expand its capabilities with each successive development cycle.

The toolbox-based optimization process contains two agile cycles:

(a) small agile cycle: build the filter database (simulation / experiment-based library) based on building phase change material (PCM) database and structure database. Generate various and new designs. The project will utilize an agile project management framework where the concept is to develop the simplest possible useful object and continue to add features/capabilities as the project continues as opposed to a multi-year development building a single object.

(b) big agile cycle: add the application-driven specifications such as polarization insensitivity, environment for the test (temperature / humidity) on the filter options from the small agile cycle.

Using the agile framework, we will quickly get to a usable prototype and expand its capabilities with each successive development cycle.

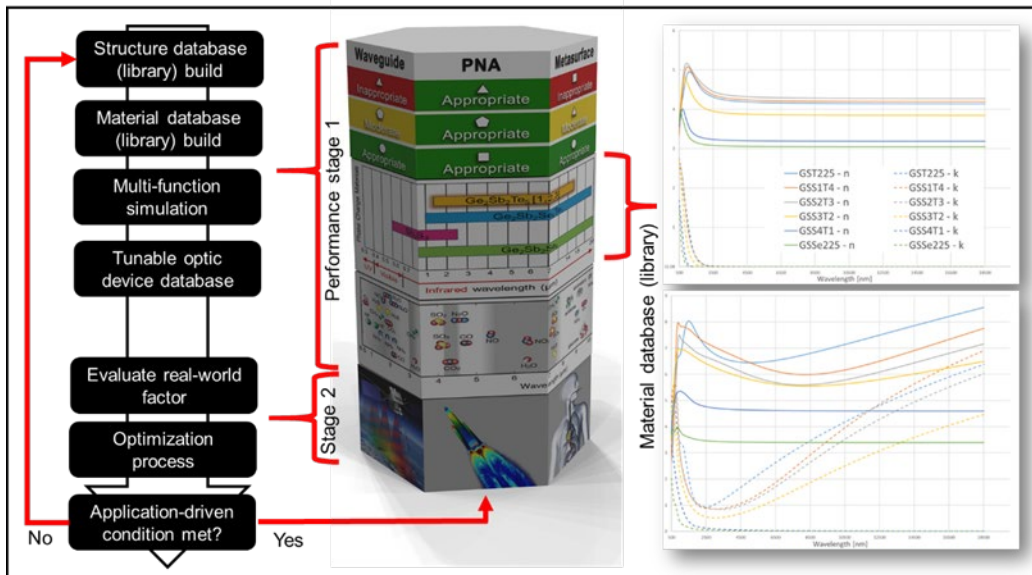


**Fig. B-1.** An overview of Phase Change Material Toolbox: Agile framework for multifunction optic device optimization.

From the (a) and (b) combination multi-objective and global optimization possible, algorithms-based framework with agile (robust) processing. The advantage of this concept is that (1) time saving (2) accuracy (3) customization / tailoring (4) can be applicable to any meta-optic design for every instrument (lidar, imager, spectrometer, etc.) at every possible wavelength (X-ray to millimeter, possibly further), and can

yield a significant size, weight, power and potential cost (SWaP-C) reduction to enable new form factors for the majority of airborne and / or spaceborne instruments.

Toolbox-based agile framework concept: The process begins with the generate both material and structure database (library) which generates an initial set of candidate unit cells to simulate. The next step is to enforce any and all design constrains (e.g., number of layers, thickness of each layer, etc. for FP cavity and refractive index and extinction coefficient of  $\text{Ge}_2\text{Sb}_2\text{Te}_5$  materials depending on wavelength variation) and alter the design structure geometries accordingly. This is the 1<sup>st</sup> stage Mix & Match process as performance evaluation. Next, simulation data (e.g., complex transmission, center wavelength, resolution based on the wavelength) is gathered and generated multi-function filter database. The simulation-based multifunction filter database is used evaluate a set of predetermined (1<sup>st</sup> screen) candidates (optic filter performance functions only) which the optimizer seeks to minimize. The values generated by the ‘only optic performances’ are then used to evaluate 2<sup>nd</sup> stage Mix & Match. The 2<sup>nd</sup> stage performance evaluation is based on other convergence criteria process (e.g., filter survive temperature and humidity, filter operation duration, altitude, platform as vibration tolerance, etc.) for application-driven real-world optimization of filter selection. Finally, data are fed back to the optimizer and the process repeats until the end condition is met. When the process is finished, an optimal set of solutions is generated. It showcases the tradeoffs between the performances achievable at binary states of the phase change material. Finally, this agile framework is used to pick the best candidate of databases for the application-driven filter design.

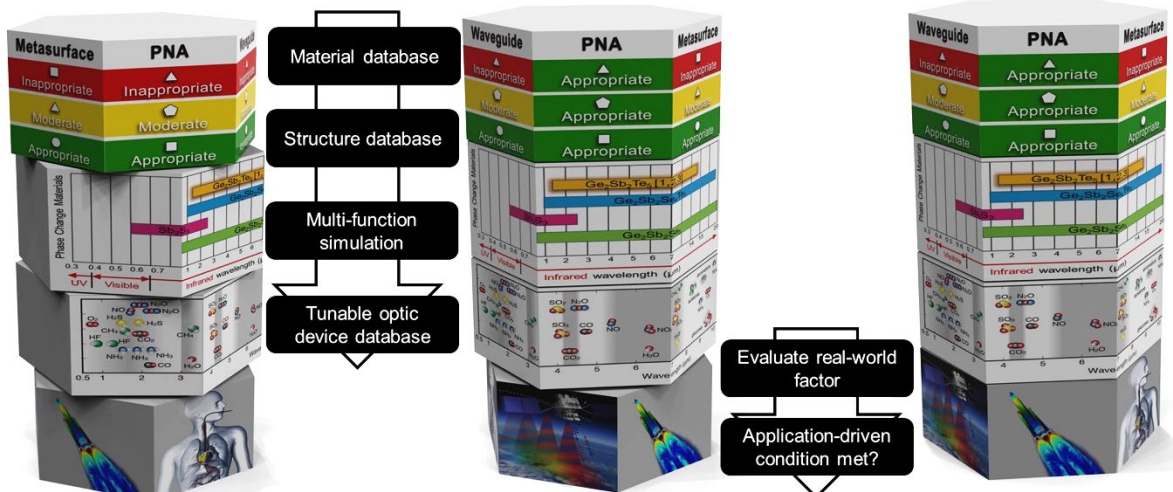


**Fig. B-2.** Toolbox' concept as the tunable spectroscopy technology platform: The bank of phase-change material (PCM) and structure resources that is useful for tailored /customized optical spectroscopy fabrication for targeted application. The ‘toolbox’ wherein nearly any combination of spectral tuning range and device performance metric can be designed for by ‘Mixing & Matching’ PCM composition and device physics.

The optimization framework is general enough to be applied to a tremendous variety of multifunctional and customized metasurface problems.

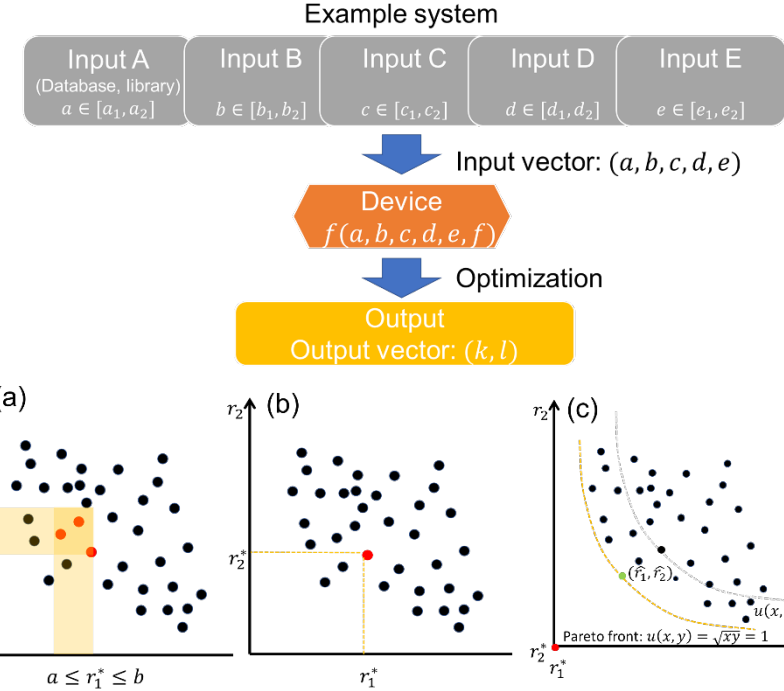


**Fig. B-3.** (a) Reverse mapping to the input values when customer sets a target range: filtering case (b) Reverse mapping to the input values for a single result selected by the customer: filtering case (c) Case where no exact target result exists: optimization needed

Methodology: The toolbox-based agile framework requires optimization techniques to generate desired set of solutions. In this section, computational optimization / filtering methods that can be implemented as a database system are presented.

Conceptual model: As discussed in the previous section, the toolbox-based agile framework involves two-step optimization design: (1) small agile cycle and (2) big agile cycle. Both cycles can be modeled as optimization of a multi-variable system that maps inputs into outputs where  $m$  and  $n$  are integer greater than 1.

$$f: (x_1, x_2, x_3, \dots, x_m) \rightarrow (y_1, y_2, y_3, \dots, y_n) \quad (\text{B.1})$$

The optimization process will be designed as a computational approach since the system might show highly non-linear characteristics. Moreover, the availability of the material and structure database that can generate an initial set of candidate unit cells makes the data-driven computational approach more feasible, with the possible construction of derived large sample sets. While the issue of how to generate / estimate more sample data for the optimization requires further investigation, the availability of data can be an important foundation that a data-based optimization system can be built on.

Fig. B-2 describes a conceptual optimization of a system that maps an input vector of  $(x_1, x_2, x_3)$  to the output result vector of  $(r_1, r_2)$ . The choice of  $m = 3$  and  $n = 2$  is to simplify the mapping and to enable visual plotting of the output results on a 2-dimensional plane for illustrative purposes. From the simulation

and material/structure database, a sample set of mapping from inputs to outputs are associated and the outputs are plotted as dots on the 2-dimensional plane.

A filtering optimization case can be considered where the desired optimal output is  $(r_1^*, r_2^*)$ . When the desired optimal output is specified as a range of  $(r_1^*, r_2^*)$  where  $a \leq r_1^* \leq b$  and  $c \leq r_2^* \leq d$ , three optimal outputs meeting this condition can be found from the plot as the shaded area (Figure B-3(a)) and the associated optimal inputs can also be found by reverse mapping. Then the associated optimal input  $(x_1^*, x_2^*, x_3^*)$  can be found (Figure B-3(b)).

Note that  $a \leq r_1^* \leq b$  and  $c \leq r_2^* \leq d$  can be considered as a type of filtering condition and other constraints for  $(r_1^*, r_2^*)$  can be applied as well. For example, an arbitrary condition of  $p_1 r_1^* + p_2 r_2^* \leq W$  can be applied to find the optimal dots from the 2-dimensional plot.

Now consider a case where further optimization is needed. Figure B-3(c) shows a case where the desired  $(r_1^*, r_2^*)$  result set does not exist in the sample set. The desired ideal  $(r_1^*, r_2^*)$  is  $(0, 0)$  but the feasible sample set does not include it. In this case, suppose we already know that the objective function (such as customer preference) is  $u(r_1, r_2) = \sqrt{r_1 r_2}$  and we want to find  $(r_1, r_2)$  such that it minimizes  $u(r_1, r_2)$ . By collecting  $u(r_1, r_2)$  for each dot, it can be seen that  $u(\cdot) = 1$  is the minimum and the  $(\hat{r}_1, \hat{r}_2)$  on the  $u(\cdot) = 1$  front becomes the optimal output result.

Overall, it can be seen that multivariable system can handle filtering / optimization scenarios, given different constraints. Implementation of the diverse filtering / optimization cases using database system will be required as a next step.

**Database design:** It is important to consider database design coupled with the conceptual system modeling since the actual input – output sample data will be stored in the database and the desired optimal input – output mapping will be found using database search. The optimization process will rely on the search performance of the database system.

While there exist several candidate database design solutions, the traditional table structure in relational database can be a starting point. As can be seen from Table B-1, the sample dataset built from simulation runs can be stored in a relational database table. (The numbers are arbitrarily generated.) Given the optimal output result of  $(r_1^*, r_2^*)$ , the corresponding input vector of  $(x_1^*, x_2^*, x_3^*)$  can be found from the table.

**Table B-1. A sample dataset built from simulation**

$x_1$	$x_2$	$x_3$	$r_1$	$r_2$
10	2	8	1	0.9
9	3	9	2.2	2
⋮				
11	4	6	1.5	3

Design considerations of the database table can be considered. First of all, number of rows in the table can be extremely long to populate candidate output result sets. This might result in slow search performance in the database system. However, since the type of the data stored are numbers that require small amount of memory, it is expected that the search performance will not be affected greatly since the total size of the database table can remain small.

Next, the table columns can grow large ( $m$  for  $x_m$  and  $n$  for  $r_n$ ) to store the actual simulation input-output data. Mostly, a large number of columns will not affect the database search performance, but it should be considered that fixing the number of columns from the start of the table design can be difficult for our toolbox-based system. For example, the table can start with  $m = 3$  and  $n = 2$  as Table B-1 shows but a new input parameter of  $x_4$  might be added later.

In this case, a relational database can show problems since the entire table structure has to be modified and reconstructed. NoSQL databases can be more desirable in this situation since NoSQL databases are designed from the start to store semi-structured, or even unstructured data. The flexibility of NoSQL databases in data structure are expected to be effective in mix-and-match design as well since the mix-and-match method will generate diverse combination of inputs and outputs.

Finally, in cases where the scale of the data should grow large for database systems, hash-based data storage system that reversely mapping from  $(r_1, r_2)$  to  $(x_1, x_2, x_3)$  can be considered as well. In this system, the output of  $(r_1, r_2)$  acts as a key that retrieves the corresponding  $(x_1, x_2, x_3)$  value. One advantage of hash-based system is that it does not perform search on the values like database systems and the retrieval speed of hash functions are faster than database search. However, it is expected that NoSQL database solution will be sufficiently fast in search and scalable in terms of data size for our scenario.

In summary, this is one example of the toolbox design, and many other model and database design concepts are possible to meet the goal of the toolbox-based agile optimization process -synthesize customized and / or tailored tunable optic device with sufficient computational resources of the material, structure, and application databased (library) to form a complete application-driven P-ACTIVE. One of the key takeaway messages from the P-ACTIVE project is that there is no “one-size-fits-all” solution, because each application prioritizes a different set of performance metrics that none of the reconfigurable / tunable PCM optics today can simultaneously meet. At least, the PCM-net and PCM toolbox can be a one of the approaches for the application-driven P-ACTIVE design.

## Conclusions

Phase change material (PCM)-integrated actively tunable filters (P-ACTIVE) have shown promise as multifunctional wide-waveband replacements for bulky filter wheels. This is achieved through the integration of a chalcogenide PCM into a Fabry-Perot multilevel bandpass filter, a plasmonic (metallic) nanohole metasurface, or an all-dielectric metasurface filter as the tunable constituent to effectively tune the transmission passband of optical filters in real time.

Although liquid crystal tunable filters (LCTF) and acousto-optic tunable filters (AOTF) are also capable of active wavelength tuning with microsecond to millisecond tuning speeds while preserving imaging integrity, PCM-based filters are more promising for remote sensing applications. Compared to P-ACTIVE, LCTFs require more complicated optics for any filtering purpose and are operated primarily in the visible. LCTF and AOTF are less commonly used for imaging purposes due to the off-axis arrangement, polarization sensitivity, low optical throughput and transmission efficiency, relatively slow switching speed, and large SWaP cost associated with packaging. Another benefit of a P-ACTIVE is the non-volatility and no continuous input power required to maintain the filter characteristics compared with other technologies. This is critical for airborne and spaceborne (SmallSat or CubeSat-based) remote sensing applications. In particular, PCM-based tunable filters offer significant advantages over the current imaging spectroscopy (IS) state-of-the-art. These include visible wavelengths for astronaut health monitoring, visible to infrared wavelengths for atmospheric gas monitoring, and infrared wavelengths for space launch vehicle thermal monitoring.

In this report, SCIFLI was used as a NASA project scenario that considered a P-ACTIVE integrated remote temperature measurement system to collect calibrated images of air/spacecraft during ascent in order to validate the thermal protection systems of vehicles and evaluate their performance. To make these measurements, state-of-the-art systems rely on motorized filter wheels which hold several (typically  $\sim 5$ ) single-notch optical filters and rotate between each filter to take a new spectral measurement. Although a filter wheel is a solution to IS, they offer no real-time tunability and are limited in overall bandwidth and temporal resolution, therefore missing out on important spectral and temporal data. PCM-based actively tunable filters can be tuned on nanosecond timescales—orders of magnitude faster than the relevant timescales of temperature drift in the measurements—enabling real-time thermography and imaging spectroscopy with high data throughput. Furthermore, Lidar missions (i.e., SAGE (Stratospheric Aerosol and Gas Experiment)) utilize the same filter wheels for chemical remote sensing. The broad waveband and robust tuning applicability of the P-ACTIVE provide unprecedented views of Earth’s atmospheric constituents and surface altimetry, significantly advancing science objectives across multiple disciplines and adding value to Lidar measurements. Added to the orders-of-magnitude reduction in total SWaP, spaceborne systems relying on PCM-based actively tunable filters will continue to be in demand into the foreseeable future.

MIT has demonstrated fully electrical tuning of PCM- based metasurfaces for optical applications such as switchable mirrors and reflection filters. They have also recently developed a novel transparent heater/electrode design based on doped Si, wherein the electrodes and heaters are one in the same and offer

broadband transparency in the infrared, making them an ideal platform for infrared filter applications. Additionally, a powerful design tool has been leveraged based on deep neural networks (DNNs) that allows for the design of P-ACTIVE elements that meet arbitrary performance specifications. This uniquely positions P-ACTIVE to address virtually any mission-driven filter requirement.

Despite the explosive progress and strategies in P-ACTIVE technology since 2018, several technological gaps still loom for real-world applications. The four key technical challenges that must be addressed before PCMs can make an impact on photonic applications are: (1) reliability improvement, (2) expanding material databases on visible and SWIR range PCMs, (3) fundamental understanding of phase change behavior, and (4) scalable manufacturing and packaging. Understanding the performance of materials under extreme conditions sets bounds to where and how they can be used and informs the range of system engineering that may be needed to enable their use in applications. Similarly, space missions necessarily come with extremely challenging and wholly inflexible performance metrics to ensure mission success – understanding the capabilities of devices comprised of such materials with respect to inflexible mission metrics is equally important.

In March 2021, twenty-four samples of various PCMs along with metasurface optical components comprised of these PCMs, were delivered to the International Space Station (ISS) as part of the Materials International Space Station Experiment (MISSE-14) test campaign. Although PCMs have previously been noted for their resilience to various forms of radiation, they had not been tested in a realistic space environment until this exposure campaign with joint NASA and MIT collaboration. During the six-month total open exposure time in low earth orbit (LEO), high-resolution cameras scanned and captured photographs of the samples to detect changes as a function of time along with on-orbit measured temperature, UV radiation, total atomic oxygen fluence, and total ionizing radiation doses. The samples were returned to NASA Langley Research Center in March 2022 for post-flight characterization. This duplicated the preflight characterization (i.e., material composition and crystallinity that limits switching speed, index contrast, loss, etc.) conducted before launch. The space sector has witnessed tremendous growth within the past decade—not only from government agencies but also entrants from the private sector. Future growth in the capabilities of Earth observation, deep space, and planetary surface missions using miniaturized spacecraft platforms can only be sustained by innovations in the design of remote sensors and other sub-systems. Active metasurface optics with enhanced tunability and reconfigurability continues to redefine the boundaries of optical science. The introduction of PCM technology and associated optical devices will help to accelerate the adoption of new architectures for reduced size, weight, power, and cost (SWaP-C) platforms in space.

In summary, this publication has attempted to answer a number of questions that have arisen as P-ACTIVE technology continues to be developed and matured: (1) What is P-ACTIVE and how does it work?, (2) Why do we need this technology?, (3) Where will P-ACTIVE be most useful?, (4) What does P-ACTIVE have to offer to mitigate the risks for high technology and manufacturing readiness levels (TRL and MRL)?, and (5) How can the technology be integrated into other optical structures and components? Given that the use of optical metamaterials is a rapidly expanding discipline, it is clear that a myriad of future applications and possibilities for this technology are possible.



## References

- [1] “Thorlabs product catalog, product number FW102C.”
- [2] M. Julian, C. Williams, S. Borg, S. Bartram, and K. Hyun Jung, “Reversible optical tuning of GeSbTe phase-change metasurface spectral filters for mid-wave infrared imaging,” *Optica*, vol. 7, pp. 746–754, Jul. 2020.
- [3] Y. Zhang *et al.*, “Electrically reconfigurable non-volatile metasurface using low-loss optical phase-change material,” *Nat. Nanotechnol.*, vol. 16, no. 6, Art. no. 6, Jun. 2021, doi: 10.1038/s41565-021-00881-9.
- [4] W. Kelliher and P. Young, “Investigation of phase-change coatings for variable thermal control of spacecraft.” NASA Technical Note (TN), Jun. 1972. [Online]. Available: <https://ntrs.nasa.gov/citations/19720018274>
- [5] A. Howes, J. R. Nolen, J. D. Caldwell, and J. Valentine, “Near-Unity and Narrowband Thermal Emissivity in Balanced Dielectric Metasurfaces,” *Adv. Opt. Mater.*, vol. 8, no. 4, p. 1901470, 2020, doi: 10.1002/adom.201901470.
- [6] Z. Wang *et al.*, “Resistive switching materials for information processing,” *Nat. Rev. Mater.*, vol. 5, no. 3, Art. no. 3, Mar. 2020, doi: 10.1038/s41578-019-0159-3.
- [7] K. Aryana *et al.*, “Interface controlled thermal resistances of ultra-thin chalcogenide-based phase change memory devices,” *Nat. Commun.*, vol. 12, no. 1, Art. no. 1, Feb. 2021, doi: 10.1038/s41467-020-20661-8.
- [8] M. Wuttig and N. Yamada, “Phase-change materials for rewriteable data storage,” *Nat. Mater.*, vol. 6, no. 11, Art. no. 11, Nov. 2007, doi: 10.1038/nmat2009.
- [9] L. Kang, R. P. Jenkins, and D. H. Werner, “Recent Progress in Active Optical Metasurfaces,” *Adv. Opt. Mater.*, vol. 7, no. 14, p. 1801813, 2019, doi: 10.1002/adom.201801813.
- [10] N. Yamada, E. Ohno, K. Nishiuchi, N. Akahira, and M. Takao, “Rapid-phase transitions of GeTe-Sb<sub>2</sub>Te<sub>3</sub> pseudobinary amorphous thin films for an optical disk memory,” *J. Appl. Phys.*, vol. 69, no. 5, pp. 2849–2856, Mar. 1991, doi: 10.1063/1.348620.
- [11] S. Guerin, B. Hayden, D. W. Hewak, and C. Vian, “Synthesis and Screening of Phase Change Chalcogenide Thin Film Materials for Data Storage,” *ACS Comb. Sci.*, vol. 19, no. 7, pp. 478–491, Jul. 2017, doi: 10.1021/acscombsci.7b00047.
- [12] M. Chen, K. A. Rubin, and R. W. Barton, “Compound materials for reversible, phase-change optical data storage,” *Appl. Phys. Lett.*, vol. 49, no. 9, pp. 502–504, Sep. 1986, doi: 10.1063/1.97617.
- [13] Q. Zhang, Y. Zhang, J. Li, R. Soref, T. Gu, and J. Hu, “Broadband nonvolatile photonic switching based on optical phase change materials: beyond the classical figure-of-merit,” *Opt. Lett.*, vol. 43, no. 1, pp. 94–97, Jan. 2018, doi: 10.1364/OL.43.000094.
- [14] Y. Zhang *et al.*, “Broadband transparent optical phase change materials for high-performance nonvolatile photonics,” *Nat. Commun.*, vol. 10, no. 1, Art. no. 1, Sep. 2019, doi: 10.1038/s41467-019-12196-4.
- [15] W. Zhang, R. Mazzarello, M. Wuttig, and E. Ma, “Designing crystallization in phase-change materials for universal memory and neuro-inspired computing,” *Nat. Rev. Mater.*, vol. 4, no. 3, Art. no. 3, Mar. 2019, doi: 10.1038/s41578-018-0076-x.
- [16] J.-Y. Raty, M. Schumacher, P. Golub, V. L. Deringer, C. Gatti, and M. Wuttig, “A Quantum-Mechanical Map for Bonding and Properties in Solids,” *Adv. Mater.*, vol. 31, no. 3, p. 1806280, 2019, doi: 10.1002/adma.201806280.
- [17] T. Siegrist *et al.*, “Disorder-induced localization in crystalline phase-change materials,” *Nat. Mater.*, vol. 10, no. 3, Art. no. 3, Mar. 2011, doi: 10.1038/nmat2934.

- [18] W. K. Njoroge, H.-W. Wöltgens, and M. Wuttig, “Density changes upon crystallization of Ge<sub>2</sub>Sb<sub>2</sub>.04Te4.74 films,” *J. Vac. Sci. Technol. A*, vol. 20, no. 1, pp. 230–233, Jan. 2002, doi: 10.1116/1.1430249.
- [19] W. Wehnic, S. Botti, L. Reining, and M. Wuttig, “Origin of the optical contrast in phase-change materials,” *Phys. Rev. Lett.*, vol. 98, no. 23, p. 236403, Jun. 2007, doi: 10.1103/PhysRevLett.98.236403.
- [20] N. Yamada *et al.*, “Phase-change material for use in rewritable dual-layer optical disk,” in *Optical Data Storage 2001*, Jan. 2002, vol. 4342, pp. 55–63. doi: 10.1117/12.453428.
- [21] F. Rao *et al.*, “Reducing the stochasticity of crystal nucleation to enable subnanosecond memory writing,” *Science*, vol. 358, no. 6369, pp. 1423–1427, Dec. 2017, doi: 10.1126/science.aao3212.
- [22] M. Wuttig, H. Bhaskaran, and T. Taubner, “Phase-change materials for non-volatile photonic applications,” *Nat. Photonics*, vol. 11, no. 8, Art. no. 8, Aug. 2017, doi: 10.1038/nphoton.2017.126.
- [23] L. Waldecker *et al.*, “Time-domain separation of optical properties from structural transitions in resonantly bonded materials,” *Nat. Mater.*, vol. 14, no. 10, Art. no. 10, Oct. 2015, doi: 10.1038/nmat4359.
- [24] M. Salanga *et al.*, “Measurement of crystal growth velocity in a melt-quenched phase-change material,” *Nat. Commun.*, vol. 4, no. 1, Art. no. 1, Aug. 2013, doi: 10.1038/ncomms3371.
- [25] J. Hegedüs and S. R. Elliott, “Microscopic origin of the fast crystallization ability of Ge–Sb–Te phase-change memory materials,” *Nat. Mater.*, vol. 7, no. 5, Art. no. 5, May 2008, doi: 10.1038/nmat2157.
- [26] “Laser-induced crystallization phenomena in GeTe-based alloys. I. Characterization of nucleation and growth: Journal of Applied Physics: Vol 78, No 8.” <https://aip.scitation.org/doi/10.1063/1.359779> (accessed Aug. 30, 2022).
- [27] I. Friedrich, V. Weidenhof, S. Lenk, and M. Wuttig, “Morphology and structure of laser-modified Ge<sub>2</sub>Sb<sub>2</sub>Te<sub>5</sub> films studied by transmission electron microscopy,” *Thin Solid Films*, vol. 389, no. 1, pp. 239–244, Jun. 2001, doi: 10.1016/S0040-6090(01)00891-4.
- [28] “Kinetics of crystal nucleation in undercooled droplets of Sb- and Te-based alloys used for phase change recording: Journal of Applied Physics: Vol 98, No 5.” <https://aip.scitation.org/doi/full/10.1063/1.2037870> (accessed Aug. 30, 2022).
- [29] “Origin of radiation tolerance in amorphous Ge<sub>2</sub>Sb<sub>2</sub>Te<sub>5</sub> phase-change random-access memory material | PNAS.” <https://www.pnas.org/doi/10.1073/pnas.1800638115> (accessed Aug. 30, 2022).
- [30] T. H. Lee and S. R. Elliott, “The Relation between Chemical Bonding and Ultrafast Crystal Growth,” *Adv. Mater.*, vol. 29, no. 24, p. 1700814, 2017, doi: 10.1002/adma.201700814.
- [31] C. Williams, N. Hong, M. Julian, S. Borg, and H. J. Kim, “Tunable mid-wave infrared Fabry-Perot bandpass filters using phase-change GeSbTe,” *Opt Express*, vol. 28, no. 7, pp. 10583–10594, Mar. 2020, doi: 10.1364/OE.390538.
- [32] M. N. Julian, C. Williams, S. Borg, S. Bartram, and H. J. Kim, “Reversible optical tuning of GeSbTe phase-change metasurface spectral filters for mid-wave infrared imaging,” *Optica*, vol. 7, no. 7, pp. 746–754, Jul. 2020, doi: 10.1364/OPTICA.392878.
- [33] S. An *et al.*, “Deep neural network enabled active metasurface embedded design,” *Nanophotonics*, vol. 11, no. 17, pp. 4149–4158, Sep. 2022, doi: 10.1515/nanoph-2022-0152.
- [34] R. Sczupak *et al.*, “Measurement and alignment of linear variable filters,” in *Photonic Instrumentation Engineering V*, Feb. 2018, vol. 10539, pp. 207–212. doi: 10.1117/12.2290689.
- [35] “Infrared Linear Variable Filters.” <https://vortexopticalcoatings.co.uk/linear-variable-filters-2/>
- [36] A. Emadi, H. Wu, G. De Graaf, and R. Wolffenbuttel, “IR microspectrometers based on linear-variable optical filters,” *Procedia Eng.*, vol. 25, pp. 1401–1404, 2011.
- [37] N. P. Ayerden, G. de Graaf, and R. F. Wolffenbuttel, “Compact gas cell integrated with a linear variable optical filter,” *Opt. Express*, vol. 24, no. 3, pp. 2981–3002, 2016.

- [38] A. Emadi, H. Wu, G. de Graaf, P. Enoksson, J. H. Correia, and R. Wolffenbuttel, “Design, fabrication and measurements with a UV linear-variable optical filter microspectrometer,” in *Optical Sensing and Detection II*, 2012, vol. 8439, p. 84390V.
- [39] C. Williams, G. Rughoobur, A. J. Flewitt, and T. D. Wilkinson, “Single-step fabrication of thin-film linear variable bandpass filters based on metal–insulator–metal geometry,” *Appl. Opt.*, vol. 55, no. 32, pp. 9237–9241, Nov. 2016, doi: 10.1364/AO.55.009237.
- [40] M. Dami *et al.*, “Ultra compact spectrometer using linear variable filters,” in *International Conference on Space Optics — ICSO 2010*, Jan. 2018, vol. 10565, pp. 743–749. doi: 10.1117/12.2309265.
- [41] M. Born *et al.*, *Principles of Optics: Electromagnetic Theory of Propagation, Interference and Diffraction of Light*, 7th edition. Cambridge: Cambridge University Press, 1999.
- [42] “Oscilloscope App.” <https://www.mathworks.com/matlabcentral/fileexchange/69847-oscilloscope-app> (accessed Aug. 31, 2022).
- [43] “EverGreen HP (50-340 mJ @ 532 nm) - Quantel.” <https://www.quantel-laser.com/en/products/item/evergreen-hp-500-mj-200-hz-340-mj-15-hz.html> (accessed Aug. 31, 2022).
- [44] J.-S. Moon *et al.*, “Reconfigurable infrared spectral imaging with phase change materials,” in *Micro- and Nanotechnology Sensors, Systems, and Applications XI*, May 2019, vol. 10982, pp. 117–121. doi: 10.1117/12.2519492.
- [45] H. J. Kim, J. Sohn, N. Hong, C. Williams, and W. Humphreys, “PCM-net: a refractive index database of chalcogenide phase change materials for tunable nanophotonic device modelling,” *J. Phys. Photonics*, vol. 3, no. 2, p. 024008, Mar. 2021, doi: 10.1088/2515-7647/abeb55.
- [46] “Space: Investment shifts from GEO to LEO and now beyond | McKinsey.” <https://www.mckinsey.com/industries/aerospace-and-defense/our-insights/space-investment-shifts-from-geo-to-leo-and-now-beyond> (accessed Sep. 02, 2022).
- [47] M. Y. Shalaginov *et al.*, “Design for quality: reconfigurable flat optics based on active metasurfaces,” *Nanophotonics*, vol. 9, no. 11, pp. 3505–3534, Sep. 2020, doi: 10.1515/nanoph-2020-0033.
- [48] K. Konstantinou, T. H. Lee, F. C. Mocanu, and S. R. Elliott, “Origin of radiation tolerance in amorphous Ge<sub>2</sub>Sb<sub>2</sub>Te<sub>5</sub> phase-change random-access memory material,” *Proc. Natl. Acad. Sci.*, vol. 115, no. 21, pp. 5353–5358, May 2018, doi: 10.1073/pnas.1800638115.
- [49] T. Gu, H. J. Kim, C. Rivero-Baleine, and J. Hu, “Active metasurfaces: lighting the path to commercial success.” arXiv, May 30, 2022. doi: 10.48550/arXiv.2205.14193.
- [50] W. Humphreys and H. J. Kim, “MISSE-14 mission entitled ‘Tunable mid-wave infrared, MWIR filters based on exotic phase change materials.’” NASA Langley Research Center, 2021.
- [51] “Cargo Dragon capsule departs space station – Spaceflight Now.” <https://spaceflightnow.com/2022/01/23/dragon-crs-24-undocking/> (accessed Sep. 16, 2022).
- [52] Z. Fang, J. Zheng, A. Saxena, J. Whitehead, Y. Chen, and A. Majumdar, “Non-Volatile Reconfigurable Integrated Photonics Enabled by Broadband Low-Loss Phase Change Material,” *Adv. Opt. Mater.*, vol. 9, no. 9, p. 2002049, 2021, doi: 10.1002/adom.202002049.
- [53] M. Finckenor and K. de Groh, “Space environmental effects.” NASA ISS Program Science Office, 2015.
- [54] K.-B. Shin, C.-G. Kim, C.-S. Hong, and H.-H. Lee, “Prediction of failure thermal cycles in graphite/epoxy composite materials under simulated low earth orbit environments,” *Compos. Part B Eng.*, vol. 31, no. 3, pp. 223–235, Apr. 2000, doi: 10.1016/S1359-8368(99)00073-6.
- [55] “Effect of low earth orbit atomic oxygen on spacecraft materials | SpringerLink.” <https://link.springer.com/article/10.1007/BF00354389> (accessed Sep. 16, 2022).

- [56] S. Avcu and B. Celik, "Structural material selection and processing for low Earth orbit spacecraft regarding atomic oxygen effects," in *Proceedings of International Conference on Recent Advances in Space Technologies, 2003. RAST '03*, Nov. 2003, pp. 589–594. doi: 10.1109/RAST.2003.1303983.
- [57] X. F. Lei, Y. Chen, H. P. Zhang, X. J. Li, P. Yao, and Q. Y. Zhang, "Space Survivable Polyimides with Excellent Optical Transparency and Self-Healing Properties Derived from Hyperbranched Polysiloxane," *ACS Appl. Mater. Interfaces*, vol. 5, no. 20, pp. 10207–10220, Oct. 2013, doi: 10.1021/am402957s.
- [58] K. V. Sreekanth, R. Medwal, Y. K. Srivastava, M. Manjappa, R. S. Rawat, and R. Singh, "Dynamic Color Generation with Electrically Tunable Thin Film Optical Coatings," *Nano Lett.*, vol. 21, no. 23, pp. 10070–10075, Dec. 2021, doi: 10.1021/acs.nanolett.1c03817.
- [59] J. Yoon *et al.*, "A clinically translatable hyperspectral endoscopy (HySE) system for imaging the gastrointestinal tract," *Nat. Commun.*, vol. 10, no. 1, Art. no. 1, Apr. 2019, doi: 10.1038/s41467-019-09484-4.
- [60] M. Y. Shalaginov *et al.*, "Reconfigurable all-dielectric metalens with diffraction-limited performance," *Nat. Commun.*, vol. 12, no. 1, Art. no. 1, Feb. 2021, doi: 10.1038/s41467-021-21440-9.
- [61] F. Ding, Y. Yang, and S. I. Bozhevolnyi, "Dynamic Metasurfaces Using Phase-Change Chalcogenides," *Adv. Opt. Mater.*, vol. 7, no. 14, p. 1801709, 2019, doi: 10.1002/adom.201801709.
- [62] M. Clampin, M. Rieke, G. Rieke, R. Doyon, and J. Krist, "ESA Science & Technology - Coronagraphic Detection of Exosolar Planets with the James Webb Space Telescope." <https://sci.esa.int/web/jwst/-/47501-clampin-m-et-al-2007> (accessed Sep. 02, 2022).
- [63] L. Zou, M. Cryan, and M. Klemm, "Phase change material based tunable reflectarray for free-space optical inter/intra chip interconnects," *Opt. Express*, vol. 22, no. 20, pp. 24142–24148, Oct. 2014, doi: 10.1364/OE.22.024142.
- [64] J. Kim, J. Seong, Y. Yang, S.-W. Moon, T. Badloe, and J. Rho, "Tunable metasurfaces towards versatile metalenses and metaholograms: a review," *Adv. Photonics*, vol. 4, no. 2, p. 024001, Mar. 2022, doi: 10.1111/1.AP.4.2.024001.
- [65] S. Dolinar, B. Moision, and B. Erkmen, "Fundamentals of free-space optical communications," *Keck Inst. Space Stud. KISS Workshop Quantum Commun. Sens. Meas. Space*, Jun. 2012, Accessed: Sep. 12, 2022. [Online]. Available: <https://trs.jpl.nasa.gov/handle/2014/42559>
- [66] C. R. de Galarreta *et al.*, "Nonvolatile Reconfigurable Phase-Change Metadevices for Beam Steering in the Near Infrared," *Adv. Funct. Mater.*, vol. 28, no. 10, p. 1704993, 2018, doi: 10.1002/adfm.201704993.
- [67] P.-Y. Madec, "Overview of deformable mirror technologies for adaptive optics and astronomy," in *Adaptive Optics Systems III*, Sep. 2012, vol. 8447, pp. 22–39. doi: 10.1117/12.924892.
- [68] M. Eichenberger, F. Giorgianni, N. Sauerwein, C. Vicario, and C. P. Hauri, "Deformable mirror for wavefront shaping of infrared radiation," *Opt. Lett.*, vol. 43, no. 9, pp. 2062–2065, May 2018, doi: 10.1364/OL.43.002062.
- [69] M. Brossard, J.-F. Sauvage, M. Perrin, and E. Abraham, "Terahertz adaptive optics with a deformable mirror," *Opt. Lett.*, vol. 43, no. 7, pp. 1594–1597, Apr. 2018, doi: 10.1364/OL.43.001594.
- [70] P.-Y. Lin, H.-T. Hsieh, and G.-D. J. Su, "Design and fabrication of a large-stroke MEMS deformable mirror for wavefront control," *J. Opt.*, vol. 13, no. 5, p. 055404, Mar. 2011, doi: 10.1088/2040-8978/13/5/055404.
- [71] E. Y. Lam, "Computational photography with plenoptic camera and light field capture: tutorial," *JOSA A*, vol. 32, no. 11, pp. 2021–2032, Nov. 2015, doi: 10.1364/JOSAA.32.002021.
- [72] J. Ko and C. C. Davis, "Comparison of the plenoptic sensor and the Shack&#x2013;Hartmann sensor," *Appl. Opt.*, vol. 56, no. 13, pp. 3689–3698, May 2017, doi: 10.1364/AO.56.003689.

- [73] J. Hu, T. Chen, X. Lin, L. Wang, Q. An, and Z. Wang, “Improved Wavefront Reconstruction and Correction Strategy for Adaptive Optics System With a Plenoptic Sensor,” *IEEE Photonics J.*, vol. 13, no. 4, pp. 1–8, Aug. 2021, doi: 10.1109/JPHOT.2021.3098014.
- [74] T. W. Fahringer, P. M. Danehy, and W. D. Hutchins, “Design of a Multi-Color Plenoptic Camera for Snapshot Hyperspectral Imaging,” in *2018 Aerodynamic Measurement Technology and Ground Testing Conference*, American Institute of Aeronautics and Astronautics. doi: 10.2514/6.2018-3627.
- [75] T. W. Fahringer, P. M. Danehy, W. D. Hutchins, and B. S. Thurow, “Design of a multispectral plenoptic camera and its application for pyrometry,” *Appl. Opt.*, vol. 61, no. 10, pp. 2459–2472, Apr. 2022, doi: 10.1364/AO.432598.
- [76] B. Chanetz, J. Déleré, P. Gilliéron, P. Gnemmi, E. R. Gowree, and P. Perrier, *Experimental Aerodynamics: An Introductory Guide*, 1st ed. 2020 edition. Springer, 2020.
- [77] K. L. Cahoy, A. D. Marinan, B. Novak, C. Kerr, and M. Webber, “Wavefront control in space with MEMS deformable mirrors,” in *MEMS Adaptive Optics VII*, Mar. 2013, vol. 8617, pp. 42–57. doi: 10.1117/12.2005685.
- [78] A. L. Carter *et al.*, “Direct imaging of sub-Jupiter mass exoplanets with James Webb Space Telescope coronagraphy,” *Mon. Not. R. Astron. Soc.*, vol. 501, no. 2, pp. 1999–2016, Feb. 2021, doi: 10.1093/mnras/staa3579.
- [79] S. Zhang *et al.*, “Extending the detection and correction abilities of an adaptive optics system for free-space optical communication,” *Opt. Commun.*, vol. 482, p. 126571, Mar. 2021, doi: 10.1016/j.optcom.2020.126571.
- [80] J. P. Leckey, R. Damadeo, and C. A. Hill, “Stratospheric Aerosol and Gas Experiment (SAGE) from SAGE III on the ISS to a Free Flying SAGE IV Cubesat,” *Remote Sens.*, vol. 13, no. 22, Art. no. 22, Jan. 2021, doi: 10.3390/rs13224664.
- [81] S. M. Davis *et al.*, “Validation of SAGE III/ISS Solar Water Vapor Data With Correlative Satellite and Balloon-Borne Measurements,” *J. Geophys. Res. Atmospheres*, vol. 126, no. 2, p. e2020JD033803, 2021, doi: 10.1029/2020JD033803.
- [82] Z. Chen *et al.*, “Evaluation of the OMPS/LP stratospheric aerosol extinction product using SAGE III/ISS observations,” *Atmospheric Meas. Tech.*, vol. 13, no. 6, pp. 3471–3485, Jun. 2020, doi: 10.5194/amt-13-3471-2020.
- [83] M. Park *et al.*, “Near-Global Variability of Stratospheric Water Vapor Observed by SAGE III/ISS,” *J. Geophys. Res. Atmospheres*, vol. 126, no. 7, p. e2020JD034274, 2021, doi: 10.1029/2020JD034274.
- [84] “Thriving on Our Changing Planet: A Decadal Strategy for Earth Observation from Space [The National Academies Press.” <https://nap.nationalacademies.org/catalog/24938/thriving-on-our-changing-planet-a-decadal-strategy-for-earth> (accessed Sep. 13, 2022).
- [85] O. US EPA, “Evolution of the Clean Air Act,” May 29, 2015. <https://www.epa.gov/clean-air-act-overview/evolution-clean-air-act> (accessed Sep. 13, 2022).
- [86] S. Solomon, R. W. Portmann, R. R. Garcia, L. W. Thomason, L. R. Poole, and M. P. McCormick, “The role of aerosol variations in anthropogenic ozone depletion at northern midlatitudes,” *J. Geophys. Res. Atmospheres*, vol. 101, no. D3, pp. 6713–6727, 1996, doi: 10.1029/95JD03353.
- [87] S. Solomon, J. S. Daniel, R. R. Neely, J.-P. Vernier, E. G. Dutton, and L. W. Thomason, “The persistently variable ‘background’ stratospheric aerosol layer and global climate change,” *Science*, vol. 333, no. 6044, pp. 866–870, Aug. 2011, doi: 10.1126/science.1206027.
- [88] *Introduction to Atmospheric Chemistry*. 2000. Accessed: Sep. 13, 2022. [Online]. Available: <https://press.princeton.edu/books/hardcover/9780691001852/introduction-to-atmospheric-chemistry>
- [89] H. J. Kim, C. Williams, A. Nehrir, and J. Smith, “Solid-state frequency agile filter for Lidar: multilayer optical design and exotic phase-change materials-based active tuning,” 2020

- [90] I. S. Glass, *Handbook of Infrared Astronomy*. Cambridge: Cambridge University Press, 1999. doi: 10.1017/CBO9780511564949.
- [91] S. Borg and H. J. Kim, “A multi-spectral imaging pyrometer utilizing tunable optics.” NASA Invention Disclosure, LAR-20119-1, Jan. 2022.
- [92] V. Naresh and N. Lee, “A Review on Biosensors and Recent Development of Nanostructured Materials-Enabled Biosensors,” *Sensors*, vol. 21, no. 4, Art. no. 4, Jan. 2021, doi: 10.3390/s21041109.
- [93] A. Roda *et al.*, “Advanced biosensors for monitoring astronauts’ health during long-duration space missions,” *Biosens. Bioelectron.*, vol. 111, pp. 18–26, Jul. 2018, doi: 10.1016/j.bios.2018.03.062.
- [94] H. Altug, S.-H. Oh, S. A. Maier, and J. Homola, “Advances and applications of nanophotonic biosensors,” *Nat. Nanotechnol.*, vol. 17, no. 1, Art. no. 1, Jan. 2022, doi: 10.1038/s41565-021-01045-5.
- [95] “How Nanophotonic Label-Free Biosensors Can Contribute to Rapid and Massive Diagnostics of Respiratory Virus Infections: COVID-19 Case | ACS Sensors.” <https://pubs.acs.org/doi/full/10.1021/acssensors.0c01180> (accessed Sep. 14, 2022).
- [96] P. Damborský, J. Švitel, and J. Katrlík, “Optical biosensors,” *Essays Biochem.*, vol. 60, no. 1, pp. 91–100, Jun. 2016, doi: 10.1042/EBC20150010.
- [97] “Advances in cost-effective integrated spectrometers | Light: Science & Applications.” <https://www.nature.com/articles/s41377-022-00853-1> (accessed Sep. 14, 2022).
- [98] K. V. Sreekanth, S. Sreejith, Y. Alapan, M. Sitti, C. T. Lim, and R. Singh, “Microfluidics Integrated Lithography-Free Nanophotonic Biosensor for the Detection of Small Molecules,” *Adv. Opt. Mater.*, vol. 7, no. 7, p. 1801313, 2019, doi: 10.1002/adom.201801313.
- [99] “Tunable infrared metamaterial-based biosensor for detection of hemoglobin and urine using phase change material | Scientific Reports.” <https://www.nature.com/articles/s41598-021-86700-6> (accessed Sep. 14, 2022).
- [100] D. J. Waterhouse, C. R. Fitzpatrick, B. W. Pogue, J. P. O’Connor, and S. Bohndiek, “A roadmap for the clinical implementation of optical-imaging biomarkers,” May 2019, doi: 10.17863/CAM.38076.
- [101] N. T. Clancy, G. Jones, L. Maier-Hein, D. S. Elson, and D. Stoyanov, “Surgical spectral imaging,” *Med. Image Anal.*, vol. 63, p. 101699, Jul. 2020, doi: 10.1016/j.media.2020.101699.
- [102] O. I. Korablyev, D. A. Belyaev, Y. S. Dobrolenskiy, A. Y. Trokhimovskiy, and Y. K. Kalinnikov, “Acousto-optic tunable filter spectrometers in space missions [Invited],” *Appl. Opt.*, vol. 57, no. 10, pp. C103–C119, Apr. 2018, doi: 10.1364/AO.57.00C103.
- [103] C. Crandall, N. Clark, and P. P. Davis, “Tunable Optical Filters for Space Exploration,” presented at the 2007 SPIE Photonics and Optics Conference, San Diego, CA, Aug. 2007. Accessed: Sep. 11, 2022. [Online]. Available: <https://ntrs.nasa.gov/citations/20070030313>
- [104] T. Kaesser, C. Fritzsch, and M. Franz, “Tunable RF Filters Based on Liquid Crystal for Space Applications,” *Crystals*, vol. 10, no. 6, Art. no. 6, Jun. 2020, doi: 10.3390/cryst10060455.
- [105] T. Erdogan and L. Wang, “Semrock VersaChrome: The first widely tunable thin-film optical filters,” *Semrock White Paper Series*. <https://www.semrock.com/semrock-versachrome-tunable-bandpass-filters.aspx> (accessed Dec. 13, 2022).
- [106] H. R. Morris, C. C. Hoyt, and P. J. Treado, “Imaging Spectrometers for Fluorescence and Raman Microscopy: Acousto-Optic and Liquid Crystal Tunable Filters,” *Appl. Spectrosc.*, vol. 48, no. 7, pp. 857–866, Jul. 1994.
- [107] M. Lequime, “Tunable thin film filters: review and perspectives,” in *Advances in Optical Thin Films*, Feb. 2004, vol. 5250, pp. 302–311. doi: 10.1117/12.516026.

- [108] Y. W. Wang, N. P. Reder, S. Kang, A. K. Glaser, and J. T. C. Liu, “Multiplexed Optical Imaging of Tumor-Directed Nanoparticles: A Review of Imaging Systems and Approaches,” *Nanotheranostics*, vol. 1, no. 4, pp. 369–388, Aug. 2017, doi: 10.7150/ntno.21136.
- [109] A. Machikhin, V. Batshev, and V. Pozhar, “Aberration analysis of AOTF-based spectral imaging systems,” *JOSA A*, vol. 34, no. 7, pp. 1109–1113, Jul. 2017, doi: 10.1364/JOSAA.34.001109.
- [110] V. Batshev *et al.*, “Polarizer-Free AOTF-Based SWIR Hyperspectral Imaging for Biomedical Applications,” *Sensors*, vol. 20, no. 16, p. 4439, Aug. 2020, doi: 10.3390/s20164439.
- [111] D. Lencer, M. Salinga, B. Grabowski, T. Hickel, J. Neugebauer, and M. Wuttig, “A map for phase-change materials,” *Nat. Mater.*, vol. 7, no. 12, pp. 972–977, Nov. 2008, doi: 10.1038/nmat2330.
- [112] S. An *et al.*, “Multifunctional Metasurface Design with a Generative Adversarial Network,” *Adv. Opt. Mater.*, vol. 9, no. 5, p. 2001433, 2021, doi: 10.1002/adom.202001433.
- [113] C. Ríos *et al.*, “Ultra-compact nonvolatile phase shifter based on electrically reprogrammable transparent phase change materials.” arXiv, Mar. 21, 2022. doi: 10.48550/arXiv.2105.06010.
- [114] H. J. Kim, J. Sohn, N. Hong, C. Williams, and W. Humphreys, “PCM-net: a refractive index database of chalcogenide phase change materials for tunable nanophotonic device modelling,” *J. Phys. Photonics*, vol. 3, no. 2, p. 024008, Mar. 2021, doi: 10.1088/2515-7647/ABEB55.
- [115] K. Shportko, S. Kremers, M. Woda, D. Lencer, J. Robertson, and M. Wuttig, “Resonant bonding in crystalline phase-change materials,” *Nat. Mater.*, vol. 7, no. 8, pp. 653–658, Aug. 2008, doi: 10.1038/nmat2226.
- [116] J. Robertson, “Mott lecture: How bonding concepts can help understand amorphous semiconductor behavior,” *Phys. Status Solidi A*, vol. 213, no. 7, pp. 1641–1652, Jul. 2016, doi: 10.1002/pssa.201532875.
- [117] B. Huang and J. Robertson, “Bonding origin of optical contrast in phase-change memory materials,” *Phys. Rev. B*, vol. 81, no. 8, p. 081204, Feb. 2010, doi: 10.1103/PhysRevB.81.081204.
- [118] W. Wełnic, S. Botti, L. Reining, and M. Wuttig, “Origin of the optical contrast in phase-change materials,” *Phys. Rev. Lett.*, vol. 98, no. 23, p. 236403, Jun. 2007, doi: 10.1103/PhysRevLett.98.236403.
- [119] M. Krbal *et al.*, “Crystalline GeTe-based phase-change alloys: Disorder in order,” *Phys. Rev. B - Condens. Matter Mater. Phys.*, vol. 86, no. 4, p. 045212, Jul. 2012, doi: 10.1103/PhysRevB.86.045212.
- [120] P. Jóvári, I. Kaban, J. Steiner, B. Beuneu, A. Schöps, and M. A. Webb, “Local order in amorphous Ge<sub>2</sub>Sb<sub>2</sub>Te<sub>5</sub> and Ge Sb<sub>2</sub>Te<sub>4</sub>,” *Phys. Rev. B - Condens. Matter Mater. Phys.*, vol. 77, no. 3, p. 035202, Jan. 2008, doi: 10.1103/PhysRevB.77.035202.
- [121] D. A. Baker, M. A. Paesler, G. Lucovsky, S. C. Agarwal, and P. C. Taylor, “Application of bond constraint theory to the switchable optical memory material Ge<sub>2</sub>Sb<sub>2</sub>Te<sub>5</sub>,” *Phys. Rev. Lett.*, vol. 96, no. 25, p. 255501, Jun. 2006, doi: 10.1103/PhysRevLett.96.255501.
- [122] A. V. Kolobov, P. Fons, A. I. Frenkel, A. L. Ankudinov, J. Tominaga, and T. Uruga, “Understanding the phase-change mechanism of rewritable optical media,” *Nat. Mater.*, vol. 3, no. 10, pp. 703–708, Sep. 2004, doi: 10.1038/nmat1215.
- [123] R. O. Jones, “Bonding in phase change materials: Concepts and misconceptions,” *Journal of Physics Condensed Matter*, vol. 30, no. 15. Institute of Physics Publishing, p. 153001, Mar. 20, 2018. doi: 10.1088/1361-648X/aab22e.
- [124] M. Wuttig, V. L. Deringer, X. Gonze, C. Bichara, and J.-Y. Raty, “Incipient Metals: Functional Materials with a Unique Bonding Mechanism,” *Adv. Mater.*, vol. 30, no. 51, p. 1803777, Dec. 2018, doi: 10.1002/adma.201803777.

- [125] B. J. Kooi and M. Wuttig, “Chalcogenides by Design: Functionality through Metavalent Bonding and Confinement,” *Adv. Mater.*, vol. 32, no. 21, p. 1908302, May 2020, doi: 10.1002/adma.201908302.
- [126] J. Feldmann *et al.*, “Calculating with light using a chip-scale all-optical abacus,” *Nat. Commun.*, vol. 8, p. 1256, Dec. 2017, doi: 10.1038/s41467-017-01506-3.
- [127] C. Ríos *et al.*, “In-memory computing on a photonic platform,” *Sci. Adv.*, vol. 5, no. 2, p. eaau5759, Feb. 2019, doi: 10.1126/sciadv.aau5759.
- [128] S. Tao, X. Yuan, and W. C. Cheong, “Comparison of amplitude- and phase-holograms,” in *Design, Fabrication, and Characterization of Photonic Devices II*, Oct. 2001, vol. 4594, p. 459. doi: 10.1117/12.446580.
- [129] C. Peng, R. Hamerly, M. Soltani, and D. R. Englund, “Design of high-speed phase-only spatial light modulators with two-dimensional tunable microcavity arrays,” *Opt. Express*, vol. 27, no. 21, pp. 30669–30680, 2019, doi: 10.1364/OE.27.030669.
- [130] A.-K. U. Michel, M. Wuttig, and T. Taubner, “Design Parameters for Phase-Change Materials for Nanostructure Resonance Tuning,” *Adv. Opt. Mater.*, vol. 5, no. 18, p. 1700261, Sep. 2017, doi: 10.1002/adom.201700261.
- [131] Y. Zhang *et al.*, “Broadband transparent optical phase change materials for high-performance nonvolatile photonics,” *Nat. Commun.*, vol. 10, p. 4279, Dec. 2019, doi: 10.1038/s41467-019-12196-4.
- [132] Y. Zhang and J. Hu, “Reconfigurable optics-a phase change for the better,” *Am. Ceram. Soc. Bull.*, vol. 99, no. 4, pp. 36–37, 2020.
- [133] W. Dong *et al.*, “Wide Bandgap Phase Change Material Tuned Visible Photonics,” *Adv. Funct. Mater.*, vol. 29, no. 6, p. 1806181, Feb. 2019, doi: 10.1002/adfm.201806181.
- [134] C. Koch *et al.*, “Enhanced temperature stability and exceptionally high electrical contrast of selenium substituted Ge<sub>2</sub>Sb<sub>2</sub>Te<sub>5</sub> phase change materials,” *RSC Adv.*, vol. 7, no. 28, pp. 17164–17172, Mar. 2017, doi: 10.1039/c7ra01140g.
- [135] S. Buller *et al.*, “Influence of partial substitution of Te by Se and Ge by Sn on the properties of the blu-ray phase-change material Ge 8Sb 2Te 11,” *Chem. Mater.*, vol. 24, no. 18, pp. 3582–3590, Sep. 2012, doi: 10.1021/cm301809g.
- [136] E. M. Vinod, K. Ramesh, and K. S. Sangunni, “Structural transition and enhanced phase transition properties of Se doped Ge<sub>2</sub>Sb<sub>2</sub>Te<sub>5</sub> alloys,” *Sci. Rep.*, vol. 5, p. 8050, Jan. 2015, doi: 10.1038/srep08050.
- [137] K. Aryana *et al.*, “Suppressed electronic contribution in thermal conductivity of Ge<sub>2</sub>Sb<sub>2</sub>Se<sub>4</sub>Te,” *Nat. Commun.*, vol. 12, p. 7187, Dec. 2021, doi: 10.1038/s41467-021-27121-x.
- [138] M. Delaney *et al.*, “Nonvolatile programmable silicon photonics using an ultralow-loss Sb<sub>2</sub>Se<sub>3</sub> phase change material,” *Sci. Adv.*, vol. 7, no. 25, p. eabg3500, Jun. 2021, doi: 10.1126/SCIADV.ABG3500.
- [139] J. Faneca *et al.*, “On-chip sub-wavelength Bragg grating design based on novel low loss phase-change materials,” *Opt. Express*, vol. 28, no. 11, p. 16394, May 2020, doi: 10.1364/oe.389598.
- [140] W. Zhang, M. Wuttig, and R. Mazzarello, “Effects of stoichiometry on the transport properties of crystalline phase-change materials,” *Sci. Rep.*, vol. 5, p. 13496, 2015, doi: 10.1038/srep13496.
- [141] Z. Sun, Y. Pan, J. Zhou, B. Sa, and R. Ahuja, “Origin of p-type conductivity in layered nGeTe•mSb 2Te 3 chalcogenide semiconductors,” *Phys. Rev. B - Condens. Matter Mater. Phys.*, vol. 83, no. 11, p. 113201, Mar. 2011, doi: 10.1103/PhysRevB.83.113201.
- [142] S. Caravati, M. Bernasconi, T. D. Kühne, M. Krack, and M. Parrinello, “First principles study of crystalline and amorphous Ge 2 Sb 2 Te 5 and the effects of stoichiometric defects ,” *J. Phys. Condens. Matter*, vol. 21, no. 49, pp. 499803–499803, Dec. 2009, doi: 10.1088/0953-8984/21/49/499803.

- [143] T. Nonaka, G. Ohbayashi, Y. Toriumi, Y. Mori, and H. Hashimoto, “Crystal structure of GeTe and Ge<sub>2</sub>Sb<sub>2</sub>Te<sub>5</sub> meta-stable phase,” *Thin Solid Films*, vol. 370, no. 1, pp. 258–261, Jul. 2000, doi: 10.1016/S0040-6090(99)01090-1.
- [144] J. Zhou, Z. Sun, Y. Pan, Z. Song, and R. Ahuja, “Vacancy or not: An insight on the intrinsic vacancies in rocksalt-structured GeSbTe alloys from ab initio calculations,” *EPL*, vol. 95, no. 2, p. 27002, Jul. 2011, doi: 10.1209/0295-5075/95/27002.
- [145] A. Lotnyk, M. Behrens, and B. Rauschenbach, “Phase change thin films for non-volatile memory applications,” *Nanoscale Advances*, vol. 1, no. 10. Royal Society of Chemistry, pp. 3836–3857, Oct. 08, 2019. doi: 10.1039/c9na00366e.
- [146] F. Yang *et al.*, “First-principles study of the properties for crystal Ge 2 Sb 2 Te 5 with Ge vacancy ARTICLES YOU MAY BE INTERESTED IN,” *AIP Adv.*, vol. 8, p. 65223, 2018, doi: 10.1063/1.5006247.
- [147] T. Cao *et al.*, “Tunable Thermal Emission Using Chalcogenide Metasurface,” *Adv. Opt. Mater.*, vol. 6, no. 16, p. 1800169, Aug. 2018, doi: 10.1002/adom.201800169.
- [148] Y. Qu *et al.*, “Thermal camouflage based on the phase-changing material GST,” *Light Sci. Appl.*, vol. 7, no. 1, p. 26, Dec. 2018, doi: 10.1038/s41377-018-0038-5.
- [149] J. Hu, L. Mawst, S. Moss, L. Petit, and D. Ting, “Feature issue introduction: mid-infrared optical materials and their device applications,” *Opt. Mater. Express*, vol. 8, no. 7, p. 2026, Jul. 2018, doi: 10.1364/ome.8.002026.
- [150] H. Qian *et al.*, “Observation of carrier localization in cubic crystalline Ge<sub>2</sub>Sb<sub>2</sub>Te<sub>5</sub> by field effect measurement,” *Sci. Rep.*, vol. 8, no. 1, p. 486, Dec. 2018, doi: 10.1038/s41598-017-18964-w.
- [151] Y. Zhang *et al.*, “Myths and truths about optical phase change materials: A perspective,” *Appl. Phys. Lett.*, vol. 118, no. 21, p. 210501, May 2021, doi: 10.1063/5.0054114.
- [152] Y. Zhang *et al.*, “Electrically reconfigurable non-volatile metasurface using low-loss optical phase-change material,” *Nat. Nanotechnol.*, vol. 16, pp. 661–666, 2021, doi: 10.1038/s41565-021-00881-9.
- [153] P. Hosseini, C. D. Wright, and H. Bhaskaran, “An optoelectronic framework enabled by low-dimensional phase-change films,” *Nature*, vol. 511, no. 7508, pp. 206–211, Jul. 2014, doi: 10.1038/nature13487.
- [154] H. K. Ji *et al.*, “Non-binary Colour Modulation for Display Device Based on Phase Change Materials,” *Sci. Rep.*, vol. 6, p. 39206, 2016, doi: 10.1038/srep39206.
- [155] Z. Ni, S. Mou, T. Zhou, and Z. Cheng, “Broader color gamut of color-modulating optical coating display based on indium tin oxide and phase change materials,” *Appl. Opt.*, vol. 57, pp. 3385–3389, 2018, doi: 10.1364/ao.57.003385.
- [156] J. Wang *et al.*, “Improving the reflectance and color contrasts of phase-change materials by vacancy reduction for optical-storage and display applications,” *Opt. Lett.*, vol. 45, no. 1, p. 244, Jan. 2020, doi: 10.1364/ol.45.000244.
- [157] C. Ríos, P. Hosseini, R. A. Taylor, and H. Bhaskaran, “Color Depth Modulation and Resolution in Phase-Change Material Nanodisplays,” *Adv. Mater.*, vol. 28, no. 23, pp. 4720–4726, Jun. 2016, doi: 10.1002/adma.201506238.
- [158] Q. Cheng, S. Rumley, M. Bahadori, and K. Bergman, “Photonic switching in high performance datacenters [Invited],” *Opt. Express*, vol. 26, no. 12, p. 16022, Jun. 2018, doi: 10.1364/OE.26.016022.
- [159] T. A. Strasser and J. L. Wagener, “Wavelength-selective switches for ROADM applications,” *IEEE J. Sel. Top. Quantum Electron.*, vol. 16, no. 5, pp. 1150–1157, Sep. 2010, doi: 10.1109/JSTQE.2010.2049345.
- [160] M. Y. Shalaginov *et al.*, “Reconfigurable all-dielectric metalens based on phase change materials,” in *Active Photonic Platforms XII*, Aug. 2020, vol. 11461, p. 18. doi: 10.1117/12.2565267.

- [161] F. Yang *et al.*, “Reconfigurable parfocal zoom metalens,” *Adv. Opt. Mater.*, vol. 10, p. 2200721, 2022, doi: 10.1002/adom.202200721.
- [162] X. Yin *et al.*, “Beam switching and bifocal zoom lensing using active plasmonic metasurfaces,” *Light Sci. Appl.*, vol. 6, no. 7, p. e17016, Jul. 2017, doi: 10.1038/lsta.2017.16.
- [163] W. Bogaerts *et al.*, “Programmable photonic circuits,” *Nature*, vol. 586, pp. 207–216, 2020, doi: 10.1038/s41586-020-2764-0.
- [164] D. Pérez *et al.*, “Multipurpose silicon photonics signal processor core,” *Nat. Commun.*, vol. 8, p. 636, Sep. 2017, doi: 10.1038/s41467-017-00714-1.
- [165] Y. Shen *et al.*, “Deep learning with coherent nanophotonic circuits,” *Nat. Photonics*, vol. 11, no. 7, pp. 441–446, Jul. 2017, doi: 10.1038/nphoton.2017.93.
- [166] D. M. Kita *et al.*, “High-performance and scalable on-chip digital Fourier transform spectroscopy,” *Nat. Commun.*, vol. 9, no. 1, p. 4405, Dec. 2018, doi: 10.1038/s41467-018-06773-2.
- [167] K. Liao *et al.*, “All-optical computing based on convolutional neural networks,” *Opto-Electron. Adv.*, vol. 4, no. 11, pp. 200060-, 2021, doi: 10.29026/OEA.2021.200060.
- [168] K. Liao *et al.*, “Matrix eigenvalue solver based on reconfigurable photonic neural network,” *Nanophotonics*, Apr. 2022, doi: 10.1515/NANOPH-2022-0109.
- [169] A. Sarangan, J. Duran, V. Vasilyev, N. Limberopoulos, I. Vitebskiy, and I. Anisimov, “Broadband Reflective Optical Limiter Using GST Phase Change Material,” *IEEE Photonics J.*, vol. 10, no. 2, p. 2200409, Apr. 2018, doi: 10.1109/JPHOT.2018.2796448.
- [170] N. Youngblood *et al.*, “Reconfigurable Low-Emissivity Optical Coating Using Ultrathin Phase Change Materials,” *ACS Photonics*, vol. 9, no. 1, pp. 90–100, Jan. 2022, doi: 10.1021/ACSPHOTONICS.1C01128/SUPPL\_FILE/PH1C01128\_SI\_002.PDF.
- [171] S. An *et al.*, “A Deep Learning Approach for Objective-Driven All-Dielectric Metasurface Design,” *ACS Photonics*, vol. 6, no. 12, pp. 3196–3207, Dec. 2019, doi: 10.1021/acsphtronics.9b00966.
- [172] J. Meng *et al.*, “Electrical Programmable Multi-Level Non-volatile Photonic Random-Access Memory.” arXiv, Jun. 21, 2022. doi: 10.48550/arXiv.2203.13337.
- [173] L. Martin-Monier *et al.*, “Endurance of Chalcogenide Optical Phase Change Materials: a Review,” *Opt. Mater. Express*, vol. 12, no. 6, pp. 2145–2167, Jun. 2022, doi: 10.1364/ome.456428.
- [174] R. Eguchi *et al.*, “Amplitude trimming of Si waveguides using phase change material,” *IEICE Electron. Express*, vol. 13, no. 6, p. 20160107, 2016, doi: 10.1109/JLT.2005.
- [175] Y. Zhang *et al.*, “Transient Tap Couplers for Wafer-Level Photonic Testing Based on Optical Phase Change Materials,” *ACS Photonics*, Jun. 2021, doi: 10.1021/ACSPHOTONICS.1C00374.
- [176] K. Kim and S. J. Ahn, “Reliability investigations for manufacturable high density PRAM,” in *IEEE International Reliability Physics Symposium Proceedings*, 2005, pp. 157–162. doi: 10.1109/relphy.2005.1493077.
- [177] E. A. Cartier *et al.*, “Reliability Challenges with Materials for Analog Computing,” in *IEEE International Reliability Physics Symposium Proceedings*, May 2019, vol. 2019–March. doi: 10.1109/IRPS.2019.8720599.
- [178] S. B. Kim, G. W. Burr, W. Kim, and S. W. Nam, “Phase-change memory cycling endurance,” *MRS Bull.*, vol. 44, no. 9, pp. 710–714, Sep. 2019, doi: 10.1557/mrs.2019.205.
- [179] S. Lee, J. H. Jeong, T. S. Lee, W. M. Kim, and B. K. Cheong, “A study on the failure mechanism of a phase-change memory in write/erase cycling,” *IEEE Electron Device Lett.*, vol. 30, no. 5, pp. 448–450, 2009, doi: 10.1109/LED.2009.2015222.
- [180] C. Kim *et al.*, “Direct evidence of phase separation in Ge<sub>2</sub>Sb<sub>2</sub>Te<sub>5</sub> in phase change memory devices,” *Appl. Phys. Lett.*, vol. 94, no. 19, p. 193504, May 2009, doi: 10.1063/1.3127223.

- [181] Y. Xie *et al.*, “Self-Healing of a Confined Phase Change Memory Device with a Metallic Surfactant Layer,” *Adv. Mater.*, vol. 30, no. 9, p. 1705587, Mar. 2018, doi: 10.1002/adma.201705587.
- [182] C. F. Chen *et al.*, “Endurance improvement of Ge<sub>2</sub>Sb<sub>2</sub>Te<sub>5</sub>-based phase change memory,” in *2009 IEEE International Memory Workshop, IMW '09*, 2009. doi: 10.1109/IMW.2009.5090589.
- [183] P. Y. Du *et al.*, “The impact of melting during reset operation on the reliability of phase change memory,” in *IEEE International Reliability Physics Symposium Proceedings*, 2012. doi: 10.1109/IRPS.2012.6241872.
- [184] A. L. Lacaita, “Phase change memories: State-of-the-art, challenges and perspectives,” in *Solid-State Electronics*, Jan. 2006, vol. 50, no. 1, pp. 24–31. doi: 10.1016/j.sse.2005.10.046.
- [185] L. Lu, W. Dong, J. K. Behera, L. Chew, and R. E. Simpson, “Inter-diffusion of plasmonic metals and phase change materials,” *J. Mater. Sci.*, vol. 54, no. 4, pp. 2814–2823, Feb. 2019, doi: 10.1007/s10853-018-3066-x.
- [186] P. Noé, C. Sabbione, N. Bernier, N. Castellani, F. Fillot, and F. Hippert, “Impact of interfaces on scenario of crystallization of phase change materials,” *Acta Mater.*, vol. 110, pp. 142–148, May 2016, doi: 10.1016/j.actamat.2016.03.022.
- [187] M. Wuttig, H. Bhaskaran, and T. Taubner, “Phase-change materials for non-volatile photonic applications,” *Nat. Photonics*, vol. 11, no. 8, pp. 465–476, Aug. 2017, doi: 10.1038/nphoton.2017.126.
- [188] Y. Ikuma *et al.*, “Small-sized optical gate switch using Ge<sub>2</sub>Sb<sub>2</sub>Te<sub>5</sub> phase-change material integrated with silicon waveguide,” *Electron. Lett.*, vol. 46, no. 5, pp. 368–369, 2010, doi: 10.1049/el.2010.3588.
- [189] S. W. Nam *et al.*, “Phase separation behavior of Ge<sub>2</sub> Sb<sub>2</sub> Te<sub>5</sub> line structure during electrical stress biasing,” *Appl. Phys. Lett.*, vol. 92, no. 11, p. 111913, Mar. 2008, doi: 10.1063/1.2899967.
- [190] S. Bordas, M. T. Clavaguera-Mora, B. Legendre, and C. Hancheng, “Phase diagram of the ternary system Ge-Sb-Te. II. The subternary Ge-GeTe-Sb<sub>2</sub>Te<sub>3</sub>-Sb,” *Thermochim. Acta*, vol. 107, no. C, pp. 239–265, Oct. 1986, doi: 10.1016/0040-6031(86)85051-1.
- [191] A. Cywar *et al.*, “Modeling of void formation in phase change memory devices,” *Solid-State Electron.*, vol. 164, p. 107684, Feb. 2020, doi: 10.1016/j.sse.2019.107684.
- [192] S. H. Oh *et al.*, “In situ TEM observation of void formation and migration in phase change memory devices with confined nanoscale Ge<sub>2</sub>Sb<sub>2</sub>Te<sub>5</sub>,” *Nanoscale Adv.*, vol. 2, no. 9, pp. 3841–3848, Sep. 2020, doi: 10.1039/d0na00223b.
- [193] X. Zhou, W. Dong, H. Zhang, and R. E. Simpson, “A zero density change phase change memory material: GeTe-O structural characteristics upon crystallisation,” *Sci. Rep.*, vol. 5, p. 11150, Jun. 2015, doi: 10.1038/srep11150.
- [194] J.-S. Moon *et al.*, “Reconfigurable infrared spectral imaging with phase change materials,” *SPIE Proc.*, vol. 10982, p. 32, May 2019, doi: 10.1117/12.2519492.
- [195] E. Yalon, I. M. Datye, J. S. Moon, K. A. Son, K. Lee, and E. Pop, “Energy-Efficient Indirectly Heated Phase Change RF Switch,” *IEEE Electron Device Lett.*, vol. 40, no. 3, pp. 455–458, Mar. 2019, doi: 10.1109/LED.2019.2896953.
- [196] L. Martin-Monier, T. Das Gupta, W. Yan, S. Lacour, and F. Sorin, “Nanoscale Controlled Oxidation of Liquid Metals for Stretchable Electronics and Photonics,” *Adv. Funct. Mater.*, vol. 31, no. 3, p. 2006711, Jan. 2021, doi: 10.1002/ADFM.202006711.
- [197] A. L. Holsteen, A. F. Cihan, and M. L. Brongersma, “Temporal color mixing and dynamic beam shaping with silicon metasurfaces,” *Science*, vol. 365, no. 6450, pp. 257–260, Jul. 2019, doi: 10.1126/SCIENCE.AAX5961/SUPPL\_FILE/AAX5961-HOLSTEEN-SM.PDF.
- [198] R. Soref and B. Bennett, “Electrooptical effects in silicon,” *IEEE J. Quantum Electron.*, vol. 23, no. 1, pp. 123–129, Jan. 1987, doi: 10.1109/JQE.1987.1073206.

- [199] A. Mekis *et al.*, “Silicon integrated photonics reliability,” in *Optics InfoBase Conference Papers*, Jul. 2017, vol. Part F52-I, p. IW3A.3. doi: 10.1364/IPRSN.2017.IW3A.3.
- [200] P. P. Iyer, M. Pendharkar, C. J. Palmstrøm, and J. A. Schuller, “III–V Heterojunction Platform for Electrically Reconfigurable Dielectric Metasurfaces,” *ACS Photonics*, vol. 6, no. 6, pp. 1345–1350, Jun. 2019, doi: 10.1021/acspophotonics.9b00178.
- [201] J. Park, S. J. Kim, V. J. Sorger, and S. J. Kim, “Electrically tunable metasurface by using InAs in a metal-insulator-metal configuration,” *Nanophotonics*, vol. 11, no. 6, pp. 1117–1126, Feb. 2022, doi: 10.1515/NANOPH-2021-0618/DOWNLOADASSET/SUPPL/J\_NANOPH-2021-0618\_SUPPL.DOCX.
- [202] E. Feigenbaum, K. Diest, and H. A. Atwater, “Unity-Order Index Change in Transparent Conducting Oxides at Visible Frequencies,” *Nano Lett.*, vol. 10, no. 6, pp. 2111–2116, Jun. 2010, doi: 10.1021/nl1006307.
- [203] Y.-W. Huang *et al.*, “Gate-Tunable Conducting Oxide Metasurfaces,” *Nano Lett.*, vol. 16, no. 9, pp. 5319–5325, Sep. 2016, doi: 10.1021/acs.nanolett.6b00555.
- [204] N. K. Emani, T.-F. Chung, X. Ni, A. V. Kildishev, Y. P. Chen, and A. Boltasseva, “Electrically Tunable Damping of Plasmonic Resonances with Graphene,” *Nano Lett.*, vol. 12, no. 10, pp. 5202–5206, Oct. 2012, doi: 10.1021/nl302322t.
- [205] B. Zeng *et al.*, “Hybrid graphene metasurfaces for high-speed mid-infrared light modulation and single-pixel imaging,” *Light Sci. Appl.*, vol. 7, p. 51, Aug. 2018, doi: 10.1038/s41377-018-0055-4.
- [206] D. Akinwande *et al.*, “Graphene and two-dimensional materials for silicon technology,” *Nature*, vol. 573, no. 7775, pp. 507–518, Sep. 2019, doi: 10.1038/s41586-019-1573-9.
- [207] P. P. Iyer, M. Pendharkar, C. J. Palmstrøm, and J. A. Schuller, “Ultrawide thermal free-carrier tuning of dielectric antennas coupled to epsilon-near-zero substrates,” *Nat. Commun.*, vol. 8, no. 1, p. 472, Dec. 2017, doi: 10.1038/s41467-017-00615-3.
- [208] T. Goh, “Recent advances in large-scale silica-based thermo-optic switches,” in *SPIE Proceedings*, Oct. 2001, vol. 4582, no. 18, pp. 49–56. doi: 10.1117/12.445076.
- [209] Y. Horie, A. Arbabi, E. Arbabi, S. M. Kamali, and A. Faraon, “High-Speed, Phase-Dominant Spatial Light Modulation with Silicon-Based Active Resonant Antennas,” *ACS Photonics*, vol. 5, no. 5, pp. 1711–1717, May 2018, doi: 10.1021/acspophotonics.7b01073.
- [210] T. Lewi, N. A. Butakov, and J. A. Schuller, “Thermal tuning capabilities of semiconductor metasurface resonators,” *Nanophotonics*, vol. 8, no. 2, pp. 331–338, 2018.
- [211] I. C. Benea-Chelmus, M. L. Meretska, D. L. Elder, M. Tamagnone, L. R. Dalton, and F. Capasso, “Electro-optic spatial light modulator from an engineered organic layer,” *Nat. Commun.*, vol. 12, p. 5928, Oct. 2021, doi: 10.1038/s41467-021-26035-y.
- [212] T. Tanemura, J. Zhang, Y. Kosugi, M. Ogasawara, and Y. Nakano, “Metasurface high-speed modulators using electro-optic polymer,” in *SPIE Proceedings*, Mar. 2021, vol. 11692, p. 1169208. doi: 10.1117/12.2583109.
- [213] A. Karvounis *et al.*, “Electro-Optic Metasurfaces Based on Barium Titanate Nanoparticle Films,” *Adv. Opt. Mater.*, vol. 8, no. 17, p. 2000623, Sep. 2020, doi: 10.1002/ADOM.202000623.
- [214] A. Karvounis, V. V. Vogler-Neuling, and R. Grange, “95 MHz Bandwidth Electro-Optic Metasurfaces based on Barium Titanate Nanocrystals,” in *2021 Conference on Lasers and Electro-Optics, CLEO 2021 - Proceedings*, May 2021, p. FTh4K.5. doi: 10.1364/cleo\_qels.2021.fth4k.5.
- [215] A. Pomerene *et al.*, “A heterogeneously integrated silicon photonic/lithium niobate travelling wave electro-optic modulator,” *Opt. Express*, vol. 28, no. 2, pp. 1868–1884, Jan. 2020, doi: 10.1364/OE.28.001868.
- [216] M. Churaev *et al.*, “Heterogeneously integrated lithium niobate photonics,” *arXiv:2112.02018*, Dec. 2021, doi: 10.48550/arxiv.2112.02018.

- [217] J. Li, S. T. Wu, S. Brugioni, R. Meucci, and S. Faetti, “Infrared refractive indices of liquid crystals,” *J. Appl. Phys.*, vol. 97, no. 7, p. 073501, Mar. 2005, doi: 10.1063/1.1877815.
- [218] R. Kowerdziej, J. Wróbel, and P. Kula, “Ultrafast electrical switching of nanostructured metadevice with dual-frequency liquid crystal,” *Sci. Rep.*, vol. 9, p. 20367, Dec. 2019, doi: 10.1038/s41598-019-55656-z.
- [219] P. C. Wu *et al.*, “Dynamic beam steering with all-dielectric electro-optic III–V multiple-quantum-well metasurfaces,” *Nat. Commun.*, vol. 10, p. 3654, Dec. 2019, doi: 10.1038/s41467-019-11598-8.
- [220] J. Lee *et al.*, “Ultrafast Electrically Tunable Polaritonic Metasurfaces,” *Adv. Opt. Mater.*, vol. 2, no. 11, pp. 1057–1063, Nov. 2014.
- [221] M. Currie, M. A. Mastro, and V. D. Wheeler, “Characterizing the tunable refractive index of vanadium dioxide,” *Opt. Mater. Express*, vol. 7, no. 5, p. 1697, May 2017, doi: 10.1364/OME.7.001697.
- [222] C. Wan *et al.*, “On the Optical Properties of Thin-Film Vanadium Dioxide from the Visible to the Far Infrared,” *Ann. Phys.*, vol. 531, no. 10, p. 1900188, Oct. 2019, doi: 10.1002/ANDP.201900188.
- [223] Z. Zhu, P. G. Evans, R. F. Haglund, and J. G. Valentine, “Dynamically Reconfigurable Metadevice Employing Nanostructured Phase-Change Materials,” *Nano Lett.*, vol. 17, no. 8, pp. 4881–4885, Aug. 2017, doi: 10.1021/acs.nanolett.7b01767.
- [224] H. Madan *et al.*, “26.5 Terahertz electrically triggered RF switch on epitaxial VO<sub>2</sub>-on-Sapphire (VOS) wafer,” in *2015 IEEE International Electron Devices Meeting (IEDM)*, Dec. 2015, p. 9.3.1-9.3.4. doi: 10.1109/IEDM.2015.7409661.
- [225] A. G. Shabalin *et al.*, “Nanoscale Imaging and Control of Volatile and Non-Volatile Resistive Switching in VO<sub>2</sub>,” *Small*, vol. 16, no. 50, p. 2005439, Dec. 2020, doi: 10.1002/SMLL.202005439.
- [226] T. Kang *et al.*, “Large-scale, power-efficient Au/VO<sub>2</sub> active metasurfaces for ultrafast optical modulation,” *Nanophotonics*, vol. 10, no. 2, pp. 909–918, Jan. 2020, doi: 10.1515/nanoph-2020-0354.
- [227] M. F. Jager *et al.*, “Tracking the insulator-to-metal phase transition in VO<sub>2</sub> with few-femtosecond extreme UV transient absorption spectroscopy,” *Proc. Natl. Acad. Sci. U. S. A.*, vol. 114, no. 36, pp. 9558–9563, Sep. 2017, doi: 10.1073/PNAS.1707602114/SUPPL\_FILE/PNAS.201707602SI.PDF.
- [228] S. Cueff *et al.*, “VO<sub>2</sub> nanophotonics,” *APL Photonics*, vol. 5, no. 11, p. 110901, Nov. 2020, doi: 10.1063/5.0028093.
- [229] K. Dong *et al.*, “A Lithography-Free and Field-Programmable Photonic Metacanvas,” *Adv. Mater.*, vol. 30, no. 5, p. 1703878, Feb. 2018, doi: 10.1002/adma.201703878.
- [230] J. Meng *et al.*, “Electrical Programmable Low-loss high cyclable Nonvolatile Photonic Random-Access Memory,” *arXiv:2203.13337*, Mar. 2022, doi: 10.48550/arxiv.2203.13337.
- [231] W. Kim *et al.*, “ALD-based confined PCM with a metallic liner toward unlimited endurance,” in *Technical Digest - International Electron Devices Meeting, IEDM*, Jan. 2017, p. 4.2.1-4.2.4. doi: 10.1109/IEDM.2016.7838343.
- [232] N. Youngblood *et al.*, “Tunable Volatility of Ge<sub>2</sub>Sb<sub>2</sub>Te<sub>5</sub> in Integrated Photonics,” *Adv. Funct. Mater.*, vol. 29, no. 11, p. 1807571, Mar. 2019, doi: 10.1002/ADFM.201807571.
- [233] J. Choe, “Intel’s 2nd Generation XPoint Memory | TechInsights.” <https://www.techinsights.com/blog/memory/intels-2nd-generation-xpoint-memory>
- [234] C. Ríos *et al.*, “Ultra-compact nonvolatile photonics based on electrically reprogrammable transparent phase change materials,” *arXiv:2105.06010*, 2021.
- [235] R. Greef, M. Kalaji, and L. M. Peter, “Ellipsometric studies of polyaniline growth and redox cycling,” *Faraday Discuss. Chem. Soc.*, vol. 88, pp. 277–289, Jan. 1989, doi: 10.1039/DC9898800277.

- [236] K. Xiong *et al.*, “Video Speed Switching of Plasmonic Structural Colors with High Contrast and Superior Lifetime,” *Adv. Mater.*, vol. 33, no. 41, p. 2103217, Oct. 2021, doi: 10.1002/ADMA.202103217.
- [237] J. Jensen, M. V. Madsen, and F. C. Krebs, “Photochemical stability of electrochromic polymers and devices,” *J. Mater. Chem. C*, vol. 1, no. 32, pp. 4826–4835, Jul. 2013, doi: 10.1039/C3TC30751D.
- [238] J. C. Lacroix, K. K. Kanazawa, and A. Diaz, “Polyaniline: A Very Fast Electrochromic Material,” *J. Electrochem. Soc.*, vol. 136, no. 5, pp. 1308–1313, May 1989, doi: 10.1149/1.2096912/XML.
- [239] J. Heinze, B. A. Frontana-Uribe, and S. Ludwigs, “Electrochemistry of Conducting Polymers—Persistent Models and New Concepts†,” *Chem. Rev.*, vol. 110, no. 8, pp. 4724–4771, Aug. 2010, doi: 10.1021/CR900226K.
- [240] Z. Li *et al.*, “Correlated Perovskites as a New Platform for Super-Broadband-Tunable Photonics,” *Adv. Mater.*, vol. 28, no. 41, pp. 9117–9125, Nov. 2016, doi: 10.1002/adma.201601204.
- [241] M. Huang *et al.*, “Voltage-gated optics and plasmonics enabled by solid-state proton pumping,” *Nat. Commun.*, vol. 10, p. 5030, Dec. 2019, doi: 10.1038/s41467-019-13131-3.
- [242] H. T. Zhang *et al.*, “Reconfigurable perovskite nickelate electronics for artificial intelligence,” *Science*, vol. 375, no. 6580, pp. 533–539, Feb. 2022, doi: 10.1126/SCIENCE.ABJ7943/SUPPL\_FILE/SCIENCE.ABJ7943\_SI\_001.PDF.
- [243] Y. Li, J. Van De Groep, A. A. Talin, and M. L. Brongersma, “Dynamic Tuning of Gap Plasmon Resonances Using a Solid-State Electrochromic Device,” *Nano Lett.*, vol. 19, no. 11, pp. 7988–7995, Nov. 2019, doi: 10.1021/ACS.NANOLETT.9B03143/SUPPL\_FILE/NL9B03143\_SI\_001.PDF.
- [244] J. Eaves-Rathert, E. Kovalik, C. F. Ugwu, B. R. Rogers, C. L. Pint, and J. G. Valentine, “Dynamic Color Tuning with Electrochemically Actuated TiO<sub>2</sub> Metasurfaces,” *Nano Lett.*, vol. 22, no. 4, pp. 1626–1632, Feb. 2022, doi: 10.1021/ACS.NANOLETT.1C04613/SUPPL\_FILE/NL1C04613\_SI\_001.PDF.
- [245] R. T. Wen, C. G. Granqvist, and G. A. Niklasson, “Eliminating degradation and uncovering ion-trapping dynamics in electrochromic WO<sub>3</sub> thin films,” *Nat. Mater.*, vol. 14, no. 10, pp. 996–1001, Aug. 2015, doi: 10.1038/nmat4368.
- [246] E. Hopmann and A. Y. Elezzabi, “Plasmochromic Nanocavity Dynamic Light Color Switching,” *Nano Lett.*, vol. 20, no. 3, pp. 1876–1882, Mar. 2020, doi: 10.1021/ACS.NANOLETT.9B05088/SUPPL\_FILE/NL9B05088\_SI\_001.PDF.
- [247] G. Wang, X. Chen, S. Liu, C. Wong, and S. Chu, “Mechanical Chameleon through Dynamic Real-Time Plasmonic Tuning,” *ACS Nano*, vol. 10, no. 2, pp. 1788–1794, Feb. 2016, doi: 10.1021/acsnano.5b07472.
- [248] C. J. Barile, D. J. Slotcavage, J. Hou, M. T. Strand, T. S. Hernandez, and M. D. McGehee, “Dynamic Windows with Neutral Color, High Contrast, and Excellent Durability Using Reversible Metal Electrodeposition,” *Joule*, vol. 1, no. 1, pp. 133–145, Sep. 2017, doi: 10.1016/J.JOULE.2017.06.001.
- [249] K. J. Palm, J. B. Murray, T. C. Narayan, and J. N. Munday, “Dynamic Optical Properties of Metal Hydrides,” *ACS Photonics*, vol. 5, no. 11, pp. 4677–4686, Nov. 2018, doi: 10.1021/acsphotonics.8b01243.
- [250] K. Tajima, Y. Yamada, S. Bao, M. Okada, and K. Yoshimura, “Flexible all-solid-state switchable mirror on plastic sheet,” *Appl. Phys. Lett.*, vol. 92, no. 4, p. 041912, 2008, doi: 10.1063/1.2839298.
- [251] J. Li, S. Kamin, G. Zheng, F. Neubrech, S. Zhang, and N. Liu, “Addressable metasurfaces for dynamic holography and optical information encryption,” *Sci. Adv.*, vol. 4, no. 6, p. eaar6768, Jun. 2018, doi: 10.1126/sciadv.aar6768.
- [252] X. Duan and N. Liu, “Magnesium for Dynamic Nanoplasmonics,” *Acc. Chem. Res.*, vol. 52, no. 7, pp. 1979–1989, Jul. 2019, doi: 10.1021/acs.accounts.9b00157.

- [253] W. Yang *et al.*, “All-dielectric metasurface for high-performance structural color,” *Nat. Commun.*, vol. 11, p. 1864, Apr. 2020, doi: 10.1038/s41467-020-15773-0.
- [254] J. Li, P. Yu, S. Zhang, and N. Liu, “A Reusable Metasurface Template,” *Nano Lett.*, vol. 20, no. 9, pp. 6845–6851, Sep. 2020, doi: 10.1021/ACS.NANOLETT.0C02876/ASSET/IMAGES/LARGE/NL0C02876\_0005.JPG.
- [255] J. Hu *et al.*, “Lattice-Resonance Metalenses for Fully Reconfigurable Imaging,” *ACS Nano*, vol. 13, no. 4, pp. 4613–4620, Apr. 2019, doi: 10.1021/acsnano.9b00651.
- [256] J. Lu *et al.*, “A Versatile Metasurface Enabling Superwettability for Self-Cleaning and Dynamic Color Response,” *Adv. Opt. Mater.*, vol. 10, p. 2101781, Jan. 2022, doi: 10.1002/ADOM.202101781.
- [257] L. Bi *et al.*, “Magneto-Optical Thin Films for On-Chip Monolithic Integration of Non-Reciprocal Photonic Devices,” *Materials*, vol. 6, no. 11, pp. 5094–5117, Nov. 2013, doi: 10.3390/ma6115094.
- [258] A. Kazlou, A. L. Chekhov, A. I. Stognij, I. Razdolski, and A. Stupakiewicz, “Surface Plasmon-Enhanced Photomagnetic Excitation of Spin Dynamics in Au/YIG:Co Magneto-Plasmonic Crystals,” *ACS Photonics*, vol. 8, no. 8, pp. 2197–2202, Aug. 2021, doi: 10.1021/ACSPHOTONICS.1C00476/SUPPL\_FILE/PH1C00476\_SI\_001.PDF.
- [259] P. Pintus *et al.*, “A low-power integrated magneto-optic modulator on silicon for cryogenic applications,” *arXiv:2109.04538*, Sep. 2021, doi: 10.48550/arxiv.2109.04538.
- [260] M. Ren *et al.*, “Nanostructured Plasmonic Medium for Terahertz Bandwidth All-Optical Switching,” *Adv. Mater.*, vol. 23, no. 46, pp. 5540–5544, Dec. 2011, doi: 10.1002/adma.201103162.
- [261] M. R. Shcherbakov *et al.*, “Ultrafast all-optical tuning of direct-gap semiconductor metasurfaces,” *Nat. Commun.*, vol. 8, no. 1, p. 17, 2017, doi: 10.1038/s41467-017-00019-3.
- [262] Y. Wu, L. Kang, H. Bao, and D. H. Werner, “Exploiting Topological Properties of Mie-Resonance-Based Hybrid Metasurfaces for Ultrafast Switching of Light Polarization,” *ACS Photonics*, vol. 7, no. 9, pp. 2362–2373, Sep. 2020, doi: 10.1021/ACSPHOTONICS.0C00858/SUPPL\_FILE/PH0C00858\_SI\_001.PDF.
- [263] M. N. Julian, C. Williams, S. Borg, S. Bartram, and H. J. Kim, “Reversible optical tuning of GeSbTe phase-change metasurface spectral filters for mid-wave infrared imaging,” *Optica*, vol. 7, pp. 746–754, 2020, doi: 10.1364/optica.392878.
- [264] C. Williams, N. Hong, M. Julian, S. Borg, and H. J. Kim, “Tunable mid-wave infrared Fabry-Perot bandpass filters using phase-change GeSbTe,” *Opt. Express*, vol. 28, no. 7, p. 10583, Mar. 2020, doi: 10.1364/oe.390538.
- [265] A. Sarangan, K. Hirakawa, and R. Heenkenda, “Tunable optical filter using phase change materials for smart IR night vision applications,” *Opt. Express*, vol. 29, no. 21, pp. 33795–33803, Oct. 2021, doi: 10.1364/OE.440299.
- [266] S. Q. Li, X. Xu, R. M. Veetil, V. Valuckas, R. Paniagua-Domínguez, and A. I. Kuznetsov, “Phase-only transmissive spatial light modulator based on tunable dielectric metasurface,” *Science*, vol. 364, no. 6445, pp. 1087–1090, Jun. 2019, doi: 10.1126/science.aaw6747.
- [267] J. Park *et al.*, “All-solid-state spatial light modulator with independent phase and amplitude control for three-dimensional LiDAR applications,” *Nat. Nanotechnol.*, vol. 16, no. 1, pp. 69–76, Oct. 2020, doi: 10.1038/s41565-020-00787-y.
- [268] I. Moreno, C. Iemmi, A. Márquez, J. Campos, and M. J. Yzuel, “Modulation light efficiency of diffractive lenses displayed in a restricted phase-mostly modulation display,” *Appl. Opt.*, vol. 43, no. 34, pp. 6278–6284, Dec. 2004, doi: 10.1364/AO.43.006278.
- [269] P. Thureja, G. K. Shirmanesh, K. T. Fountaine, R. Sokhoyan, M. Grajower, and H. A. Atwater, “Array-level inverse design of beam steering active metasurfaces,” *ACS Nano*, vol. 14, no. 11, pp. 15042–15055, Nov. 2020, doi: 10.1021/ACSNANO.0C05026/SUPPL\_FILE/NN0C05026\_SI\_002.AVI.

- [270] C. H. Liu *et al.*, “Ultrathin van der Waals Metalenses,” *Nano Lett.*, vol. 18, no. 11, pp. 6961–6966, Nov. 2018, doi: 10.1021/ACS.NANOLETT.8B02875/ASSET/IMAGES/LARGE/NL-2018-02875U\_0004.JPG.
- [271] J. Hua, W. Qiao, and L. Chen, “Recent Advances in Planar Optics-Based Glasses-Free 3D Displays,” *Front. Nanotechnol.*, vol. 4, p. 829011, Mar. 2022, doi: 10.3389/FNANO.2022.829011/BIBTEX.
- [272] D. Fattal *et al.*, “A multi-directional backlight for a wide-angle, glasses-free three-dimensional display,” *Nature*, vol. 495, no. 7441, pp. 348–351, Mar. 2013, doi: 10.1038/nature11972.
- [273] D. Wen, J. J. Cadusch, J. Meng, and K. B. Crozier, “Light field on a chip: metasurface-based multicolor holograms,” *Adv. Photonics*, vol. 3, no. 2, p. 024001, Feb. 2021, doi: 10.1111/1.AP.3.2.024001.
- [274] G. Arya, W. F. Li, C. Roques-Carmes, M. Soljačić, S. G. Johnson, and Z. Lin, “End-to-End Optimization of Metasurfaces for Imaging with Compressed Sensing,” *arXiv:2201.12348*, Jan. 2022.
- [275] L. Huang, S. Zhang, and T. Zentgraf, “Metasurface holography: From fundamentals to applications,” *Nanophotonics*, vol. 7, no. 6, pp. 1169–1190, Jun. 2018, doi: 10.1515/NANOPH-2017-0118/ASSET/GRAPHIC/J\_NANOPH-2017-0118 FIG\_006.JPG.
- [276] J. Li, P. Yu, S. Zhang, and N. Liu, “Electrically-controlled digital metasurface device for light projection displays,” *Nat. Commun.*, vol. 11, no. 1, p. 3574, Jul. 2020, doi: 10.1038/s41467-020-17390-3.
- [277] H. Gao *et al.*, “Recent advances in optical dynamic meta-holography,” *Opto-Electron. Adv.*, vol. 4, no. 11, pp. 210030-, 2021, doi: 10.29026/OEA.2021.210030.
- [278] S. G. Carrillo *et al.*, “A Nonvolatile Phase-Change Metamaterial Color Display,” *Adv. Opt. Mater.*, vol. 7, no. 18, p. 1801782, Sep. 2019, doi: 10.1002/adom.201801782.
- [279] H. Liu *et al.*, “Switchable All-Dielectric Metasurfaces for Full-Color Reflective Display,” *Adv. Opt. Mater.*, vol. 7, no. 8, p. 1801639, Apr. 2019, doi: 10.1002/ADOM.201801639.
- [280] O. Hemmatyar *et al.*, “Enhanced Meta-Displays Using Advanced Phase-Change Materials,” *arXiv:2107.12159*, Jul. 2021.
- [281] J. Zhang *et al.*, “Electrical tuning of metal-insulator-metal metasurface with electro-optic polymer,” *Appl. Phys. Lett.*, vol. 113, no. 23, p. 231102, Dec. 2018, doi: 10.1063/1.5054964.
- [282] A. Otomo, J. Zhang, T. Tanemura, Y. Nakano, and Y. Kosugi, “Active metasurface modulator with electro-optic polymer using bimodal plasmonic resonance,” *Opt. Express*, vol. 25, no. 24, pp. 30304–30311, Nov. 2017, doi: 10.1364/OE.25.030304.
- [283] A. She, S. Zhang, S. Shian, D. R. Clarke, and F. Capasso, “Adaptive metalenses with simultaneous electrical control of focal length, astigmatism, and shift,” *Sci. Adv.*, vol. 4, no. 2, p. eaap9957, Feb. 2018, doi: 10.1126/sciadv.aap9957.
- [284] R. J. Zawadzki *et al.*, “High-speed adaptive optics for imaging of the living human eye,” *Opt. Express*, vol. 23, no. 18, pp. 23035–23052, Sep. 2015, doi: 10.1364/OE.23.023035.
- [285] X. Guo, Y. Ding, Y. Duan, and X. Ni, “Nonreciprocal metasurface with space–time phase modulation,” *Light Sci. Appl.*, vol. 8, p. 123, Dec. 2019, doi: 10.1038/s41377-019-0225-z.
- [286] X. Wang, A. Díaz-Rubio, H. Li, S. A. Tretyakov, and A. Alù, “Theory and Design of Multifunctional Space-Time Metasurfaces,” *Phys. Rev. Appl.*, vol. 13, no. 4, p. 044040, Apr. 2020, doi: 10.1103/PHYSREVAPPLIED.13.044040/FIGURES/13/MEDIUM.
- [287] L. Zhang and T. J. Cui, “Space-Time-Coding Digital Metasurfaces: Principles and Applications,” *Research*, vol. 2021, p. 9802673, May 2021, doi: 10.34133/2021/9802673.
- [288] A. Howes *et al.*, “Optical Limiting Based on Huygens’ Metasurfaces,” *Nano Lett.*, vol. 20, no. 6, pp. 4638–4644, Jun. 2020, doi: 10.1021/ACS.NANOLETT.0C01574/SUPPL\_FILE/NL0C01574\_SI\_001.PDF.

- [289] S. A. Mann *et al.*, “Ultrafast optical switching and power limiting in intersubband polaritonic metasurfaces,” *Optica*, vol. 8, no. 5, pp. 606–613, May 2021, doi: 10.1364/OPTICA.415581.
- [290] Y. Liu *et al.*, “Dynamic thermal camouflage via a liquid-crystal-based radiative metasurface,” *Nanophotonics*, vol. 9, no. 4, pp. 855–863, Apr. 2020, doi: 10.1515/NANOPH-2019-0485/ASSET/GRAPHIC/J\_NANOPH-2019-0485 FIG\_004.JPG.
- [291] “A New Family of Ultralow Loss Reversible Phase-Change Materials for Photonic Integrated Circuits: Sb<sub>2</sub>S<sub>3</sub> and Sb<sub>2</sub>Se<sub>3</sub> - Delaney - 2020 - Advanced Functional Materials - Wiley Online Library.” <https://onlinelibrary.wiley.com/doi/full/10.1002/adfm.202002447> (accessed Sep. 09, 2022).
- [292] “Guided-wave intensity modulators using amplitude-and-phase perturbations | IEEE Journals & Magazine | IEEE Xplore.” <https://ieeexplore.ieee.org/document/4021> (accessed Sep. 03, 2022).
- [293] X. Y. Sun *et al.*, “Single-Step Deposition of Cerium-Substituted Yttrium Iron Garnet for Monolithic On-Chip Optical Isolation,” *ACS Photonics*, vol. 2, no. 7, pp. 856–863, Jul. 2015, doi: 10.1021/acsphotonics.5b00026.
- [294] “Unravelling the interplay of local structure and physical properties in phase-change materials | Nature Materials.” <https://www.nature.com/articles/nmat1539> (accessed Sep. 03, 2022).
- [295] F. Rao *et al.*, “Reducing the stochasticity of crystal nucleation to enable subnanosecond memory writing,” *Science*, vol. 358, no. 6369, pp. 1423–1427, Dec. 2017, doi: 10.1126/science.aao3212.
- [296] J. Kalikka, J. Akola, and R. O. Jones, “Simulation of crystallization in Ge<sub>2</sub> Sb<sub>2</sub> Te<sub>5</sub>: A memory effect in the canonical phase-change material,” *Phys. Rev. B - Condens. Matter Mater. Phys.*, vol. 90, no. 18, p. 184109, Nov. 2014, doi: 10.1103/PhysRevB.90.184109.
- [297] W. Zhang, R. Mazzarello, M. Wuttig, and E. Ma, “Designing crystallization in phase-change materials for universal memory and neuro-inspired computing,” *Nature Reviews Materials*, vol. 4, no. 3. Nature Publishing Group, pp. 150–168, Mar. 01, 2019. doi: 10.1038/s41578-018-0076-x.
- [298] T. Matsunaga *et al.*, “From local structure to nanosecond recrystallization dynamics in AgInSbTe phase-change materials,” *Nat. Mater.*, vol. 10, no. 2, pp. 129–134, Feb. 2011, doi: 10.1038/nmat2931.
- [299] B. S. Lee *et al.*, “Observation of the role of subcritical nuclei in crystallization of a glassy solid,” *Science*, vol. 326, no. 5955, pp. 980–984, Nov. 2009, doi: 10.1126/science.1177483.
- [300] M. Salinga *et al.*, “Measurement of crystal growth velocity in a melt-quenched phase-change material,” *Nat. Commun.*, vol. 4, p. 2371, Aug. 2013, doi: 10.1038/ncomms3371.
- [301] J.-S. Park *et al.*, “All-Glass, Large Metalens at Visible Wavelength Using Deep-Ultraviolet Projection Lithography,” *Nano Lett.*, vol. 19, no. 12, pp. 8673–8682, Dec. 2019, doi: 10.1021/acs.nanolett.9b03333.
- [302] T. Hu *et al.*, “CMOS-compatible a-Si metalenses on a 12-inch glass wafer for fingerprint imaging,” *Nanophotonics*, vol. 9, no. 4, pp. 823–830, Apr. 2020, doi: 10.1515/nanoph-2019-0470.
- [303] M. A. Verschueren, M. W. Knight, M. Megens, and A. Polman, “Nanoscale spatial limitations of large-area substrate conformal imprint lithography,” *Nanotechnology*, vol. 30, no. 34, p. 345301, Jun. 2019, doi: 10.1088/1361-6528/ab1c86.